Issue no. 1/2006
ECR Edition

MAGNETOM FLASH

www.siemens.com/magnetom-world

Price 10,- EUR

Content

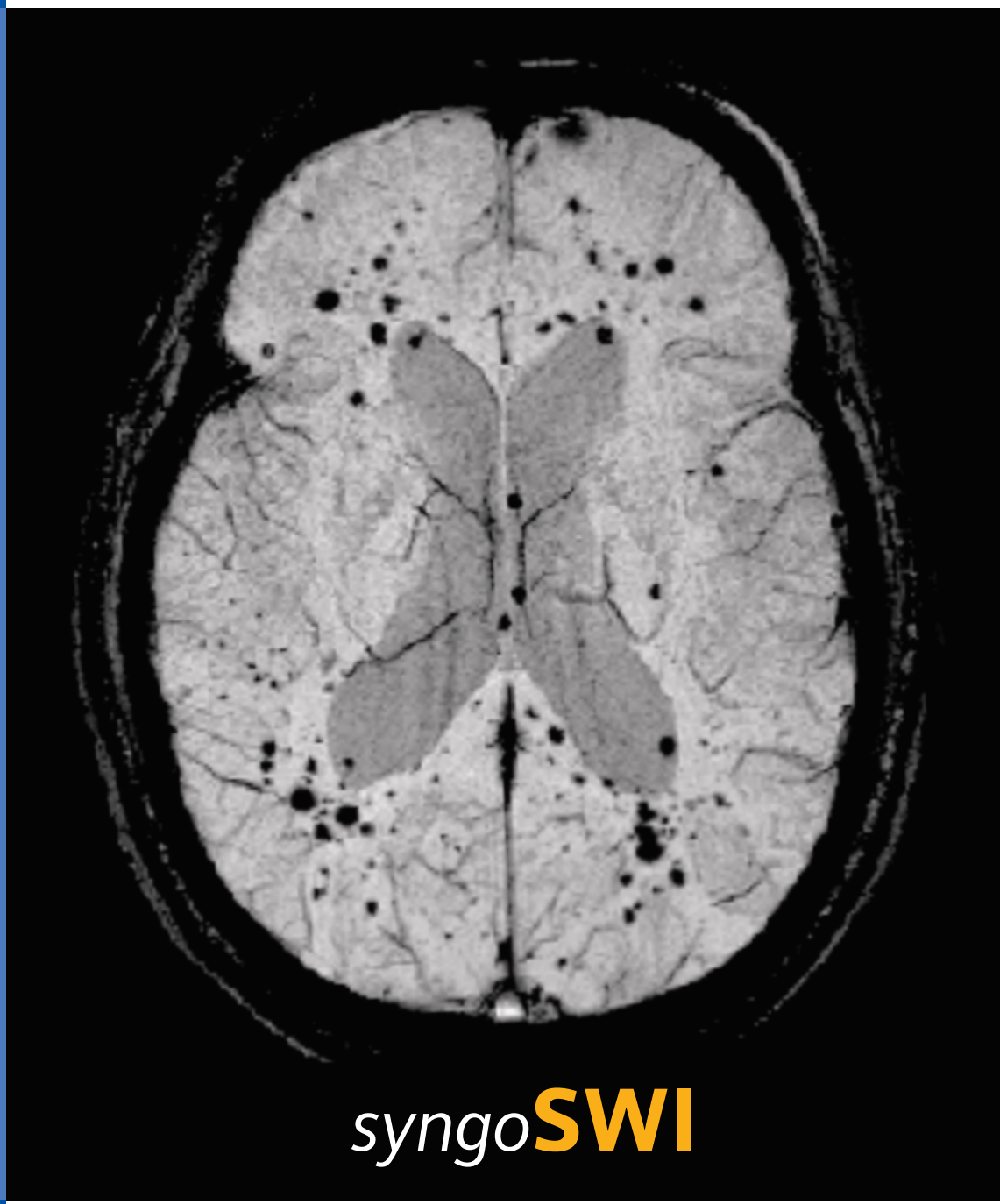

32

SIEMENS
medical

Dear MAGNETOM User,

See More & Work Faster

At this year's RSNA, one of the big hits at the MR booth was SWI (Susceptibility Weighted Imaging). This technique – long TE flow compensated gradient echo imaging providing enhanced contrast with the combination of phase and magnitude information – has provided surprising results in detecting intracranial bleeding and seeing minute intracranial vascular malformations. The verdict was unanimous: "You definitely see more with SWI". Starting on page 70 you will find SWI case reports.

SWI is not a brand new sequence; in fact, it has been around quite a long time. But integrating this sequence within the clinical routine had always been difficult due to long examination times of up to 11 minutes. However, times have changed and today's Tim technology (Total imaging matrix) with GRAPPA Parallel Imaging technique allows this sequence to be run in just 3 to 4 minutes. Whatever the application area – body imaging with VIBE in 12 seconds, whole body imaging in less than 10 minutes, ultra fast dynamic MR Angiography (MRA) or new sequences like SWI – you always work faster with Tim and GRAPPA.

The 2005 MAGNETOM World Summit came to Singapore. The images on pages 116 ff. and a short summary of some of the presentations will offer you a taste of a very successful Summit, with attendance numbers of 350 MAGNETOM users and an unsurpassed number of presentations covering almost every area in MR, including molecular imaging.

But don't worry if you have missed it, the 5th MAGNETOM World Summit in San Diego, California, USA is just around the corner. Between June 8 and June 11, 2006 you'll find an excellent platform to establish personal contacts, exchange valuable information, learn from the experience of other users and to share your own expertise. For a glance at the agenda and registration please visit us at www.siemens.com/magnetom-world.

Enjoy reading MAGNETOM Flash

A. Nejat Bengi

The Editorial Team

We appreciate your comments.
Please contact us at magnetomworld.med@siemens.com

Lisa Reid,
US Installed Base Manager,
Malvern, PA

Dagmar Thomsik-Schröpfer, Ph.D.
MR Marketing-Products, Erlangen

Antje Hellwich
Associate Editor

A. Nejat Bengi, M.D.
Editor in Chief

Heike Weh,
Clinical Data Manager,
Erlangen

Bernhard Baden,
Clinical Data Manager,
Erlangen

Tony Enright, Ph.D.
Asia Pacific Collaborations,
Australia

Milind Dhamankar, M.D.
Manager Clinical MR
Research Collaborations,
Siemens Medical
Solutions USA

Peter Kreisler, Ph.D.
Collaborations & Applications,
Erlangen

Gary R. McNeal, MS (BME)
Advanced Application Specialist,
Cardiovascular MR Imaging
Siemens Medical Solutions USA

Cécile Mohr, Ph.D
Head of Market Segment
Management, Erlangen

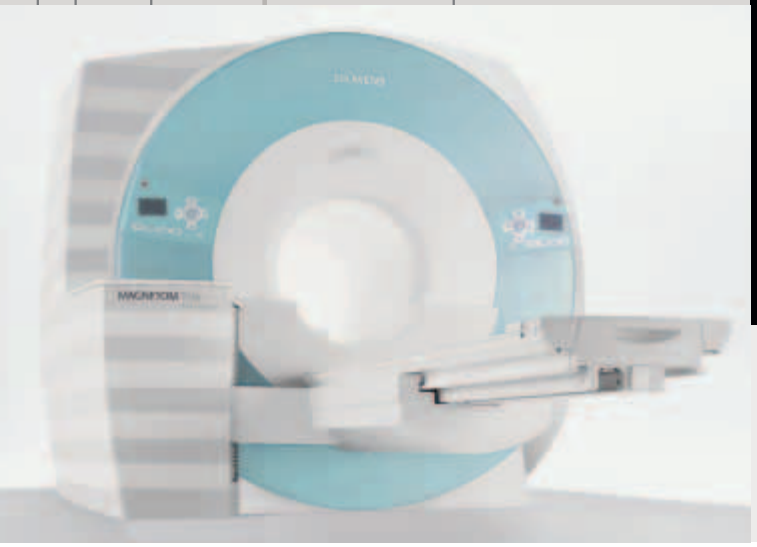

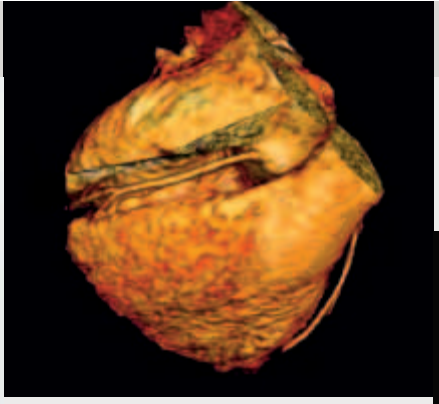

Coronary MRA. ***Page 19***

Interventional MRI. ***Page 39***

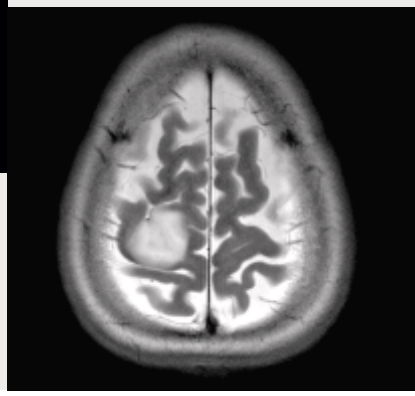

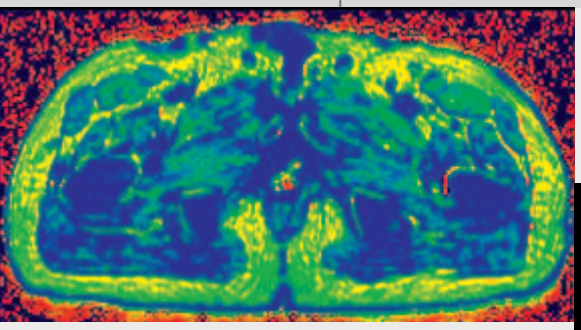

T2 maps in diagnosis of lymph node metastasis.* ***Page 44***

Perioperative use of DTI. ***Page 40***

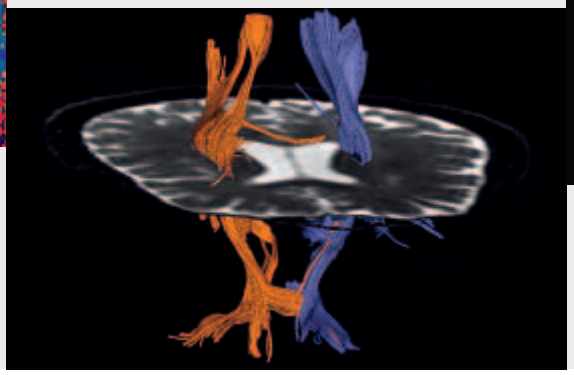

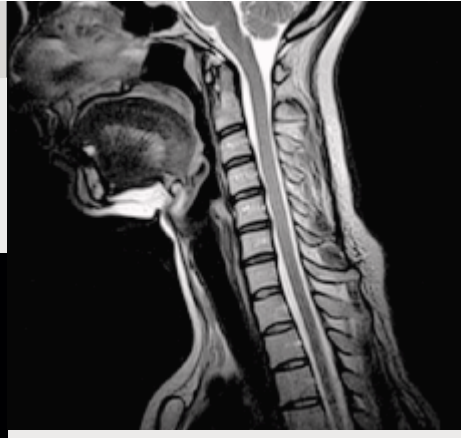

MAGNETOM C! Cervical spine. ***Page 118***

TECHNOLOGY

LIFE

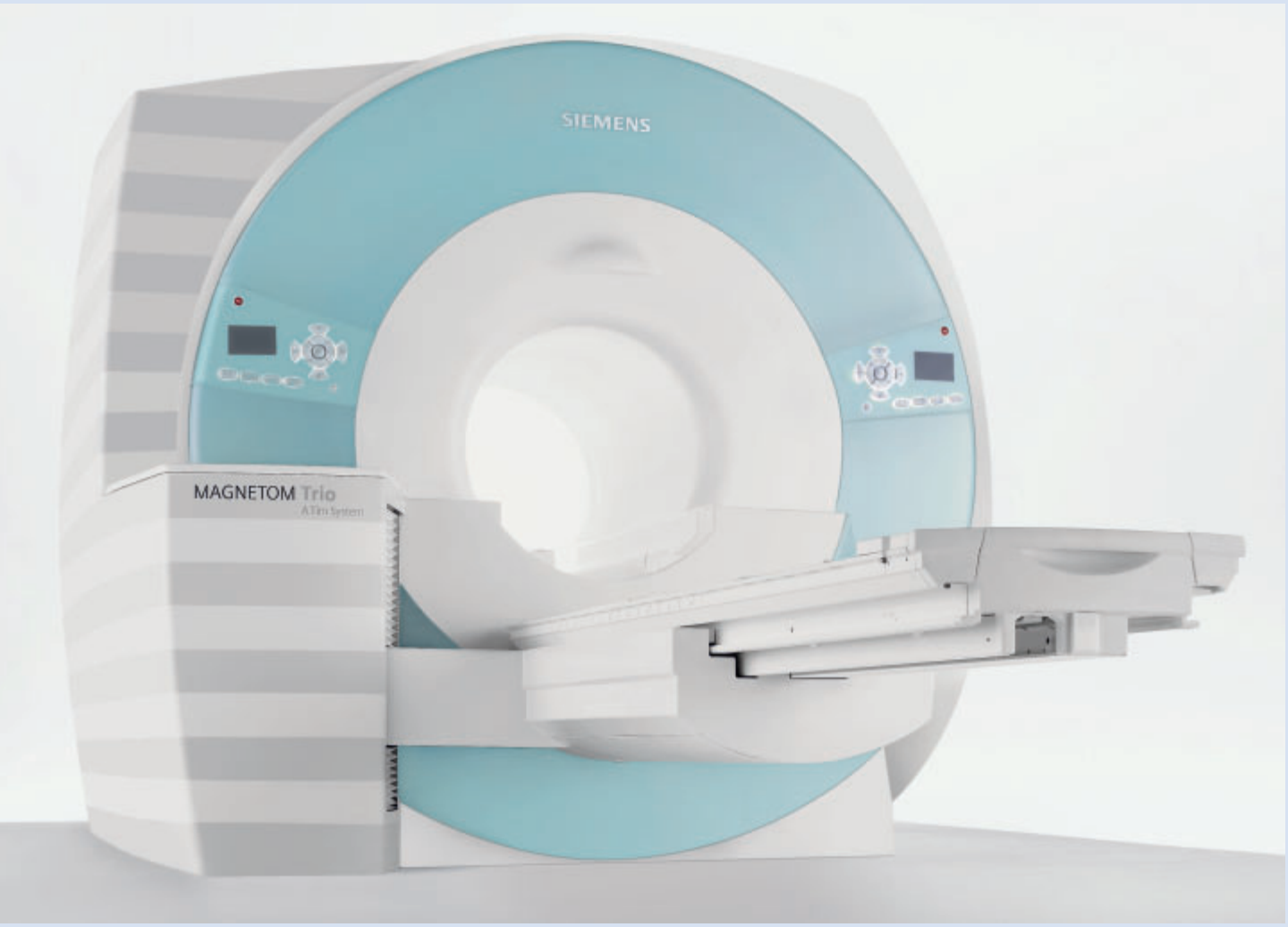
SIEMENS
MAGNETOM Trio


SIEMENS

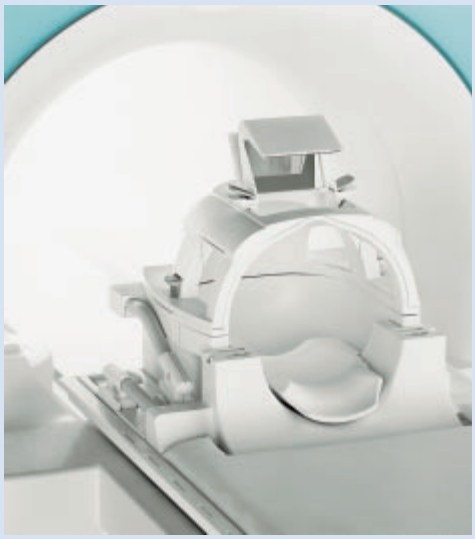

BLADE – For Clear-Cut Imaging

Innovation for every day use

BLADE is a technique that incorporates a k-space trajectory radial in nature and a motion correction which reduces dramatically sensitivity to movement. BLADE works fully automatically.

BLADE eliminates repeats

BLADE ensures that you get the best results all the time, from the youngest to the oldest patients, without having to worry if the images will be good enough. With BLADE, you can confidently acquire the data and make the diagnosis. No need to repeat the measurement and no need to recall the patient to rescan.

BLADE reduces the sedation rate

With BLADE's low sensitivity to motion, you can now start thinking about reducing sedation rate in pediatric or anxious patients. And this is not only good for your patient but also increases your time-efficiency.

BLADE for all contrasts and all orientations

BLADE supports your workflow. Whatever orientation – axial, sagittal or coronal – or contrast – T1, T2 and Dark Fluid – you need.

BLADE is coil-independent

BLADE works with Tim coils, the multi-channel Matrix coils such as the 12-channel Head Matrix, the 16-channel Head-Neck Matrix combination, dedicated array coils, as well as accessory coils.

BLADE at all field strengths

Discover BLADE on Tim Upgrades and all Tim systems – at 1.5T MAGNETOM Avanto, Espree, Symphony and at 3T MAGNETOM Trio.

BLADE – All contrasts, all orientations

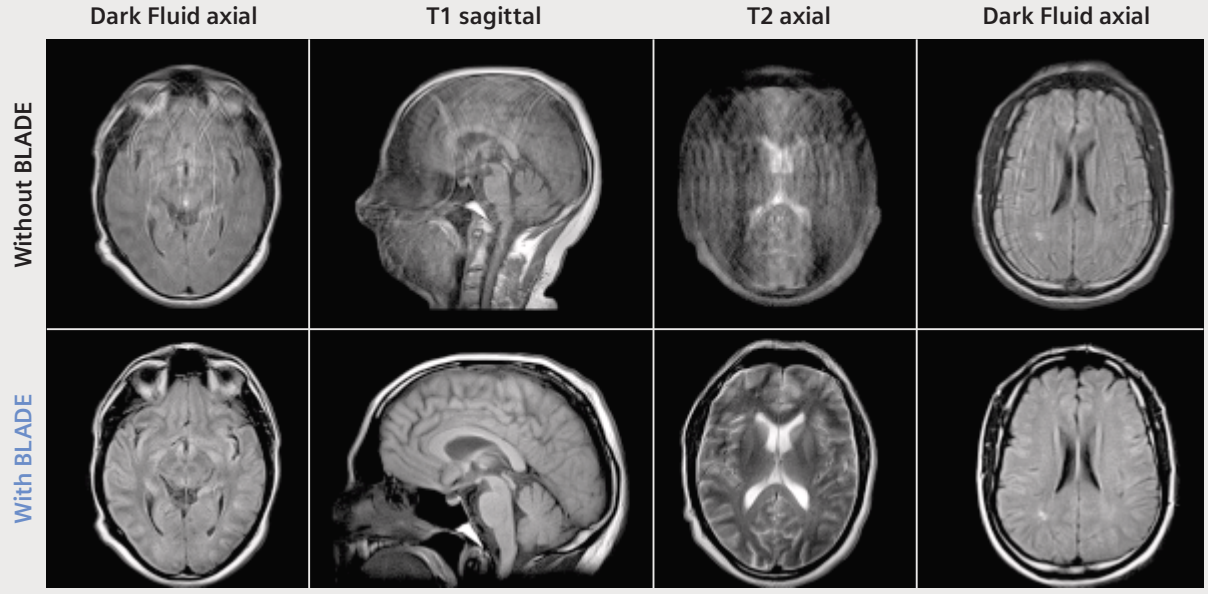

MAGNETOM Trio and MAGNETOM Espree with Tim.

Courtesy of Klinikum Bremen Mitte, Germany and Mayo Clinic, Jacksonville, Florida, USA

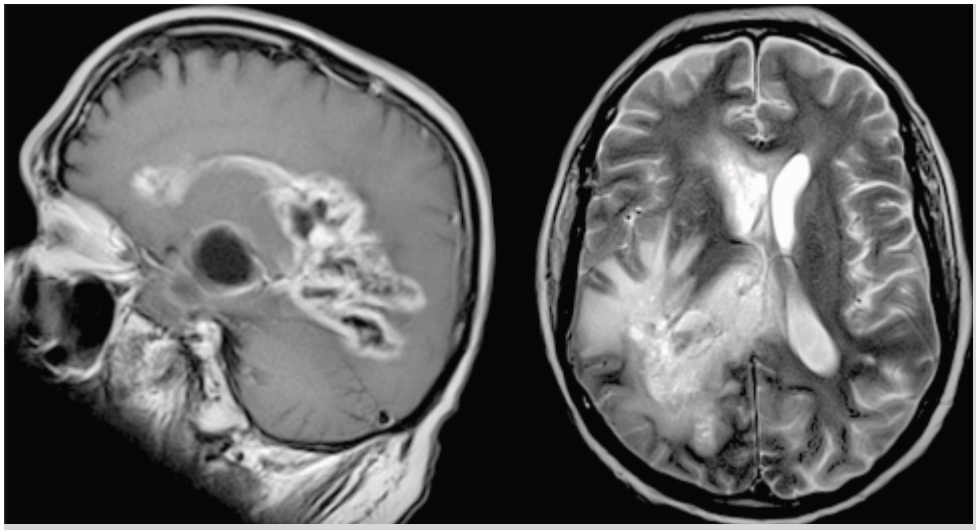

Tumor
MAGNETOM Avanto 12-channel Head Matrix. T1 sagittal post contrast with BLADE.
Courtesy of Northwestern Memorial Hospital, Chicago, USA

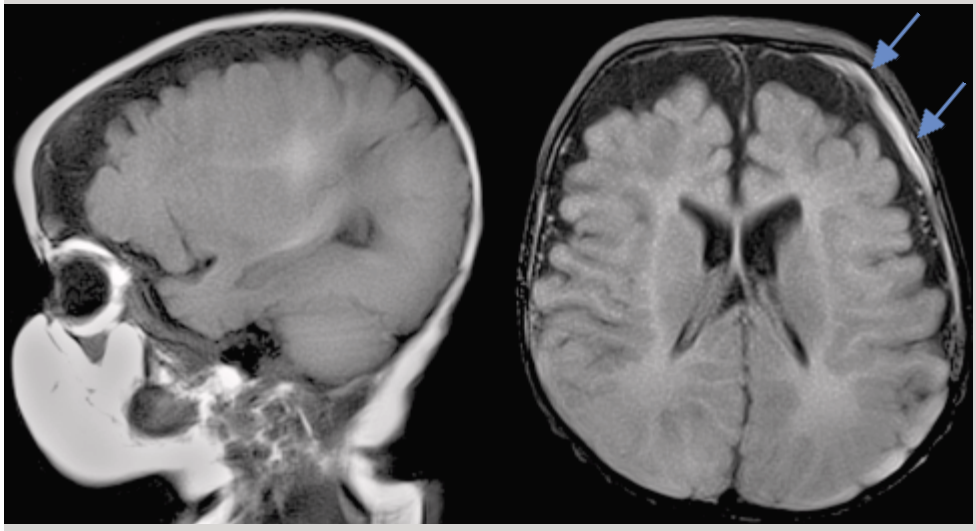

Pediatric imaging. Left fronto-temporal subdural hematoma. Non-sedated child 3-month-old. MAGNETOM Avanto 12-channel Head Matrix. T1 sagittal with BLADE Dark Fluid axial with BLADE.
Courtesy of Children's Hospital of Philadelphia, USA

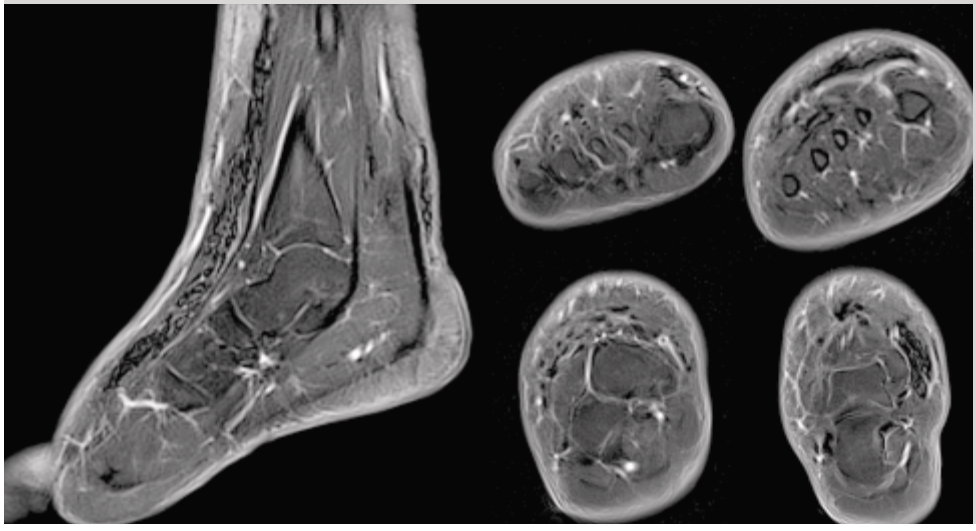

Orthopedic imaging with fat suppression in the bone marrow of a 15-year-old child. MAGNETOM Avanto 12-channel Head Matrix. T2 TIRM sagittal and axial with BLADE.
Courtesy of Children's Hospital of Philadelphia, USA

Abdomen and Pelvis

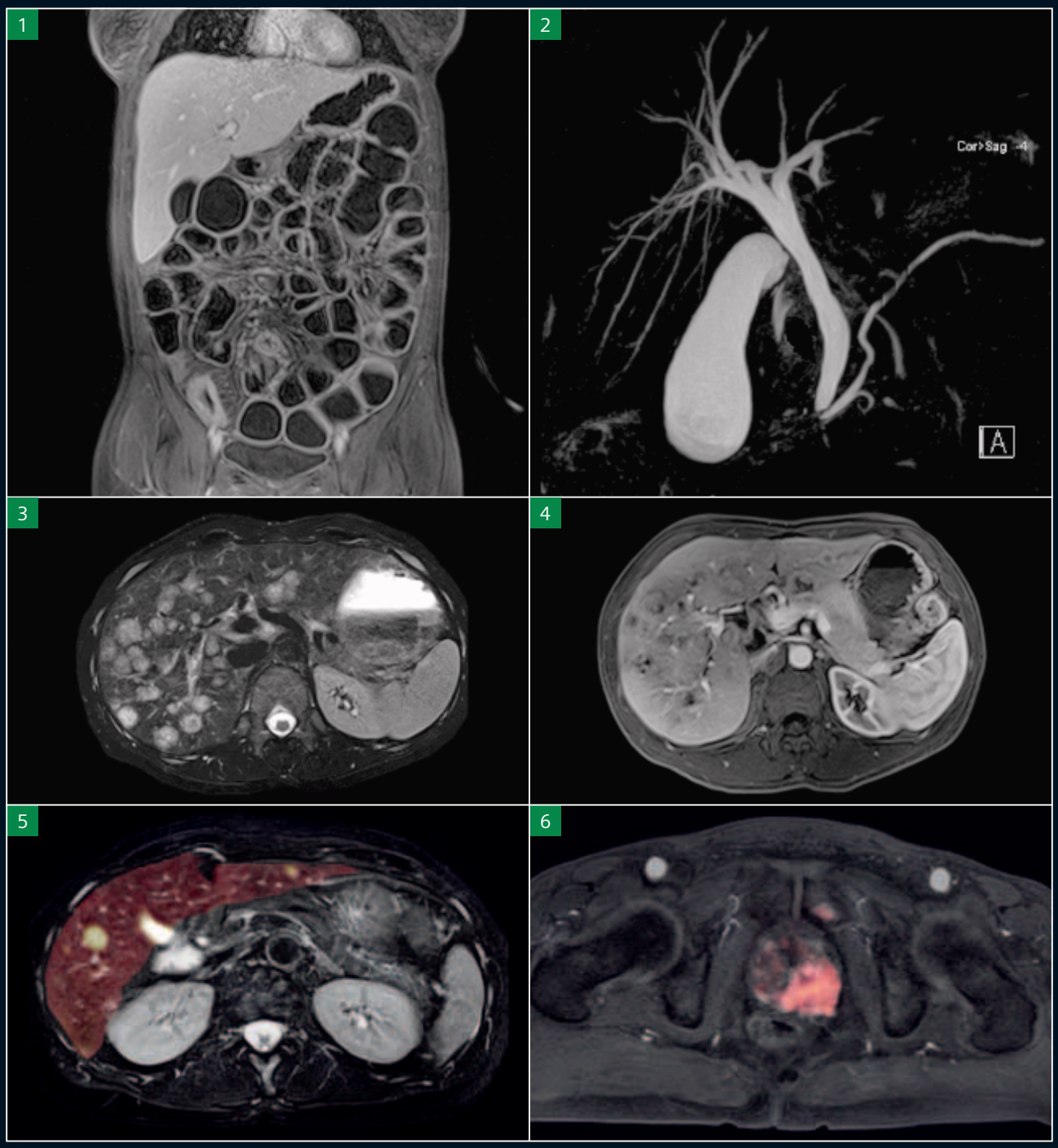

[1, 3, 4, 5] Courtesy of LMU Grosshadern, Munich, Germany
[2] Courtesy of St. Vincent's Melbourne, Melbourne, Australia
[6] Courtesy of Gunma Cancer Center, Gunma, Japan

Early Gastric Cancer Diagnosis using Body Diffusion Imaging

Noriatsu Ichiba, M.D.

Tokyo Jikei University School of Medicine, Tokyo, Japan

Patient history

55-year-old male; chief complaint was epigastralgia.

Sequence details

Respiratory triggered diffusion-weighted imaging (DWI) with PACE (Prospective Acquisition CorrEction). Axial scan, CHESS pulse, TR 1400, TE 64, Bandwidth 2368, Averaging 5, GRAPPA factor 2, b = 50 and b = 800, FOV 500 mm, Matrix 192, slice thickness 7 mm, number of slices 32, respiratory triggering with PACE.

Results

There was no remarkable abnormality on the T1-weighted image (Fig.1), the T2-weighted image (Fig. 2) and early phase (Fig. 3) and delayed phase (Fig. 4) of contrast enhanced dynamic MRI.

There was a flat membranous lesion on gastric lesser curvature with slightly high signal on low b-value DWI (b = 50, Fig. 5) and high b-value DWI (b = 800, Fig. 6). This finding was suggestive of early gastric cancer, corresponding with endoscopic finding. Additionally, a small lymph node showed high signal on DWI, suggestive of metastasis.

Discussion

Early gastric cancer was detected with diffusion-weighted imaging (DWI). With use of antiperistalsis agents, the detectability of membranous lesion may improve on DWI.

Scanner	*MAGNETOM Avanto 1.5T with SQ-engine*
Coils	*Body Matrix Coil, Spine Matrix Coil*
Software version /add-on	*syngo MR 2004V / Work-in-progress sequence**

*This information about this product is preliminary. The product is under development and not commercially available in the US and its future availability cannot be ensured.

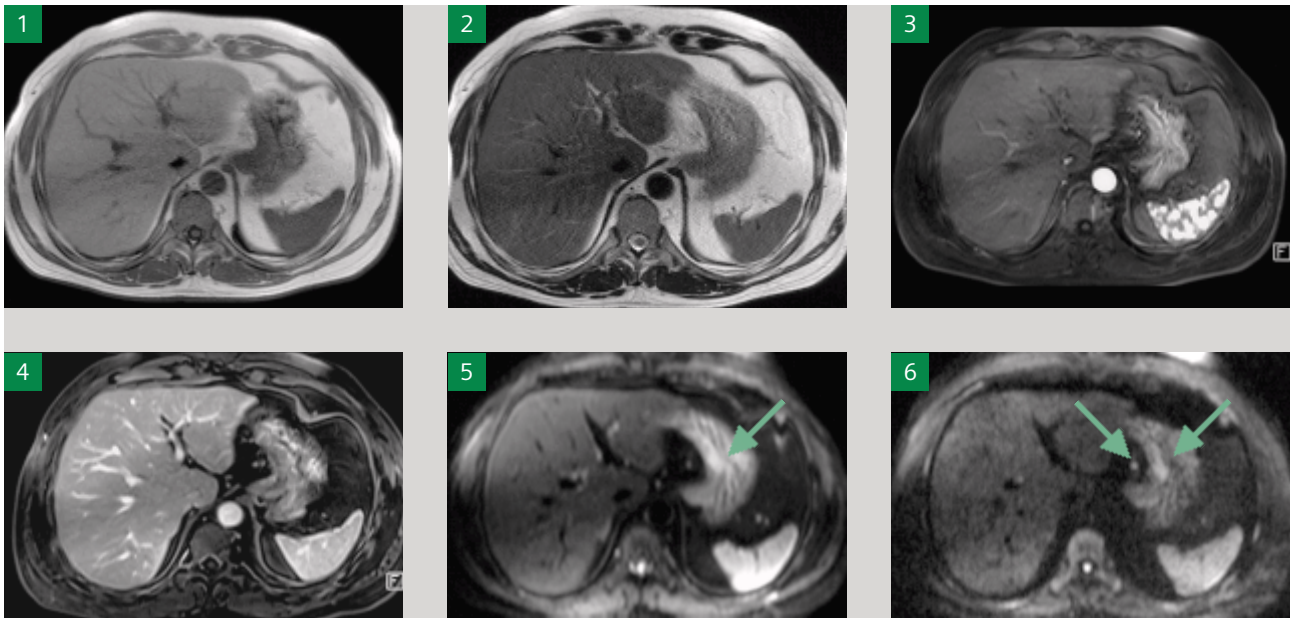

Detection of Esophageal Cancer Using Body Diffusion Imaging

Takashi Koyama, M.D., Ph.D.

Dept. of Radiology, Kyoto University Hospital, Kyoto, Japan

Patient history

A 65-year-old asymptomatic man who was diagnosed with esophageal cancer of T1b stage (with invasion into the submucosal layer) during a routine endoscopy examination. The patient was referred for an MR examination.

Sequence details

Initially, T2-weighted fast Spin Echo images were obtained for defining anatomy and localizing the tumor. The location of the esophageal tumor was estimated by rough clinical information. Following T2-weighted imaging (T2WI) with sagittal or oblique sagittal plane along the course of the esophagus, diffusion-weighted imaging (DWI) with same plane was obtained utilizing a single shot echo-planar sequence with respiratory-triggering. Parameters for DWI included TR of 4000 ms, TE of 74 ms, b factors of 0 and 500 (s/mm^2), PAT factor of 2 using GRAPPA (PAT = Parallel Acquisition Technique), length of echo train (EPI factor) of 110, bandwidth of 1346 Hz/pixel, matrix of 128 x 128, and number of acquisition of 5. Both T2-weighted and diffusion-weighted images were uniformed with a section thickness of 3 mm without intersection gap, and a field of view of 350 mm.

Results

We have investigated the difference in detectability of esophageal cancer between diffusion-weighted images and T2-weighted images. Our study population included pathologically proven 13 patients with age ranging from 47 to 74 years old (mean: 62). The histologic diagnosis of the tumor was squamous cell carcinoma in all patients. The pathologic stage of esophageal cancer in 13 patients who were surgically treated were T3 (n=7), T2 (n=2) and T1b (n=4). T2-weighted images failed to demonstrate four T1b cancers, whereas fusion images with T1b and T2-weighted images failed to demonstrate only one T1b cancer.

Discussion

MRI has achieved limited clinical use in the evaluation of esophageal cancer. Reasons for this include the substantial artifacts from breathing and cardiac motion, long examination times, and as a result, poor imaging quality and reliability. Our study shows that DWI with respiratory-triggering can successfully demonstrate esophageal cancer as high intensity lesions in a majority of the patients. One of the big advantages of DWI over ordinary MR images is that this technique can demonstrate esophageal cancers with excellent tissue contrast, whereas T2WI demonstrates mere wall thickening of the esophagus. Even the esophageal cancers with T1b stage, which are confined within submucosal layer of the esophagus, can be demonstrated on DWI, whereas these tumors are generally hardly recognized on ordinary T2WI. The excellent tissue contrast on DWI may be explained by the difference of water diffusion between the cancer and normal esophagus. In the esophageal cancers, movement of water molecules may be restricted due to the increased cellularity and nuclear to cytoplasmic ratio.

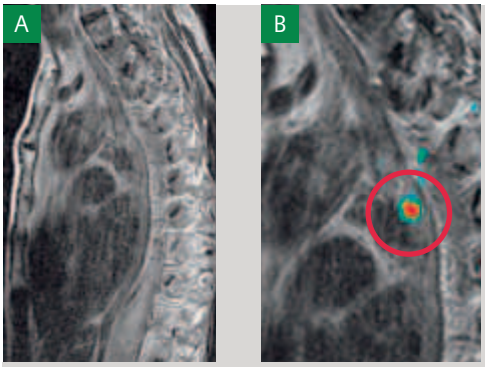

[A] *Free-breathing T2WI with PACE (Prospective Acquisition CorrEction) hardly shows any abnormality in the esophagus.*
[B] *Fusion image of DWI onto T2WI shows a focal area of increased signal intensity in the upper thoracic esophagus. The lesion was confirmed to be esophageal cancer of T1b stage at surgery.*

Scanner	*MAGNETOM Symphony*
Coils	*CP Body Array Coil, CP Spine Array Coil*

Case Report MAGNETOM Avanto
Complicated Rectal Fistula

Arnd-Oliver Schäfer, M.D.

University Hospital Freiburg, Department of Radiology, Freiburg, Germany

Patient history

38-year-old man with gluteal abscess had undergone incision. Delayed healing and persistent secretion gave rise to the suspicion of an underlying fistula. Subtraction MR-Fistulography was performed to exclude the suspected diagnosis.

Image findings

At coronal TIRM sequence high signal intensity abscess is shown within the left gluteus muscle (Fig. 1A) which communicates with a fluid-filled formation above the level of the levator muscle surrounding the lower rectum (Fig. 1B). Note

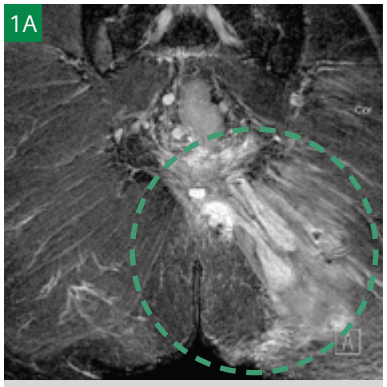

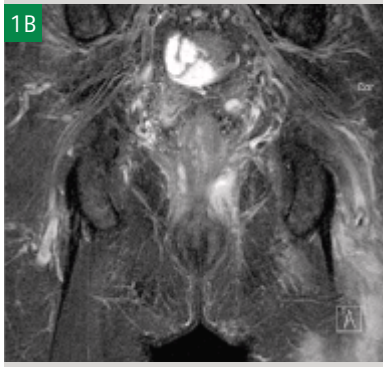

[Figure 1] *Coronal Turbo Inversion Recovery Magnitude –TIRM.*

TI	*150 ms*
TR	*5289 ms*
TE	*60 ms*
slice thickness	*3 mm*
matrix	*512 x 512*
FoV	*250 mm*
flip angle	*150°*
BW	*130 Hz/Px.*

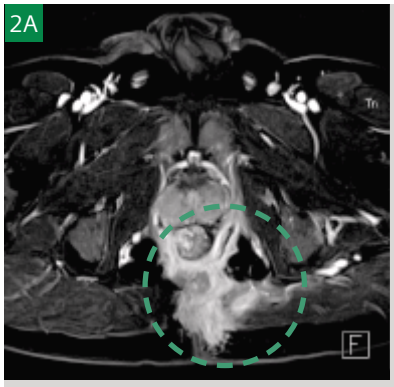

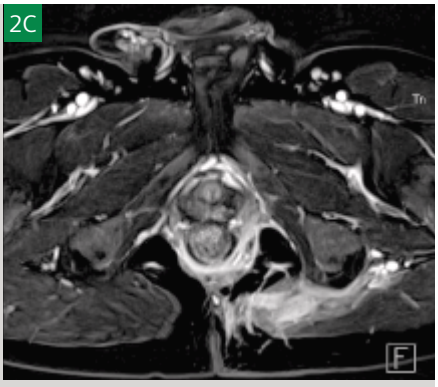

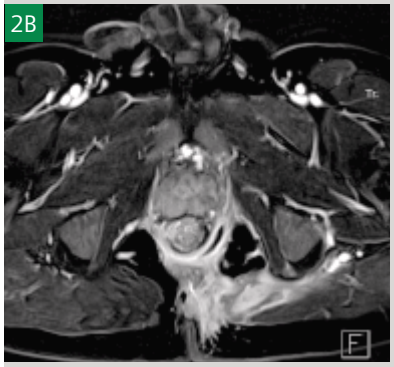

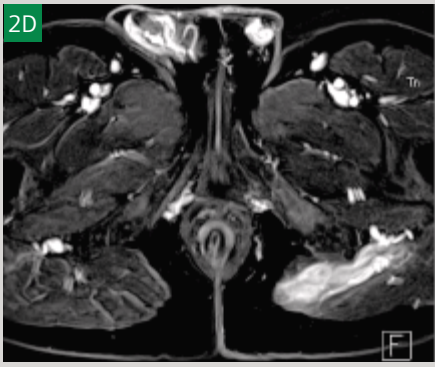

[Figure 2] *Axial Fast Low Angle Shot-3D – 3D FLASH*

TR	*7 ms*
TE	*2.7 ms*
slice thickness	*2 mm*
matrix	*512x 256*
FoV	*250 mm*
flip angle	*45°*
BW	*130 Hz/Px.*

also the reactive lymph nodes inside the mesorectum (Fig. 1A). On the axial contrast-enhanced 3D FLASH sequence after image subtraction a rectal fistula is clearly delimitable, forming a supralevatoric horseshoe (Fig. 2A). The internal opening is located at 9 o'clock lithotomy position. The fistula passes the levator muscle at 4 o'clock (Fig. 2B) towards the fat of the left-sided ischiorectal fossa. The fistula retains pus and is directly connected to the residual gluteal abscess (Figs. 2C, D). MIP-reconstruction of the data derived from the 3D FLASH sequence is giving a survey of the whole extent of inflammation (Fig. 3).

Discussion

To detect and precisely assess the extent of anorectal fistulas subtraction, MR-fistulography is extremely helpful. Contrast-agent based, gradient-echo imaging provide excellent anatomic resolution and the capability to perform image reconstructions on the one hand as well as thin-sections and high sensitivity for inflammation on the other hand.

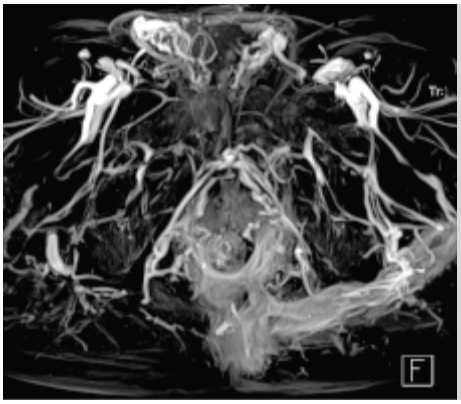

[Figure 3] *3D FLASH, Maximum Intensity Projection (MIP) reconstruction.*

Case Report MAGNETOM Avanto
Recurrent Rectal Cancer Evaluation with VIBE and SPACE

Arnd-Oliver Schäfer, M.D.

University Hospital Freiburg, Department of Radiology, Freiburg, Germany

Patient history

48-year-old woman with cancer of the lower rectum received transanal endoscopic microsurgery (TEM) in 2003. In that year a recto-vaginal fistula was also closed. Currently, the patient presented with perianal pain and recurrent rectal cancer was diagnosed. Pelvic MRI was performed to determine the extent of the recurrent tumor.

Image findings

A sagittal T2-TSE sequence demonstrates the recurrent rectal cancer located above the anal canal infiltrating the right-sided levator muscle (Figs. 1A, B, C). Additionally, fluid is accumulated in the vaginal lumen after rectal water filling indicating ano-vaginal fistula. On the axial T2 SPACE sequence (Figs. 2A, B, C) and the corresponding axial contrast-enhanced VIBE sequence (Figs. 3A, B, C) the tumor is infiltrating the mesorectal fat, the mosrectal fascia and the parietal peritoneal fascia along a scar formation on the right side with small amounts of ascites indicative for peritoneal spread (Fig. 2A). Infiltration of the right levator muscle is seen (Figs. 2, 3). There are no lymph nodes present.

Discussion

Pelvic anatomy can be imaged exquisitely with the 3D, high-resolution T2 SPACE sequence as well as with the high-resolution contrast-enhanced T1 VIBE sequence. A combination of both appears to be useful particularly for local staging of rectal cancer.

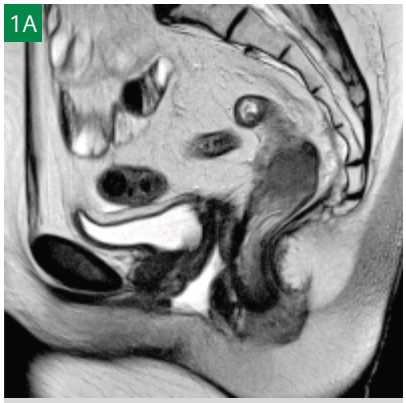

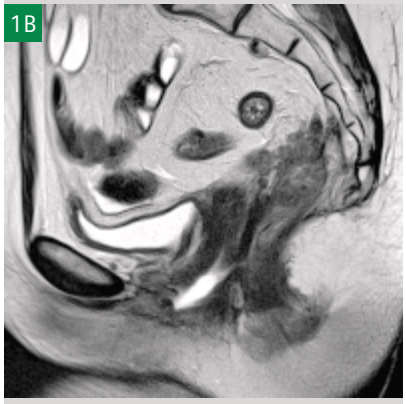

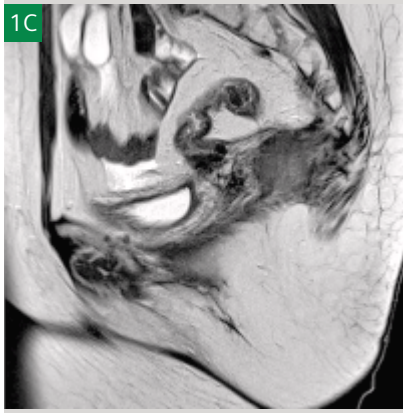

[Figure 1] *Sagittal T2-weighted Turbo Spin Echo –TSE.*

TR	*4960 ms*
TE	*126 ms*
slice thickness	*6 mm*
matrix	*512 x 256*
FoV	*280 mm*
flip angle	*150°*
BW	*195 Hz/Px.*

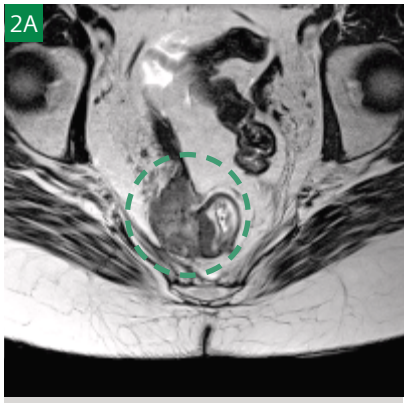

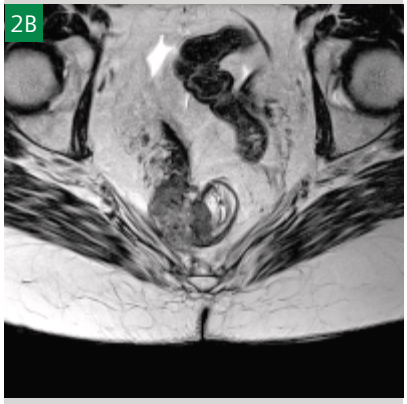

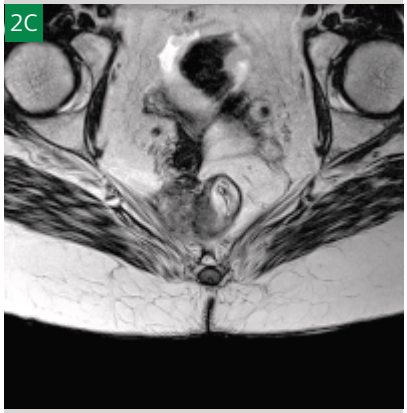

[Figure 2] *Axial T2 SPACE (Sampling Perfection with Application optimized Contrasts using different flip angle Evolutions).*

TR	*1500 ms*
TE	*166 ms*
slice thickness	*2 mm*
matrix	*512 x 256*
FoV	*250 mm*
flip angle	*150°*
BW	*444 Hz/Px.*
iPAT	*PAT 2, GRAPPA.Hz/Px.*

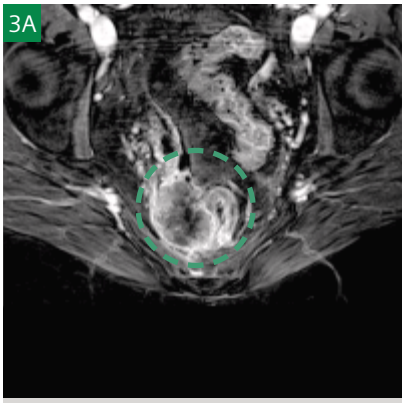

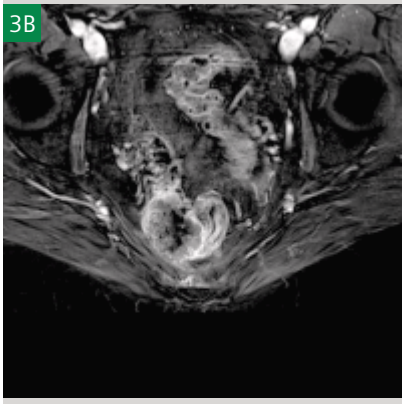

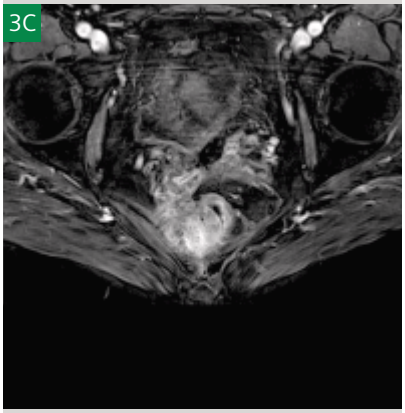

[Figure 3] *Axial Volume Interpolated Breathhold Examination – VIBE.*

TR	*8.30 ms*
TE	*3.23 ms*
slice thickness	*2.5 mm*
matrix	*512 x 256*
FoV	*250 mm*
flip angle	*125°*
BW	*150 Hz/Px.*

Cardiac

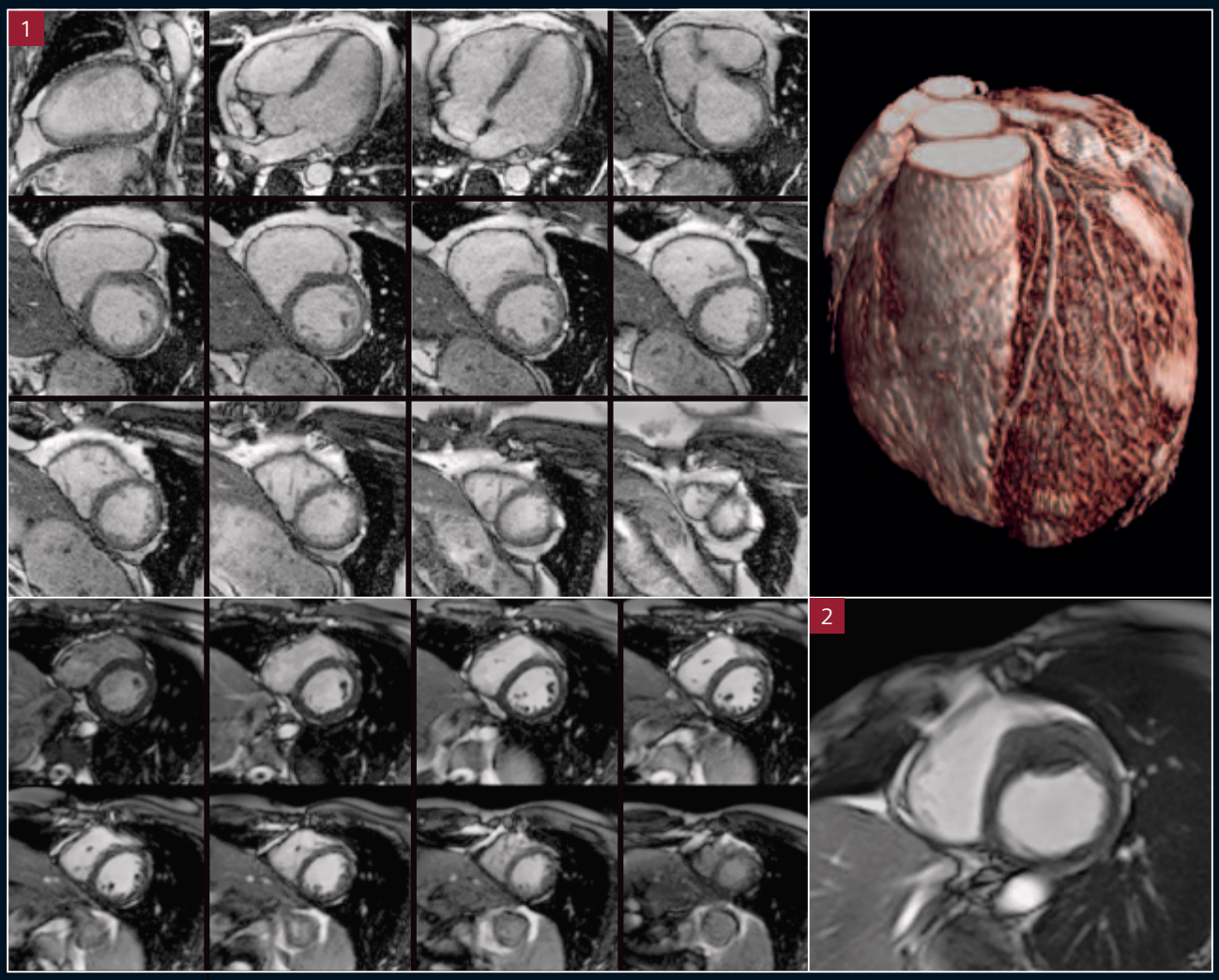

[1] Courtesy of P. Kellman, NHLBI, NIH, Bethesda, USA
[2] Courtesy of Dr. K. Teraoka, Tokyo Medical Univ., Japan

Whole Heart MRI – Adopting the CT Approach
3D Coronary Tree & Cardiac Morphology

Gary R. McNeal

MS (BME), Siemens Medical Solutions Inc., USA

Cardiovascular MR (CMR) is already established as a non-invasive technique for the assessment of coronary artery disease looking at heart function, morphology and tissue characterization. CMR therefore provides valuable information about the tissue damage caused by coronary artery stenosis, e.g showing the distribution of myocardial scar at the subendocardial level. The non-invasive visualization of the coronary arteries themselves is currently a domain of cardiac CT, which provides excellent images of the whole heart within 10–15 s with an isotropic resolution below 0.5 mm. With Tim

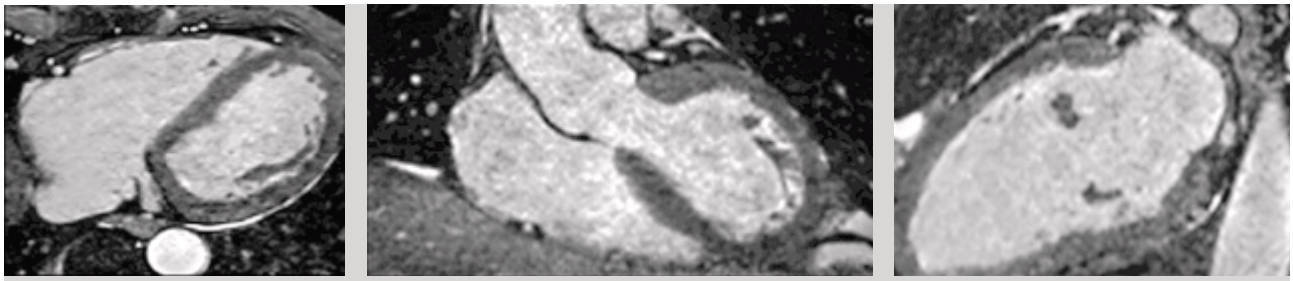

An isotropic 3D TrueFISP data set allows not only the visualization of the complete coronary tree but also a look at cardiac morphology in any orientation, which is especially useful in congenital heart disease. Fast heart rates and small cardiac structures like coronary arteries require highest system performance. The MAGNETOM Avanto system with Tim and iPAT provides excellent results even for the most demanding patients, including children.

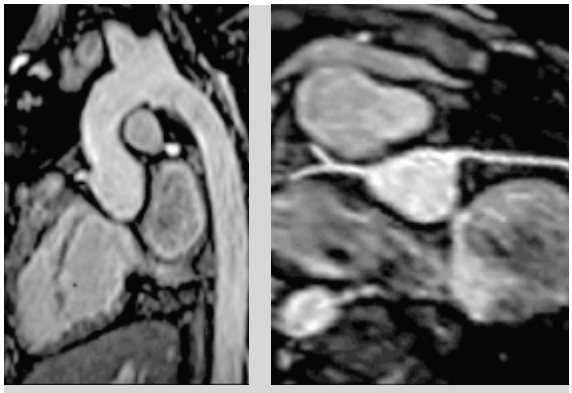

Aortic coarctation after repair, 6-year-old girl, thin MIP images of the aorta and proximal coronaries from an isotropic data set using free-breathing 3D TrueFISP with PACE, acquired in 11:45 min, resolution 1.2 x 1.2 x 1.2 mm^3.

Courtesy of BC Children's Hospital, Vancouver, Canada.

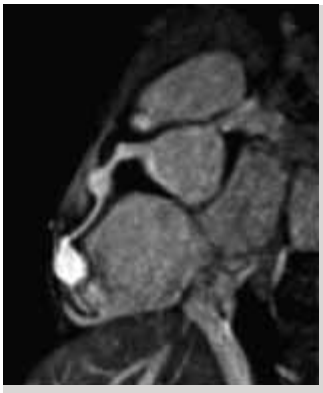

Kawasaki Syndrome, 6-year-old boy, thin MIP images of aneurysms of the coronary vessel shown with free-breathing 3D TrueFISP navigator PACE, acquired in 4:43 min, resolution 1.0 x 1.0 x 1.0 mm^3.

Courtesy of Dr. Abolmaali, Univ. Frankfurt, Germany.

technology (Total imaging matrix) and the MAGNETOM Avanto system, Siemens has now introduced CT-like techniques for coronary imaging in CMR.
The capabilities of Tim and iPAT technology (integrated Parallel Imaging Technique) together with the MAGNETOM Avanto system's hardware performance (fast gradients, excellent homogeneity), Siemens CMR techniques now allow you to image the complete 3D coronary vessel tree in one measurement, with easy imaging techniques, similar to CT but without the use of contrast agent, beta-blockers and without radiation. The whole heart can be imaged at a resolution of approximately 0.7 mm, showing even the distal branches of the vessel tree. And with the PACE (Prospective Acquisition Correction) navigator technique, the patient can breathe comfortably and freely during the measurement.

Near-isotropic Sub-millimeter Resolution Shows Distal Branches

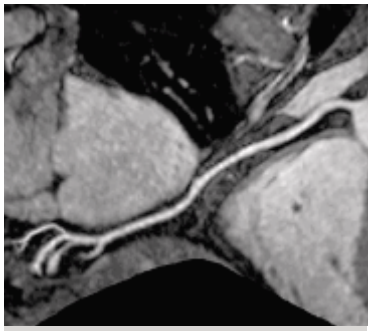

T2-prepared 3D TrueFISP with PACE navigator, acquired in 11 min, resolution 0.7 x 0.7 x 1.1 mm^3, thin MIP images.

Courtesy of Jikei University, Japan.

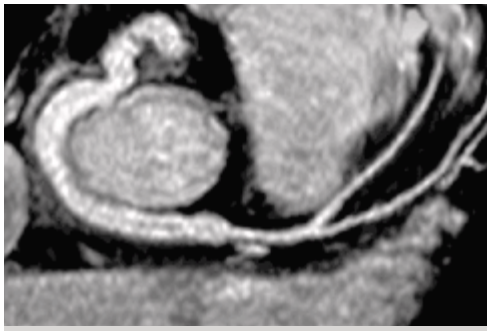

Marfans syndrome with bypass, 3D TrueFISP with PACE navigator, acquired in 12 min, resolution 1.0 x 1.0 x 1.3 mm^3, thin MIP images.

Courtesy of Dr. Li, Northwestern University, Chicago, USA.

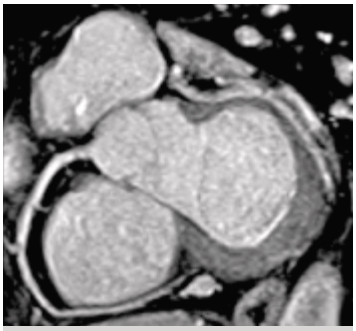

3D TrueFISP with iPAT2, acquired in one breath-hold of 21 s, resolution 1.1 x 1.1 x 1.0 mm^3, thin MIP images.

Courtesy of Drs. Finn, Laub, Deshpande, UCLA, Los Angeles, USA.

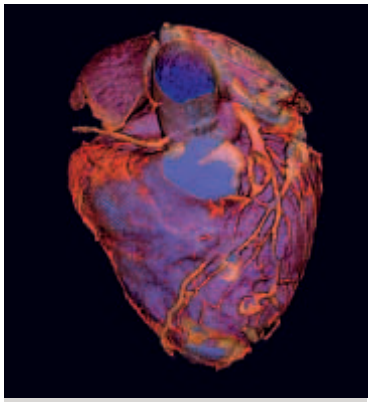

Whole heart coronary MRA acquired with T2-prepared 3D TrueFISP sequence with PACE navigator. Volume rendered images.

Courtesy of Dr. Teraoka, Tokyo Medical University, Tokyo, Japan.

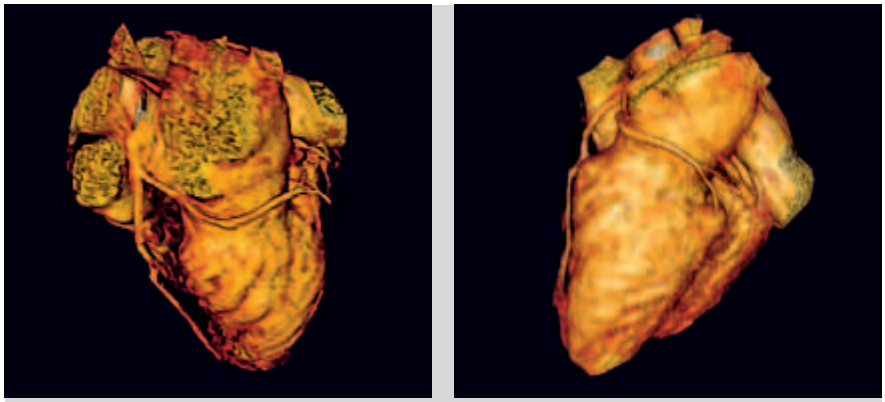

Whole heart coronary MRA acquired with T2-prepared 3D TrueFISP sequence with PACE navigator. Volume rendered images.

Courtesy of Drs. Finn, Laub, Deshpande, UCLA, Los Angeles, USA.

Consistently Excellent Image Quality

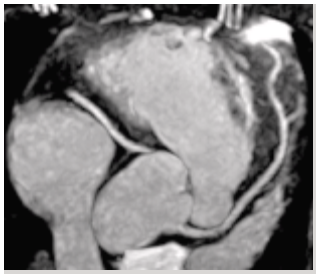

RCA & LAD (Thin MIP)

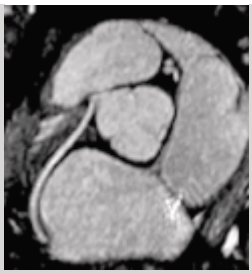

RCA & LAD (Thin MIP)

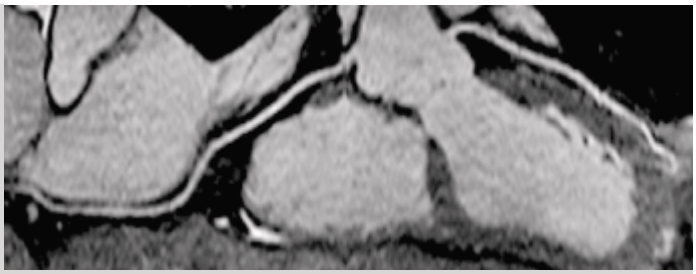

RCA & LAD (Curved Thin MIP)

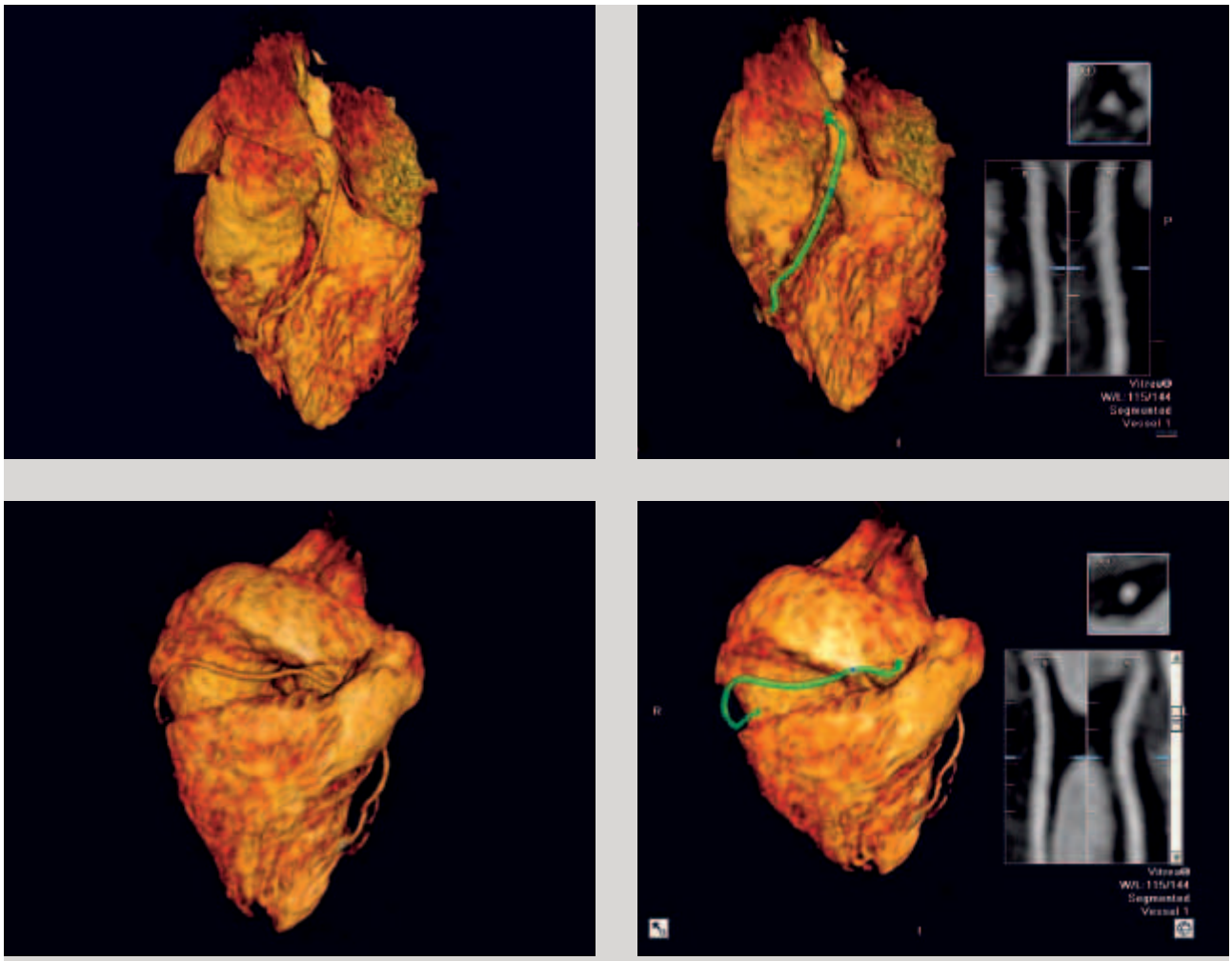

Volume rendered images with automatic vessel tracking (top: LAD, bottom: RCA).

FOV	*190 x 320 mm²*
Matrix	*380 x 640 (i)*
TR/TE	*3.3/1.5 ms*
Flip Angle	*90°*
T2 Prep	*40 ms*

BW	*975 Hz/pixel*
No. of Slices & Slice thickness	*120 Slices @ 1.0 mm (i)*
Time	*10:10 min*
Navigator Acceptance	*69%*

Courtesy of Drs. Finn, Laub, Deshpande, UCLA, Los Angeles, USA

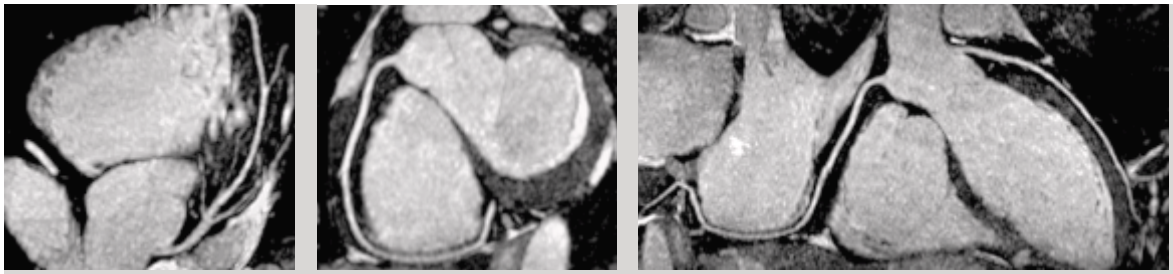

LAD (Thin MIP) *RCA (Thin MIP)* *RCA & LAD (Curved Thin MIP)*

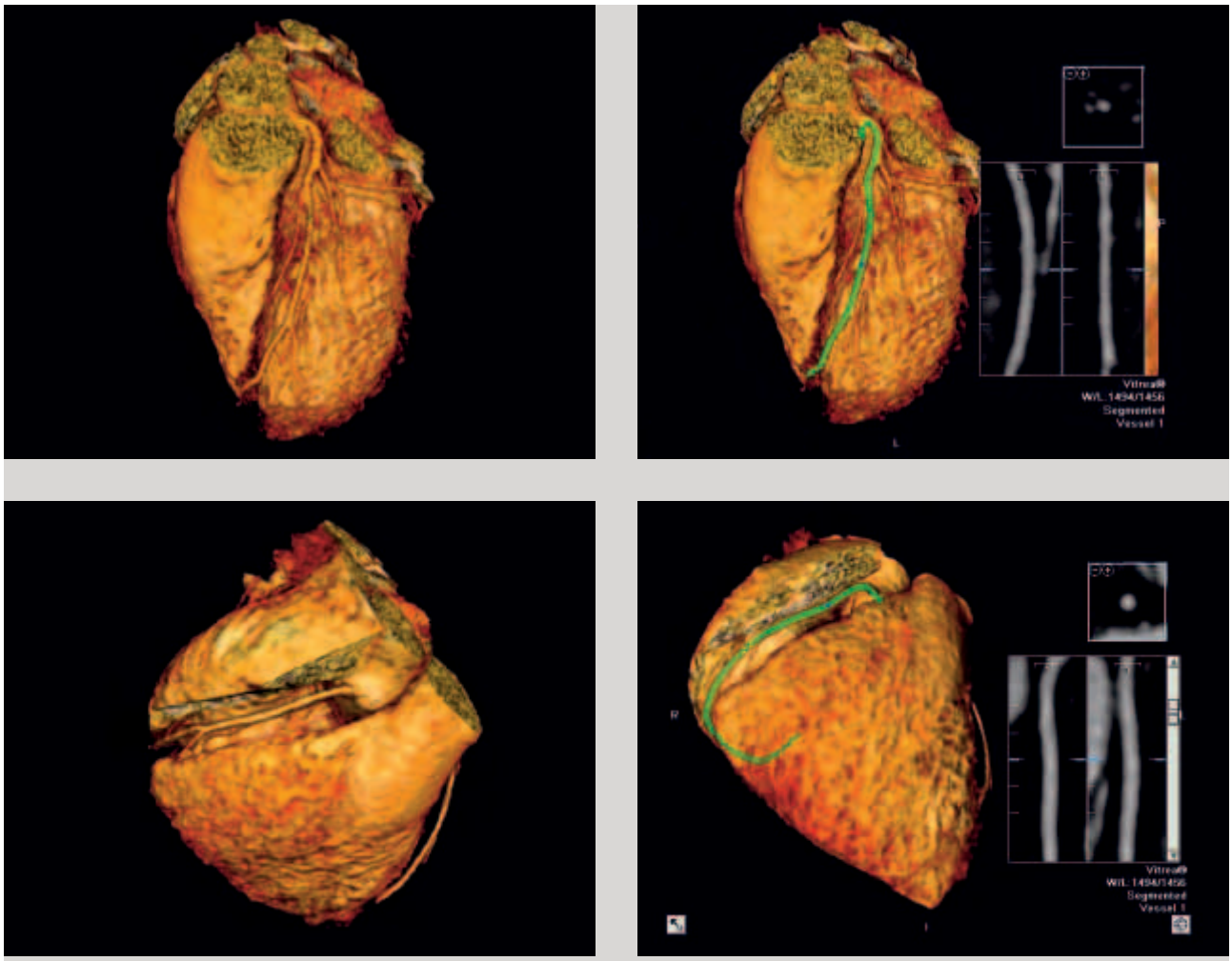

Volume rendered images with automatic vessel tracking (top: LAD, bottom: RCA).

FOV	*190 x 320 mm²*
Matrix	*342 x 640 (i) (p2)*
TR/TE	*3.3/1.5 ms*
Flip Angle	*90°*
T2 Prep	*40 ms*

BW	*975 Hz/pixel*
No. of Slices & Slice thickness	*160 Slices @ 0.75 mm (i)*
Time	*8:51 min*
Navigator Acceptance	*56%*

Courtesy of Drs. Finn, Laub, Deshpande, UCLA, Los Angeles, USA

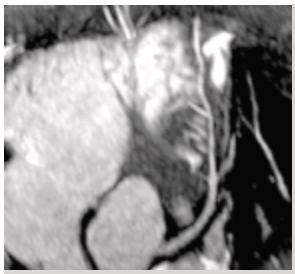

LAD (Thin MIP)

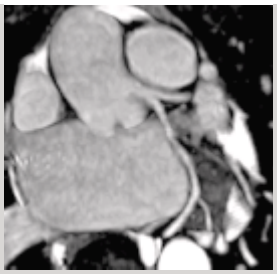

LCX (Thin MIP)

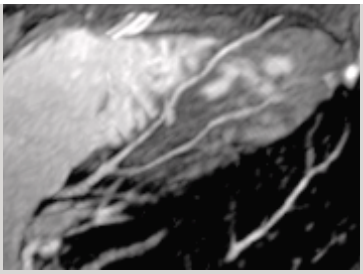

LAD & Diagonal (Thin MIP)

The visualization of major coronary arteries with MRI.

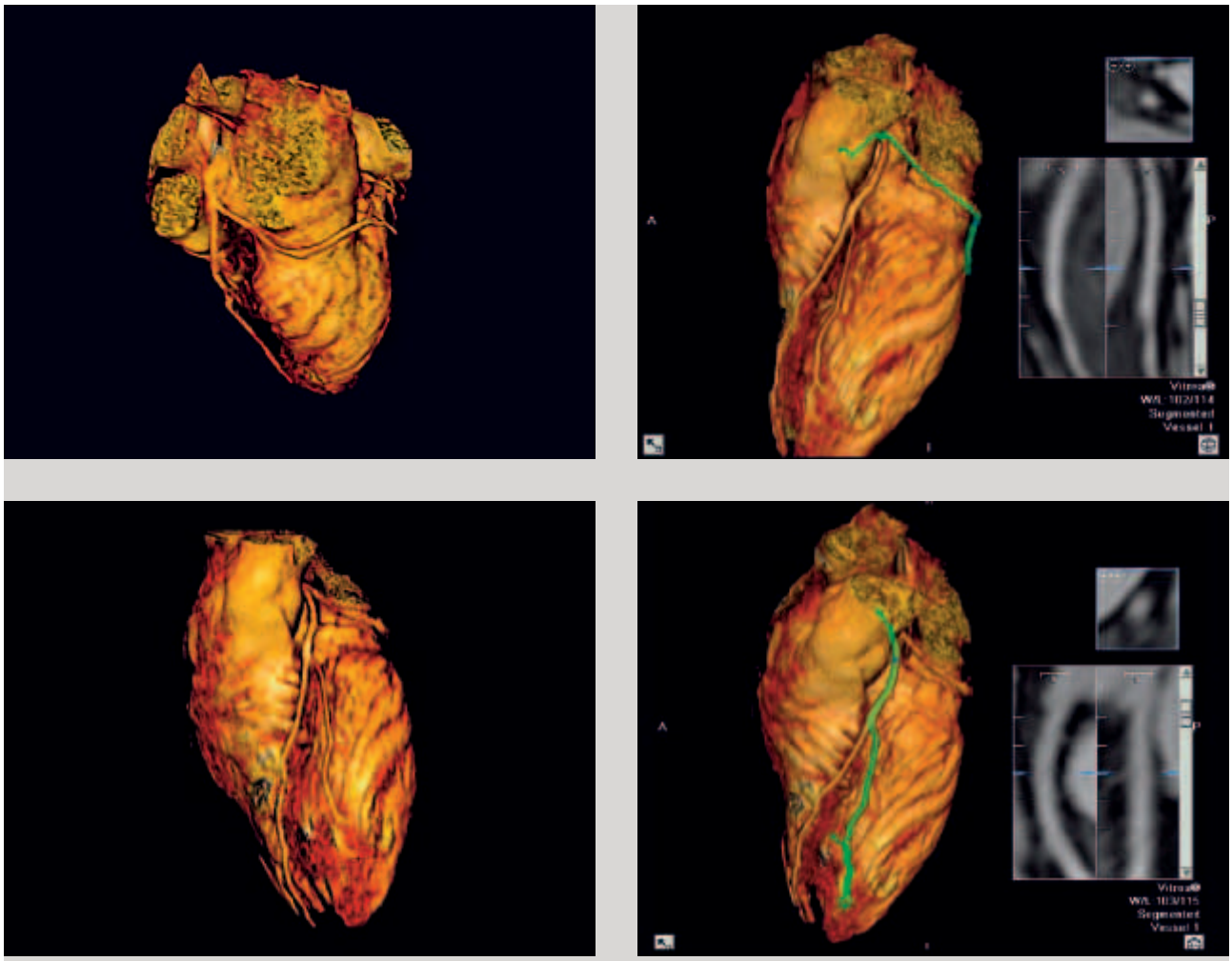

Volume rendered images with automatic vessel tracking (top: LCX, bottom: LAD & Diagonal).

FOV	*190 x 320 mm²*
Matrix	*342 x 640 (i)*
TR/TE	*3.3/1.5 ms*
Flip Angle	*90°*
T2 Prep	*40 ms*

BW	*975 Hz/pixel*
No. of Slices & Slice thickness	*88 Slices @ 1.5 mm (i)*
Time	*11:50 min*
Navigator Acceptance	*42%*

Courtesy of Drs. Finn, Laub, Deshpande, UCLA, Los Angeles, USA

Abbreviations: RCA = Right coronary artery, LAD = Left anterior descending

How does this Fantastic Technology Work?

When using a balanced steady-state free-precession pulse sequence for coronary artery imaging, the data have to be acquired in signal transience to steady-state to preserve the effect of the fat saturation pulse. Therefore, due to the requirement of ECG-triggering, the signal has a relatively strong proton density weighting as opposed to the T2/T1 weighting found in typical steady-state TrueFISP imaging. This reduces the blood-myocardial contrast. As the coronary arteries are in close proximity to fat and myocardial tissue, a higher blood-background contrast is desirable to improve delineation of the vessels. For best contrast in coronary artery imaging, T2-preparation has been added to an ECG-triggered, navigator-gated, fatsat TrueFISP 3D pulse sequence. The basic pulse sequence structure is a segmented 3D approach with 'n' phase-encode lines acquired per heartbeat. The partition gradient is incremented after 'm' heartbeats. In each heartbeat, a T2-preparation is applied after an appropriate trigger delay time, followed by the navigator pulse for respiratory gating, a fat suppression pulse, TrueFISP preparation cycles, data acquisition, and a flipback pulse, followed finally by a gradient spoiler.

This schematic of the ECG-triggered, navigator-gated, T2-prepared, segmented TrueFISP pulse sequence shows the T2prep Pulse (user defined), Navigator Pulses (~40 ms), Fat Suppression Pulse (~20 ms), Linear Flip Angle Preparation Pulses, Data Acquisition Time (user defined), and the Spoiler Pulse (~ 8 ms). The TR shown on the *syngo* user interface taskcard includes all these pulses except the time for the Navigator Pulses. In other words, the time necessary to play out all the sequence events in a cardiac cycle is actually 40 ms greater than the minimum TR in the user interface taskcard. Several new parameters have been added to the Sequence / Specials taskcard: Data Acquisition Time, Trigger to Data Acquisition Time, T2prep Switch, T2prep Time, and Frequency Offset.

Segmented TrueFISP

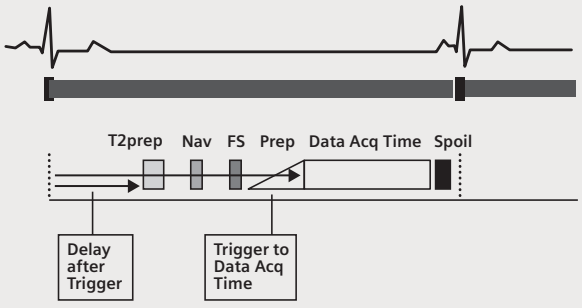

- **Data Acquisition Time:** This parameter defines the duration during which data is acquired.
- **Trigger to Data Acquisition Time:** This parameter will be visible only if triggering is ON. Its value is equal to the time from the R-wave of the ECG trigger to the first line of data acquisition.
- **T2prep Switch:** T2prep can be switched ON or OFF using this switch.
- **T2prep Time:** This parameter will be activated only if the T2prep switch is ON. The T2prep time controls the T2-weighting that the magnetization will undergo before data acquisition.
- **Frequency Offset:** This parameter changes the RF phase cycling in TrueFISP. The phase cycling is equal to 180° when the frequency offset is 0.
- **Frequency Offset**: The frequency offset on the protocol menu changes the phase cycling for the RF pulses. This parameter may be used to optimize the TrueFISP image quality by reducing or eliminating any off-resonance banding artifacts if present. It is recommended that the initial value should be set to 0, and then changed only if necessary. Any change in this parameter does not change the MR frequency used by the system. Therefore, general characteristics, such as fatsat, or slice position do not change when using this frequency offset parameter in the TrueFISP sequence.
- **Navigator Gating:** To acquire a navigator echo, two intersecting slices are excited – one with a 90° pulse and the other with a 180° pulse. The intersection of these slices (a column of tissue) then generates a spin echo, which is used to track the diaphragm (liver-lung boundary). The navigator echo takes approximately 40 ms to run.

How do I Perform the Whole Heart Coronary Exam?

Localizers

1. To estimate the end expiration position of the heart, a free-breathing single slice coronal scout is performed at the level of the heart, with multiple repeated measurements at the same slice position over approximately 18 s. Images that show the end expiration position of the heart will be used to position the imaging slab of the whole heart scan.
2. A free-breathing stack of transverse slices acquired at the dome of the diaphragm will be used to position the navigator pulses of the whole heart scan.

Free-Breathing Cine

1. A free-breathing cine scan is performed to determine the mid-diastolic phase when the heart is relatively stationary. The cine slice is positioned on an axial scout image such that a cross section of the left ventricle is acquired in the cine. The optimal trigger delay and acquisition window for the whole heart scan are determined from the cine images such that data acquisition occurs when the heart is relatively stationary.

2. Find the early to mid diastolic image in the cine series when the heart first stops moving, and note the "TT" time from that image as T_{start}.

3. Find the mid to end diastolic image in the cine series when the heart starts again moving, and note the "TT" time from the prior image as T_{end}.

Whole Heart Protocol Optimization

1. Calculate the optimal data acquisition window as $T_{opt} = T_{end} - T_{start}$ and adjust the number of "Segments" on the Physio Taskcard until the "Data Acquisition Time" on the Sequence / Specials Taskcard is equal to or slightly less than T_{opt}.

2. On the Physio Taskcard set the "TR" to its minimum value, set the "Trigger Delay" to 0, and set the "Acquisition Window" to T_{end}.

3. On the Physio Taskcard adjust "Trigger Delay" such that the "Trigger to Data Acquisition Time" on the Sequence / Specials Taskcard is equal to or slightly greater than T_{start}.

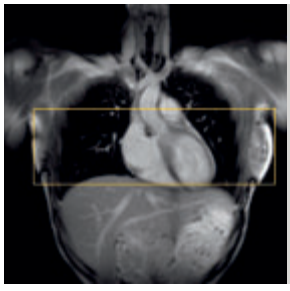

Whole Heart 3D Imaging Slab Positioning
The high-resolution axial 3D imaging slab is positioned on a coronal scout image showing the heart at its end-expiratory position. The number of 3D partitions may be adjusted as needed to cover the heart from base to apex. However, the more partitions used, the longer the scan will be.

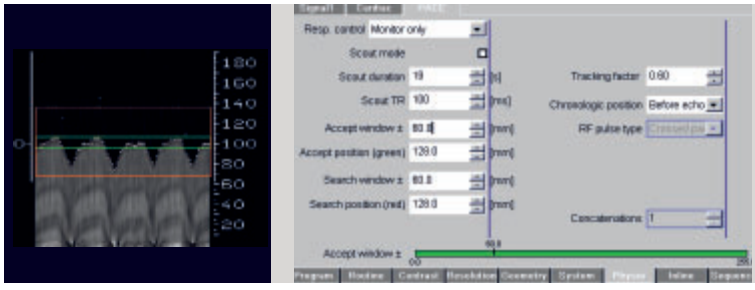

Whole Heart Navigator Scout Mode
The sequence should be run with Scout Mode ON (Physio / PACE Taskcard) to determine if the data acceptance window (green box) coincides with the end-expiratory peaks of the respiratory waveform. If necessary, adjust the Acceptance Position (green), then repeat with Scout Mode ON to ensure correct positioning.

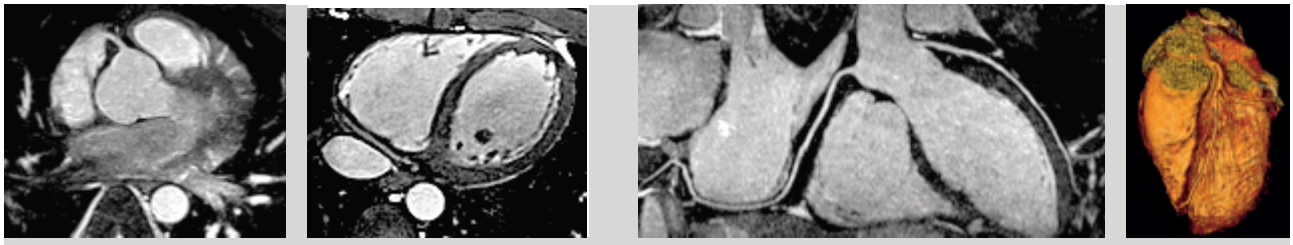

Original Axial Slices *Curved Thin MIP & Volume Rendered*

Whole Heart Image Acquisition Mode
Turn the Scout Mode OFF and run the sequence to acquire the image data as a free-breathing exam. The scan time will vary depending upon heart rate, respiration rate, spatial resolution, and acceptance rate (typically 5–10 min). Original axial images should be reviewed as well as Thin-MIP and Volume-Rendered images.

Head and Neck

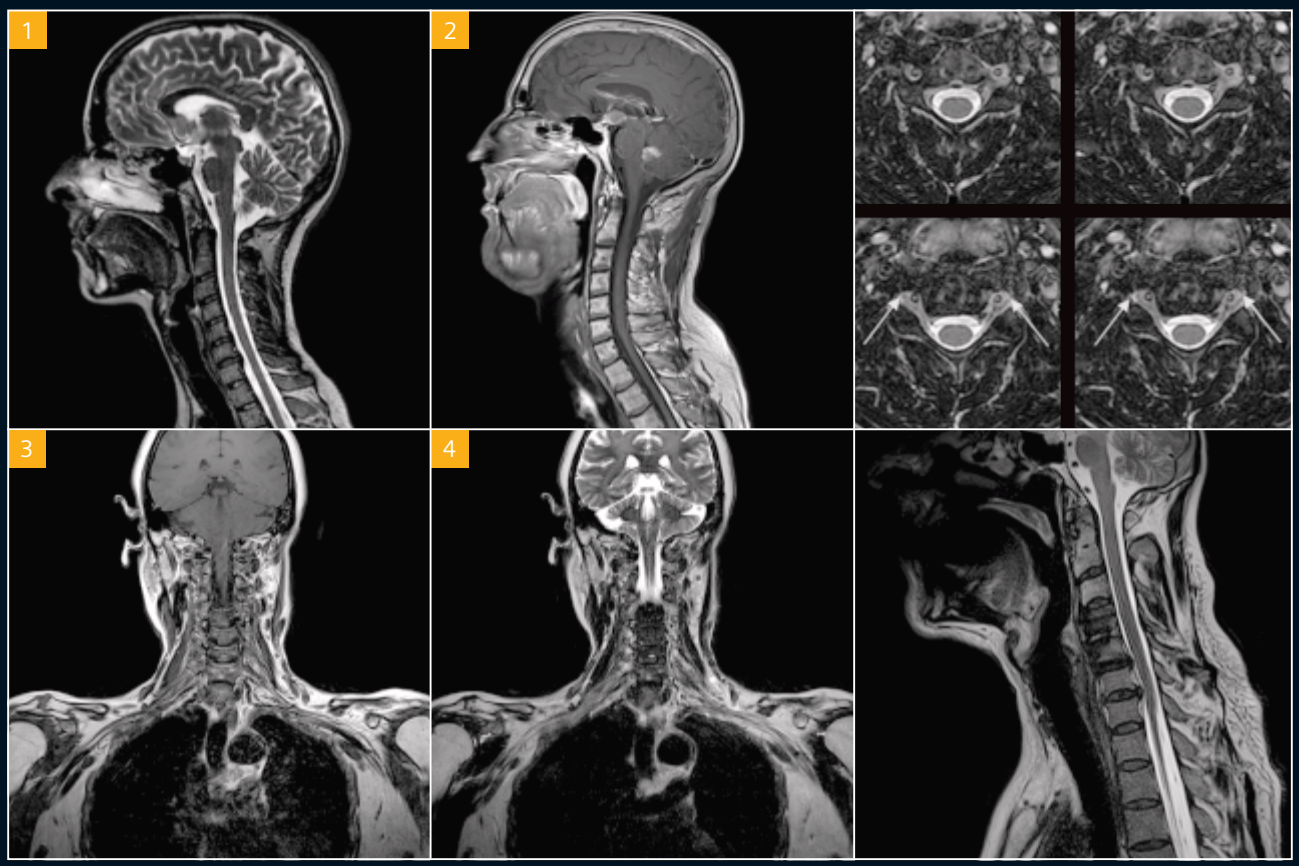

[1, 2] Courtesy of NYU, New York, USA
[3, 4] Courtesy of HKSK, Hong Kong

Non-EPI Diffusion-Weighted MR Imaging in the Diagnosis of Cholesteatoma

Bert De Foer, M.D.[1], Bernard Pilet, M.D.[1], Jean-Phillipe Vercruysse, M.D.[2], Jan W. Casselman, M.D. Ph.D.[1,3]

[1]*Department of Radiology, A.Z. Sint-Augustinus, Antwerp, Belgium*
[2]*University Department of ENT, A.Z. Sint-Augustinus, Antwerp, Belgium*
[3]*Department of Radiology, A.Z. Sint-Jan AV, Bruges, Belgium*

Introduction

MR imaging has an additional value in the detection and delineation of congenital temporal bone and acquired middle ear cholesteatoma. The combination of standard MRI sequences with intravenous gadolinium administration and Spin Echo Echo Planar Diffusion-Weighted (SE EPI DWI) images seems to have – up until now – the highest sensitivity. However SE EPI DWI still has major limitations due to susceptibility-related artefacts, relatively thick slices and low spatial resolution. We report our first experience with a single-shot Turbo Spin Echo diffusion-weighted imaging (single-shot TSE DWI) sequence for the detection and delineation of middle ear cholesteatoma, as well as congenital cholesteatoma, primary acquired cholesteatoma and pre-second look residual cholesteatoma.

MRI Protocol

The protocol for imaging cholesteatoma in our institution consists of 5 sequences. Images are acquired 45 minutes after the intravenous administration of gadolinium on a MAGNETOM Avanto using the standard Head Matrix coil and 2 locally built 7 cm surface ring coils, each connected via its own flex interface. The main difference between SE EPI DWI and single-shot TSE DWI is that the latter sequence uses a 180° RF refocusing pulse for each measured echo.

Protocol for imaging cholesteatoma

Sequence name	Slice orientation	Matrix	SL (mm)	FOV (mm x mm)	Position
TSE T2-WI	coronal	192 x 256	2,0	128 x 170	Suspected pathological ear
Ss TSE DWI	coronal	134 x 192	3,0	220 x 220	Both ears
3D TSE T2-WI	transverse	228 x 448	0,4	107 x 210	Both ears
TSE T1-WI	coronal	192 x 256	2,0	128 x 170	Suspected pathological ear
TSE T1-WI	transverse	144 x 256	2,0	128 x 170	Suspected pathological ear

The total examination time is about 23 minutes.

Case Report 1

13-year-old girl presenting with a small epitympanic congenital cholesteatoma at otoscopy.

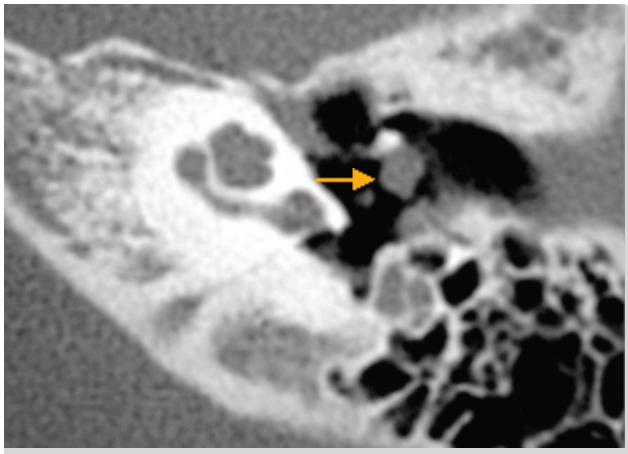

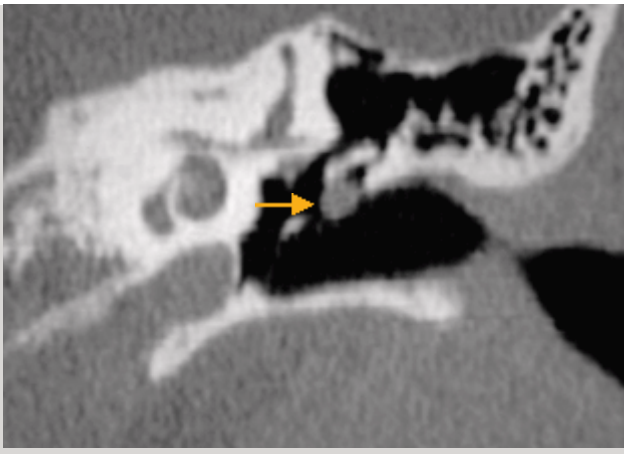

[Figure 1A] *Transverse and coronal high resolution CT image shows a small soft tissue lesion adjacent to the neck of the hammer suggestive of a small cholesteatoma (arrows). The intact tympanic membrane and the lack of chronic inflammatory alterations in the middle ear suggest a small congenital cholesteatoma (size 2 to 3 mm).*

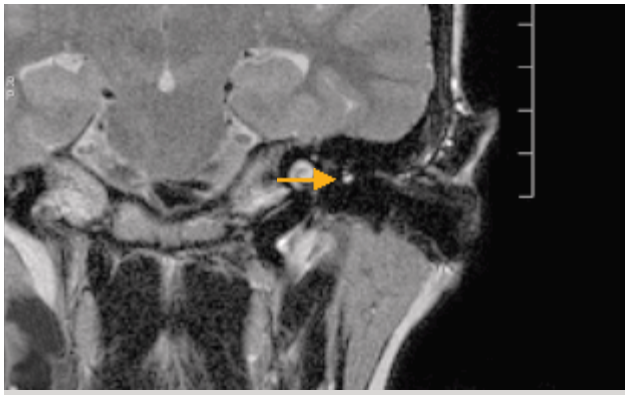

[Figure 1B] *Coronal T2-weighted imaging (T2-WI) shows a small hyperintense nodular lesion in the signal loss region of the temporal bone (arrow). When comparing to Figure 1a the small hyperintense nodular lesions present the small congenital cholesteatoma*

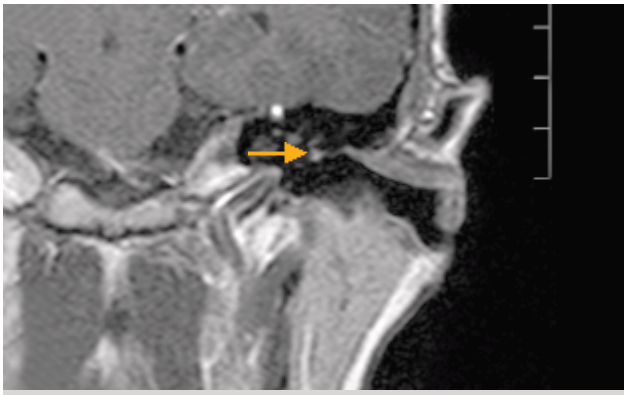

[Figure 1C] *Coronal T1-weighted imaging (T1-WI) shows a small nodular lesion in the temporal bone corresponding to the small congenital cholesteatoma (arrow).*

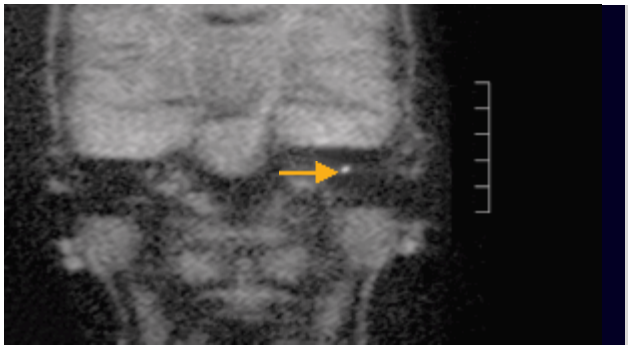

[Figure 1D] *Coronal single-shot Turbo Spin Echo Diffusion-weighted imaging (TSE DWI) clearly shows the small hyperintensity in the temporal bone corresponding to the small congenital cholesteatoma (arrow).*

Case Report 2

76-year-old male with chronic ear discharge.

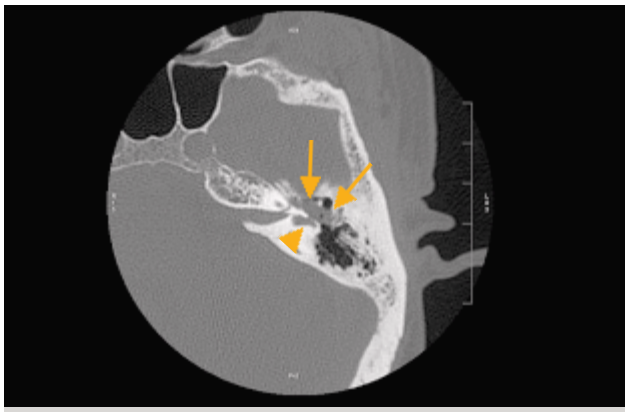

[Figure 2A] *Transverse high resolution CT image shows soft tissue in the attic (arrows) with ossicular erosion and disruption of the anterior part of the lateral semicircular canal (arrowhead).*

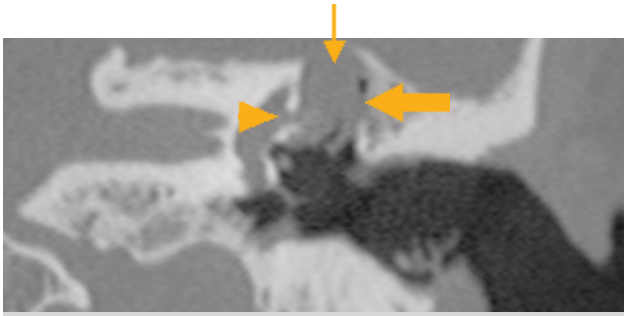

[Figure 2B] *Coronal reformation of a transverse multi slice data set clearly shows the lesion in the attic (large arrow) with suspected erosion of the tegmen (small arrow) and the lateral semicircular canal (arrowhead).*

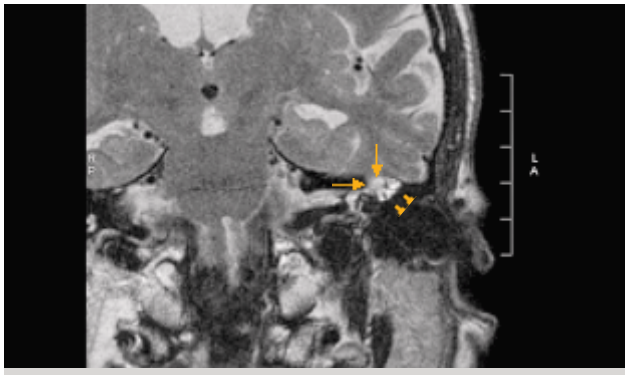

[Figure 2C] *Coronal TSE T2-WI through the temporal bone at the level of the lateral semicircular canal clearly shows the slightly hyperintense cholesteatoma (arrows) surrounded by hyperintense fluid (arrowheads).*

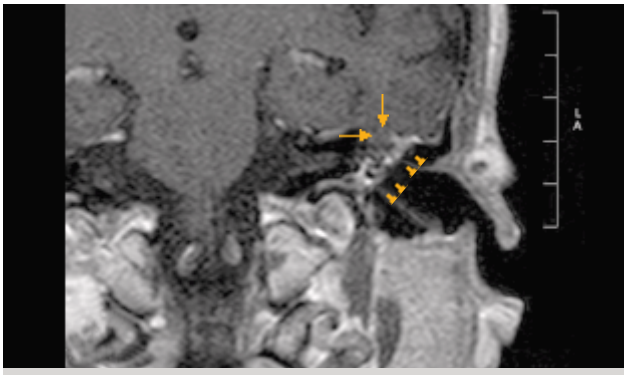

[Figure 2D] *Coronal TSE T1-WI (same level as 2C) 45' after iv Gd shows the enhancing inflammatory tissue (arrowheads) in middle ear and attic surrounding the non-enhancing cholesteatoma under the tegmen (arrows).*

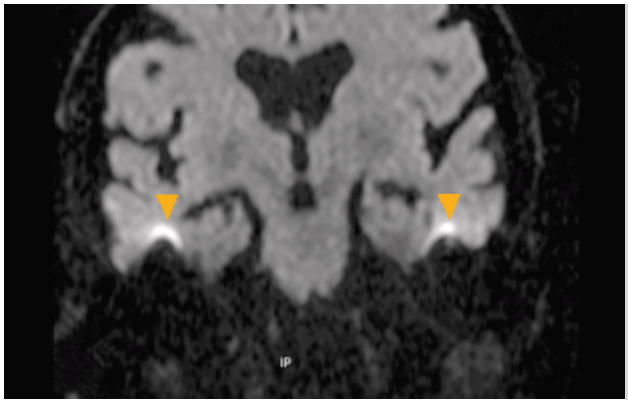

[Figure 2E] *Coronal SE EPI DWI shows the typical interface artefact between temporal lobe and temporal bone (arrowheads). The cholesteatoma cannot be seen due to the artefact.*

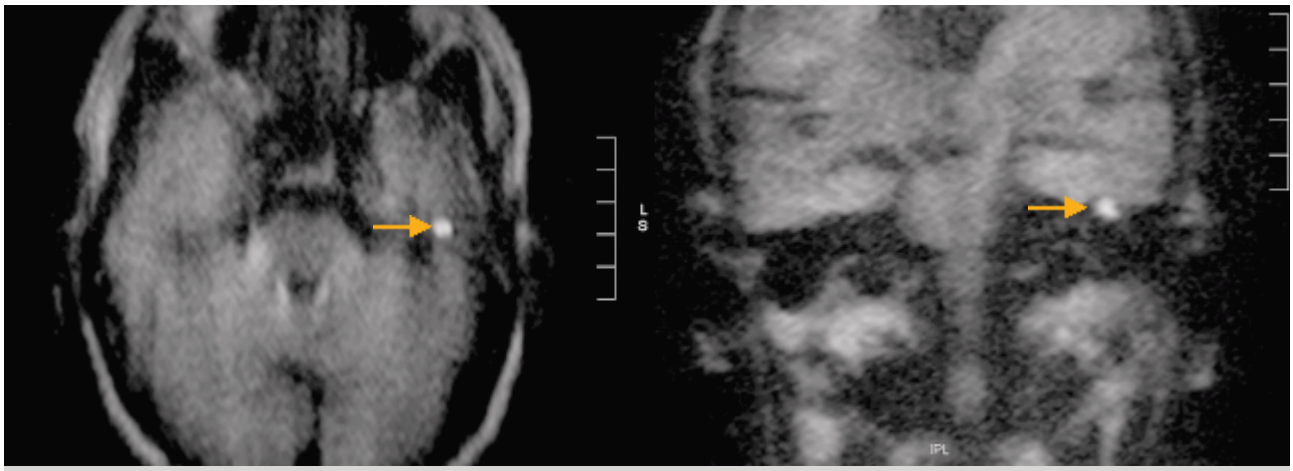

[Figure 2F] *Coronal and transverse single-shot TSE DWI clearly show the small very hyperintense lesion under the tegmen on the left side compatible with cholesteatoma. Note the complete lack of artefacts at the interface between temporal lobe and temporal bone. The lesion can be clearly visualized on both transverse and coronal images (arrows). Compare to figure 2E. In retrospect, the lesion can merely be suspected in the interface artefact of figure 2E on the left side.*

Case Report 3

17-year-old boy with prior surgery for cholesteatoma with primary bony obliteration technique on both sides. In this technique the mastoidectomy cavity is filled with bone chips and bone paté in order to avoid recurrent cholesteatoma. Patient was presented for evaluation of the right side.

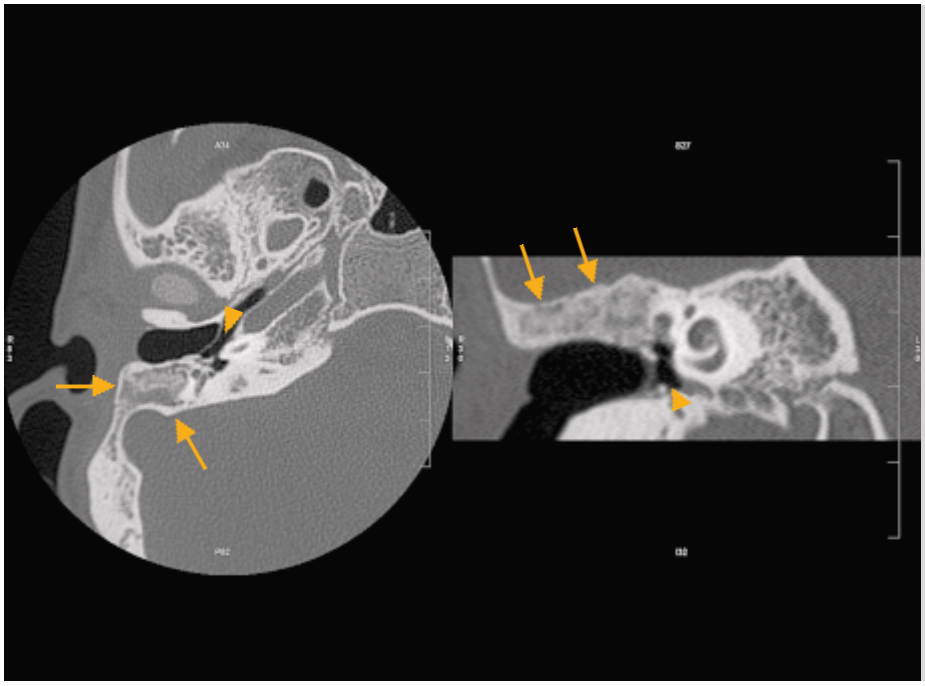

[Figure 3A] *Transverse and coronal CT images show a complete homogeneous opacification of the right mastoidectomy cavity with bony material (arrows). The residual middle ear cavity remains well aerated (arrowheads). On CT, there is no suspicion for cholesteatoma in the obliterated cavity nor in the aerated residual middle ear cavity on the right side.*

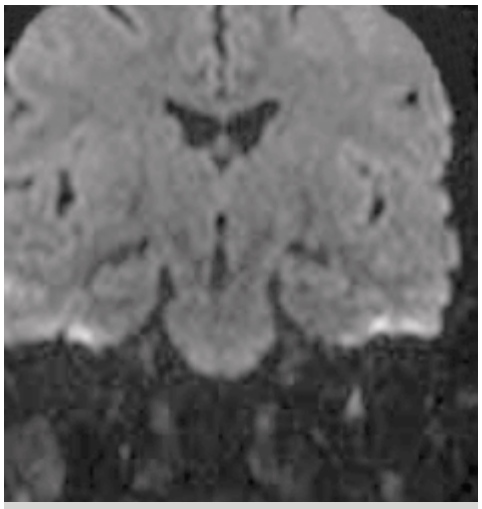

[Figure 3B] *Coronal SE EPI DWI shows no clear hyperintense abnormalities on either right or left side.*

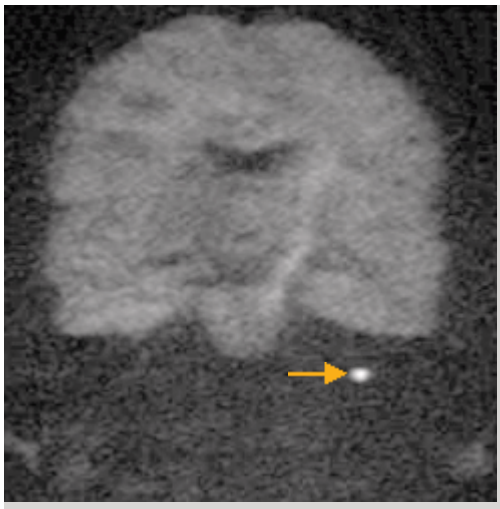

[Figure 3C] *Coronal single-shot TSE DWI shows no clear hyperintensity on the right side but, surprisingly, there is a clear nodular hyperintensity on the left side (arrow), suggestive of a small residual cholesteatoma. Compare to figure 3B. Note the homogeneous signal of the lesion and the complete absence of the interface artefact.*

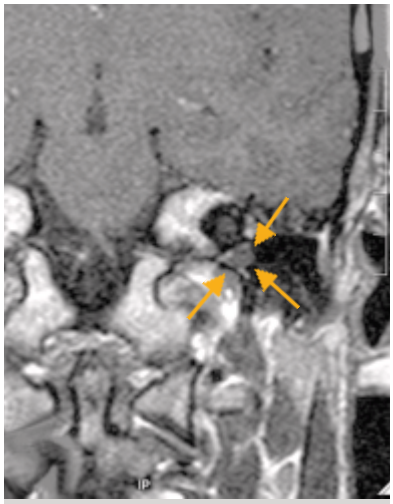

[Figure 3D] *TSE T1-WI 45' after iv Gd shows a corresponding nodular non-enhancing lesion in the hypotympanon on the left side (arrows), compatible with a small residual cholesteatoma.*

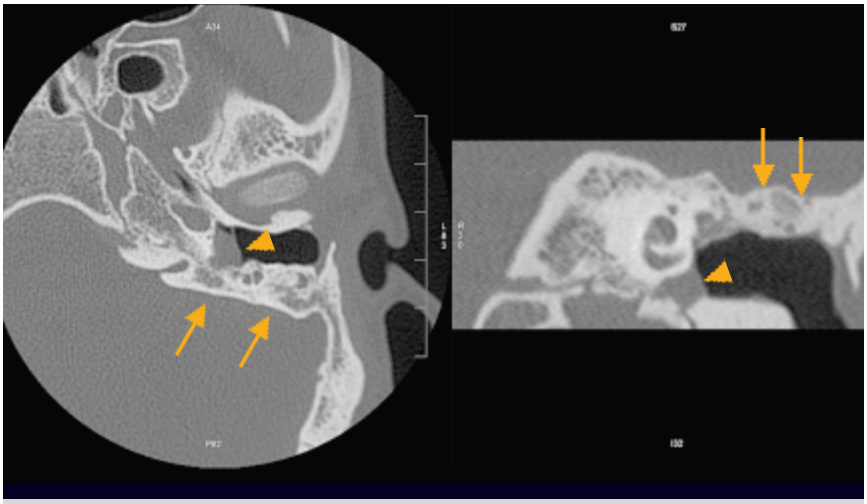

[Figure 3E] *Transverse and coronal CT image through the left middle ear shows a complete and homogeneous opacification of the left mastoidectomy cavity with bony material (arrows). There is a clear nodular soft tissue lesion in the hypotympanum compatible with a cholesteatoma (arrowheads). Compare to figure 3C and 3D.*

Discussion

High resolution CT scan still remains the primary examination tool for the evaluation of a patient suspected of having a middle ear cholesteatoma. It gives excellent information on the extension of the lesion, ossicular erosion and delineation of the tympanic segment of the facial nerve. It also clearly reveals erosion of the lateral semicircular canal and tegmen (1). In selected cases, MRI has an additional value for the evaluation of cholesteatoma extension and for the assessment of

possible complications such as erosion of the lateral semicircular canal, invasion in the membranous labyrinth and invasion in the middle cranial fossa through an eroded tegmen (1). Several past reports have discussed the aspect of cholesteatoma on MRI. The aspect of a congenital temporal bone cholesteatoma or an acquired cholesteatoma on standard MRI sequences is well known. On T2-weighted images cholesteatoma has a slightly higher signal intensity than brain tissue (gray matter). On T1-weighted images, it has an isointense appearance with peripheral matrix enhancement. As cholesteatoma is avascular tissue, the center of the cholesteatoma never enhances contrary to inflammatory and/or granulation tissue (2, 3).

Recently, the aspect of cholesteatomatous tissue on echo planar diffusion-weighted MR images (SE EPI DWI) has been described. Congenital temporal bone cholesteatoma as well as acquired middle ear cholesteatoma exhibit a high signal on SE EPI DWI probably caused by a combination of restricted diffusion and a T2-shine through effect (4, 5, 6, 7). The major limitation seems to be the important air-bone interface artefact at the skull base, the distortion of the images and the low spatial resolution. Furthermore, smaller lesions (less than 5 mm) are still missed using the SE EPI DWI (8).

Moreover, in the past, several studies have shown the failure of MRI in demonstrating and delineating residual cholesteatoma before second-look surgery (9, 10). Therefore, second-look surgery, performed about one year after first-look surgery, remains the gold standard for detection of residual cholesteatoma up until now.

The combination of standard post-contrast MRI sequences combined with SE EPI DWI -up until now- seems to have the highest sensitivity for the detection of residual cholesteatoma. Again, a high number of residual cholesteatomas can be missed due to the often small size of these residual cholesteatoma pearls (2 to 4 mm) and the air-bone interface artefact noted at the skull base (8, 11, 12, 13, 14).

Recently, the use of late post-contrast T1-weighted images has been demonstrated to be of a great value in differentiating cholesteatoma from inflammatory and granulation tissue. It is stated that post-operative inflammatory and granulation tissue show a slow centripetal contrast uptake and can thus only be differentiated from (non-enhancing) cholesteatomatous tissue by using late post-contrast T1-WI images (15, 16).

By using single-shot TSE DWI we succeeded in overruling the above-mentioned major limitations of SE EPI DWI. Our first results show that prior size limitations to cholesteatoma detection seem to be overruled (Fig. 1). Furthermore, single-shot TSE DWI has no interface artefact at the temporal bone – temporal lobe border (Fig. 2). Further investigations and studies using the new combination of late post-contrast T1-WI and single-shot TSE DWI for the detection and delineation of small acquired middle ear cholesteatoma and pre-second look residual cholesteatoma have currently been started. We hope that the combination of late post-contrast T1-WI and single-shot TSE DWI has the highest sensitivity and specificity in order to replace second-look surgery for acquired middle ear cholesteatoma (Fig. 3).

*This information about this product is preliminary. The product is under development and not commercially available in the US and its future availability cannot be ensured

References

[1] Lemmerling M, De Foer B. Imaging of cholesteatomatous and non-cholesteatomatous middle ear disease. In: M. Lemmerling, S.S.Kollias. Radiology of the Petrous Bone, 1st edn. Springer Verlag Berlin Heidelberg New York pp 31–47.

[2] Martin N, Sterkers O, Nahum H. Chronic inflammatory disease of the middle ear cavities: Gd-DTPA-enhanced MR imaging. Radiology. 1990; 176: 399–405.

[3] Ishii K, Takahashi S, Kobayashi T, et al. MR imaging of middle ear cholesteatomas. J Comput Assit Tomogr. 1991; 15: 934–937.

[4] Robert Y, Carcasset S, Rocourt N, et al. Congenital cholesteatoma of the temporal bone: MR findings and comparison with CT. Am J Neuroradiol 1995; 16: 755–761.

[5] Fitzek C, Mewes T, Fitzek S, et al. Diffusion-weighted MRI of cholesteatomas of the petrous bone. J Magn Reson Imaging 2002; 15: 636–641.

[6] Maheshwari S, Mukherji SK. Diffusion-weighted imaging for differentiating recurrent cholesteatoma from granulation tissue after mastoidectomy: case report. Am J Neuroradiol 2002; 23: 847–849.

[7] Mark AS, Casselman JW. Anatomy and disease of the temporal bone. In: Atlas SW, Eds. Magnetic Resonance imaging of the brain and spine, 3rd edn. Philadelphia: Lippincott, Williams and Wilkins, 2001; 1363–1432.

[8] De Foer B, Casselman JW, Govaere F, et al. The role of MRI and diffusion-weighted images in the diagnosis of middle ear cholesteatoma. Acta Radiol Port 2002; 14: 89 (abstract).

[9] Kimitsuki T, Suda Y, Kawano H, et al. Correlation between MRI findings and second-look operation in cholesteatoma surgery. ORL J Otorhinolaryngol Relat Spec. 2001; 63: 291–3.

[10] Vanden Abeele D, Coen E, Parizel PM, et al. Can MRI replace a second look operation in cholesteatoma surgery? Acta Otolaryngol. 1999; 119: 555–61.

[11] Aikele P, Kittner T, Offergeld C, et al. Diffusion-weighted MR imaging of cholesteatoma in pediatric and adult patients who have undergone middle ear surgery. AJR Am J Roentgenol. 2003 ; 181: 261–5.

[12] Stasolla A, Magluilo G, Parrott D, et al. Detection of Postoperative Relapsing/Residual Cholesteatomas with diffusion-weighted echo-planar magnetic resonance imaging. Otol Neurotol 2004: 25; 879–884.

[13] J-Ph Vercruysse, B. De Foer et al. The value of Diffusion-Weighted MR-imaging in the Diagnosis of Primary Acquired and Residual Cholesteatoma: a surgical verified study in 100 patients. Submitted for European Radiology.

[14] B. De Foer, J-Ph Vercruysse et al. The value of high resolution CT and MR imaging including diffusion-weighted images in the detection of post-operative residuel cholesteatoma. Submitted for European Radiology.

[15] Williams MT, Ayache D, Alberti C, et al. Detection of postoperative residual cholesteatoma with delayed contrast-enhanced MR imaging initial findings. Eur Radiol. 2003; 13: 169–74.

[16] Veillon F, Riehm S, Enachescu B, et al. Diffusion versus delayed post gadolinium FAT-SAT T1-weighted imaging of cholesteatoma of the petrous bone. Acta Radiol Port 2002; 14: 89 (abstract).

The Utility of Surface Coils and New Sequences in Orbital and Ocular MR Imaging

Smita Kori, M.D., Meher Ursekar, M.D., Bhavin Jankharia, M.D., Pradeep Krishnan, M.D.

Jankharia Imaging Centre, Mumbai, India

Introduction

MRI of the orbit has become an important diagnostic tool in ophthalmology. The development and refinement of surface coils, increased speed of scanning and newer pulse sequences such as post-contrast dark fluid or FLAIR sequences have improved visualization of fine details of orbital and ocular structures.

We routinely perform high resolution MRI of the orbit when clinically indicated, using phased array coils. Fat suppressed (FS) T1-weighted (T1W), T2-weighted (T2W) and dark fluid sequences are obtained in the axial, coronal and sagittal views. This has helped us in making definitive diagnoses in a number of patients.

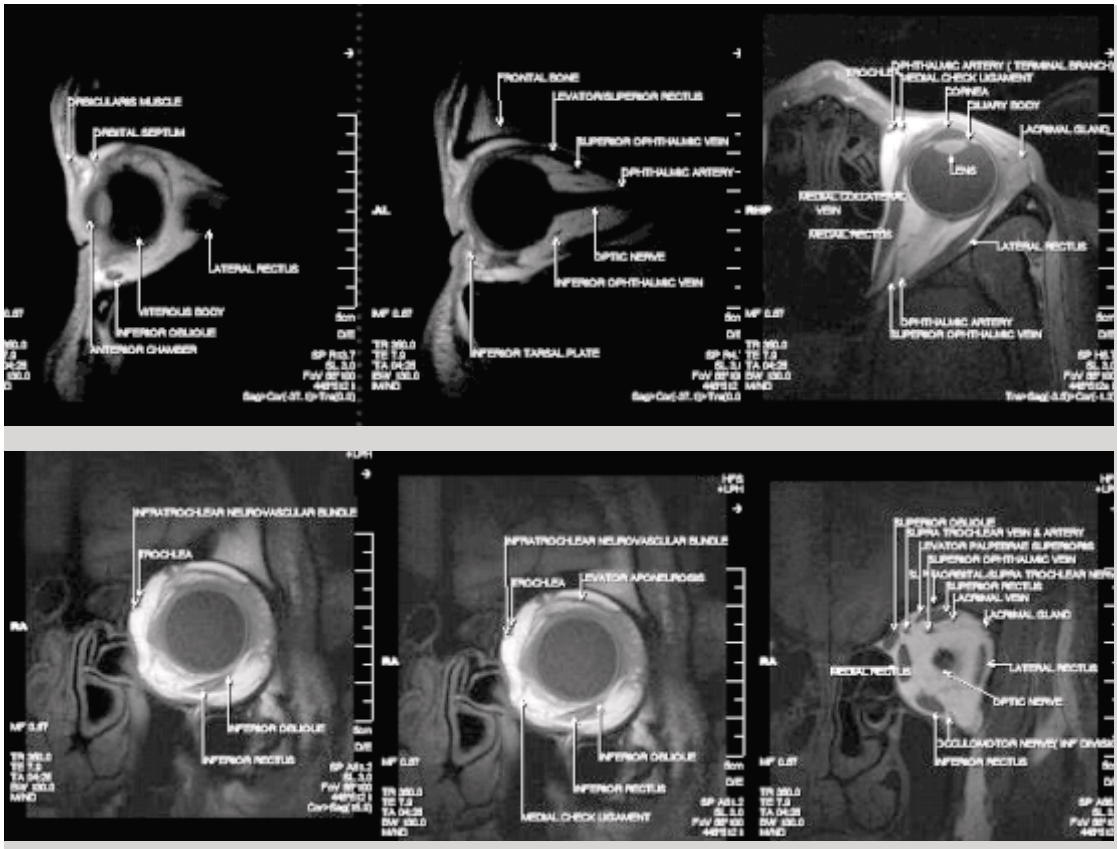

Head coil (T2-weighted)

T2 dark fluid

Comparison of the orbit. *Surface coil and head coil. Ocular layers are clearly seen on the surface coil image. The septum orbitale (arrow) is also well delineated.*

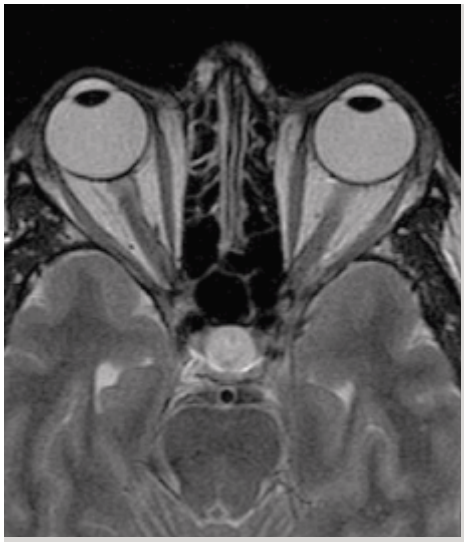

Head coil (T2-weighted)

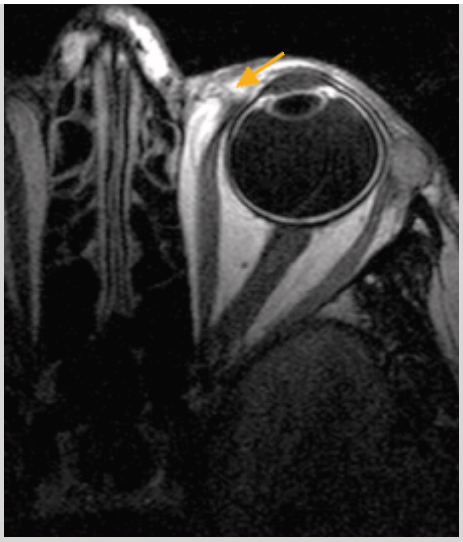

T2 dark fluid

Comparison of the orbit surface coil and head coil. *Ocular layers are clearly seen on the surface coil image. The septum orbitale (arrow) is also well delineated.*

Technique

The patients were instructed to avoid eye movements during the study. Studies were performed on a 1.5 Tesla system (MAGNETOM Sonata, Siemens Medical Solutions, Erlangen) using a surface coil with a 6 cm diameter. Oblique axial and sagittal images were planned parallel to the long axis of the optic nerve.

Findings

The higher spatial resolution coupled with increase in signal-to-noise ratio (SNR) afforded by the use of surface coils combined with rapid scanning (thus reducing motion artifacts), and pulse sequences like dark fluid, allows visualization of small details. Vitreous is effectively suppressed on dark fluid sequences and the ocular layers are better delineated. Small structures like the palpebral layers, septum orbitale and levator aponeurosis are distinguishable, allowing differentiation of the preseptal and postseptal spaces, which is important in orbital disease.

Protocol details

Sequence	TR ms	TE ms	TI	FOV mm	Matrix	S.T	No. slices	Flip angle	Band width	Time (min)
T1	350	7.9		100	256 x 256	3	14	90	130	4.32
T2	3000	98		100	512 x 512	3	14	150	130	4.26
Dark fluid	6000	99	2000	100	256 x 179	3	14	150	210	4.38

Case Studies

Complicated Sinusitis: Subperiosteal orbital inflammation secondary to left ethmoid and maxillary sinusitis.

This patient came with a history of pain in the left eye that began 15 days previously.

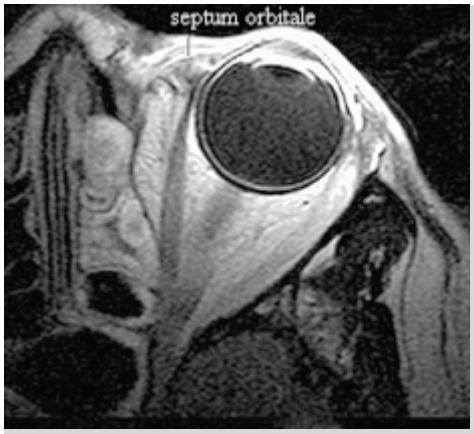

Post-contrast T1W axial

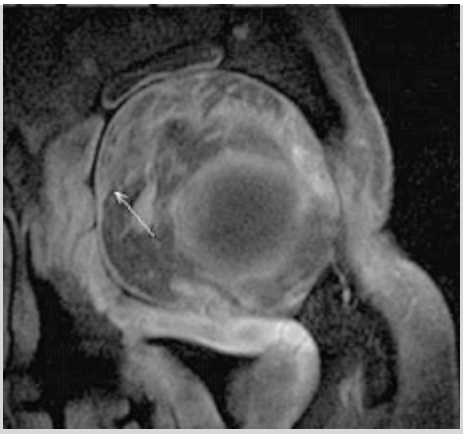

Post-contrast T1W coronal

Findings: *Streaky, enhancing inflammatory soft tissue consistent with orbital cellulitis, displacing the medial rectus and the superior oblique muscles. The good resolution images helped us to confidently exclude loculated abscess, which may have required surgical drainage, and also showed the inflammation to be confined within the postseptal space.*

Myositis of extraocular muscle

An 8-year-old female child presented with pain in the left eye that began 3 weeks previously and mild proptosis.

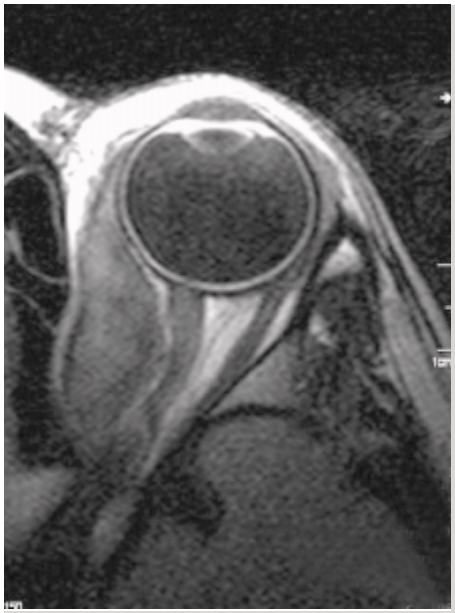

T1W axial

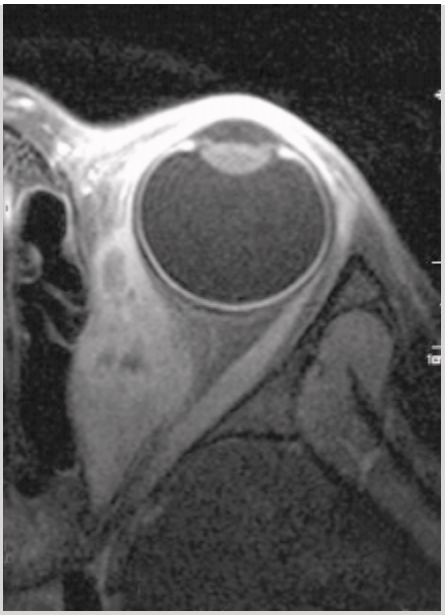

Post-contrast T1W axial

Findings: *Marked fusiform thickening of the medial rectus muscle of the left orbit, involving the muscle belly with focal indentation of the optic nerve. Heterogeneous enhancement with multiple small foci of necrosis are seen. The anterior tendon insertion was thickened and there was no focal scleral enhancement. There was no infiltration of the septum orbitale, helping to differentiate this from aggressive tumor.*

Optic nerve glioma in Neurofibromatosis type I

T1W axial

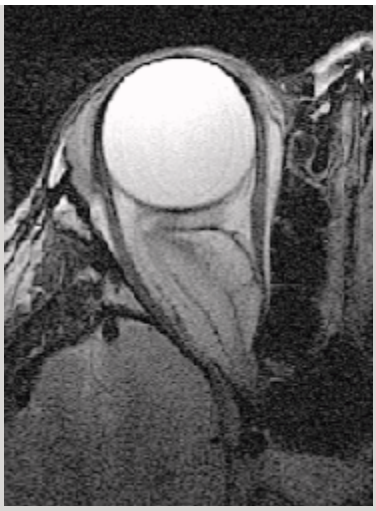

T2W axial

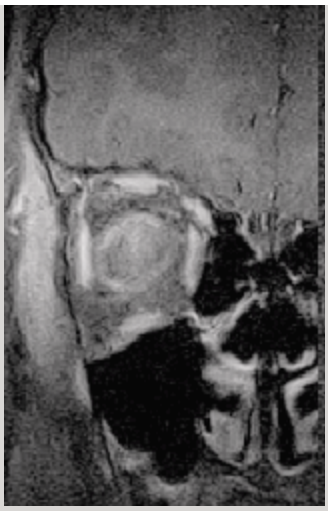

Post-contrast T1W fat suppressed coronal

Enlargement of optic nerve is noted. The optic nerve is isointense on the T1W images with hyperintense tumor surrounding the nerve sheath. Septations were seen within it and the rim found to enhance. Infiltration of the intra-canalicular segment of the nerve was seen. The tumor preserves the nerve shape and has a bulky extra-neural component that has infiltrated the sheath. This was well seen on the surface coil study.

Retinal detachment

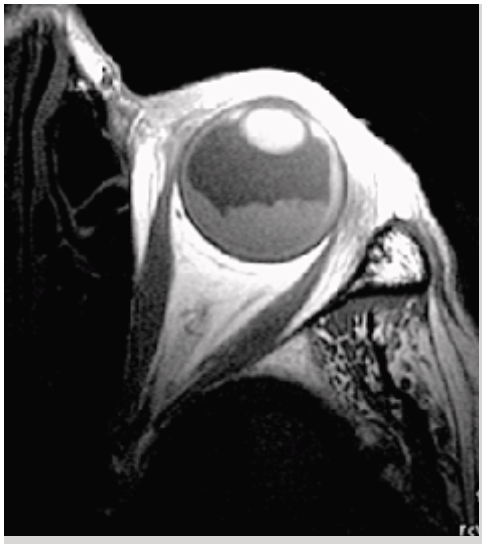

Dark fluid axial

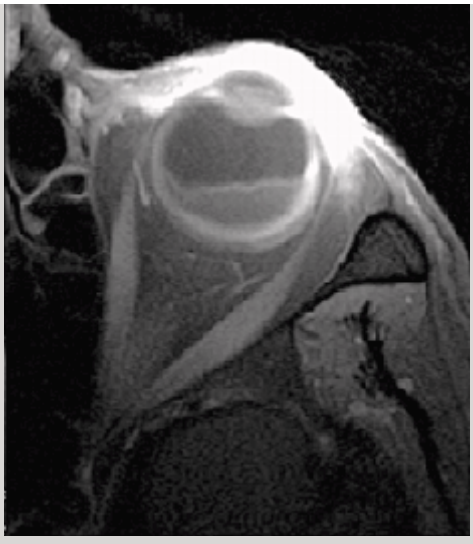

T1W axial

Homogeneous clear fluid is seen to have accumulated beneath the retinal detachment. An underlying focal mass lesion is confidently excluded, but there is diffuse thickening of the choroidal membrane due to hemangioma.

Melanoma

A 47-year-old male presented with reduced vision in the left eye which began 1 week previously.

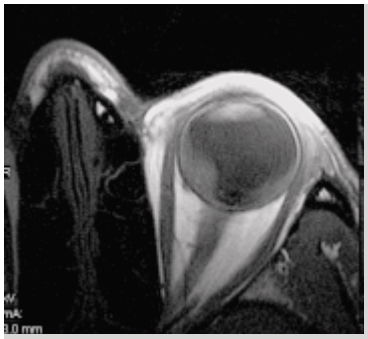

T1W axial

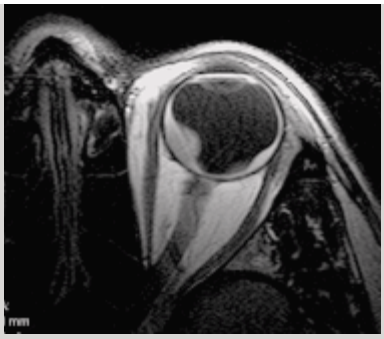

Dark fluid post-contrast axial

A focal nodular enhancing, lesion is seen in the nasal quadrant within the posterior segment of the eye. The lesion is subretinal and is associated with retinal detachment and subretinal effusion. This turned out to be a metastasis.

Lacrimal cyst

A 34-year-old male reported with swelling in the right lateral canthus.

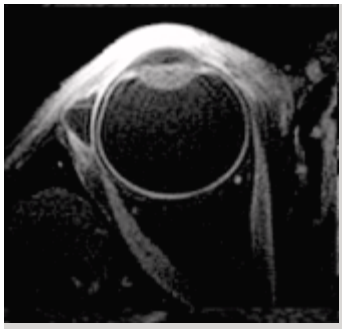

Post-contrast T1W

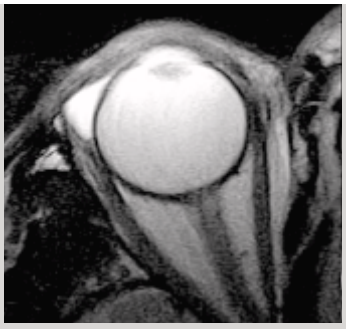

T2W

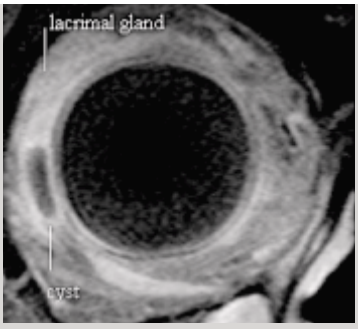

Post-contrast T1W coronal

A cystic lesion is seen in the inferior tip of the lacrimal gland (coronal image) with clear fluid within. The wall is thin and enhances. The insertion of the lateral rectus is uninvolved. Surface coil images helped confirm that the lesion was entirely within the lacrimal and was therefore, probably a benign lacrimal cyst.

Trochlear injury

Patient with head injury 4 months ago. Suspected left trochlear nerve injury.

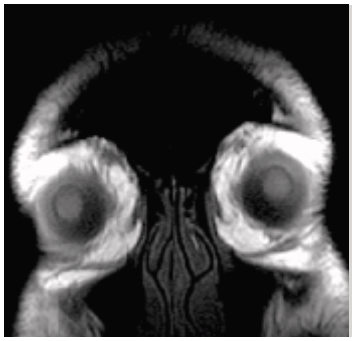

Asymmetry in the thicknesses of the superior oblique muscles is seen, with thinning of the left superior oblique belly anteriorly, near the reflected segment through the trochlea. The thinning of the insertion of the superior oblique muscle was very well appreciated.

Retinal angioma

A 25-year-old female with clinical suspicion of Von Hipple Lindau syndrome reported with complaints of reduced vision in the right eye.

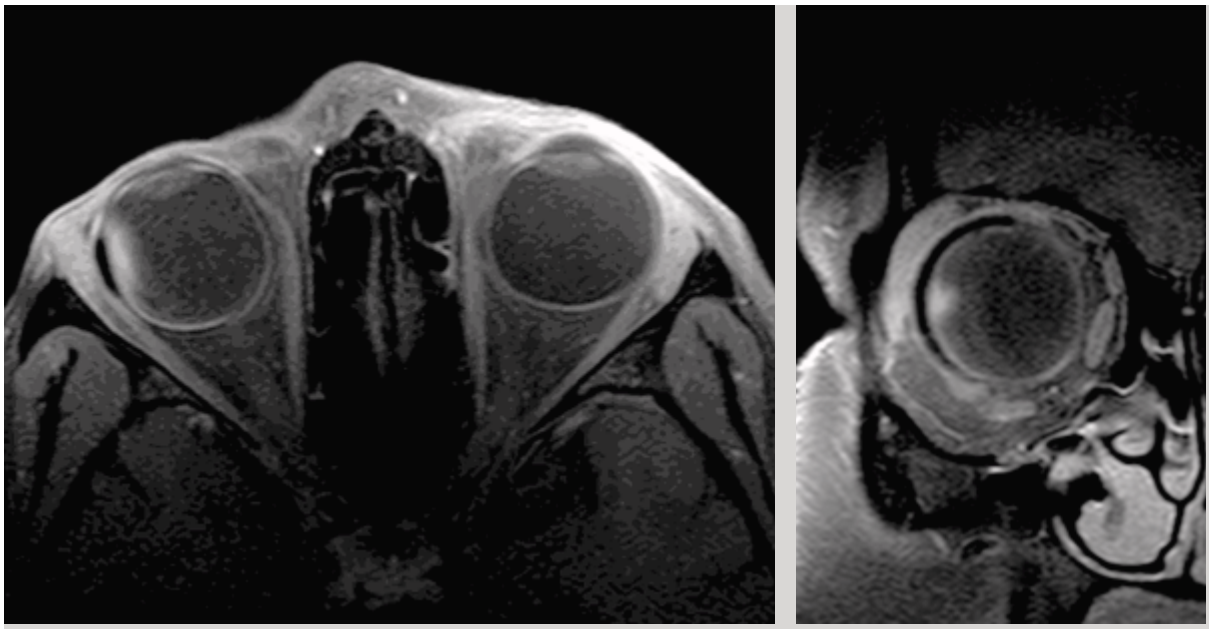

Focal enhancement along the uveal coat in the right globe laterally represents retinal angioma. MRI of the brain showed a small enhancing hemangioblastoma in the inferior vermis.

Extraocular cysticercosis

A 35-year-old male complained of pain in the right eye with accompanying right sided headaches.

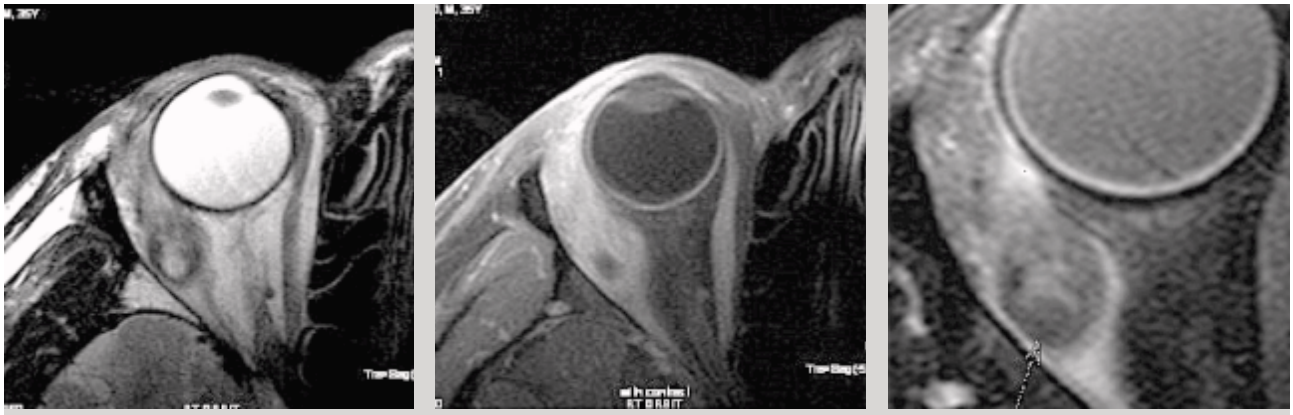

T2W Axial | *Post-contrast T1W axial* | *Post-contrast dark fluid axial*

A cystic lesion is seen within the belly of the right lateral rectus muscle. The cyst wall is thick and appears relatively hypointense on the T2-weighted images. There is thick enhancement of the cyst wall and surrounding muscle on the post-contrast image. An enhancing internal structure is seen within the cyst only on the high resolution post-contrast, fat suppressed dark fluid or FLAIR sequence. This is diagnostic of the scolex of cysticercus.

Differentiating Primary Parotid Gland Lesions by Diffusion-Weighted MR Imaging

C. R. Habermann[1], M.D., J. Graessner[2], M.Sc., M. C. Cramer[1], M.D., F. Weiss[1], M.D.

[1]*Department of Diagnostic and Interventional Radiology, University of Hamburg, Germany*
[2]*Siemens AG, Medical Solutions, Hamburg, Germany*

Introduction

The most important clinical application of Diffusion-weighted (DW) magnetic resonance imaging (MRI) is the detection and characterization of cerebral ischemia (1). Recently, a few studies were published to determine the value of DW MRI in healthy parotid glands and systemic disorders affecting parotid glands by measuring ADC values under physiologic and pathologic conditions, or after irradiation (2–4).

In the Department of Otorhinolaryngology in Hamburg, Germany between 80 and 120 patients with tumors are operatively treated per year. Comparable to the literature, between 60 to 80% of these patients suffer from pleomorphic adenoma or Warthin tumors. The missing twenty percent show primary malignant tumors of the parotid gland, or prove to have metastatic disease within the parotid gland. So, most patients are treated under the assumption of a benign primary disease. The difficulty is not only that the operative approach differs among benign and malignant tumorous disease but also that pleomorphic adenoma has to be treated more aggressively in comparison to Warthin tumors, due to their higher recurrence rate (5).

Methods

All examinations were performed using a MAGNETOM Symphony with a Quantum gradient system, with 30 mT/m maximum gradient capability and a maximum slew rate of 125 mT/m/sec. The lower part of the circularly polarized (CP) head coil and a standard two-element CP neck array coil were used. The flexibility of the neck array coil allowed positioning the N1 element right next to the parotid gland. An axial diffusion-weighted EPI (echo-planar imaging) sequence (TR 1,500 ms / TE 77 ms) was obtained with a matrix of 119 x 128, a field of view of 250 x 250 mm (pixel size 2.10 x 1.95 mm), 6 excitations, and a section thickness of 5 mm with an interslice gap of 1 mm. A parallel imaging technique (modified Sensitivity Encoding algorithm (mSENSE)) with an acceleration factor of two with twelve additional lines for self calibrating was applied. A bandwidth of 1502 Hz/pixel was used and 12 slices were acquired. The b factors used were 0 s/mm^2, 500 s/mm^2 and 1,000 s/mm^2. Fat suppression was achieved by placing the frequency-selective radio-frequency pulse before the pulse sequence. The automatic 3D-shim routine of the magnet used the slice block as the shim volume. The total acquisition time of this sequence was 1:14 mins.

Evaluation of the ADC maps were performed using the analyzing software MRIcro (Chris Rorden, University of Nottingham, Great Britain), which lists every pixel intensity of each ADC slice in a single ROI output file per patient.

Conclusion

DW MR imaging seems to be a valuable tool to differentiate not only benign from malignant lesions, as shown in the two patients above, but also to differentiate between malignant and benign primary lesions of parotid glands (6). In our ENT department it has become an obligatory second line imaging tool prior to surgery for planning the operative strategy. Up to now, 135 patients with primary lesions of parotid and submandibular glands were examined with DW MR imaging, with no failure to provide the diagnosis.

References

[1] Fiehler J, Fiebach JB, Gass A, et al. Diffusion-weighted imaging in acute stroke – a tool of uncertain value? Cerebrovasc Dis 2002; 14: 187–196.

[2] Sumi M, Takagi Y, Uetani M, et al. Diffusion-weighted echoplanar MR imaging of the salivary glands. AJR Am J Roentgenol 2002; 178: 959–965.

[3] Patel RR, Carlos RC, Midia M, Mukherji SK. Apparent diffusion coefficient mapping of the normal parotid gland and parotid involvement in patients with systemic connective tissue disorders. AJNR Am J Neuroradiol 2004; 25: 16–20.

[4] Habermann CR, Cramer MC, Graessner J, et al. Functional imaging of parotid glands: diffusion-weighted echo-planar MRI before and after stimulation. Rofo 2004; 176: 1385–1389.

[5] Donovan DT, Conley JJ. Capsular significance in parotid tumor surgery: reality and myths of lateral lobectomy. Laryngoscope 1984; 94: 324–329.

[6] Habermann CR, Gossrau P, Graessner J, et al. Diffusion-weighted echo-planar MRI: a valuable tool for differentiating primary parotid gland tumors? Rofo 2005; 177: 940–945.

Case 1

46-year-old female patient with a palpable, painless mass of the right cheek.

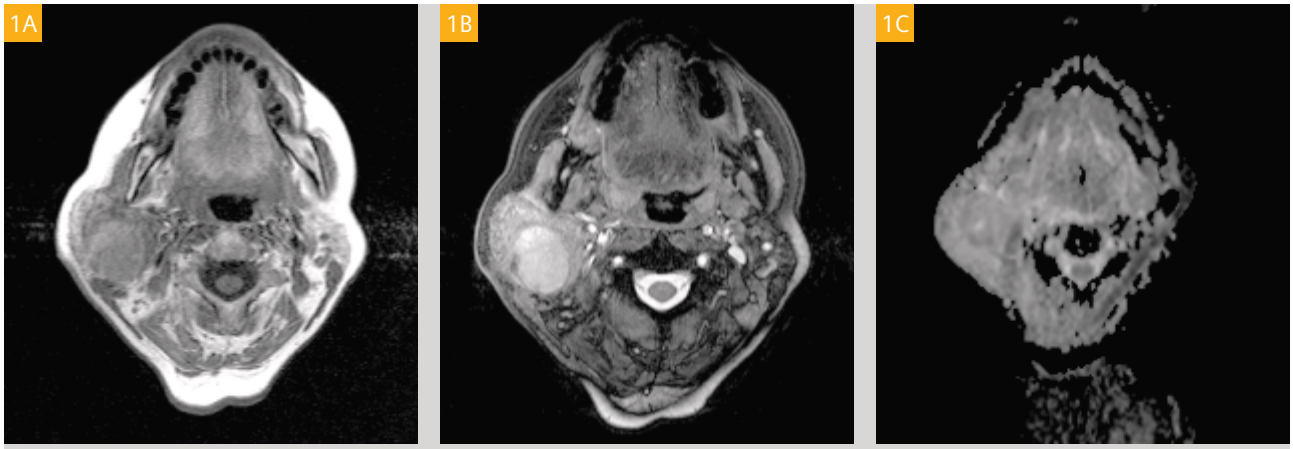

The T1-weighted images (1) showed a tumor in the right parotid gland with muscle isointense appearance. The T2-weighted images (A) showed an intraparotideal mass with higher signal intensity as the surrounding parotid gland tissue and the muscles. Concerning the ADC images a fairly low value could be obtained (1.28 x 10–3 $mm^2/s \pm 0.11 \times 10–3\ mm^2/s$). Images show a histologically proven salivary duct carcinoma.

Case 2

76-year-old male patient with a palpable, painless mass of the right cheek.

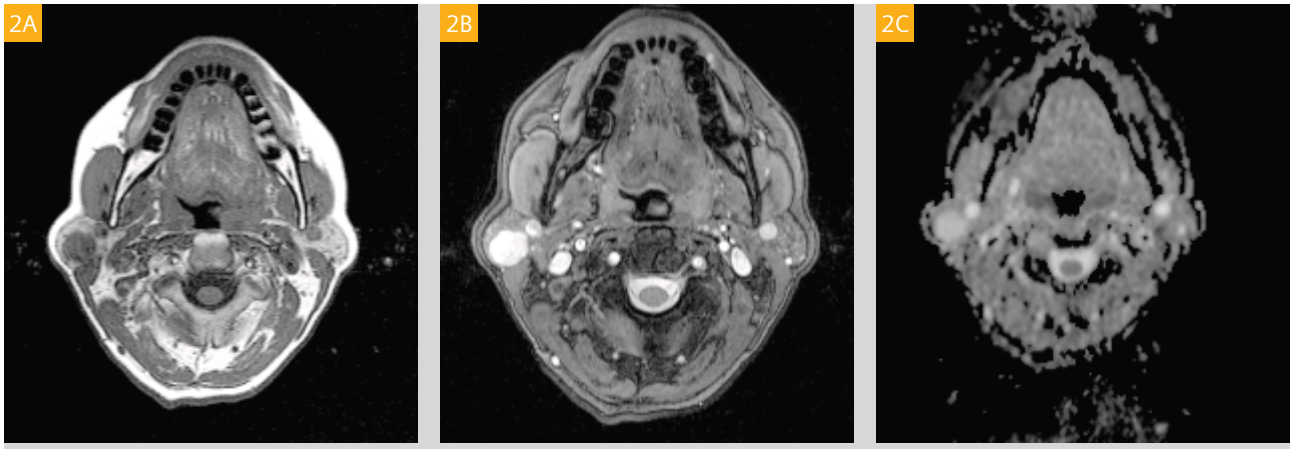

The morphologic appearance of this tumor is very similar to the tumor presented in case 1. In both patients contrast enhancement gave no additional information regarding the tumor. In contrast to case 1, the ADC images showed an obvious higher diffusion within the tumor (2.06 x 10–3 $mm^2/s \pm 0.15 \times 10–3\ mm^2/s$). Histology revealed a pleomorphic adenoma.

3T Ultra High-Field Intraoperative MR with Twin Room Concept

Alp Dinçer, M.D.[1], M.Necmettin Pamir, M.D.[2]

Acibadem Kozyatağı Hospital, Dept. of Radiology (1) and Neurosurgery (2), Istanbul, Turkey

Introduction

Intraoperative MR (IoMR) has gained acceptance over the last decades. IoMR during neurosurgical intervention has allowed not only improvement of the precision of navigation, optimization of the surgical approach and maximal preservation of normal brain tissue and function, but also an assessment of the completeness of tumor resection and the ability to exclude surgical complication (1). As IoMR has been evolving, many different system configurations – with their own advantages and disadvantages – have been developed (1–3). The main disadvantage of low field scanners is low SNR that affects not only the image quality and scan time, but also restricts the many new intraoperative applications such as functional MR, MR Spectroscopy (MRS), and Diffusion Tensor Imaging (DTI) Fiber Tractography. As the image quality is strictly related to the strength and homogeneity of the static and gradient magnetic fields, we chose the state-of-the-art 3T MR system for our dedicated neurosurgery hospital to be able to perform newer MR applications. Due to economic trade-offs (with our approach), instead of putting the magnet in the operating room, we preferred the twin room concept with a floating table that allows the transfer of the patient from one room to another easily. Furthermore, this configuration allows us to use every kind of surgical equipment including the microscope out of the 5 Gauss line without any compromise.

Method

Our 3T MRI site is built next to the operating theatre dedicated to neurosurgical operations. The magnet room and the operating theatre, which are connected to each other by a door, are both RF-shielded. In daily practice, we use the 3T MRI (MAGNETOM Trio, Siemens, Erlangen) as a clinical scanner. Before the operation, the magnet and the console rooms are disinfected. Whenever the neurosurgeon needs imaging during the operation, the door between the magnet room and the operating theatre is opened, and the patient is transferred from the operating table to the magnet cradle with a floating table in a maximum of three minutes. All of the equipment in the magnet room is compatible with 3T MR. Since all of the surgical equipment including the microscope is out of the 5 Gauss line, we can use all of it safely. Initially, we used the body coil to transmit and receive signal in 25 patients because we did not have the head coil compatible with the head holder. Over the last three months, we have used a dedicated head holder with a specially designed 8-channel head coil. Axial, sagittal and/or coronal TSE T2, SE T1 and 3D FLASH T1-weighted images (slice thickness 1–6 mm, gap 0–1 mm, matrix 192-256 x 256-512, FOV 200–260 mm) are obtained according to the lesion. Total examination time including the transfer of the patient, the analysis of the images and the final decision is approximately 10 minutes. At the end of the examination we decide to continue or terminate the operation. If we decide to go on, the examination procedure is repeated. If the operation is terminated, the door between the magnet room and the operating theatre is closed, and routine outpatient examinations begin immediately.

Discussion

The image quality of the MR was acceptable and diagnostic in the examinations using the body coil at the beginning. The image quality and the spatial resolution of the MR exams using the 8-channel head coil are excellent without any compromise. Hemorrhage and susceptibility do not cause any significant artifacts at the high 3T field strength. There were no complications attributable to the procedure.

The main advantage of this setup is the shorter (10 min) examination time. The 3T state-of-the-art scanner gives us an opportunity to perform high resolution morphologic work-up in a reasonable time. Furthermore, the ability to perform more sophisticated techniques preoperatively has now become a reality.

Case 1

A 67-year-old female patient was admitted due to seizure. Immediate preoperative MRI and functional MRI (left hand finger tapping paradigm) showed that there was a mass in the right frontal lobe including the eloquent motor cortex (Figs. 1A and B). Intraoperative MRI with the body coil demonstrated complete resection (Figs. 2A, B and C). One day later the follow-up examination confirmed the completeness of resection (Figs. 3A and B). Fiber tractography showed that there was no difference between preoperative (Figs. 4A and B) and postoperative (Figs. 5A and B) corticospinal tracts. Pathological exam revealed the mass as anaplastic astrocytoma. 6 months later, the patient was able to walk without assistance.

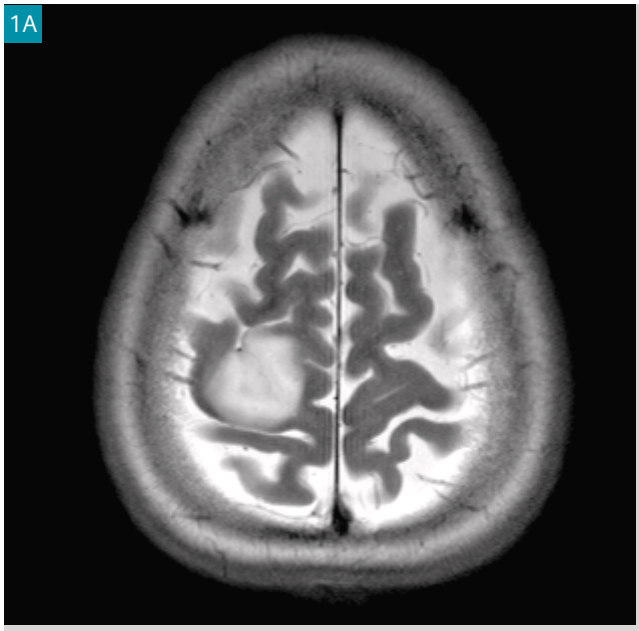

[Figure 1A] *Axial TSE T2-weighted (T2W) image.*

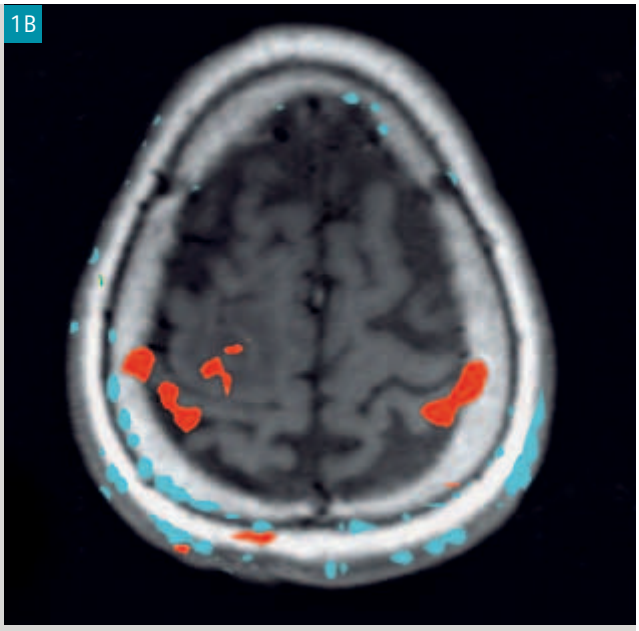

[Figure 1B] *Color coded parametric map.*

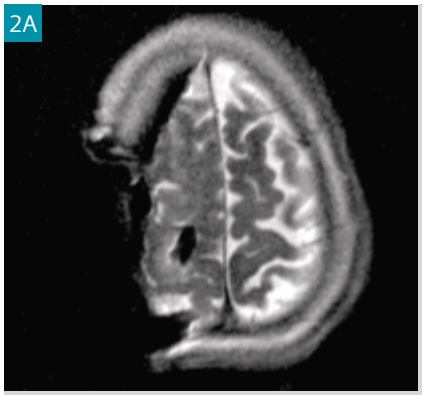

[Figure 2A] *Axial TSE T2W image.*

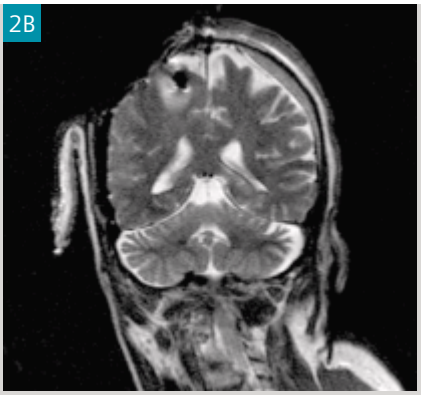

[Figure 2B] *Coronal TSE T2W image.*

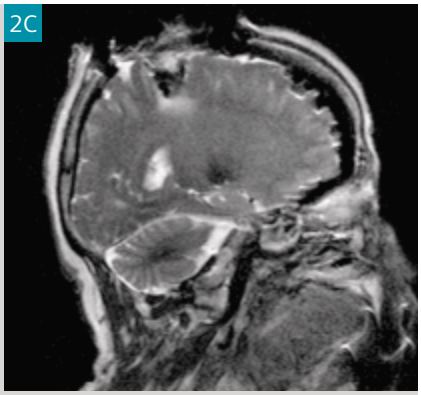

[Figure 2C] *Sagittal TSE T2W image.*

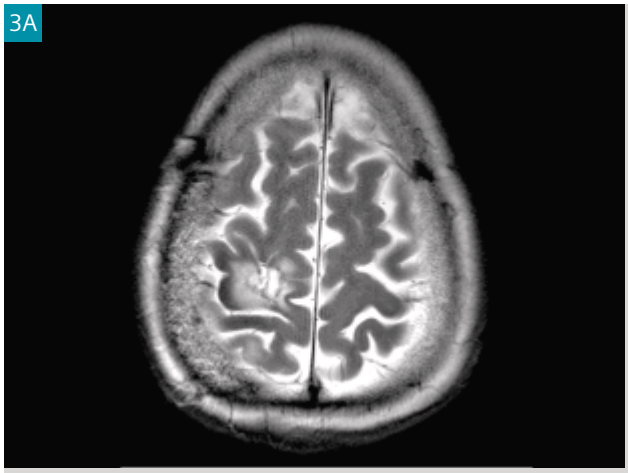

[Figure 3A] *Axial TSE T2W image.*

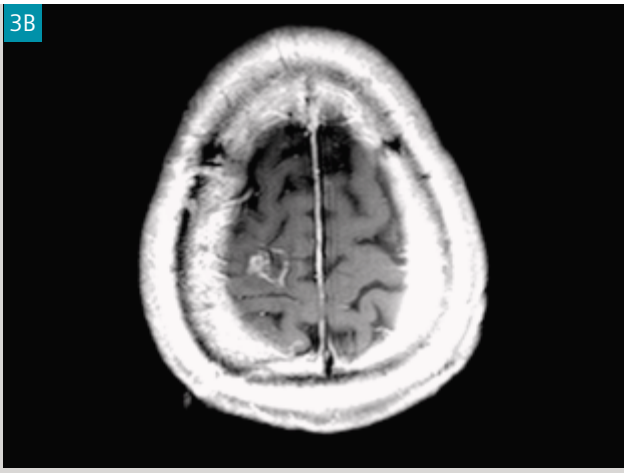

[Figure 3B] *Axial SE T1W image without contrast.*

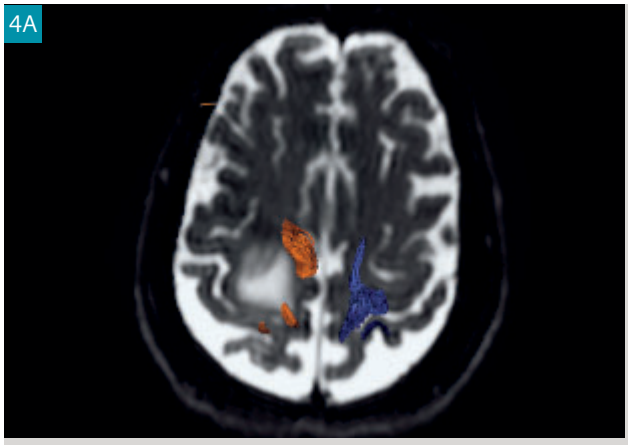

[Figure 4A] *Pre-operative DTI.*

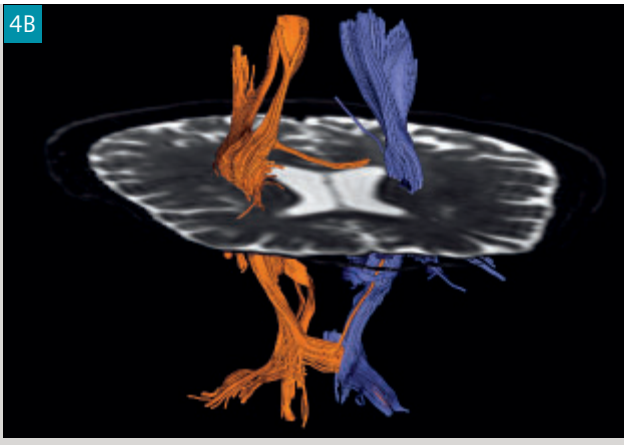

[Figure 4B] *Pre-operative DTI showing cortico spinal tracts.*

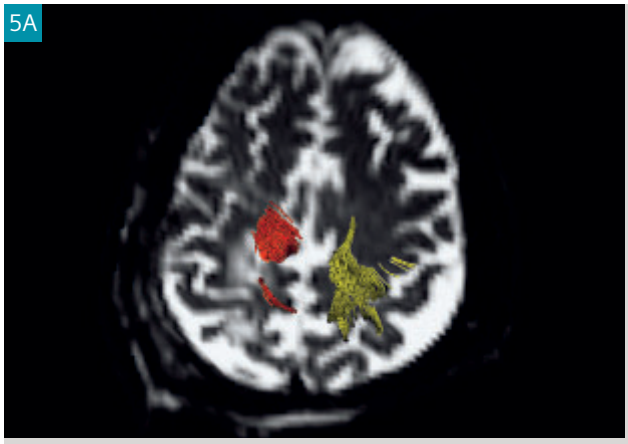

[Figure 5A] *Post-operative DTI.*

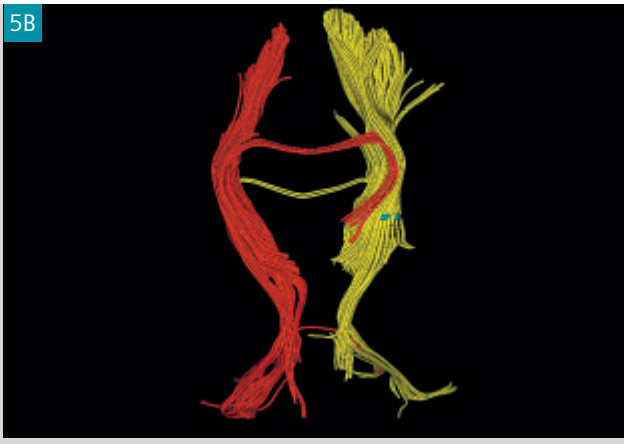

[Figure 5B] *Post-operative DTI showing corticospinal tracts showed no difference to the pre-operative ones.*

Case 2

A 70-year-old male had had 3 operations in another center due to non-functional macroadenoma of the pituitary gland. Follow-up MR examination carried out at another center revealed recurrence (Figs. 6A and B). During the operation the MR examination with the 8-channel head-coil (Figs. 7A and B) showed residual tumor in the suprasellar cistern near the stalk. The neurosurgeon decided to continue operating. A 24-hour follow-up exam demonstrated total resection (Figs. 8A and B).

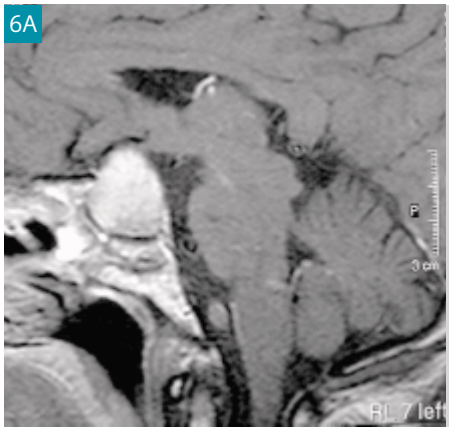

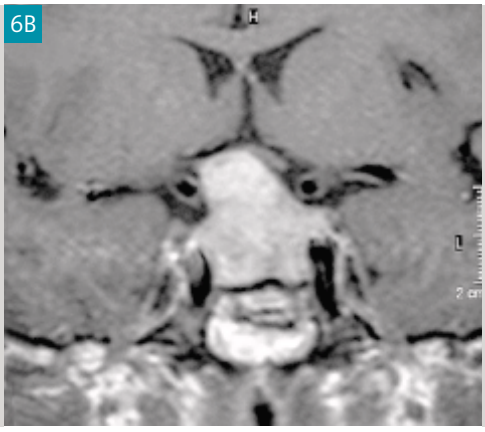

[Figure 6A]
Sagittal SE T1W with contrast

[Figure 6B]
Coronal SE T1W image with contrast

[Figure 7A]
Coronal TSE T2

[Figure 7B]
Sagittal TSE T2W image

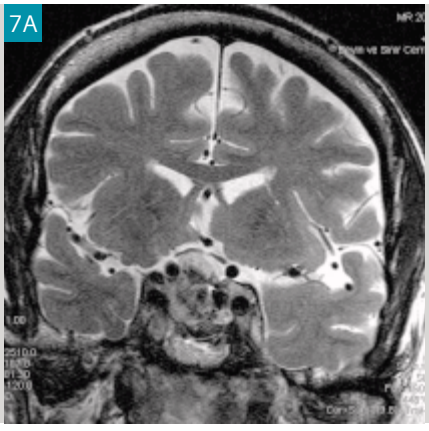

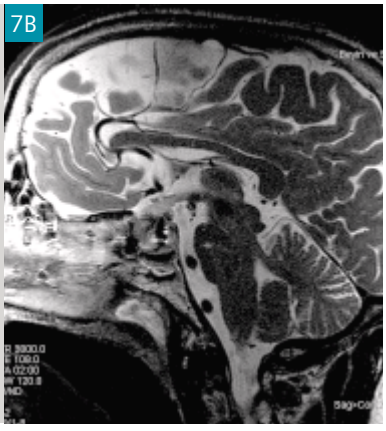

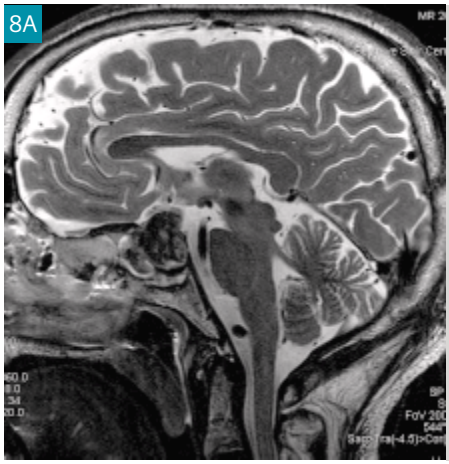

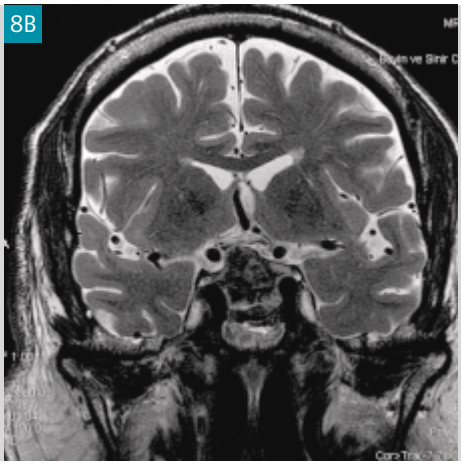

[Figure 8A]
Sagittal TSE T2W image

[Figure 8B]
Coronal TSE T2 image

Case 3

A 37-year-old male was admitted to the hospital due to seizure. He had undergone an operation 3 years previously for low grade astrocytoma of the left temporal lobe. After control MRI (Figs. 9A and B), which had revealed recurrent left temporal mass, the patient was operated on. Intraoperative MR (Fig. 10) showed incomplete resection of the tumor: the neurosurgeon decided to continue the operation. The imaging after further resection showed no residual tumor. (Fig. 11). Postoperative 24-hour follow-up examination with contrast also confirmed total resection of the tumor (Fig. 12).

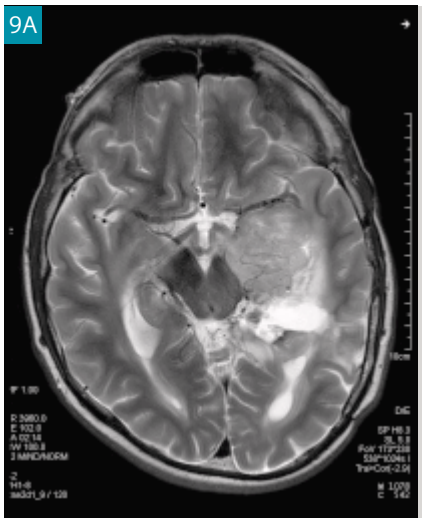

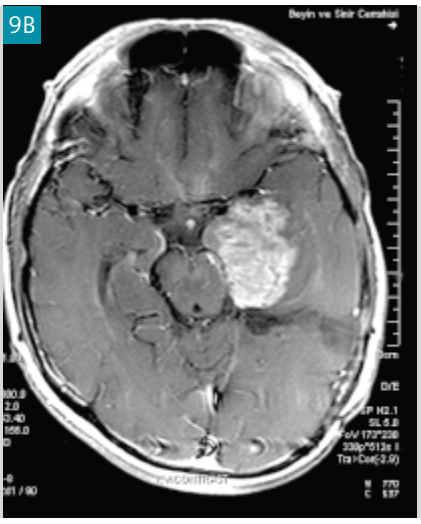

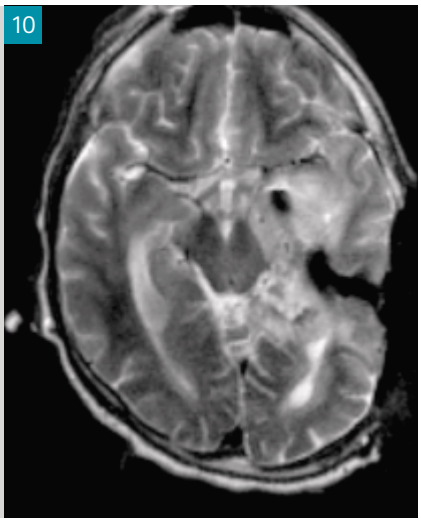

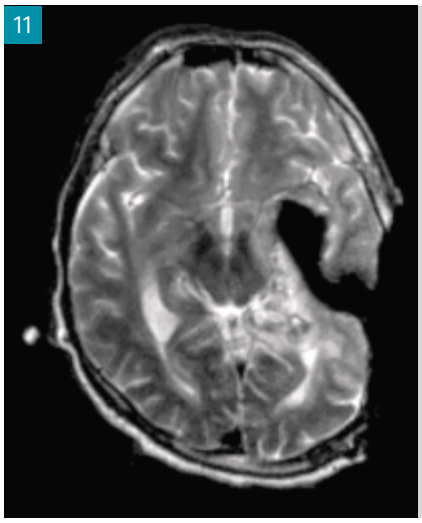

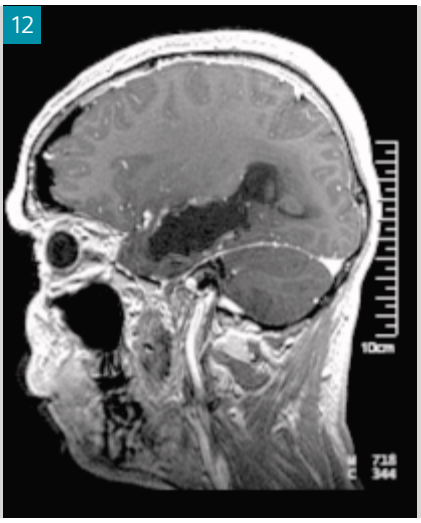

[Figure 9A] *Axial T2W image*

[Figure 9B] *Axial T1W image with contrast*

[Figure 10] *Axial T2W Image*

[Figure 11] *Axial T2W image*

[Figure 12] *Sagittal 3D MP-RAGE with contrast*

References

[1] Fenchel S, Boll DT, Lewin JS. Intraoperative MR imaging. Magn Reson Imaging Clin N Am 2003;11: 431–447.

[2] Nimsky C, Gansland O, Hastreiter P, Wang R, Benner T,Sorensen AG, Fahlbusch R. Preoperative and intraoperative diffusion tensor imaging-based fiber tracking in glioma surgery. Neurosurgery 2004; 56: 130–138.

[3] Nimsky C, Gansland O, Fahlbusch R. Comparing 0.2 Tesla Intraoperative With 1.5 Tesla Intraoperative Magnetic Resonance Imaging: Analysis of setup, Workflow, and Efficiency. Acad Radiol 2005; 12: 1065–1079.

Iron-Oxide Enhanced Susceptibility-Weighted Imaging of Lymph Node Metastasis

Ravi Seethamraju, Ph.D.[1], Milind Dhamankar, M.D.[1], Mukesh Harisinghani, M.D.[2]

[1]*Siemens Medical Solutions, Malvern, PA, USA*
[2]*Massachusetts General Hospital, Boston, MA, USA*

Introduction

Detection of local and regional lymph node metastases is important for determining therapy and prognosis in patients with various primary malignancies. Currently cross sectional imaging modalities like contrast enhanced* CT and MRI rely solely on size criterion as the primary yardstick for detection of malignant lymph nodes. However nodal size is not an accurate method, as not all malignant nodes are enlarged and conversely not all large nodes are malignant [1]. Thus a more robust and accurate technique is needed for staging lymph nodes which characterizes lymph nodes independent of their size. MRI enhancement with ultra-small super-paramagnetic iron oxide particle (USPIO) has shown to be an accurate and reliable imaging technique for detection of minimal nodal metastatic disease independent of lymph node size.

Commercial preparation of USPIOs like Ferumoxtran-10 (Combidex [Advanced Magnetics, Cambridge, Mass]; also known as Sinerem, AMI-7227, AMI-227, and BMS 180549) target the reticulo-endothelial system and have been specifically developed for MR lymphangiography. These agents are composed of an iron oxide crystalline core of 4.3–6.0 nm covered by low-molecular-weight dextran. Their T1 and T2 relaxations are 2.3 x 10^4 and 5.3 x 10^4 mol^{-1} sec^{-1} (20 MHz, 39°C), respectively, in 0.5% agar.

Upon intravenous injection, these contrast agents are transported to the lymph nodes binding to specific receptors within the nodal macrophages. If the lymph nodes are benign, the macrophages function normally and phagocytose the intravenously administered nanoparticles. Thus normal lymph nodes show a drop in signal intensity on MRI imaging after Ferumoxtran-10 administration due to the susceptibly from phagocytosed nanoparticles. In contrast, malignant infiltration results in lack of macrophages and hence these regions, due to the lack of iron oxide uptake, retain their high signal intensity. This is the underlying principle behind MR lymphangiography.

Imaging

Metastasis in normal-sized lymph nodes can be of the order of 4–9 mm [2], hence from the MR viewpoint it is very essential that the maximum voxel dimension should not exceed 2 mm for capturing even the least amount of metastasis in a lymph node. While this restriction was routine in the case of in-plane dimensions, through-plane dimensions were restricted in the case of multi-echo gradient echo (MEGE) sequences. MEGE sequences are very essential for MR lymphangiography as they facilitate the computation of T2* which is an indicator of malignancy. This problem has been alleviated with the development of the new works in progress T2*-weighted Multi-Contrast Gradient Echo (MCGE) sequence at Siemens Medical Solutions.

The Sequence

Currently the MCGE sequence supports a maximum of 12 contrasts with the facility to choose a bi-polar or mono-polar readout. While bi-polar readouts are standard for Gradient Echo sequences, they suffer from chemical shift artifacts that shift between echoes. This essentially destroys any in-plane resolution advantage as they tend to spoil the computation of T2* in the regions that are chemically shifted. The mono-polar readout, however, maintains the chemical shift by using a gradient rewinder between readouts so that all the k-space lines are acquired in the same direction. The availability of integrated Parallel Acquisition Techniques (iPAT) in these sequences further saves acquisition time.

The Protocol

Currently the protocol has been optimized for pelvic studies and has been successfully tested on patients. Apart from the MCGE sequence, a VIBE and T2-weighted spin echo sequences are used for obtaining spatial and anatomical characterization of the nodes. The protocol is applied twice, once before the administration of the contrast agent and 24 hours after the administration of the contrast agent. The individual compo-

nents of the protocol as currently tested on a 1.5T MAGNETOM Avanto are as follows:

1. A T1-weighted (T1W) 3D VIBE non breath-hold sequence with TE 1.9 ms, Flip Angle = 12°, TR 5 ms, BW 260 Hz/Px, FOV 340 x 340 mm and 1.3 x 1.3 mm and interpolated slice thickness of 2.68 mm acquired coronally to cover around 100 slices acquired in 2 minutes. These images are required for a MIP of the vasculature that will serve as a reference for location of the nodes.
2. A T2-weighted TSE non breath-hold sequence with TE 76 ms, Flip Angle 90°, TR 4000 ms, BW 160 Hz/Px, FOV 340 x 340 mm and slice thickness of 2.68 mm acquired axially to cover around 30 slices acquired in roughly 3 minutes. Though the T2-weighted images are not preferred for quantification of the metastasis, they are excellent in terms of signal-to-noise ratio (SNR) and devoid of blooming artifacts resulting from the susceptibility of iron, so node delineation and identification is easier on these images.
3. The T2*-weighted MCGE non breath-hold sequence with TE 8.8 ms to 70 ms (12 contrasts), Flip Angle 75°, TR 1800 ms, BW 130 Hz/Px, FOV 214 x 380 mm and slice thickness of 2 mm acquired axially to cover 45 slices in 6 minutes with iPAT factor of 2. All sequences use a 0 mm gap between slices.

Initial Experiences

After initially experimenting on an oil-water phantom, the protocol was tried on a patient. The T2* MCGE sequence was also run in the bi-polar mode for comparison. In the case of bi-polar mode the acquisition time was reduced roughly by a factor of two due to the absence of the rewinder between echoes. The images from the first echo and the corresponding T2* computed from the echoes are presented in Fig. 1. It can be seen very clearly that for the same echo time and windowing that the image from the monopolar sequence is crisper and hence the computed T2* is more reliable.

Fig. 2 shows pre- and post-contrast T2-weighted images. Note how the node is easy to discern, especially the partial fatty infiltration. Fig. 3 is a VRT rendering of the vasculature

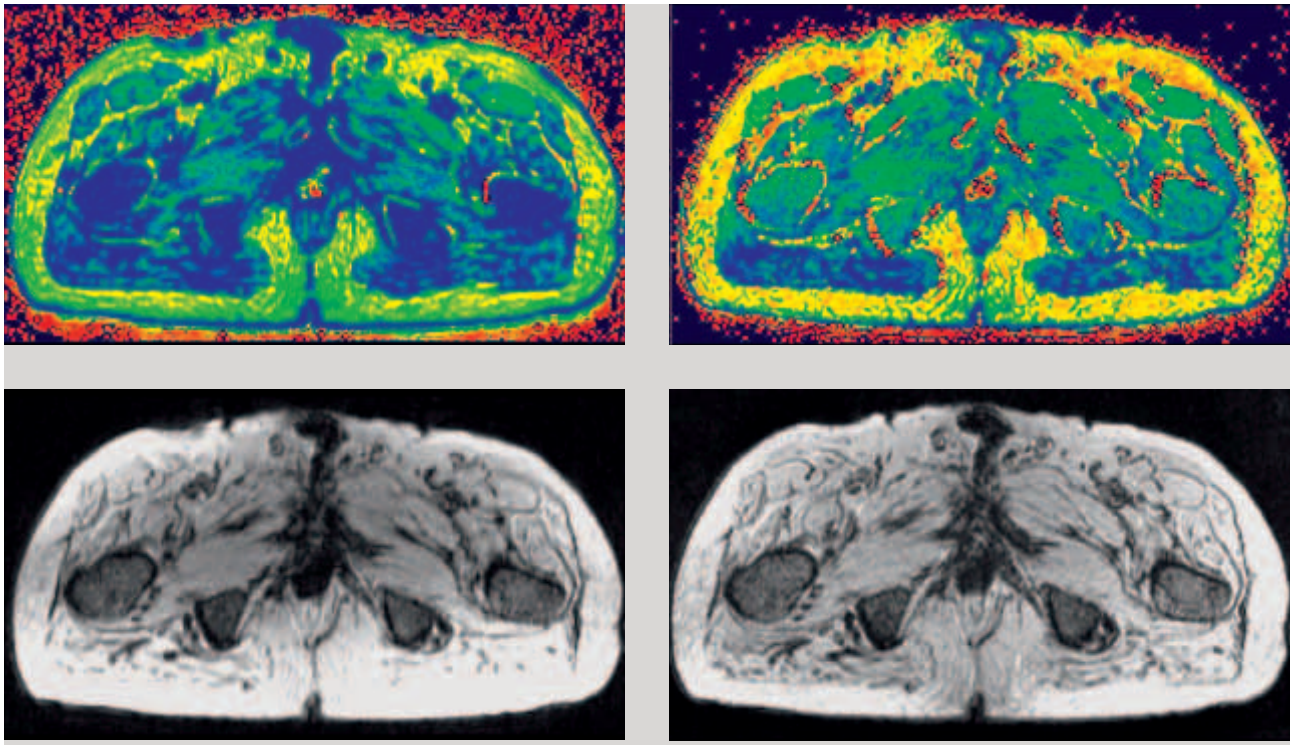

[Figure 1] *Comparison between bi-polar and mono-polar images. Images in top row are T2* maps and bottom row are single echo images at same echo time. Images on the left are from the bi-polar sequence and on the right are from the mono-polar sequence. Note how the images from the mono-polar sequence have more detail than those from the bi-polar sequence. This is due to the averaging effect of the alternating phase shifts in the bi-polar sequence.*

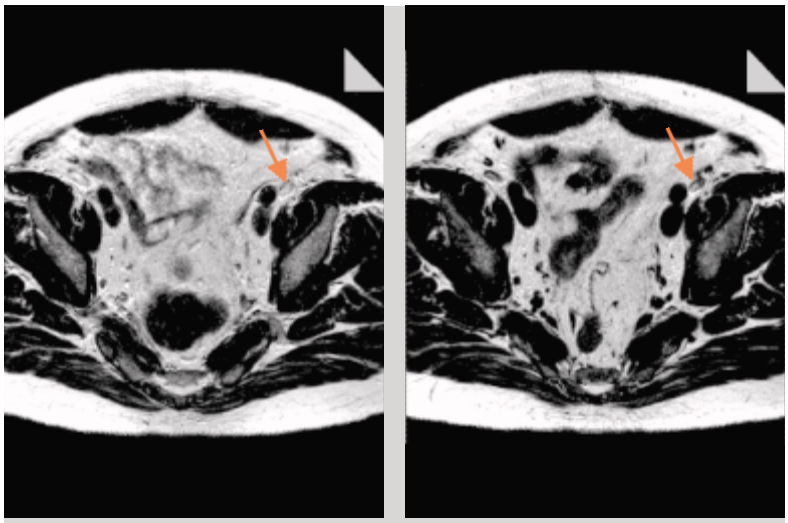

[Figure 2] *T2-weighted TSE axial slice showing partial fatty infiltration in the node. The image on the left is pre-contrast and on the right is post-contrast. Note that on the post-contrast image a portion of the node still remains bright while the rest of the node has become very dark. This is because the USPIO is not absorbed by the fatty infiltration. To differentiate fatty infiltration from metastases, the shape of the lymph node and the hypo intensity need to be taken into account. A fat suppressed T1 can also give clues on the fatty infiltration.*

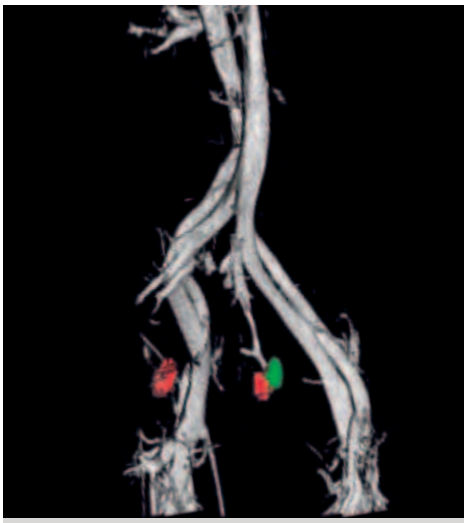

[Figure 3] *Segmented nodes color coded on a VRT rendered vasculature. Information from segmented nodes is coded with unique values that are then combined with information from the T1-weighted 3D VIBE images to obtain the VRT rendering of the nodes on the vasculature. Benign nodes are coded green and malignant red.*

with segmented nodal information from the T2 images superimposed with color coded information from the T2*s. This has been achieved by the use of a works in progress *syngo* task card that has been optimized for the workflow of the current protocol.

Conclusion

With the usage of a mono-polar multi-contrast GRE sequence it has been demonstrated that the estimation of T2* is vastly improved, thereby improving the detection of metastatic lymph nodes.

Future Directions

With Tim (Total imaging matrix) technology, it is now possible to flexibly combine coils to increase the field of view for metastatic evaluation beyond a localized region.

Implementation on 3T would offer interesting insights and challenges. While there will be an improvement in SNR and reduction in acquisition time, susceptibility artifacts will be more pronounced.

Optimization with respect to echo times and number of echoes is in progress. Reduction in number of echoes without any increase in noise would greatly help reduce the acquisition time, since with breath-holding in the case of abdominal studies time will be a factor. Addition of navigators on the other hand would also help in the case of abdominal studies.

Acknowledgements

We wish to acknowledge John Kirsch of Siemens Medical Solutions whose expert advice was crucial to the optimization of the protocols.

* This information about this product is preliminary. The product is under development and not commercially available in the US, and its future availability cannot be ensured.

References

[1] Harisinghani M.G., Weissleder R., Sensitive, Noninvasive Detection of Lymph Node Metastases, PLOS 2004, Vol. 1., (3): 202–209.

[2] Deserno W.M.L.L.G., Harisinghani M.G., et. Al., Urinary Bladder Cancer: Preoperative Nodal Staging with Ferumoxtran-10 enhanced MR Imaging, Radiology 2004; 233: 449–456.

Intravenous Cellular MR Contrast Agent* with a Great Clinical Potential

Jelle Barentsz, M.D., Ph.D.

Department of Radiology, UMCN, Nijmegen, The Netherlands

Introduction

Pelvic lymph node metastases have a significant impact on the prognosis of patients with malignancies. In prostate cancer, for example, even micro metastases in a single node rule out surgical cure by the available treatment protocols. For bladder cancer lymph node metastases are also significant. More than 5 lymph node metastases or extra capsular growth precludes curative surgical treatment. Thus, the status of the lymph nodes largely dictates the management of the primary tumour.

Surgical open pelvic lymph node dissection (PLND), considered to be the only reliable method for assessing lymph node status, is an invasive procedure associated with potential complications and side effects. A noninvasive, reliable method for detecting and staging nodal metastasis would reduce unnecessary surgery. Routine cross-sectional imaging modalities like CT and MRI lack the desired sensitivity in identifying metastases as they largely rely on size criteria only, and small metastases in normal size nodes can be missed. Moreover, differences in signal intensity on MR images between normal and cancerous nodes as well as gadolinium enhancement have also proven to be unreliable. Although very promising in metastatic lung cancer, the role of ^{18}FDG PET-scanning is limited in the urinary tract region, as ^{18}Fluorodeoxyglucose accumulates in the urinary bladder and kidneys. This makes an evaluation of metastases at this site difficult. Also in various tumors like prostate and bladder cancer this method is further limited by its low uptake in metastatic nodes. Although the sensitivity of ^{18}FDG PET is

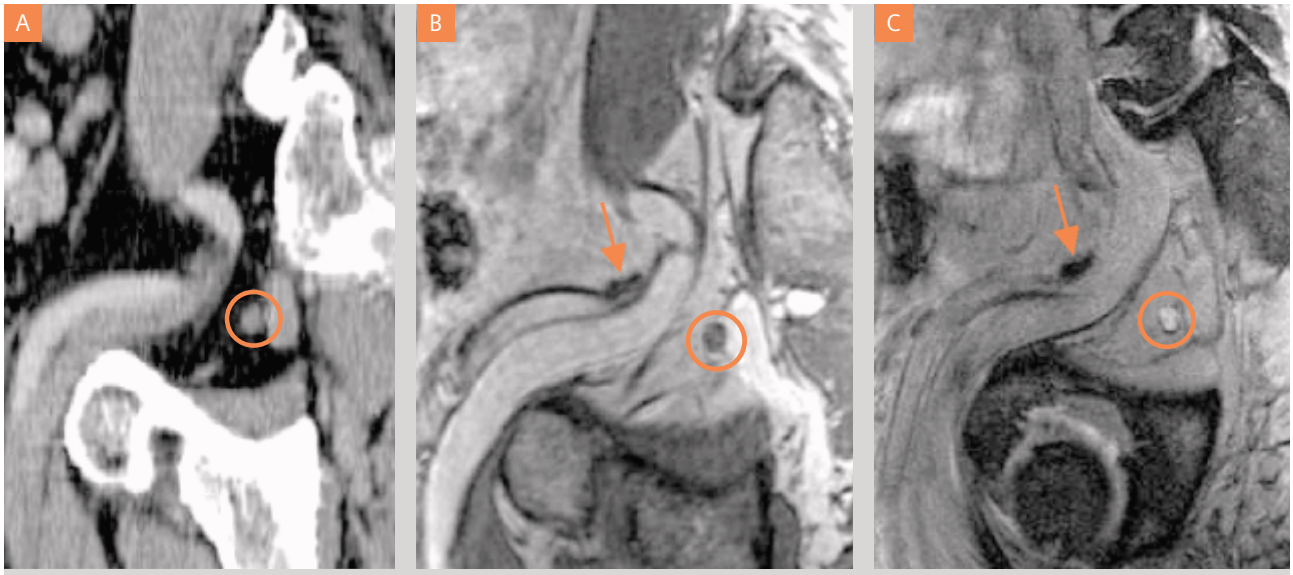

[Figure 1] ***Normal node and small positive node in 60-year-old male with prostate cancer.*** [A] *CT scan in semi-sagittal plane shows normal size (6 mm) node (circle).* [B] *Post ferumoxtran-10 T1-weighted TSE MR image (which is insensitive to iron) shows 2 grey normal size nodes (circle, arrow).* [C] *On post ferumoxtran-10 T2*-weighted MEDIC MR image (which is iron sensitive) one node is black (arrow) and the other one is white (circle). On histopathology the black node was normal and the white one was metastatic.*

slightly better (67%) compared to those of CT and unenhanced MR imaging, this value is, however, not high enough to replace pelvic lymph node dissection.

Ultra small super paramagnetic iron oxide particles (ferumoxtran-10) with a long plasma circulation time have been shown to be suitable as an MR contrast agent for intravenous MR lymphangiography [1, 2]. After IV injection, the ferumoxtran-10 particles are taken up by macrophages are transported to the interstitial space and from there through the lymph vessels to the lymph nodes (Figure 2). Thus this contrast agent is cell specific (for macrophages). Once within normally functioning nodes, the intracellular ferumoxtran-10 within the macrophages reduces the signal intensity of normal node tissue, because of the T1 and T2*- susceptibility effect of iron oxide, thus producing a signal drop or negative enhancement. In areas of lymph nodes that are involved with malignant cells, macrophages are replaced by cancer cells. Therefore, there is in these areas no uptake of the ferumoxtran-10 particles. In addition, due to increased vascular permeability and increased diffusion in cancer tissue, there is minimal leakage of ferumoxtran-10 particles into the extra cellular space of malignant metastatic areas, which produces a low local concentration and non-clustering of ferumoxtran-10 particles at these sites [3]. Through their T1-relaxivity this can induce an increase in signal intensity on T1-weighted images, producing positive enhancement [4]. Thus the ability of post ferumoxtran-10 MRI exams to identify metastatic areas in the lymph nodes depends primarily on the degree of uptake of ferumoxtran-10 by the macrophages in normal lymph node tissue and the leakage of ferumoxtran-10 particles in the metastatic area itself. Twenty-four hours after intravenous injection of ferumoxtran-10 normal lymph node and malignant tissue have different signal intensity on MR images. Therefore, this non-invasive technique may result in the detection of metastatic deposits in normal-size nodes (Figure 1).

Optimal evaluation of post ferumoxtran-10 images should be done by comparing pre- with post-contrast MR images in the same plane. On the pre-contrast images the shape, the size, and the location of the nodes can be assessed. On the post-contrast MRI the signal intensity change can be evaluated. However, this requires two MRI examinations, which limits this technique. This problem can be solved by only performing a post-ferumoxtran-10 MR exam, using both a sequence which is insensitive for iron such as a T1- or proton weighted TSE sequence, and a sequence which is sensitive to iron. For the latter purpose a good sequence is a high resolution T2*-weighted MEDIC (TE ~18 ms). The T1/PW TSE sequences yield high resolution images without (susceptibility) artifacts, whereas the T2*-sequence gives information about the iron content of the nodes. It is, therefore, important to apply both sequences with the same resolution and slice positioning parameters. In pelvic tumors (prostate cancer), this can be best done in a plane parallel to the psoas muscles (obturator, or semi-sagittal plane, Figure 1), and the axial plane, covering the para-aortic until the femoral region (Figure 3). In the "reading" of the images, a one-by-one comparison gives the best results (Figure 1). Incidentally in this way even a 2 mm metastatic node can be found (Figure 3).

Uptake mechanism of ferumoxtran-10

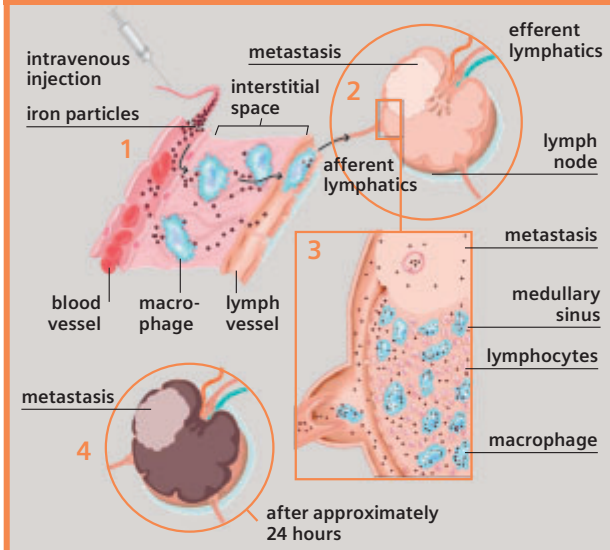

[Figure 2] *IV injected particles slowly extravasate from vascular to interstitial space (1) and then are transported to lymph nodes via lymphatic vessels (2). In lymph nodes, particles are internalized by macrophages (3), and these intracellular iron-containing particles cause normal nodal tissue to have low signal intensity. Disturbances of lymph flow or nodal architecture by metastases lead to abnormal accumulation patterns depicted by the lack of decreased signal intensity (4).*
Reprinted with permission of authors from Radiology.[6]

Clinical value

When using high resolution MR-technique small metastases can be prospectively recognized in small (3–10 mm) size lymph nodes [5]. These small lymph nodes would be considered to be benign in plain MRI or CT examinations. In addition, hyperplastic enlarged nodes can be correctly recognized as non metastatic, based on their low signal intensity. This results in improved sensitivity (~ 90%), with remaining

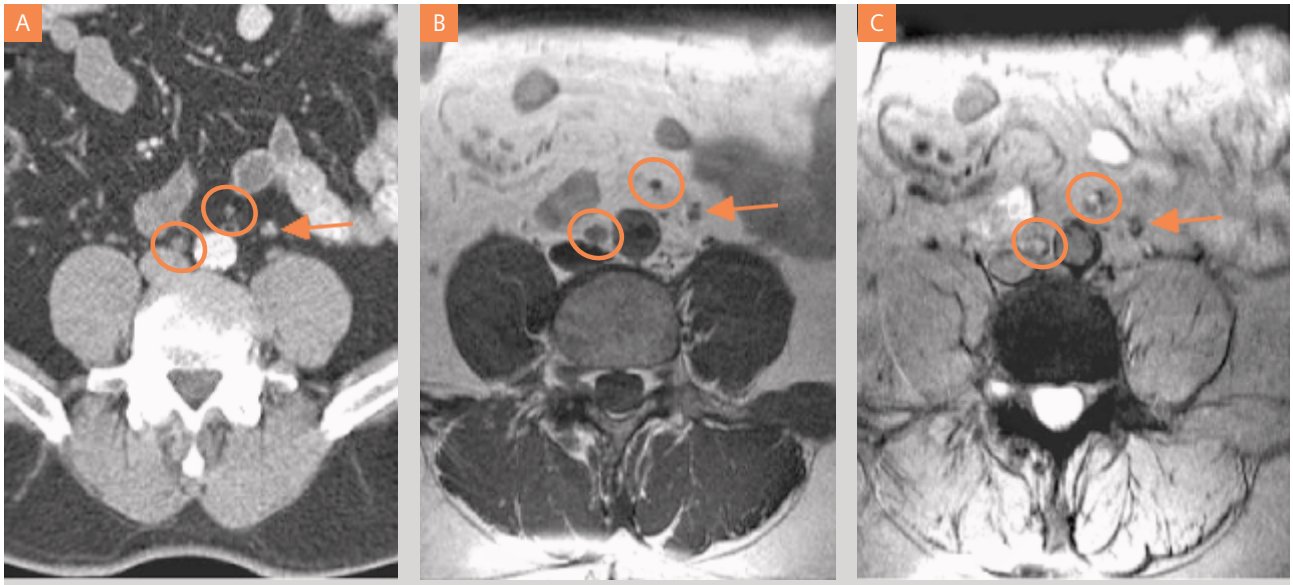

[Figure 3] *58-year-old patient treated for prostate cancer with nodal recurrence. CT and MRI obtained 2 years after lymphadenectomy, prostatectomy and hormonal therapy. Now PSA increased from 0 to 1.8.* [A] *CT scan in axial plane shows 3 normal size node (circle right 5 mm; circle left 2 mm).* [B] *Post ferumoxtran-10 T1-weighted TSE MR image (which is insensitive to iron) shows the same 3 grey nodes (circles, arrow).* [C] *On post ferumoxtran-10 T2*-weighted MEDIC MR image (which is iron sensitive) one node is black (arrow) and the other 2 are white (circles). On histopathology the black node was normal and the whites were metastatic.*

equal high specificity (~ 95%) in various tumors (Figure 4) [5–8]. In prostate cancer, contrast-enhanced CT and conventional MRI have a low sensitivity (40%), which is improved to 100% on a patient level and to 90% on a nodal level [5].

In urinary bladder cancer, 10/12 metastatic normal size lymph nodes were detected with ferumoxtran-10 MRI only. This resulted in an improved sensitivity (from 76% to 96%), whereas the specificity did not change significantly (from 99% to 95%) [6]. When using ferumoxtran-10 MRI, patients may be reliably selected for cystectomy, prostatectomy or radiotherapy without the need for invasive and costly procedures such as open and laparoscopic PLND. Furthermore, if the node is > 5 mm the presence of malignancy can be confirmed by image guided biopsy, and thus also avoid PLND in these patients. This was the case in 5/80 (6%) patients in the study of Harisinghani and Barentsz. All 5 nodes were confirmed positive. Finally, with ferumoxtran-10 MRI all pelvic nodes are visualized. Harisinghani and Barentsz showed that in 11% of their patients thanks to ferumoxtran-10 MRI metastatic nodes were detected, which were outside the classical field of lymph node resection [5]. In patients with a suspicion for a recurrence, e.g. in patients with a PSA-relapse after treatment, this technique may show metastatic nodes when they still are small (Figure 3), thus allowing earlier adequate therapy. Finally, identifying small pathologic nodes will facilitate more appropriate use of sophisticated radiation therapy. For example when positive nodes are accurately identified, precise intensity modulated radiotherapy can be performed. This results in an increased dose on the malignant nodes and a decreased dose, with reduced side-effects, on normal tissues.

In head and neck cancers, 25% lymph nodes are positive despite negative preoperative imaging (contrast CT and US biopsy) as metastatic nodes are small (5–10 mm). In addition PET is nonspecific and does not provide anatomic location. Therefore, extensive surgery -radical neck dissection- is performed in virtually all patients. This results in cosmetic deformity and a complication rate of 36-54%. Mack et al. reported that ferumoxtran-10 MRI was accurate in 26/27 (96%) patients, which resulted in reduction in surgery by 26% of patients [7]. Early results with ferumoxtran-10 MRI scans in breast cancer show a sensitivity of 78%, a specificity of 96% and a negative predictive value of 97% (Figure 5) [8]. The sentinel lymph node procedure in breast cancer has a 3% to 10% false negative rate. Furthermore, positive internal mammary lymph nodes are missed in 17% of cases. Finally, the sentinel lymph node is the only positive node in 61% lymph node positive patients.

These patients all undergo axillary dissection, with a subsequently high rate of clinically significant lymph edema. Thanks to its high negative predictive value, potentially in patients with a negative ferumoxtran-10 MRI, the axillary dissection may be avoided. Further studies are underway to validate this statement.

Finally, we believe that novel 3D reconstruction techniques would be of particular help in displaying and analyzing the massive amount of high resolution data. In this sense it should be feasible to display both normal and abnormal lymph nodes and their location with respect to important surgical landmarks like vessels, obturator nerves and ureters in 3D.

Summary

The combination of a macrophage (= cell) specific MR-contrast agent and high resolution MR imaging allows the detection of small and otherwise undetectable lymph node metastases in patients with pelvic cancer. This has an important clinical impact, as the diagnosis will be more precise and can be obtained in a less invasive maner. Subsequently this will reduce morbidity and healthcare costs. However, thorough knowledge of sequence parameters and planes, lymph node anatomy, appearance of normal and abnormal nodes, and pitfalls is essential when using this technique. This implies a very important role for education by expert radiologists, MR-manufacturers, and contrast agent companies.

**This article discusses clinical uses which are not commercially available in the US.*

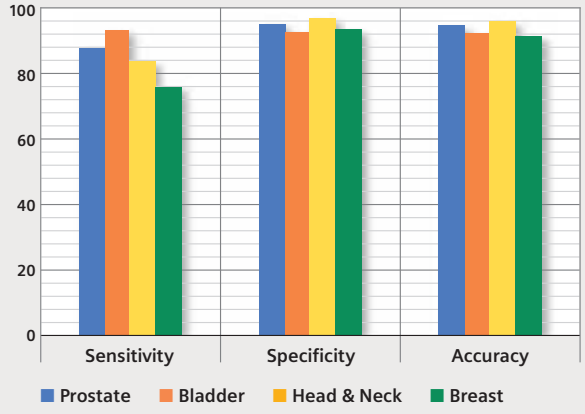

[Figure 4] *Results of ferumoxtran-10 of various tumors [5–8].*

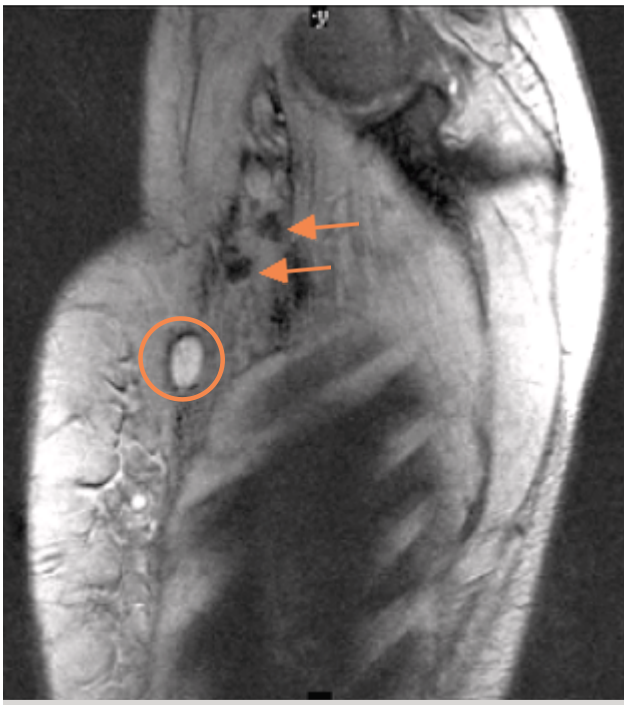

[Figure 5] ***55-year-old patient with breast cancer and positive lymph node.*** *Sagittal post ferumoxtran-10 T2*-weighted MEDIC MR image shows one white (circle) and 2 dark nodes (arrows). The white node showed on histopathology metastases, the dark ones were normal.*

References

[1] Vassallo P, Matei C, Heston WDW, et al. AMI-227-enhanced MR Lymphography: usefulness for differentiating reactive from tumor bearing lymph nodes. Radiology 1994; 193: 501–506.

[2] Weissleder R, Elizondo G, Wittenberg J et al. Ultrasmall paramagnetic iron oxide: an intravenous contrast agent for assessing lymph nodes with MR imaging. Radiology 1990; 175: 494–498.

[3] Gerlowski LE, Jain RK. Microvascular permeability of normal and neoplastic tissues. Microvasc. Res. 1986; 31: 288–305.

[4] Bellin MF, Roy C, Kinkel K, Thoumas D, Zaim D et al. Lymph node metastases: safety and effectiveness of MRI with Ultrasmall Superparamanetic Iron Oxide Particles. Initial clinical experience. Radiology 1998; 207: 799–808.

[5] Harisinghani M & Barentsz J, Hahn P, Deserno W, et al. Noninvasive detection of clinically occult lymph-node metastases in prostate cancer. NEJM 2003; 348: 2491–2499.

[6] Deserno WM, Harisinghani MG, Taupitz M, Jager GJ, Witjes JA, Mulders PF, Hulsbergen van de Kaa CA, Kaufmann D, Barentsz JO. Urinary bladder cancer: preoperative nodal staging with ferumoxtran-10-enhanced MR imaging. Radiology 2004; 233: 449–56.

[7] Mack MG, Balzer JO, Straub R, Eichler K, Vogl TJ. Superparamagnetic Iron Oxide-enhanced MR Imaging of Head and Neck Lymph Nodes. Radiology 2002; 222: 239–244.

[8] Michel SCA, Keller TM, Fröhlich JM, Fink D, Caduff R, Seifert B, Marincek B, Kubik-Huch R. Preoperative Breast Cancer Staging: MR Imaging of the Axilla with Ultrasmall Superparamagnetic Iron Oxide Enhancement. Radiology 2002; 225: 527–536.

Hold the date for the MAGNETOM World Meeting at ISMRM 2006 Seattle, Washington, USA

Monday, May 8th, 7:30 p.m. – 11:00 p.m., Benaroya Hall, 200 University Street, Seattle

Now you can get the latest information about hot topics in MRI at the Benaroya Hall. Siemens invites the MAGNETOM World members to a memorable scientific information session. This meeting also offers the opportunity to join other MAGNETOM World members, share thoughts and exchange ideas with them.

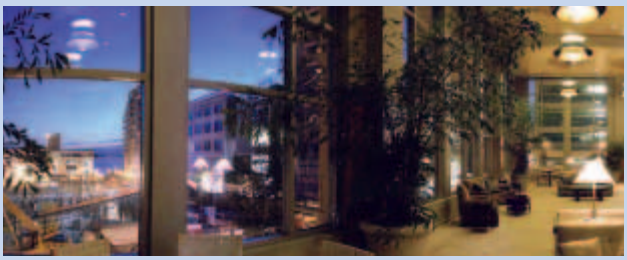

Benaroya Hall lies in the heart of downtown Seattle. It occupies the entire block between 2nd & 3rd Avenues, and Union & University Streets. The public entrance to the Hall is along 3rd Avenue.

All attendees must register prior to April 24th at
➔ **http://siemens.remoteevent.com/ISMRM2006**

Neurology

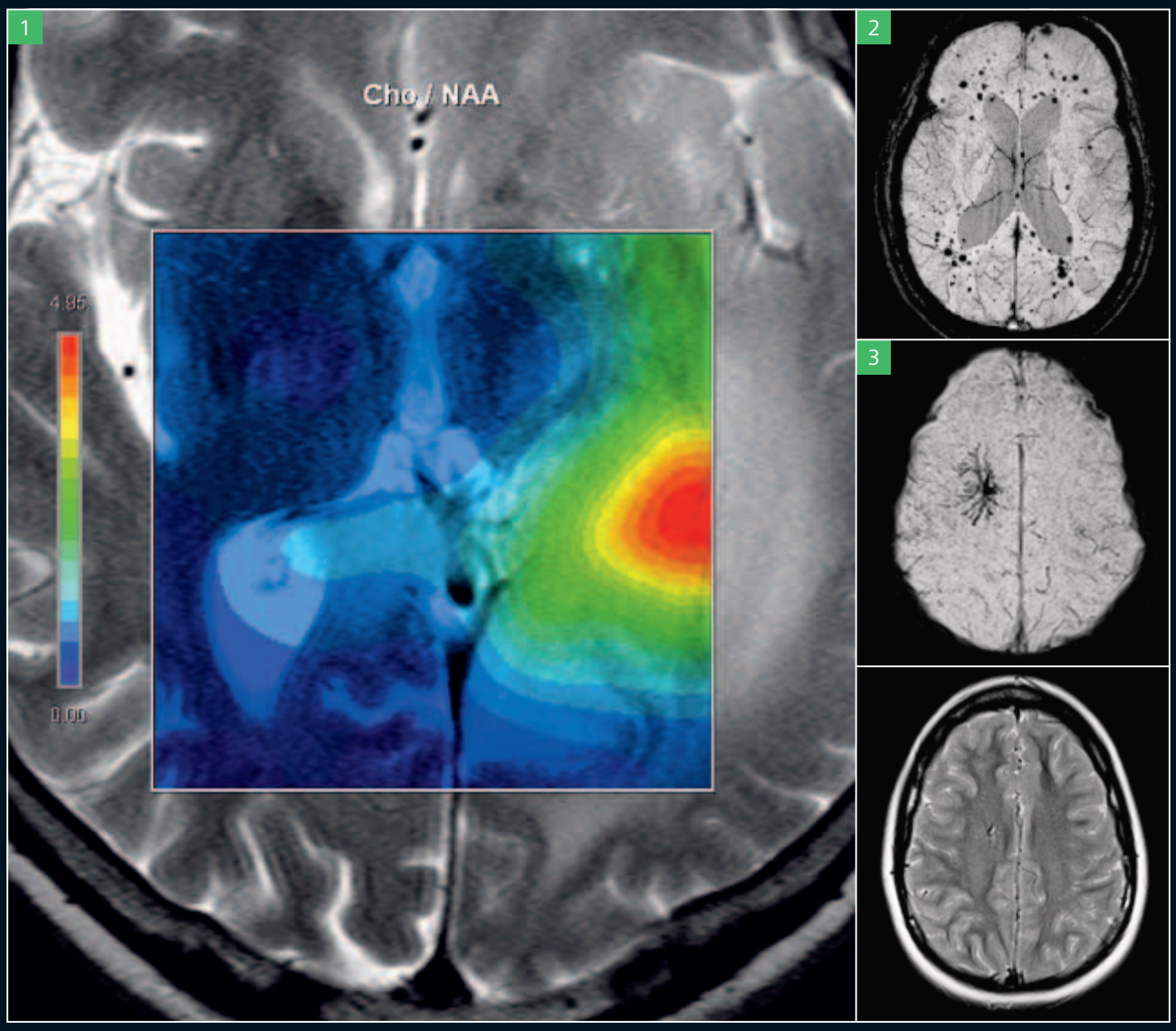

[1] Courtesy of Klinikum Bremen Mitte, Bremen, Germany
[2] Courtesy of Tokyo Metropolitan Ebara Hospital, Japan
[3] Courtesy of St. Vincent's Melbourne, Melbourne, Australia

Use of Turbo GRAPPA Inversion Recovery (IR) Imaging in Parkinson's Disease

Gonzalo M. Rojas, B.S.[1], Ulrich Raff, Ph.D.[1], Pedro Chaná, M.D.[2], Carlos Juri, M.D.[3], Isidro Huete M.D.[3], Nelson Lafont, R.T.[3], Michael Hutchinson M.D., Ph.D.[4]

[1]*Department of Physics, University of Santiago de Chile, Santiago, Chile*
[2] *School of Medicine, University of Santiago de Chile, Santiago, Chile*
[3] *School of Medicine, Catholic University of Chile, Santiago, Chile*
[4] *School of Medicine, New York University, NY, USA*

Abstract

Segmented inversion recovery ratio imaging (SIRRIM) was introduced in previous works to investigate selective neurodegeneration in idiopathic Parkinson's disease. Turbo GRAPPA inversion recovery is now explored to assess neurodegeneration in the substantia nigra.

Introduction

Idiopathic Parkinson's disease (IPD) is a progressive neurological disorder of unknown etiology that affects mainly the motor system in some 2% to 3% of the population at a late stage in adult life. IPD is due to the loss of pigmented dopaminergic neurons located in a small elongated nucleus in the mesencephalon known as substantia nigra pars compacta (SNC). An essay on paralysis agitans was first described by James Parkinson as early as 1817 [1]. Though depression seems to be the first symptom of the disease, the principal symptoms of this initial phase are rigidity, bradykinesia, tremor at rest in the extremities and shuffling gait accompanied with balance problems. Secondary symptoms appear inter alia as speech, dysphagia, sialorrhea, dystonia, weight loss and gastrointestinal problems. Eventually patients suffer from dementia at the end-stage of their lives. The socio-economical cost of IPD is enormous and therefore has received great attention in the medical community. A comprehensive overview of Parkinson's disease has been published by Lang and Lozano with an extensive list of references [2, 3].

The neural condition known as IPD is treatable as opposed to other neurological disorders. It appears of great importance to find diagnostic tools which allow better differential diagnosis of IPD since 25% of the patients diagnosed with IPD fall into the nearby category of Parkinsonism including progressive supranuclear palsy (PSP), multi system atrophy (MSA which includes Shy Drager symptom, olivopontocerebellar atrophy and striatonigral degeneration), and cortical-basal ganglionic degeneration (CBGD). Effective treatment of IPD delivers levodopa combined with carbidopa which supplies the nigro striatal pathways with the missing dopamine. Most IPD patients respond to the administration of levodopa which is the first indication of the disease. IPD develops generally rather slowly and many patients respond many years to the appropriate pharmacological treatment.

Patients and Methods

We have recently implemented an MRI technique to image the midbrain using inversion recovery (IR) sequences and confirmed that neurodegeneration follows defined patterns [4, 5, 6, 7, 8]. Standard IR sequences were originally used to image the mesencephalon in a group of eleven IPD patients and eleven age-matched control subjects (NYU School of Medicine). Imaging was performed using a 1.5 Tesla MAGNETOM Vision scanner. Two IR sequences have been implemented: one was designed to suppress white matter (WMS images) and the second sequence was used to generate gray matter suppressed images (GMS). Ratio images (WMS / GMS) were then used to quantitate neurodegeneration of the SNC in the cerebral peduncle. IR WMS images were obtained with the following sequence: TE = 20 ms, TI = 250 ms and TR = 1450 ms while GMS images were obtained with TE = 20 ms, TI = 420 ms and TR = 2000 ms. The field of view was 200 mm and the image matrix was set to 256 x 256 with Number of Acquisitions = 2. Four axial slices were acquired above the pons perpendicular to the longitudinal axis of the cerebral peduncle [7]. Total imaging time for both sets of images was 45 minutes which was considered acceptable during the initial research phase of the project.

The long scanning times are clearly unacceptable in a routine clinical setting. Therefore modulus Turbo IR sequences [9, 10]

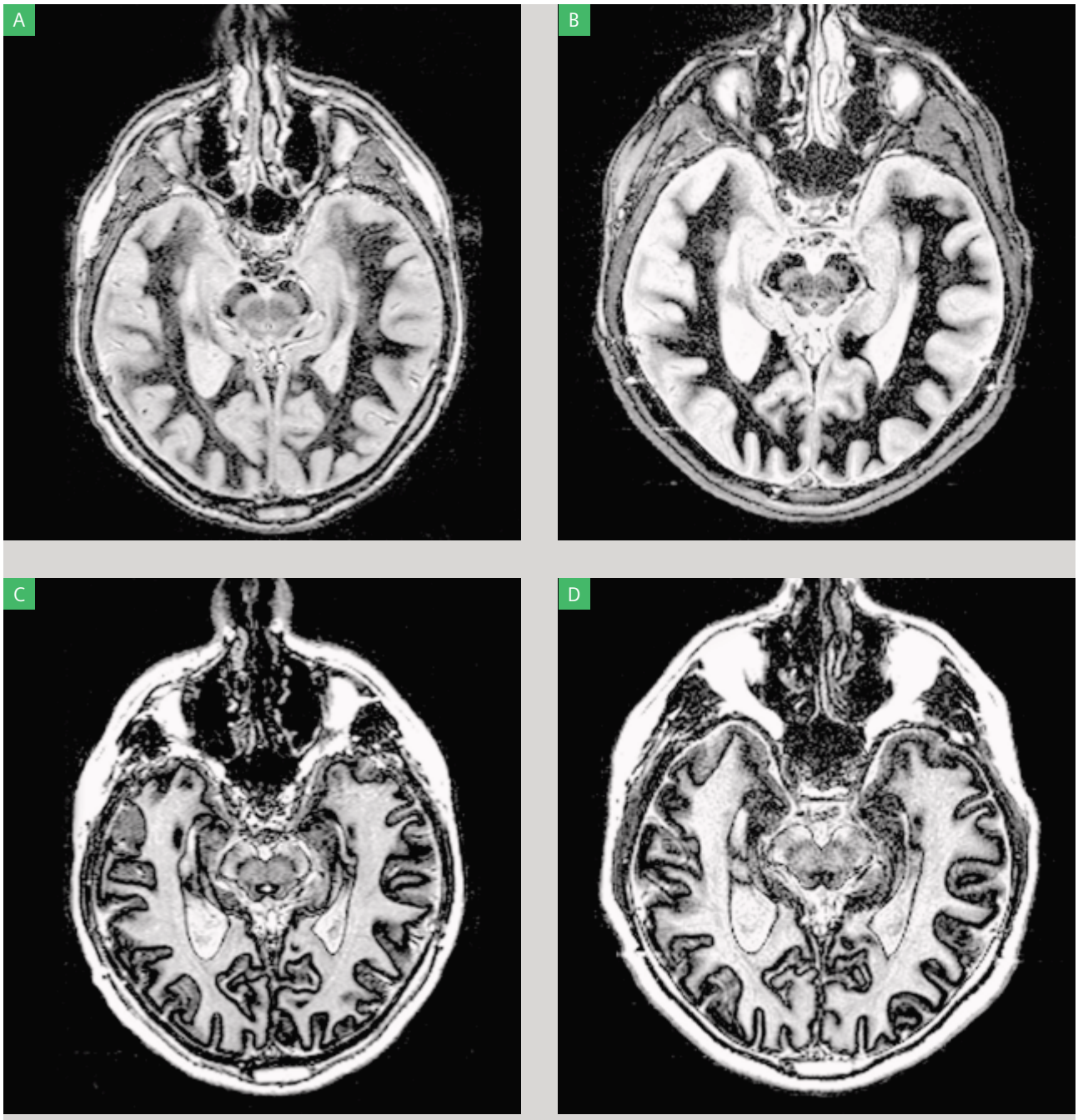

[Figure 1] *White matter suppressed (WMS) and gray matter images (GMS) from a normal volunteer obtained with a 1.5T MAGNETOM Vision scanner using a conventional inversion recovery sequence (A and C respectively). The same WMS and GMS obtained with IR Turbo GRAPPA with the Avanto 1.5 T scanner are displayed as B and D respectively.*

and modulus Turbo IR sequences combined with the recently developed technique called GRAPPA (Generalized Auto calibrating Partially Parallel Acquisitions) were implemented in a 1.5 Tesla MAGNETOM Avanto system [11, 12] of the University Hospital of the Catholic University, Santiago de Chile. The Turbo Factor was 3. The iPAT acceleration factor was 2. Acquisition time for both IR sequences was reduced to 15 minutes which was considered acceptable though not yet optimal for IPD patients. Inversion times were adjusted such that white matter and gray matter were maximally suppressed by scanning a neurologically normal volunteer. During this initial phase, one neurological normal subject, one age-matched subject (UR) and two early-stage hemiparkinsonian patients were scanned using the GRAPPA Turbo IR sequences. The age-matched normal volunteer (UR) had also been imaged in the past using the conventional IR sequences described above.

Results and discussion

Figure 1 shows the results for one normal volunteer (UR) whose WMS and GMS images were obtained with both afore mentioned techniques. Figures 1A (WMS image) and 1C (GMS image) are the images obtained with the 1.5 Tesla MAGNETOM Vision. Figures 1B (WMS image) and 1D (GMS image) are the images acquired with the 1.5 Tesla MAGNETOM Avanto unit. At a first glance, the images obtained at the approximate same anatomical level with conventional IR and Turbo GRAPPA look quite equivalent, including a better contrast in the cortex area of the WMS image of the Turbo GRAPPA sequence. Nevertheless, comparing the two WMS images (1A) and (1B) reveals a lower signal-to-noise ratio in (1B) with loss of details in the center of the image. It strikes the viewer that this effect can be observed when comparing (1C) and (1D). Both images (1B) and (1D) show degraded central areas which are not observed in (1A) and (1C). Note however that visually assessed details and signal-to-noise look equivalent in the cortex regions in (1A) and (1B) as well as (1C) and (1D) which correspond to the WMS and GMS images acquired with the two techniques. A possible explanation of this finding could be the use of GRAPPA, which would have to be confirmed in the future.

Figure 2 confirms lower signal-to-noise ratio especially in the region of the mesencephalon. Figures 2A and 2B show the IR and Turbo GRAPPA IR results for the WMS images. Though the contrast in image (2B) is superior to the contrast in (2A), the signal-to-noise ratio of the red nucleus (green arrows) and the SNC pointed out with red arrows is worse in (2B) than in (2A). In addition the substantia nigra pars reticulata (SNR) pointed out with blue arrows in (2A) is barely visible if not completely lost in (2B). Figures (2C) and (2D) show a similar scenario: low signal-to-noise ratio in Figure (2D) with bad definition of the SNC outline may seem surprising. A possible explanation was given in the aforementioned discussion of Figure 1.

Figure 3 shows the results obtained with the Turbo GRAPPA IR sequence for a young normal volunteer to assess the potential of the presently used sequences. Figures (3A), (3B), (3C) show the WMS peduncle, the GMS peduncle and the ratio image respectively. Image (3D) displays the segmented SNC using the data fusion technique described in References [7, 8]. The lower row corresponds to the lower slice through the midbrain showing the WMS (3E), GMS (3F)

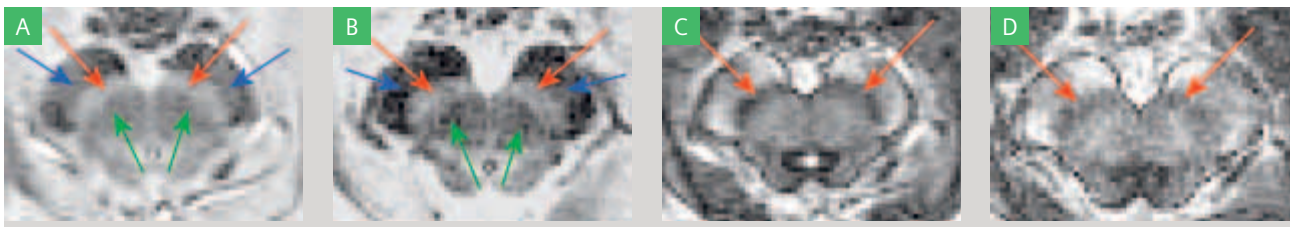

[Figure 2] *The upper row shows the mesencephalon of the WMS images (A and B) obtained with the two inversion recovery sequences. The lower row displays the two GMS images (C and D). Red arrows point out the substantia nigra pars compacta. Green arrows point out the red nucleus while the blue arrows indicate the substantia nigra pars reticulata which is not identified in (B).*

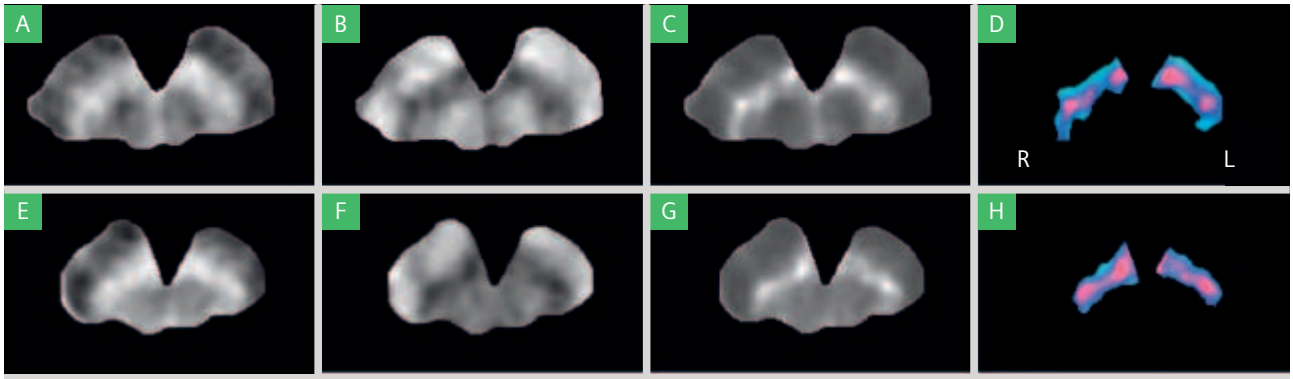

[Figure 3] *The upper row shows WMS, GMS, ratio image (WMS/GMS) and segmented fusion image of the substantia pars compacta of the upper slice (A, B, C and D respectively) of a normal volunteer. The lower row displays the WMS, GMS, Ratio and fusion images of the lower slice (E, F, G, and H respectively). Turbo IR GRAPPA was used in this case. The images were obtained with a normal volunteer.*

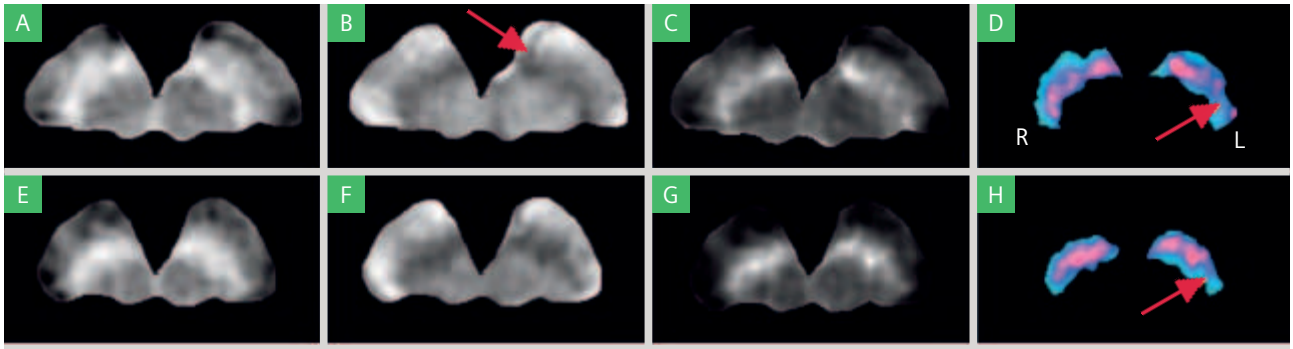

[Figure 4] *The same sequence of images for upper and lower slices as displayed in Fig. 3 were obtained for a hemiparkinsonian early stage IPD patient. The arrows in images (D) and (H) point out the loss of neural cells in the left lateral segments of the SNC. The red arrow in the GMS image (B) points out an unknown artifact.*

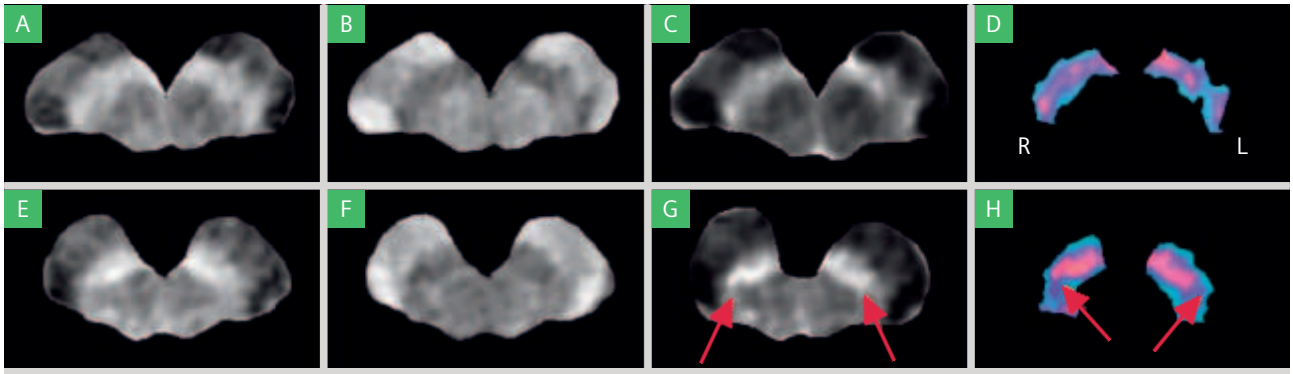

[Figure 5] *The same sequence of images for upper and lower slices as displayed in Fig. 4 were obtained for another hemiparkinsonian early stage IPD patient. The red arrows in the ratio image of the lower slice (G) and in the segmented fusion image (H) point out neurodegeneration in the lower slice. The radiological right side of the patient (R) shows slightly more neural cell loss than the left side (L).*

and ratio (3G) images respectively of cerebral peduncle. Figure (3H) again shows the results of image fusion similar to (3D) which remains difficult to interpret. The radiological index RI as defined in Refs. [5, 6] turned out to be RI = 2, which is well within the normal range given approximately by -6 ≤ RI ≤ 6. This result is very encouraging and stimulated the investigation of early IPD stages with the described IR technique.

Figure 4 displays the same sequence of peduncular images as in Fig. 3. The early IPD patient was hemiparkinsonian, i.e. with unilateral symptoms. Indeed his RI was equal to RI = 12 and indeed the red arrows in (4D) and (4H) point out neurodegeneration in the lateral section of the left side of the SNC. The lateral to medial neural cell loss corroborates the pathological findings of Fearnley and Lees [13]. The patient had slight symptoms (tremor) in his right lower limb when off medication which agrees with the visual and quantitative results of Fig. (4). The red arrow in (4B) points out some unexplained artifact or real structure which resembles a motion artifact.

Figure 5 shows the results for another early hemiparkinsonian IPD patient. Upper and lower rows follow the same description as in Figures 3 and 4. Loss of neural cells is clearly visualized in (4H) showing lateral to medial neurodegeneration which is the pattern observed in neuropathology [13]. The black and white ratio image displayed in (5G) clearly reveals loss of neurons as well. The patient presented symptoms in his left extremity which is corroborated by the red arrow (R) in (4H). Nevertheless the radiological left side (L) of the SNC shows lateral to medial neurodegeneration as well, which possibly could indicate a presymptomatic phase of the disease in this particular case. The radiological index RI turned out to be RI = 13 which corresponds to a value to be expected in early IPD patients.

It is clear that Turbo IR sequences and a fortiori Turbo GRAPPA IR sequences will reduce the scanning time allowing potential routine clinical use when IPD has to be confirmed or ruled out. It was expected nevertheless, that the standard IR sequence could yield better results at the cost of prohibitive imaging time. We are currently investigating improvements of the promising sequence used with the 1.5 Tesla MAGNETOM Avanto scanner.

The authors wish to acknowledge the support of Bernardo Nehm P. (Manager Siemens Medical Solutions, Santiago de Chile) and Dailton da Silva Britto (MR Application Engineer, Siemens Latin America).

Data acquisition of WMS and WMS images shown in Figure 1A and Figure 1C were obtained at NYU School of Medicine thanks to a grant of Myra Fox and Max Smedresman Foundation for Research into Parkinson's disease.

References

[1] Parkinson J. An essay on the shaking palsy. London: Whittingham and Rowland, 1817.

[2] Lang AE, Lozano AM. Parkinson's disease. First of two parts. N Engl J Med 1998; 339: 1044–1053.

[3] Lang AE, Lozano AM. Parkinson's disease. Second of two parts. N Engl J Med 1998; 339: 1130–1143.

[4] Hutchinson M, Raff U. Parkinson's disease: a novel MRI method for determining the structural changes in the substantia nigra. J. Neurol. Neurosurg. Psychiatry 1999; 67: 815–818.

[5] Hutchinson M, Raff U. Structural changes in the substantia nigra in Parkinson's Disease as revealed by MR imaging. Am. J. Neuroradiology 2000; 21: 697–701.

[6] Hutchinson M, Raff U, Lebedev S. MRI correlates of pathology in parkinsonism: segmented inversion recovery ratio imaging (SIRRIM). NeuroImage 2003; 20: 1899–1902.

[7] Raff U, Rojas GM, Huete I, Hutchinson M. Computer assessment of Neurodegeneration in Parkinson disease using data fusion techniques with MR images. Acad Radiol 2003; 10: 1036–1044.

[8] Rojas GM, Raff U, Quintana JC, Hutchinson M. Data Image Fusion in Neuroradiology: Some techniques and potential use in MRI of Parkinson Disease. Submitted to Am J Roentgenol.

[9] Hauer MP, Uhl M, Allmann KH, Laubenberger J, Zimmerhackl LB, Langer M. Comparison of turbo inversion recovery magnitude (TIRM) with T2-weighted turbo spin-echo and T1-weighted spin-echo MR imaging in the early diagnosis of acute osteomyelitis in children. Pediatr Radiol. 1998; 28: 846–850.

[10] Pooley RA. AAPM/RSNA physics tutorial for residents: fundamental physics of MR imaging. Radiographics 2005; 25: 1087–99.

[11] Griswold MA, Jakob PM, Heidemann RM, Nittka M, Jellus V, Wang J, Kiefer B and Haase A. Generalized Autocalibrating Partially Parallel Acquisitions (GRAPPA). Mag Res Med 2002; 47: 1202–1210.

[12] Tintera J, Gawehn J, Bauermann T, Vucurevic G, Stoeter P. New partially parallel acquisition technique in cerebral imaging preliminary findings. Eur Radiol. 2004; 14: 2273–2281.

[13] Fearnley JM, Lees AJ. Aging and Parkinson's disease: substantia nigra regional selectivity. Brain 1991;114: 2283–2301.

The Neuro3D Task Card

Stuart H. Schmeets, BSRT (MR), Siemens Medical Solutions, USA

The Neuro3D task card is a *syngo* software application. It combines morphologic or structural imaging with functional MRI information in an easy-to-use platform offering the clinician a more comprehensive view of the neural activation picture.

Unlike most accessory software applications, the Neuro3D task card can be used interactively during the fMRI examination to evaluate the progress of the experiment.

What is BOLD imaging?

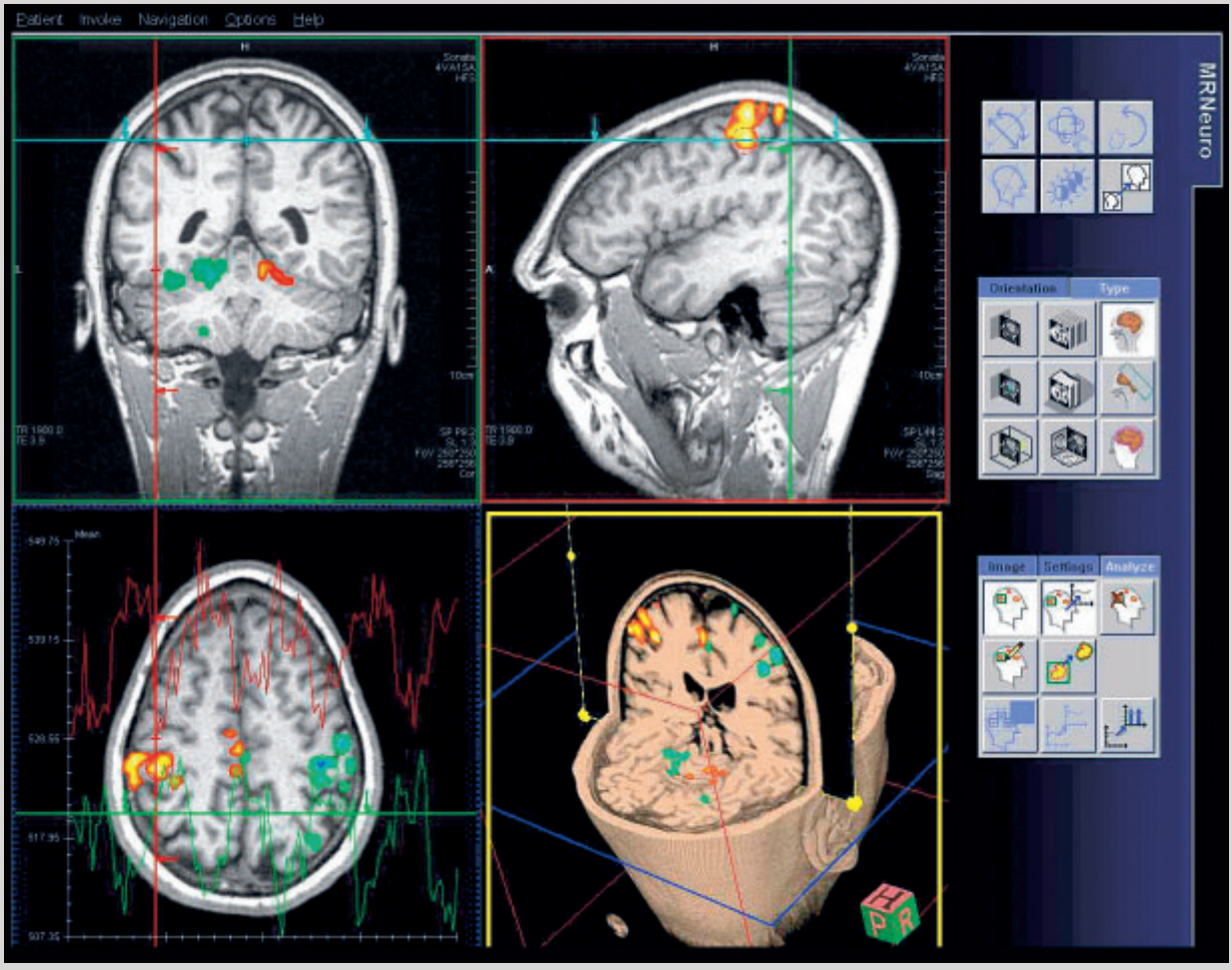

Blood Oxygen Level Dependence imaging (BOLD), the most common type of functional magnetic resonance imaging, involves the exploitation of the decrease in magnetic susceptibility caused by small changes in the volume of oxygenated blood to a specific region of the brain during and following increased neuronal activity [1]. In other words, as a certain portion of the brain becomes more active it uses more oxygen causing a reactive increase in blood flow to the area. The increase in blood flow results in a localized change in magnetic susceptibility measurable with BOLD imaging.

Why BOLD at 3T?

Magnetic susceptibility relates to the ability of a material to become magnetized within an externally applied magnetic field and is measured by the magnetization of the material divided by the field strength. [1] Therefore, if field strength is doubled (e.g. 1.5T to 3T), susceptibility is increased by a factor of four. Since the BOLD phenomenon is based on minute changes in susceptibility this fourfold increase leads to higher levels of visible activation.

Performing the examination

The first step in a successful fMRI experiment of the brain is to acquire the morphologic or structural information. This is often T1- or T2-weighted 3D volumetric datasets that will be used to overlay the functional activation information.
It is also important to collect a gradient field map that will be used later to interrogate the combined data for spatial differences caused by susceptibility-induced distortions that are often generated at air-tissue interfaces in EPI based measurements. These protocols can be found within the Siemens protocol tree under the head region and Bold-Imaging program. The protocols labeled Neuro3D_ Pace and Neuro-3D_ Pace_ Filter have been designed to be used in conjunction with the Neuro3D task card.
Once acquired, the volumetric data is loaded into the Neuro3D task card by selecting the dataset in the browser and then selecting Applications Neuro3D. The task card will open and the selected data will be loaded.

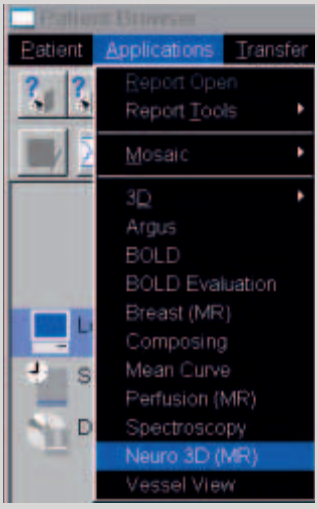

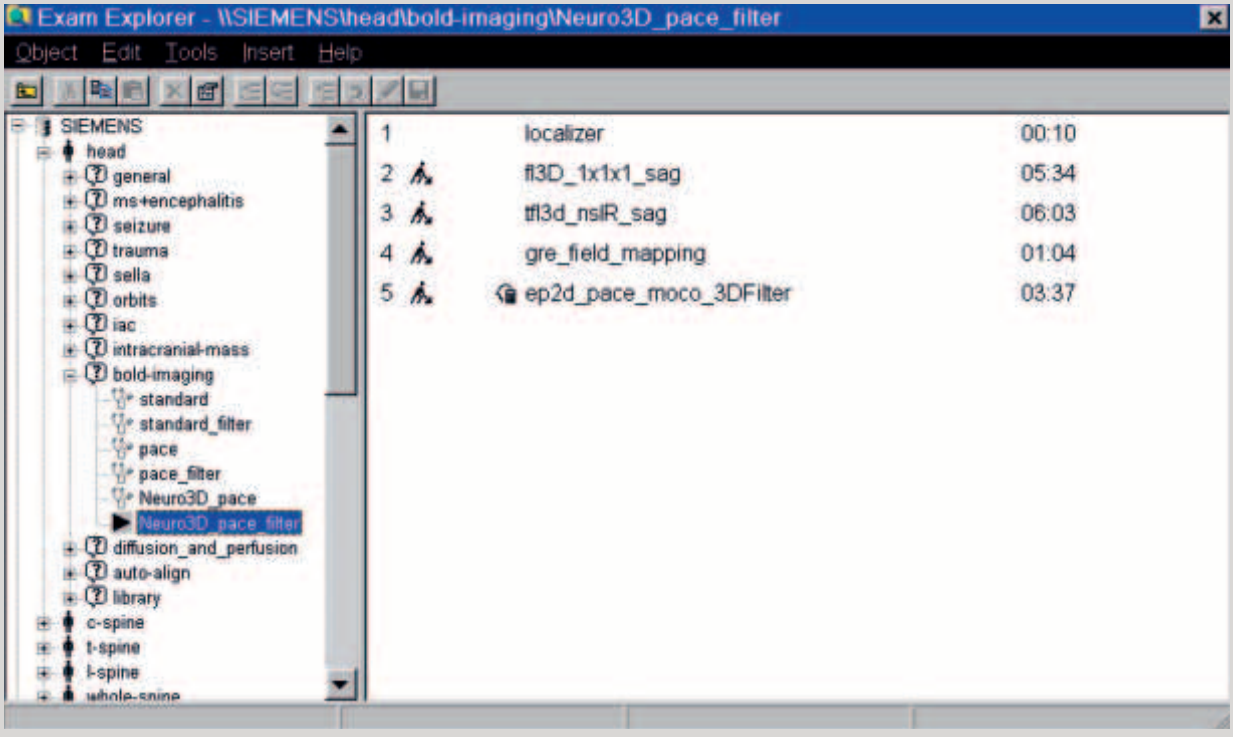

Analysis mode vs. Inline mode

The Neuro3D task card has two processing modes. The analysis mode is off-line and designed for processing data after the examination is completed. The Inline mode is an interactive application where BOLD data is sent to the Neuro3D task card during the examination. This allows the user to follow the progress of the examination in real-time fashion. If you are using the Neuo3D task card in offline or analysis mode and have already acquired the functional data, it can be loaded at this time for analysis. However, if online mode is desired select the 'Start Online Mode' button on the Neuro3D task card. All data acquired will automatically be loaded into the Neuro3D task card for interactive analysis.

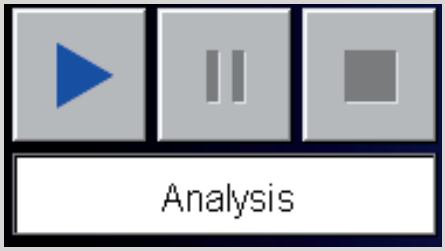

Functional paradigms

Various functional paradigms from simple finger tapping to complex visual and thought experiments can be implemented based on the users level of experience and clinical or research objective. There are several computerized paradigm generation systems available on the market today that can be integrated into the *syngo* environment.

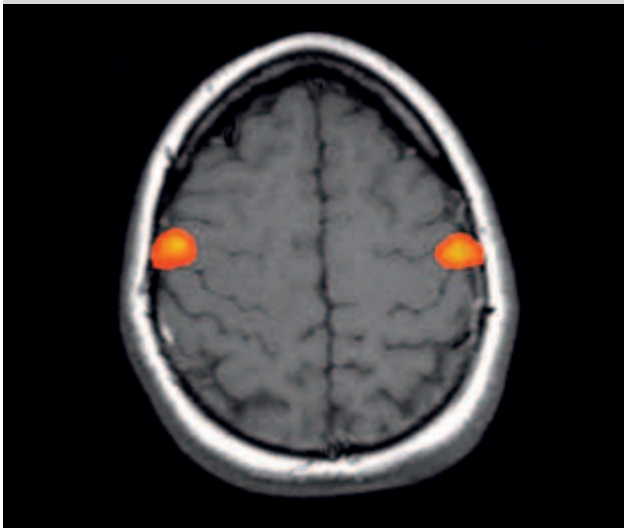

Analysis of the data

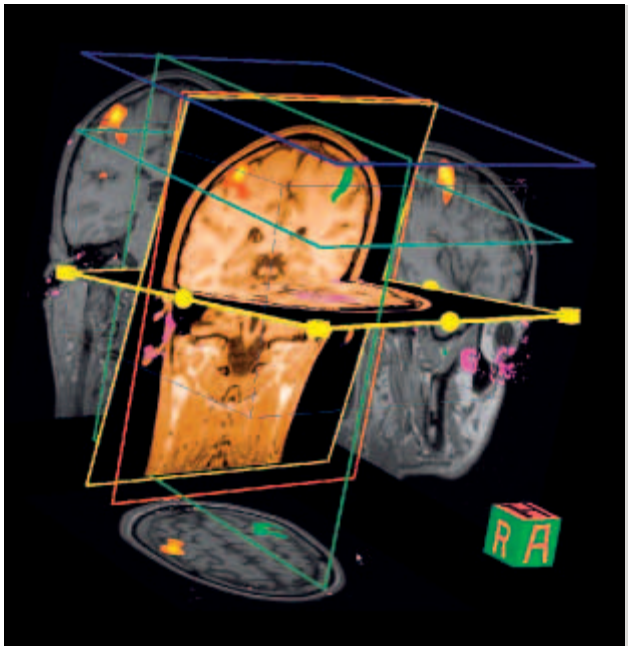

Clip planes
Clip planes are an interactive method of navigating the 3D volumetric data to better resolve the location of BOLD activity within the anatomic volume. Orientation possibilities are abundant and can be tailored to the individual patient. A full description of clip plane functionality is available in the *syngo* Neuro3D user manual.

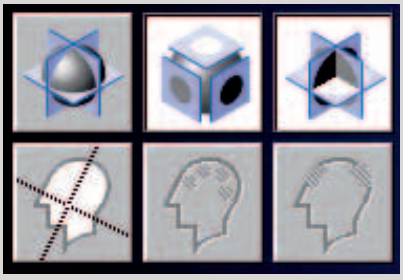

Orthogonal localization

Selecting a specific area within the anatomic volume will adjust the three orthogonal images within the task card to match this location.

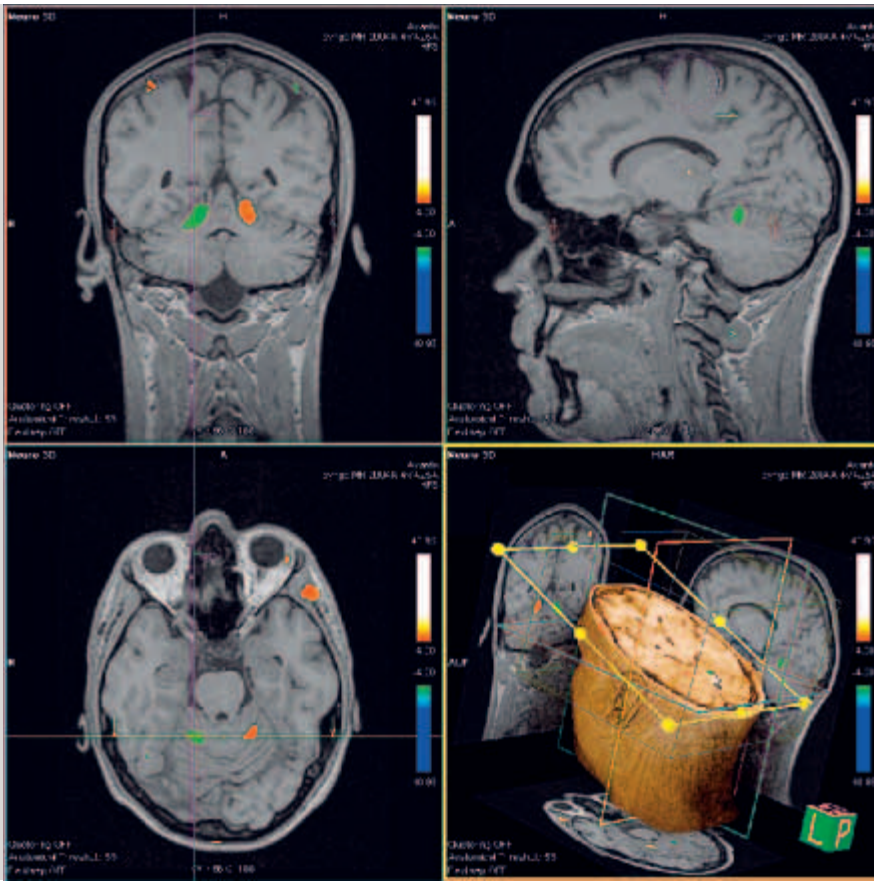

Gradient field map

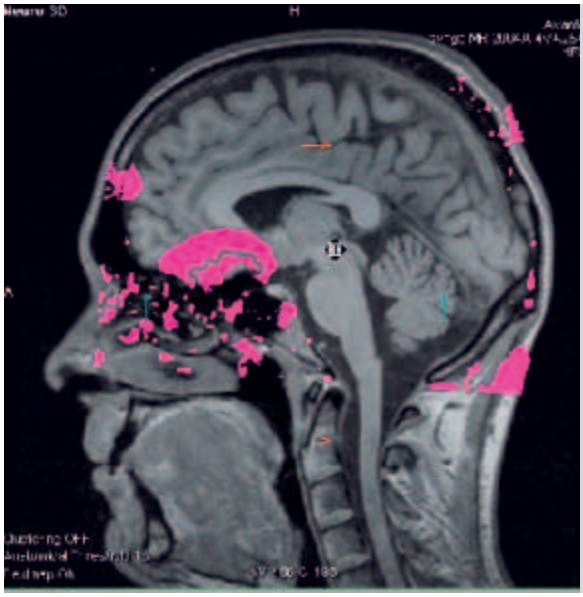

EPI based sequences such as those used in BOLD, DTI, and Diffusion-weighted imaging are especially susceptible to geometric distortions at air-tissue interfaces where magnetic susceptibility changes dramatically. In some cases these geometric distortions can cause a mis-registration of the BOLD activation information on the anatomic 3D volume.
The gradient field map is generated to display areas of high magnetic susceptibility and possible geometric distortion.
If acquired, the gradient field map will be automatically loaded when BOLD activation data is added to the Neuro3D card or when the 'Start On-line Mode' button is selected.
If a gradient field map is not acquired, an error message will be displayed although normal analysis is still possible. It is important to note that reducing the number of phase encoding steps in EPI measurements reduces the susceptibility-induced distortion.

Signal time course

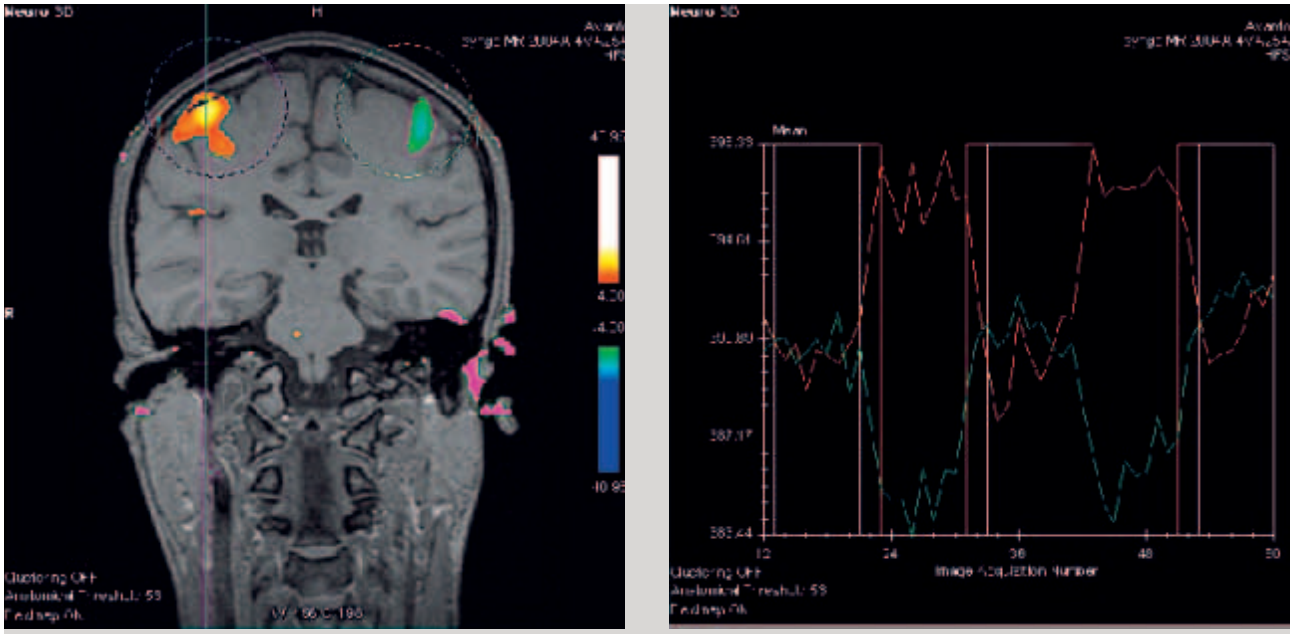

The analysis mode allows the user to draw regions of interest (ROIs) around areas of activation. This in turn will generate a graph of signal changes within the region over time. This graph is referred to as a Signal Time Course. Bilateral activation paradigms result in two, color-coded time course lines within the graph.

Future advancements

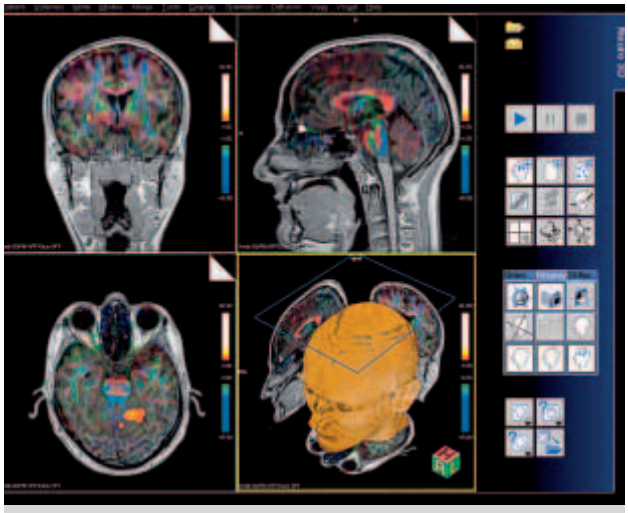

The next version of the Neuro3D task card will allow the user to incorporate Diffusion Tensor Maps such as Apparent Diffusion Coefficient (ADC), Fractional Anisotropy (FA), and TRACE-weighted images.

Image examples from 3T

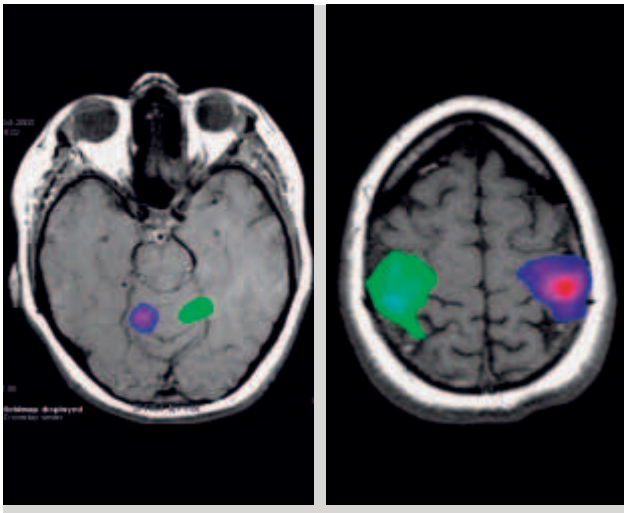

The images depict a bilateral finger tapping experiment. Strong activation is seen within the motor cortex and well as ipsilateral activation in the cerebellum.

References [1] Runge VM, Nitz WR, Schmeets SH, Faulkner WH, Desai NK. The physics of clinical MR taught through images. 2005; 61: 131.

Functional High-Resolution 3D Examinations of the Cervical Spine with MRI and the NeuroSwing Device*

K. E. W. Eberhardt[1], R. Schindler[2], J. Liebisch[1]

[1]*Division of Neuroradiology, Department of Neurosurgery, Erlangen-Nuremberg University, Erlangen, Germany*
[2]*Inside, Functional Diagnostic Technology GmbH, Schweinfurt, Germany*

Introduction

Functional examinations of the cervical spine have been performed since the mid-1990s. All of the mechanical systems implemented to date have specific disadvantages, such as the lack of reproducibility, the often unphysiological pattern of motions, the significantly poorer signal-to-noise ratio of the measurements as compared to studies in the standard position, and the general limitation to one plane of movement. Moreover, the lack of a sequence specifically adapted to the requirements of the neck region is another limiting factor that has prevented high-resolution examinations in the past. Even open MRI systems are subject to the same limiting factors in spite of their improved patient accessibility. As a result, although several functional examinations of the cervical spine have been published [1–6], they have not become a part of the clinical routine. The principal utility of cervical spine examinations is the detection of primary changes in the intervertebral disks and the bony spinal canal as well as lesions of structures important for movement, such as ligaments and vertebral joints. Certain pathologies can be imaged for the first time (such as lesions from whiplash injuries, displacement of vertebra during inclination and reclination, or lateroflexion as in spondylolisthesis [1–6]). Decisions regarding therapy (conservative or surgical) can be adapted better to the individual anatomic conditions of patients and surgical requirements, especially for extensive degenerative diseases. Surgical interventions have lower risks, and the rehabilitation phase after surgery can be shortened. For this purpose, the development of an auxiliary device for functional MRI examinations of the cervical spine has to address three primary requirements:

1. Enable reproducible high-resolution MRI examinations in all desired functional positions.
2. Permit rapid functional survey (screening) in all functional planes in less then 10 min as an aid for planning high-resolution examinations.
3. Offer sufficient reliability to allow standardization for routine use.

This paper demonstrates the first results of a study that examines the use of a newly developed device as well as a 3D myelography sequence specifically adapted to the requirements of the neck region.

Materials and Methods

All measurements were performed using a 1.5 Tesla whole-body MRI system (MAGNETOM Sonata, Siemens AG, Medical Solutions, Erlangen). A combination of surface coils was used to optimize the signal-to-noise ratio. The following sequences were used:

HASTE-3D, this strongly T_2-weighted sequence has been used previously for functional examinations with the Single Shot technique to follow movements [8]. However, adapting it to susceptibility artifacts that occur more frequently in the cervical spine required readjustment of the sequence parameters to obtain sufficient resolution for 3D examinations. The following combination of parameters was used for the first time in functional cervical spine examinations: TR = 7200 ms; TE = 165 ms; slice thickness = 1 mm; FoV = 250 mm; matrix = 256 x 256. The bandwidth was reduced to 150 Hz to maintain an adequate signal-to-noise ratio. The fatty tissue was suppressed via frequency-selective Water Excitation. The measurement time is 3.30 min.

MEDIC-2D and TSE: T_2- and T_1-weighted, as routine sequences with modified parameters:
MEDIC-2D: TR = 81 ms; TE = 27 ms; flip angle = 14°;
slice thickness = 3 mm; FoV = 200 mm;
matrix = 256 x 256 mm; bandwidth = 130 Hz.
The measurement time for 30 slices was approx. 3.30 min.
T_2-weighted TSE: TR = 6400 ms; TE = 165 ms;
slice thickness = 3 mm; FoV = 250 mm;

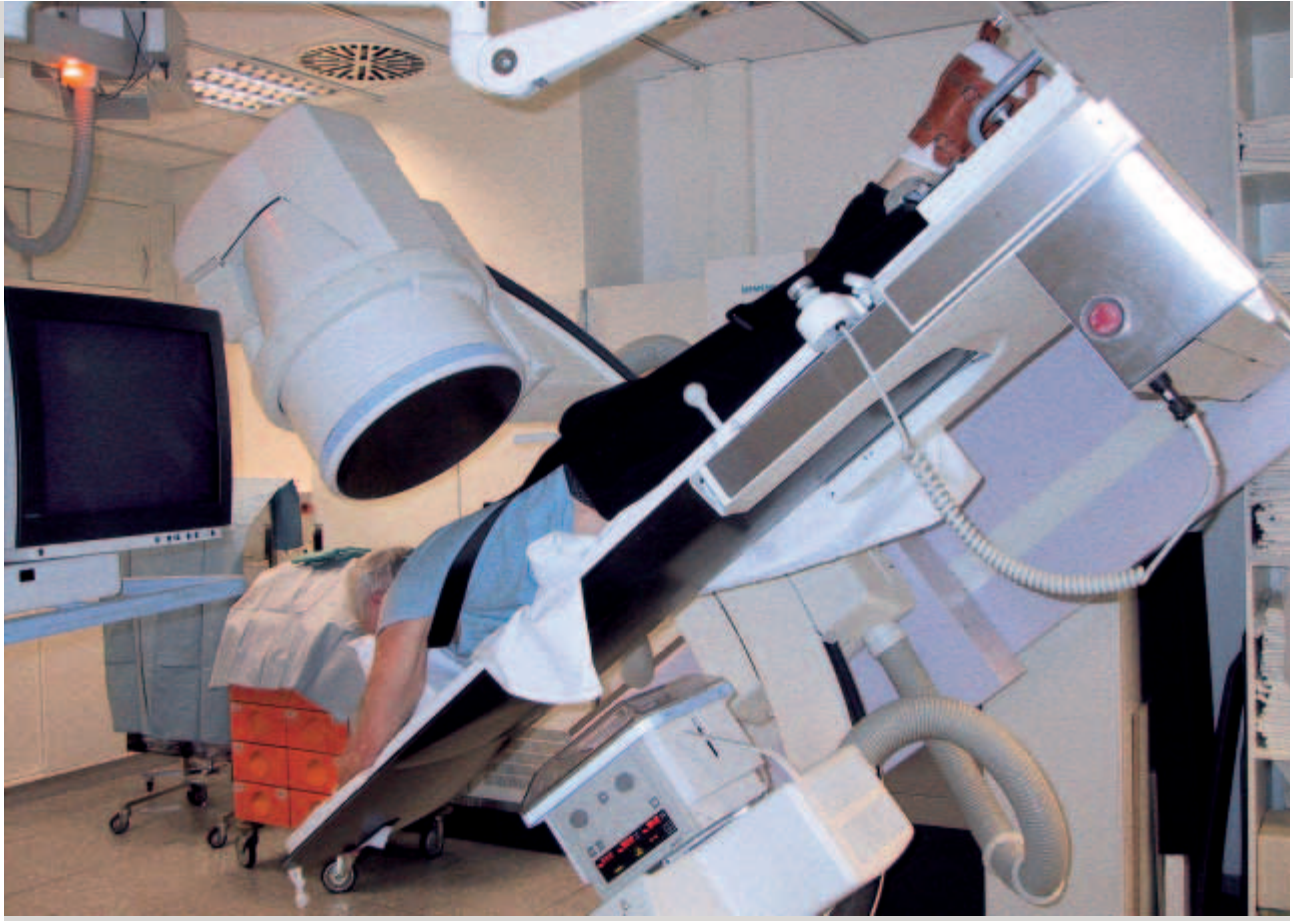

[Figure 1] *Demonstrates the procedure of an X-ray myelography.*

matrix = 256 x 256; measurement time = 0.56 min.
T_1-weighted TSE: TR = 500 ms; TE = 27 ms;
slice thickness = 3 mm; FoV = 250 mm;
matrix = 256 x 256; measurement time = 0.56 min.
TrueFISP (real time) with a TR of 200 ms.

The subjects were positioned in a newly developed, pneumatically operated, device that allowed for step-less, i. e. smooth passive movement of the spine, NeuroSwing (Inside, Funktionelle Diagnosetechnik, Schweinfurt, Germany). This device can be moved passively into any desired position for inclination and reclination by means of an externally controlled pneumatic drive. Movement for lateroflexion and rotation can be either active or passive.
Combining movements in all three axes easily provides any desired position. A combination of three surface coils (CP small flex, CP Neck Array and Spine Array) is integrated into the device to obtain sufficient signal-to-noise ratio. Reproducibility of results is assured by inflation of the pneumatically operated device by a predetermined air volume allowing for comparable extents of inclination and reclination, and by the use of measuring scales for lateroflexion and rotation.
Subject Information: 13 female and 12 male subjects were examined. The average age of the subjects was 30.4 years (SDev: 8.6 years). The average height was 174.6 cm (SDev: 7.2 cm), and the average weight was 69.6 kg (SDev: 11.3 kg).
Measurements: HASTE-3D, MEDIC-2D, TrueFISP and TSE with T_1 and T_2-weighting were performed for each of the 25 subjects in the standard position, inclination, reclination, lateroflexion and rotation. The slices were performed sagittally for inclination and reclination, and coronally or axially for lateroflexion and rotation. The phase encoding direction was craniocaudial except for the examination in rotation, when it was directed right-left. Reproducibility tests were performed with 5 subjects. These measurements were repeated 5 times by three examiners, independently of each other.
Post-Processing: Post-processing, including image fusion, segmentation, 3D visualization and volumetry, was performed at a separate workstation (*syngo* MultiModality Workplace a.k.a. Leonardo, Siemens AG, Medical Solutions, Erlangen).
Image fusion: An automatic, anatomically correct image fusion was performed. 3D-HASTE data-sets and T_2 -weighted images were overlayed using the implemented fusion algorithm. For this HASTE and TSE data-sets were defined as MPR, before they were loaded into a workstation.
Segmentation: Because of the heavy T_2-weighting and the frequency selective suppression of fatty tissue, a threshold-based (implicit) segmentation of the 3D data sets from the HASTE sequence was adequate for visualization.
Visualization: Visualization was enabled via Volume Rendering (VR).
Endoscopy: Virtual endoscopy of the subarachnoidal space enabled via Surface Shaded Display (SSD).
Volumetry: Automatically volumetric measurement of 3D-

HASTE data-sets was performed. For this transverse MPR data-sets of a defined Region of Interest (ROI) underwent a threshold based voxel count.

Determination of the Ranges of Movement: The data from the T_1-weighted TSE sequence was used for the measurements as recommended by Penning [9]. The differences in the angles in the functional positions indicated the range of motion.

To determine the mobility in lateroflexion, we measured the angle between the tangent to the bony basis of the particular vertebra and a fixed line, which was a perpendicular through the bony basis of cervical vertebra 2 (Dens axis) in the standard position.

In rotation, a tangent to the rear edge of the particular vertebra was used to determine the angle. The reference line was a horizontal line through the hard palate in the standard position.

To determine the extent of sagittal motion (inclination-reclination), we determined the angle of a straight line between the rear edge of the Dens axis and the cranial end of the rear edge of thoracic vertebra 1 and a perpendicular.

To establish the extent of coronal motion, we defined a straight line from the medial Dens surface to the vertical through the middle of the cover plate of thoracic vertebra 1 and determined the angle.

The angle for the extent of movement in rotation was determined by a straight line through the middle of the hard palate and the rear edge of thoracic vertebra 1 to the perpendicular. That was done in each case by superimposing the first and last image of the motion examination.

Evaluation: The examinations were evaluated centrally by three experienced radiologists. The examiners were not involved in the evaluations performed using the *syngo* Multi-Modality Workplace (Leonardo). Graphic motion diagrams were generated for the principal functional planes for each subject by plotting the segment level against the segmental angle.

Statistics: Mean values and standard deviations were calculated for all data and angular measurements using the program SPSS 9 (SPSS Software, Munich, Germany).

Results

The HASTE-3D sequence visualized structures in the subarachnoid space with the highest spatial resolution and provided very good signal-to-noise ratio. The intradural resolution allowed good differentiation of the nerve fiber bundle up to the axilla, where the nerve fibers leave the dura. Extremely small extradural masses can be recognized very well indirectly at recesses for cerebrospinal fluid. Surrounding structures, on the contrary, cannot be differentiated adequately. Therefore, this sequence is particularly suitable for implicit segmentation, defined by a fixed transfer function, and subsequent visualization by Volume Rendering Technique (VRT). Post-processing via VRT generates a three-

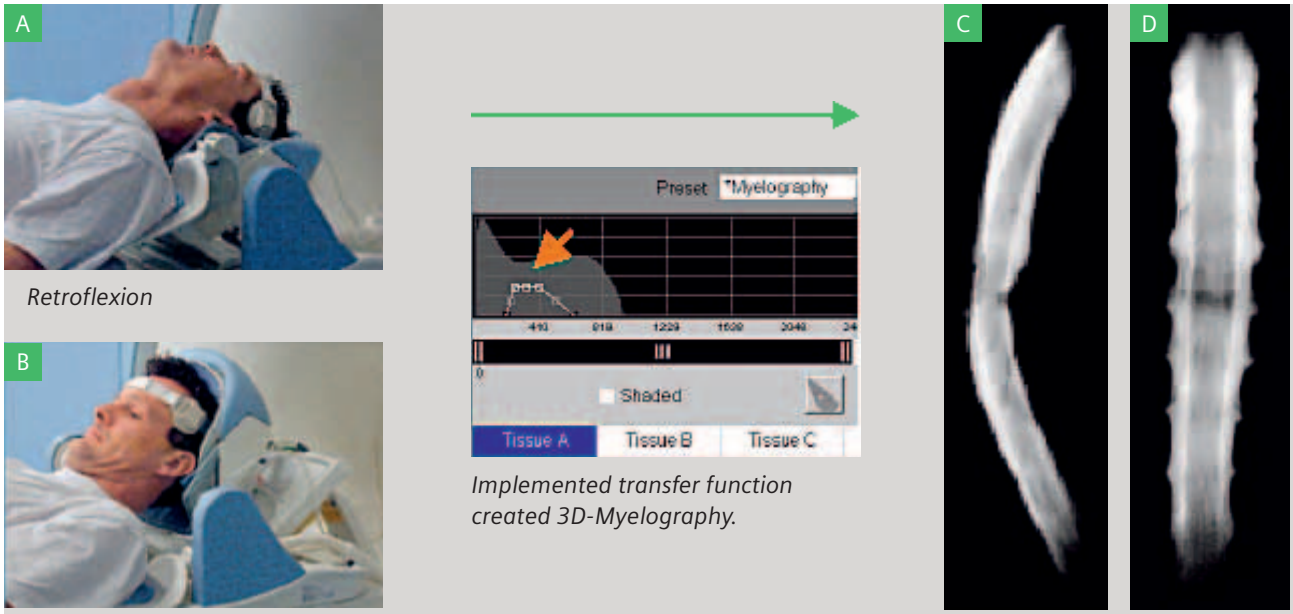

Retroflexion

Anteflexion

Implemented transfer function created 3D-Myelography.

Retroflexion

[Figure 2] *Procedure for cinematography, 3D-Myelography and volumetric measurement of the CSF (cerebrospinal fluid).*

dimensional image of the subarachnoid space (3D myelography) from the slice images of the HASTE-3D sequence [10]. Analogous to conventional myelography, the spinal nerves are distinguished as low signal structures within the subarachnoid space. Fig. 1 shows the complex procedure of conventional myelography for a patient with bony constriction of the spinal canal (spinal stenosis). After the puncture, the patient must be positioned in reclination in the prone position, so that the contrast agent applied in the subarachnoid space can reach the cervical spine. Fig. 2 shows, for comparison the procedure for functional 3D MR myelography and volumetry. To obtain an assignment to an anatomic segment, the MR myelographs were superimposed with T_1-weighted TSE sequences.

We did not observe signal attenuation due to flow (flow void artifacts) in the subjects with the HASTE-3D. With the isotropic set of volume data, slice images could be produced in any arbitrary reconstruction plane without loss of resolution (MPR).

Angle Measurements: Fig. 3 shows T_1-weighted TSE image of a healthy volunteer using the auxiliary system. The range of movement is demonstrated. A reduced TSE matrix (measurement time 30 s) was used. The images show good motion function and an adequate range of motion.

Table 1 presents the results for the segmental mobility, i. e., the maximum range of movement between inclination and reclination. The total range of movement was 106.16°, with a standard deviation of 4.96 °. The segmental mobility, in contrast, deviated substantially (SDev: 2.89-6.79°) and was distinctly greater in the cranial segments of the cervical spine than in the cranial segments (C0/1: 6.79°; C7/8: 5.51°). The values were determined from 25 young and healthy subjects.

The functional mobility for lateroflexion was 25.3° on the left side and 22.5° on the right side, with small standard deviations (left: 1.3°; right: 0.9°). In contrast with the sagittal

Segmental mobility

Segmenta Level	Mean	Standard deviation
C0/1	11.72	6.79
C1/2	6.96	4.36
C2/3	6.28	3.17
C3/4	10.20	2.89
C4/5	14.64	4.52
C5/6	17.40	5.35
C6/7	18.52	5.32
C7/8	20.64	5.51
Total	106.16	4.90

[Tab. 1] *Range of functional measurements in ante- and retroflexion.*

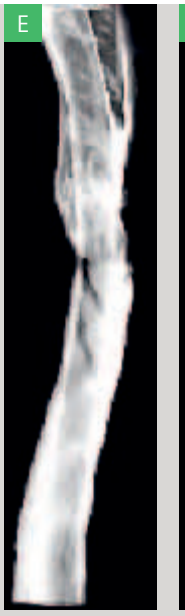

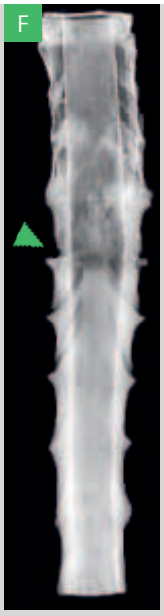

Anteflexion

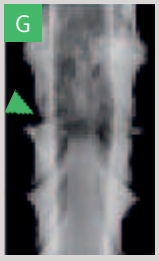

Only in anteflexion a lesion of the C6 nerve root could be visualized.

Automatic volumetry of the CSF is available.

plane of motion, the mobility varies less among the individual segments (2.3° and 5.4°). The deviation is substantial (1.3°–4.3°), as in the sagittal plane.

The total range of motion of the axial plane was 59.1° to the right and 56.9° to the left. The standard deviation is somewhat higher than in the sagittal and coronal planes (right: 12.5°; left: 13.6°). The segmental mobility deviates less and appears to be more uniform without great differences between the sides.

In summary, our results show clearly that although the total ranges of motion are comparable for the individual subjects, there are different segmental ranges of motion.

Reproducibility: Reproducibility tests were done with 5 subjects. Our results show that repeated examinations at defined functional positions are possible with high repetitive accuracy. In inclination, the standard deviation was from 1.5% to 3% of the initial value. In reclination, deviations from the expected value are between 3% and 8%. They are from 2.5% to 5% in lateroflexion and between 2% and 3% in rotation. In summary, our results show high reliability for functional examinations with the device used.

Discussion

Numerous publications have appeared in recent years which treat functional examinations of the cervical spine in various conditions, especially degenerative, inflammatory, and post-traumatic conditions [1–6]. In these cases, functional examinations of the cervical spine are performed in the end position, i.e., at the maximum for movement, or in firmly defined stages [5, 6, 11]. One group used a device, which was continuously adjustable in the sagittal plane. To date, there have been no studies regarding the extent to which functional examinations of the cervical spine are reproducible; or at least they have not been reported in the applicable literature. Although body coils were required in the past for measurement, it is now possible to use surface coils with better signal-to-noise ratio.

One group has reported on the related possibility of improved spatial resolution [12]. In that case, however, gradient echo sequences were used (with all the associated disadvantages including high susceptibility to artifacts) to attain sufficiently high spatial resolution. Our group selected a sequence in (turbo) spin-echo technique for a high-resolution examina-

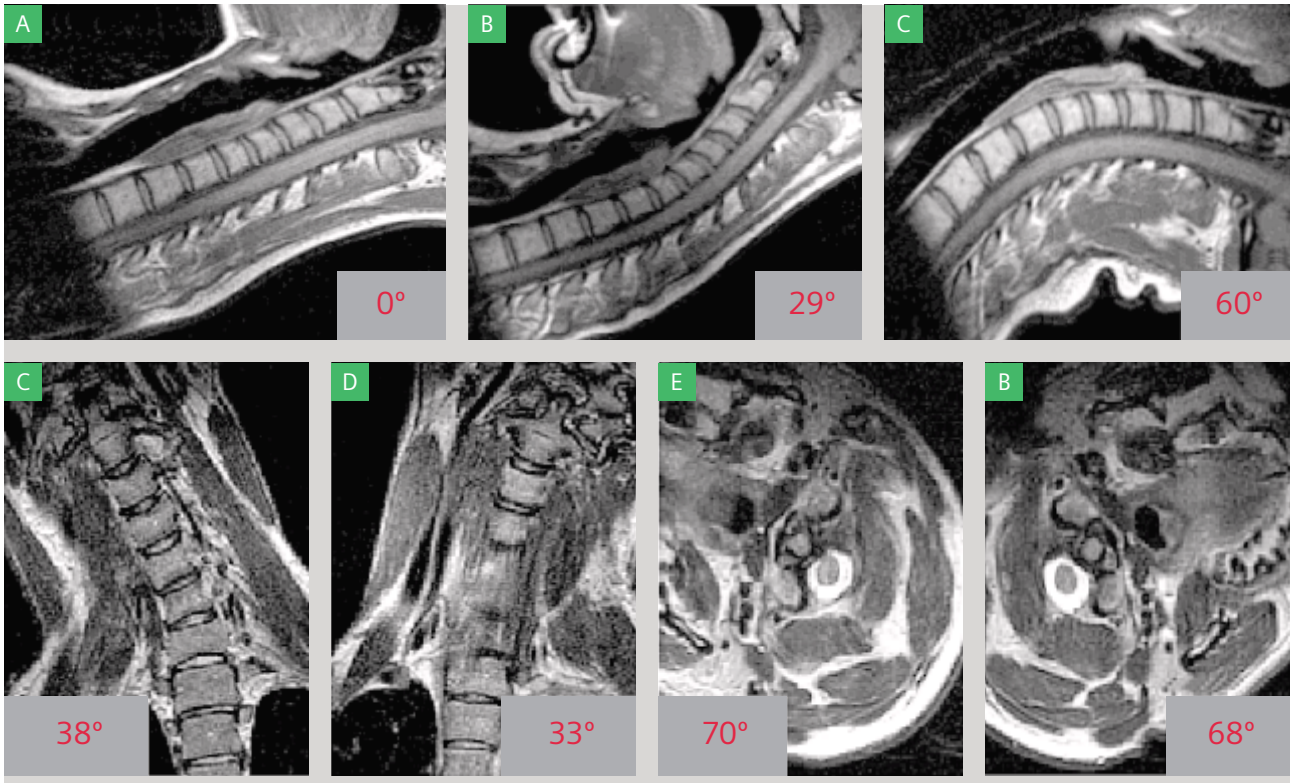

[Figure 3] *Functional range of movement of a volunteer. Neurtral position (A) Anteflexion (B) Retroflexion (C) Lateroflexion (D, E) Rotation (F, G).*

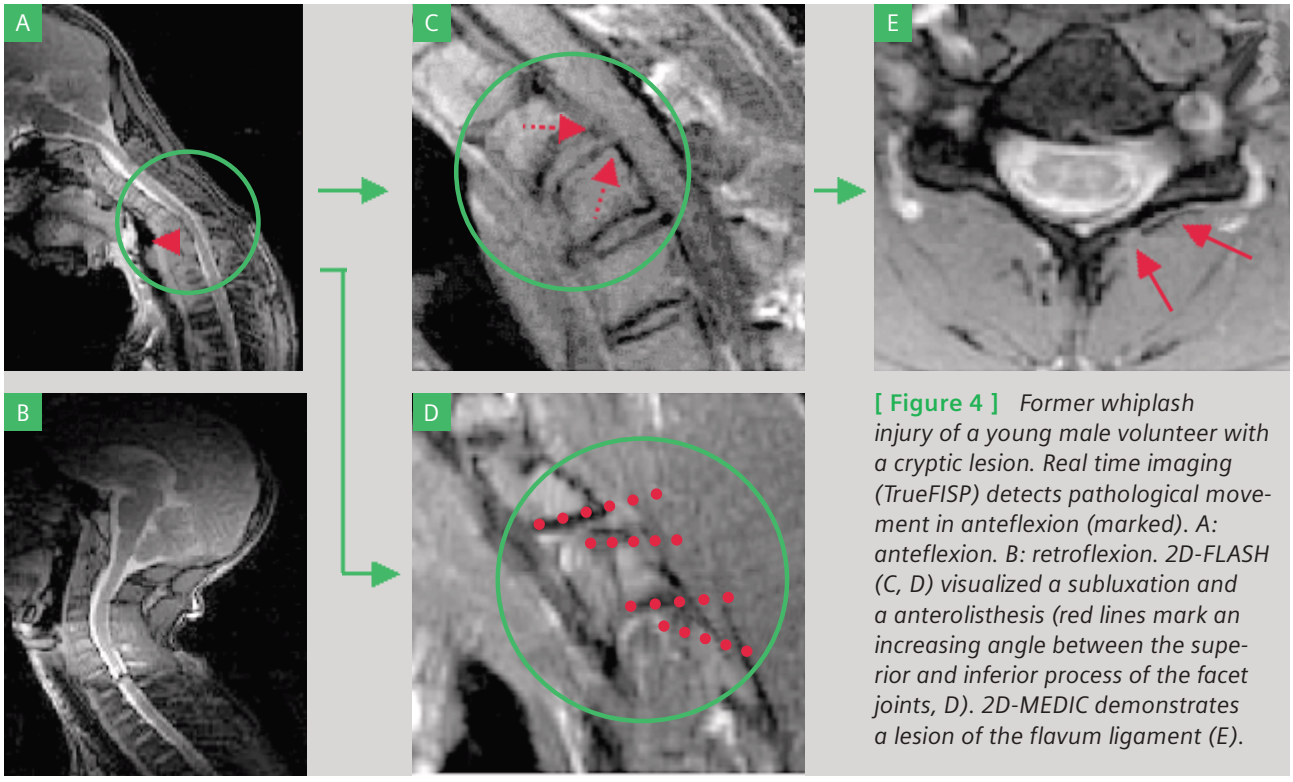

[Figure 4] *Former whiplash injury of a young male volunteer with a cryptic lesion. Real time imaging (TrueFISP) detects pathological movement in anteflexion (marked). A: anteflexion. B: retroflexion. 2D-FLASH (C, D) visualized a subluxation and a anterolisthesis (red lines mark an increasing angle between the superior and inferior process of the facet joints, D). 2D-MEDIC demonstrates a lesion of the flavum ligament (E).*

tion, and utilized parameters optimized for the examination. The spatial resolution obtained by other groups [12] using the gradient echo technique is limited, especially in the slice-selection direction. Multiplanar reconstructions have just as many limitations in application, because of voxel anisotropy, as do the more sophisticated visualization techniques such as VRT [12]. Until now, it has not yet been possible to establish a method comparable to the visualization aspect of conventional myelography. The same group presented 2D evaluations (diameter of subarachnoid space, myelon and neuroforamen) in functional studies [12]. Limitation to one plane, usually the sagittal plane, has been another limitation of functional MR examinations. Examinations in rotation have indeed been reported [12], but they are limited to a few stages of motion. Reports on reproducibility of the examinations are lacking.

Isolated examinations in lateroflexion have been attempted using open systems. Step-less, i. e. smooth movements which can be combined arbitrarily have not been described to date [11]. In the present study, a newly developed device called NeuroSwing was utilized. The NeuroSwing device allows both passive (sagittal plane) and active (lateroflexion and rotation) movements which can be freely combined in all three planes. A sequence adapted to the specific requirements of the cervical spinal region was modified for the examinations, i. e. a TSE sequence with half-Fourier space sampling was selected instead of 3D gradient echo sequences. A MEDIC-2D sequence with modified parameters was also used to evaluate the myelon, so that the entire cervical spine could be

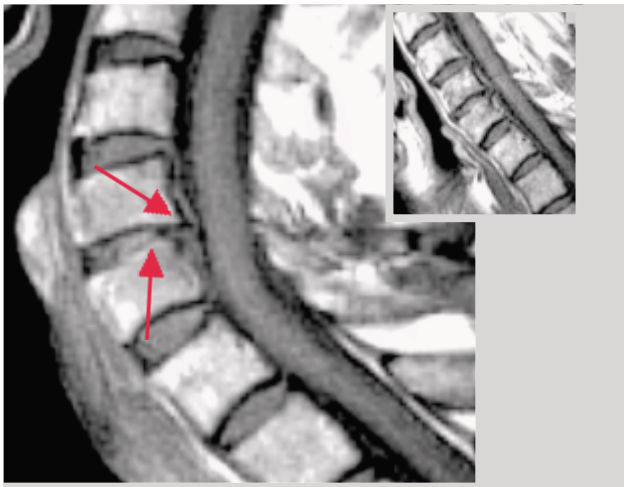

[Figure 5] *Former whiplash injury and disc herniation. Retrolisthesis (marked) could be detected only in retroflexion (TSE).*

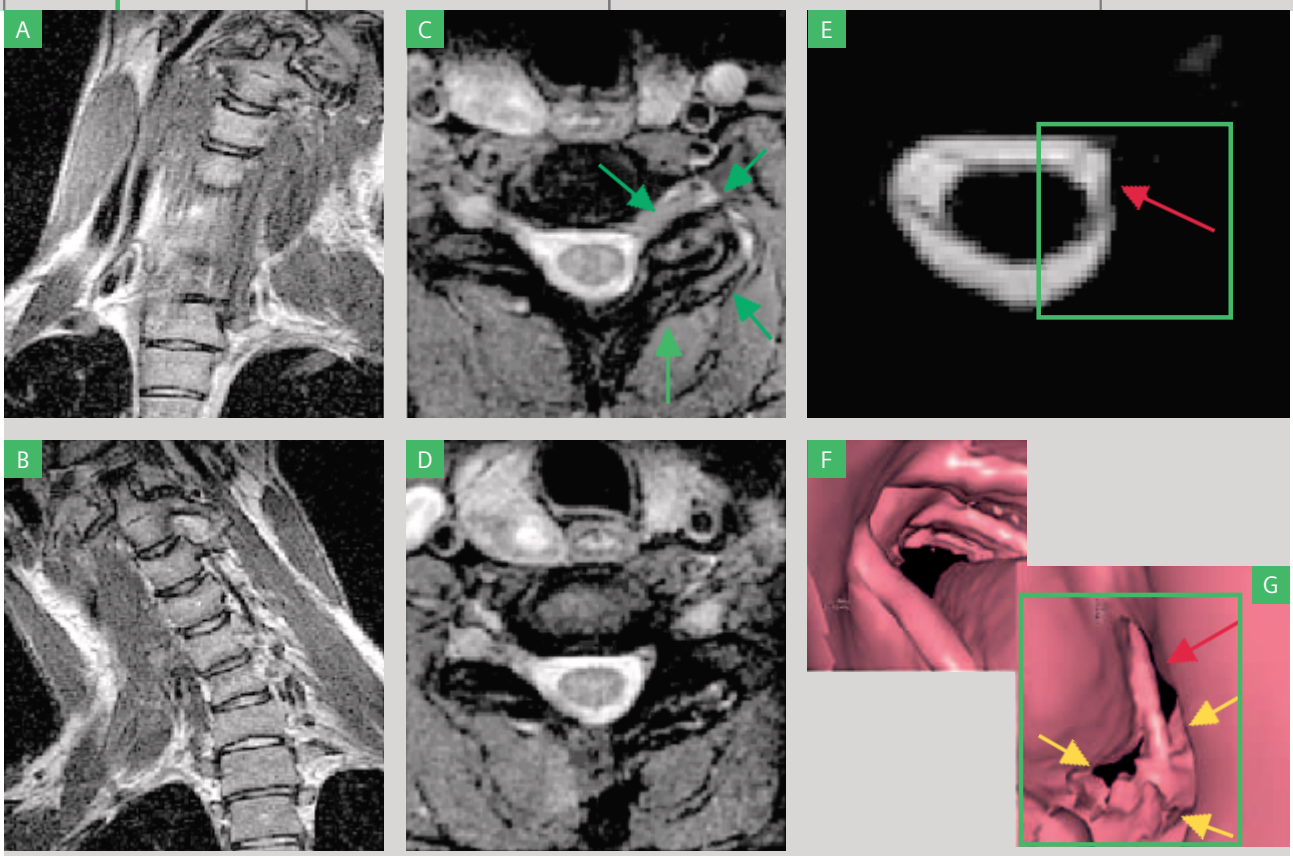

[Figure 6] *Degeneration of the left facet joint. Only in lateroflexion to the left side (A) a compression of the CSF space and the posterior radix (E, marked with red arrow) caused by a hypertrophy of the facet joint (C) could be detected. Endoscopy of the CSF (VESAS) visualized an extradural mass (marked with yellow arrows) with contact to the posterior radix (G, marked with red arrow). TSE (A, B). 2D-MEDIC (C, D). 3D-HASTE (E), VESAS (F, G).*

examined axially with adequate resolution and good signal-to-noise ratio in a measurement time of approx. 4 min. The results from the subjects examined show that the range of motion in the sagittal plane agrees with the values from previously published conventional functional examinations [13]. Here it is interesting that the total range of motion in healthy subjects shows little variation (SDev: 4.96°), but the segmental mobility shows substantial fluctuations even in clinically healthy subjects (SDev: 2.89° to 6.79°). This applies not only to sagittal movement but similarly also for coronal movement (SDev: 0.9° to 1.2° for the total range of motion, and 1.3° to 4.3° for the segmental range of motion) and to the axial plane (SDev: 12.5° to 13.6° for the total range of motion and 1.5° to 10.4° for the segmental range of motion). Comparative reports on the axial range of motion are derived from functional CT examinations [13]. We do not yet have information about the segmental range of motion in the coronal plane, i. e., in lateroflexion. Our examinations are reproducible, as is clearly shown by a series of 5 subjects (SDev: 0.5° to 0.8° in inclination, 0.6° to 1.4° in reclination, 0.5° to 1.2° in lateroflexion, and 1.5° to 2.2° in rotation). In reproducibility examinations, defined functional positions were carried out 5 times by each of the three independent examiners, with the patient repositioned each time. The evaluation was performed independently by three experienced radiologists. Because of the good repetitive accuracy of the NeuroSwing device and the described procedure, it was possible to save time by repeating arbitrary positioning without a new topogram.

If the examination needed to be interrupted briefly because of disturbances, for instance, it could be repeated easily after a brief pause. This is an especially important aspect in the case of time-consuming high-resolution examinations. The visualization results with VRT as 3D MR myelography show that high-resolution examinations are possible with a modified 3D-HASTE sequence. In this case, an isotropic matrix is possible down to a spatial resolution of 0.5 x 0.5 x 0.5 mm in the cervical spinal region. The signal-to-noise ratio of the 3D-HASTE sequence used is very good. The intradural nerve roots can be differentiated well from the CSF and dura. The transition to the extradural segment, i.e. the true axilla section, can be visualized without artifacts. Our results show that it is entirely comparable with a high-resolution MEDIC-2D sequence. Due to the isotropic matrix, multiplanar reconstructions (MPR) are quite possible in all reconstruction planes as an alternative to 3D visualization. No artifacts due to CSF pulsation or vessel movement appeared. Despite the low bandwidth of the HASTE sequence, no chemical shift

artifacts appeared, because of the frequency-selective presaturation of the fatty tissue surrounding the dura. In the present study, to save time, we considered a voxel size of 1 x 1 x 1 mm adequate for functional examinations. In 7 of 25 volunteers cryptic lesions (3 former whiplash injuries) could be detected only using functional imaging. Real time imaging using TrueFISP gives sufficient information about disc, subarachnoidal space and vertebrae. TrueFISP (200 ms / image) can be used for fast screening. Spondylolisthesis could be detected and measured using TSE. Ligamental lesion could be visualized best using 3D-MEDIC. 3D-HASTE data-sets allow high-resolution 3D-visualization of the CSF within the nerve roots in an endoscopic view. Critical care patients can be examined in less than a minute. High-resolution MR-Myelography can be performed in all functional positions in 3–4 minutes. Reproducible high-resolution investigations in arbitrary functional positions could be performed [3].

Summary and Prospect

Our study shows that high-resolution MRI examinations are functionally possible by means of the NeuroSwing auxiliary device and the sequences specially modified for the particular area of examination. Since the individual segmental mobilities are quite different, in our opinion it is best to perform a rapid survey first so that the course of the subsequent examination can be planned better. Due to the high reproducibility of our method, a high-resolution, patient-friendly diagnostic imaging examination can then be planned with confidence. If necessary, the examination may be interrupted briefly at any time, without requiring a new topogram to plan the examination. Since the clinical utility of functional examinations has been proven adequately, the functional examination method should become increasingly available for routine use. The positioning aid used can quickly and easily be integrated into the examination table. This would perhaps enable future cervical examinations to be performed exclusively using a variable positioning device. The coil combinations commonly used in the cervical spine region and other vertebral regions are integrated into the auxiliary device, enabling supplemental examination of the segments of the vertebral column caudally adjacent to the cervical spine without having to interrupt the examination.

*This information about this product is preliminary. The product is under development and not commercially available in the US and its future availability cannot be ensured.

Abbreviations

CP	Circular Polarized
CSF	Cerebrospinal Fluid
FLASH	Fast Low Angle Shot
FoV	Field of View
HASTE	Half-Fourier Single Shot Turbo Spin Echo
MAP	Multi Angle Projection
MEDIC	Multi Echo Data Image Combination
MRI	Magnetic Resonance Imaging
MRP	Multiplanar Reconstruction
SDev	Standard Deviation
SINOP	Simultaneous In-Phase Oppose-Phase
TR	Time Repetition
TSE	Turbo Spin Echo
VRT	Volume Rendering Technique

Literature

[1] Pfirrmann CW, Binkert CA, Zanetti M, Boos N, Hodler. Functional MR imaging of the craniocervical junction. Correlation with alar ligaments and occipito-atlantoaxial joint morphology: a study in 50 asymptomatic subjects. Schweiz Med Wochenschr 2000; 130(18): 645–51.
[2] Chiavassa H, Sans N, Galy-Fourcade D, Giobbini K, Manelfe C, Raihac J. HASTE sequence and and cine-MRI evaluation of the cervical spinal canal: evaluation in 11 healthy subjects. J Radiol 2000; 81(6):611–17.
[3] Muhle C, Metzner J, Weinert D, Falliner A, Bringmann G, Mehdorn MH, Heller M, Resnick D. Classification system based on kinematic MR imaging in cervical spondylitic myelopathy. AJNR 1998; 19(9):1763–71.
[4] Van Goethem JW, Biltjes IG, Van den Hauwe L, Parizel PM, De Schepper AM. Whiplash injuries: is there a role for imaging. Eur J Radiol 1996; 22(1): 30–7.
[5] Muhle C, Wiskirchen J, Brinkmann G, Falliner A, Weinert D, Reuter M, Heller M. Kinematic MRI in degenerative cervical changes. RöFo Fortschr Röntgenstr 1995; 163(2): 148–54.
[6] Schnarkowski P, Weidenmaier W, Heuck A, Reiser MF. MR functional diagnosis of the cervical spine after strain injury. RöFo Fortschr Röntgenstr 1995; 162(4): 319–24.
[7] Eberhardt KEW, Tomandl BF, Rezk-Salama C, Schindler R, Huk W, Lell M. Funktionelle hochauflösende 3D-Untersuchungen der Lendenwirbelsäule mit Hilfe der Magnetresonanztomographie. Electromedica 2002; 1: 74–81.
[8] Kiefer B, Gössner J, Hausmann R. Image aquisition in a second with half fourier aquired single shot turbo spin echo. JMRI 1994; 4: 86.
[9] Penning L. Radiologische Analyse der normalen Bewegungsmechanik der HWS C0/3. Schweiz.Rsch. Med. Praxis 1976; 65:1053–58.
[10] Eberhardt KEW, Dütsch M, Schindler R, Liebisch J, Stauffenberg C v., Fischer H, Weigl J, Fellner FA, Funktionelle hochauflösende 3D-Untersuchungen der Halswirbelsäule mit Hilfe der Magnetresonanztomographie. Electromedica 2002; 2:123–132.
[11] Tacke J, Pfeffer JK, Glowinski A, Birnbaum K, Gunther RW. A smooth pneumatic motion device for dynamic MRI imaging of the cervical spine. RöFo Fortschr Röntgenstr 1996; 171(3): 249–53.
[12] Muhle C, Bischoff L, Weinert D, Lindner V, Falliner A, Maier C, Ahn JM, Heller M, Resnick D. Exacerbated pain in cervical radiculopathy at axial rotation, flexion, extention, and coupled motion of the cervical spine: evaluation by kinematic magnetic resonance imaging. Invest Radiol 1998; 33(5): 279–88.
[13] Dvorak J, Antinnes JA. „Age and gender related normal motion of the cervical spine". Spine 1992; 17(10): 393–98.

Susceptibility-Weighted Imaging (SWI) Case Reports

Karen A. Tong, M.D.

Dept. of Neuroradiology, Loma Linda University Medical Center, CA, USA

Case 1

A 14-year-old female who was ejected 20 feet from an automobile in a motor vehicle accident. She had an initial Glasgow Coma Score (GCS) of 3. She was in a coma for 8 days, and in hospital for 93 days. MRI was obtained 11 days after injury. SWI images showed numerous small hemorrhages throughout the deep brain, consistent with diffuse axonal injury. In these images, the small hemorrhages in the corpus callosum and thalami are better seen on the SWI image than on the conventional GRE (Gradient Echo) image. On long-term follow-up she had severe disability.

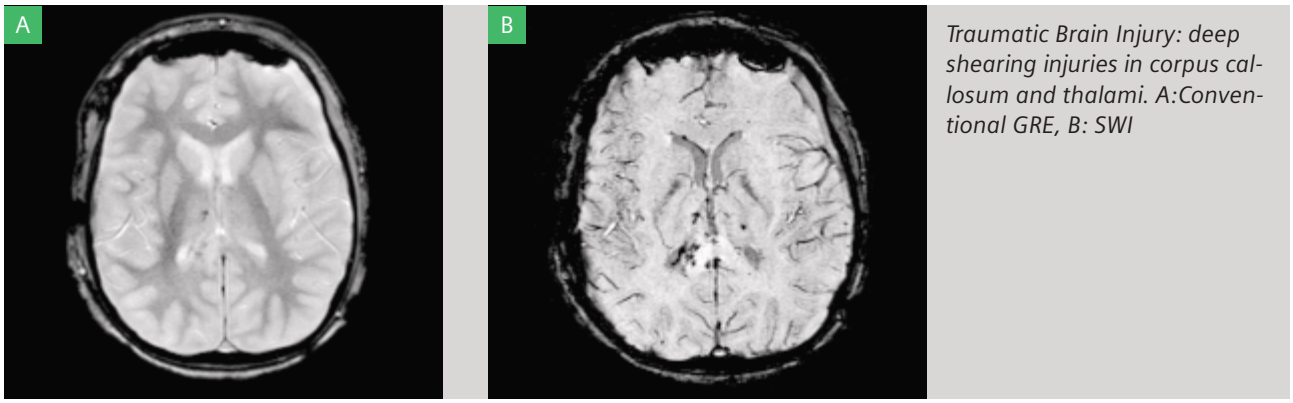

Traumatic Brain Injury: deep shearing injuries in corpus callosum and thalami. A:Conventional GRE, B: SWI

Case 2

A 12-year-old female who was a passenger in an automobile that struck a pole. Her initial GCS was 6. She was in a coma for 6 days and in the hospital for 29 days. MRI was obtained 3 days after injury. SWI images showed multiple small hemorrhages throughout the deep brain, consistent with diffuse axonal injury. In these images, the small hemorrhages in the temporal lobes and occipital horns are better seen on the SWI image than on the conventional GRE image. On long-term follow-up she had moderate disability.

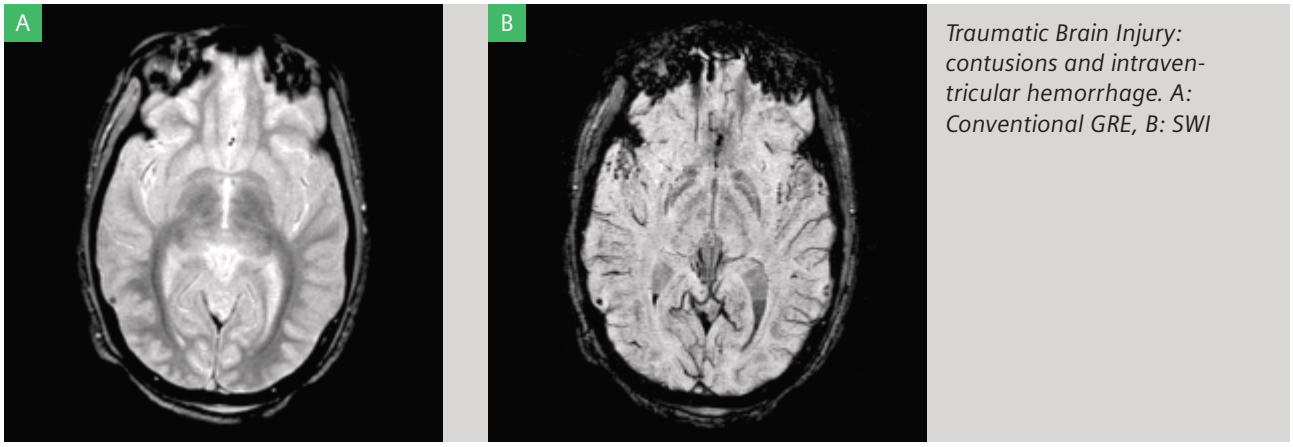

Traumatic Brain Injury: contusions and intraventricular hemorrhage. A: Conventional GRE, B: SWI

Case 3

An 11-year-old male who was riding a motorcycle when struck by an automobile. His initial GCS was 6. He was in a coma for 26 days, and was in hospital for 105 days. MRI was obtained 8 days after injury. SWI images showed multiple small hemorrhages throughout the deep brain, consistent with diffuse axonal injury. In these images, the small hemorrhages in frontal and temporal lobes, and midbrain, are better seen on the SWI image than the conventional GRE image. On long-term follow-up he had moderate disability.

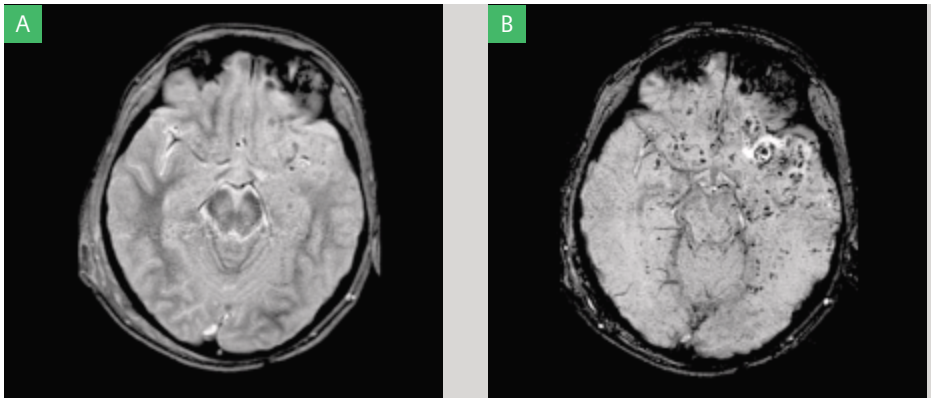

Traumatic Brain Injury: contusions & shearing Injuries.
A: Conventional GRE, B: SWI

Case 4

A 60-year-old male who was involved in a rollover motor vehicle accident and was trapped under a semi-tractor trailer. SWI shows extensive dark signal outlining the surface of the brain, consistent with subarachnoid hemorrhage. A dark fluid or FLAIR image shows bright signal in the parietal sulci, confirming recent bleeding. Hyperdense subarachnoid hemorrhage was also seen on computed tomography images (not shown).

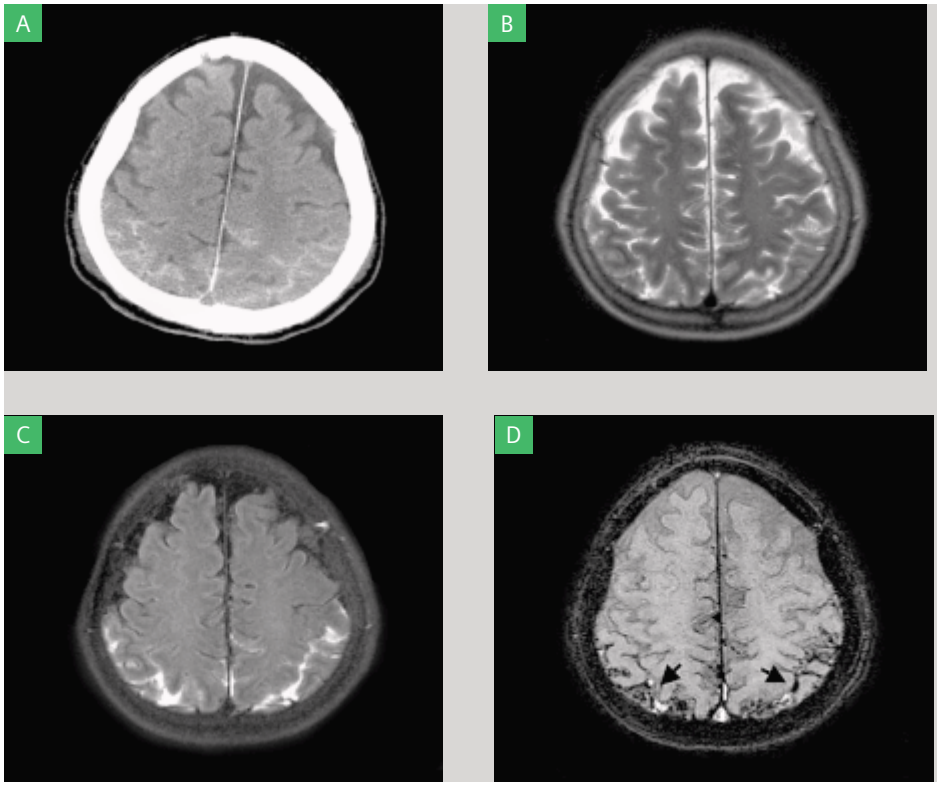

Traumatic Brain Injury: subarachnoid hemorrhage
A: CT examination,
B: T2 weighted image,
C: Dark Fluid,
D: SWI

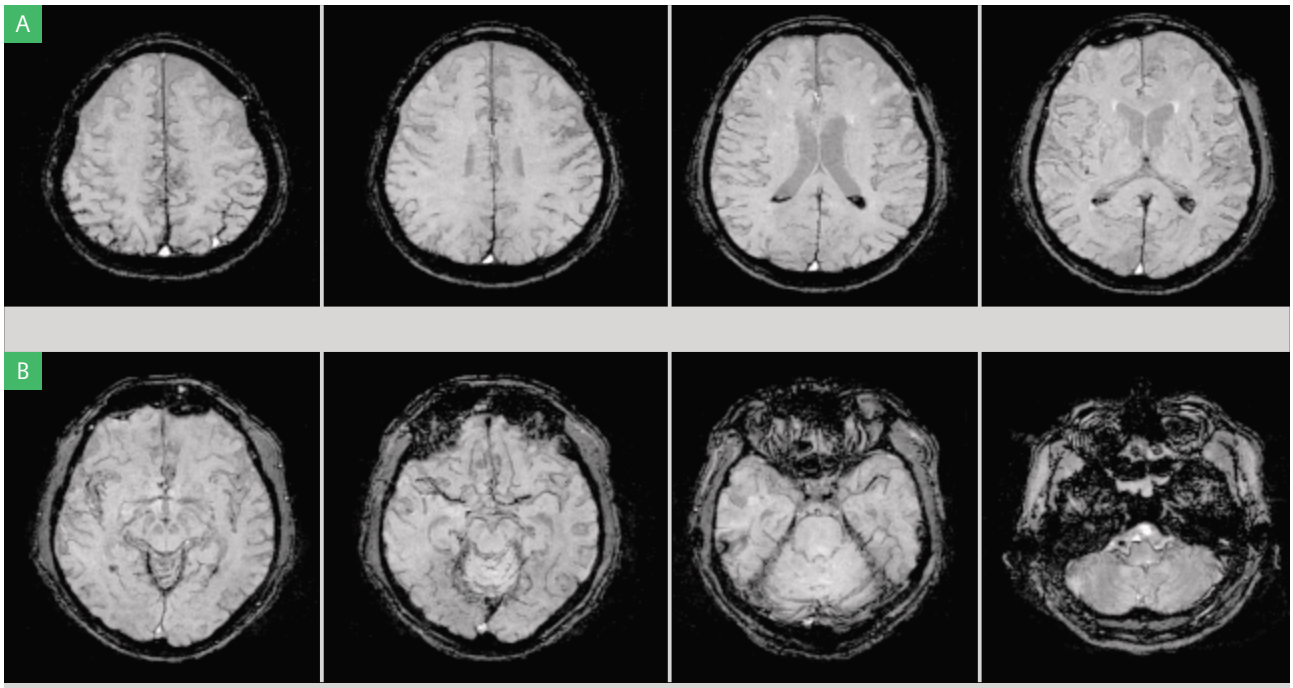

Traumatic Brain Injury: subarachnoid hemorrhage. SWI images.

Case 5

A 57-year-old female with chronic headaches. An incidental venous angioma was found in the right hemisphere. This is best seen on the SWI images, and is barely visible on the TSE (Turbo Spin Echo) T2 image.

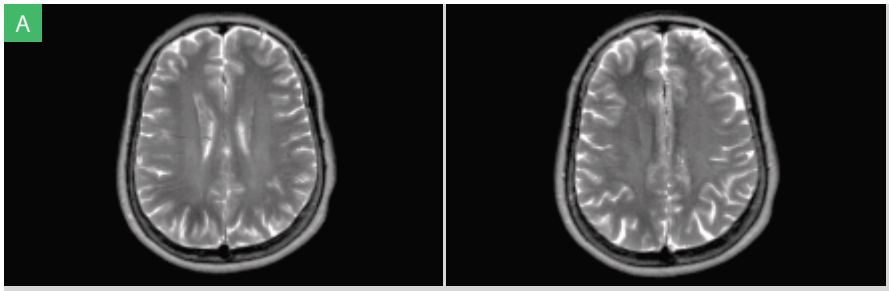

Venous Angioma
T2

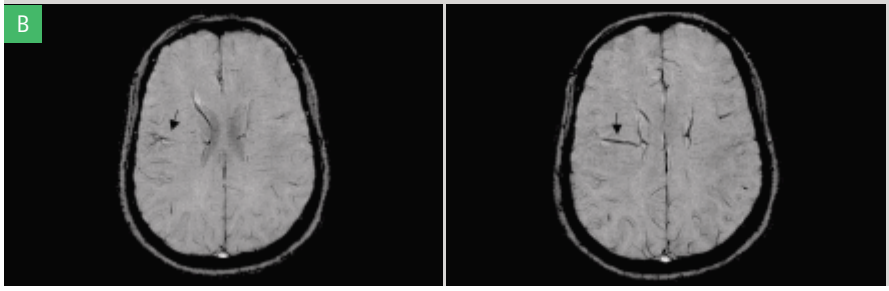

Venous Angioma
SWI

Case 6

A 7-year-old male who presented with visual disturbance. He was found to have multiple cavernomas in the brain on MRI, best seen on the SWI images, compared to the GRE and TSE T2 images.

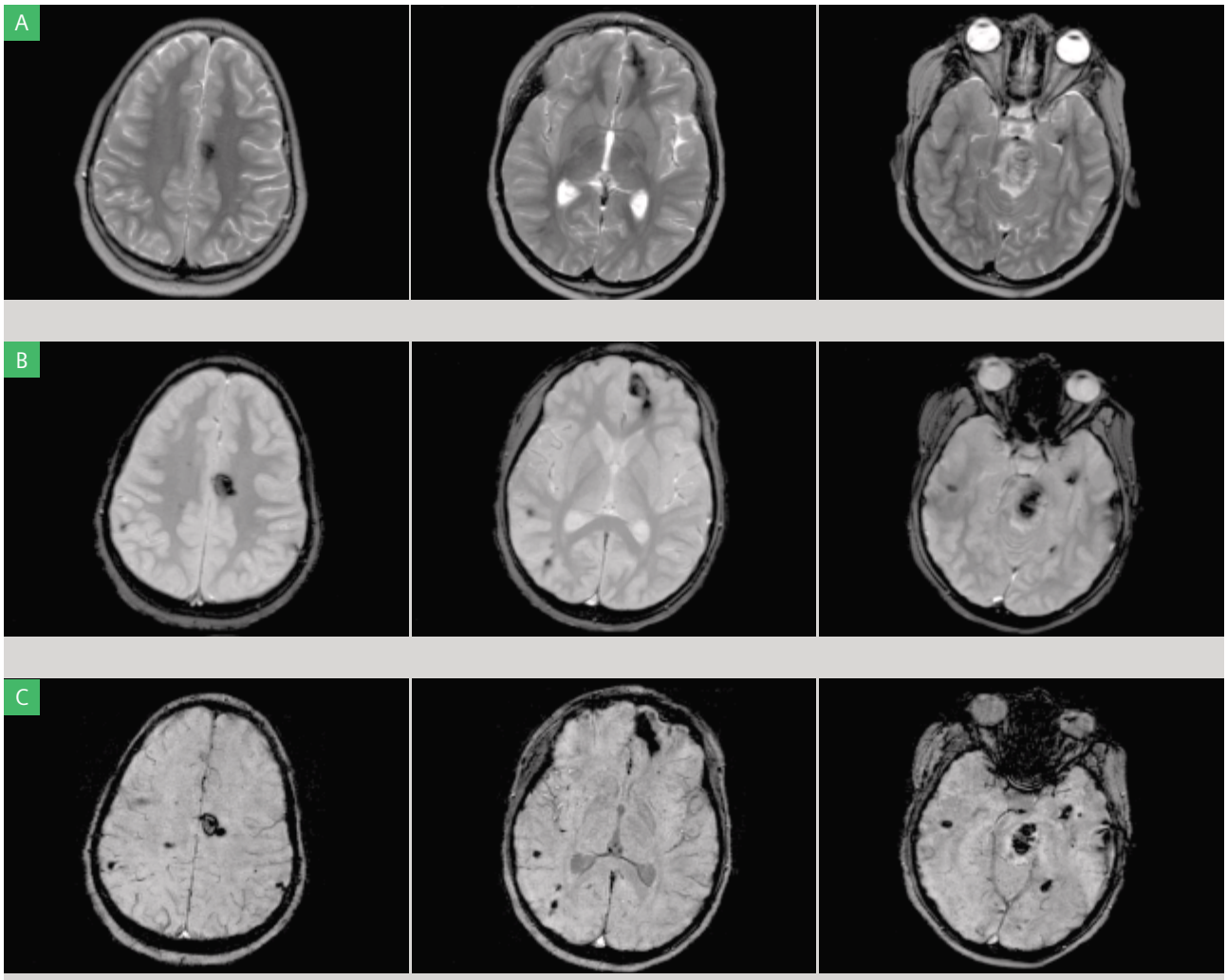

Multiple Cavernomas, A: T2, B: T2, C: SWI.*

Sequence Details

Scanner	*Conventional 1.5T system*	*MAGNETOM Avanto 1.5T*
	Susceptibility-weighted imaging – SWI [3D FLASH]	
slice thickness	*64 partitions 2 mm*	*56 slices, 2 mm*
TR/TE	*57 / 40*	*48 / 40*
TI	*–*	*–*
TA	*9:46 min*	*2:58 min PATx2***
Matrix	*256 x 512*	*256 x 512*
FoV	*5/8 FoV 240*	*173 x 230*
Bandwidth	*78*	*80*

** post-processing*
*** almost three times faster than a conventional 1.5T system*

Whole-Body MRI

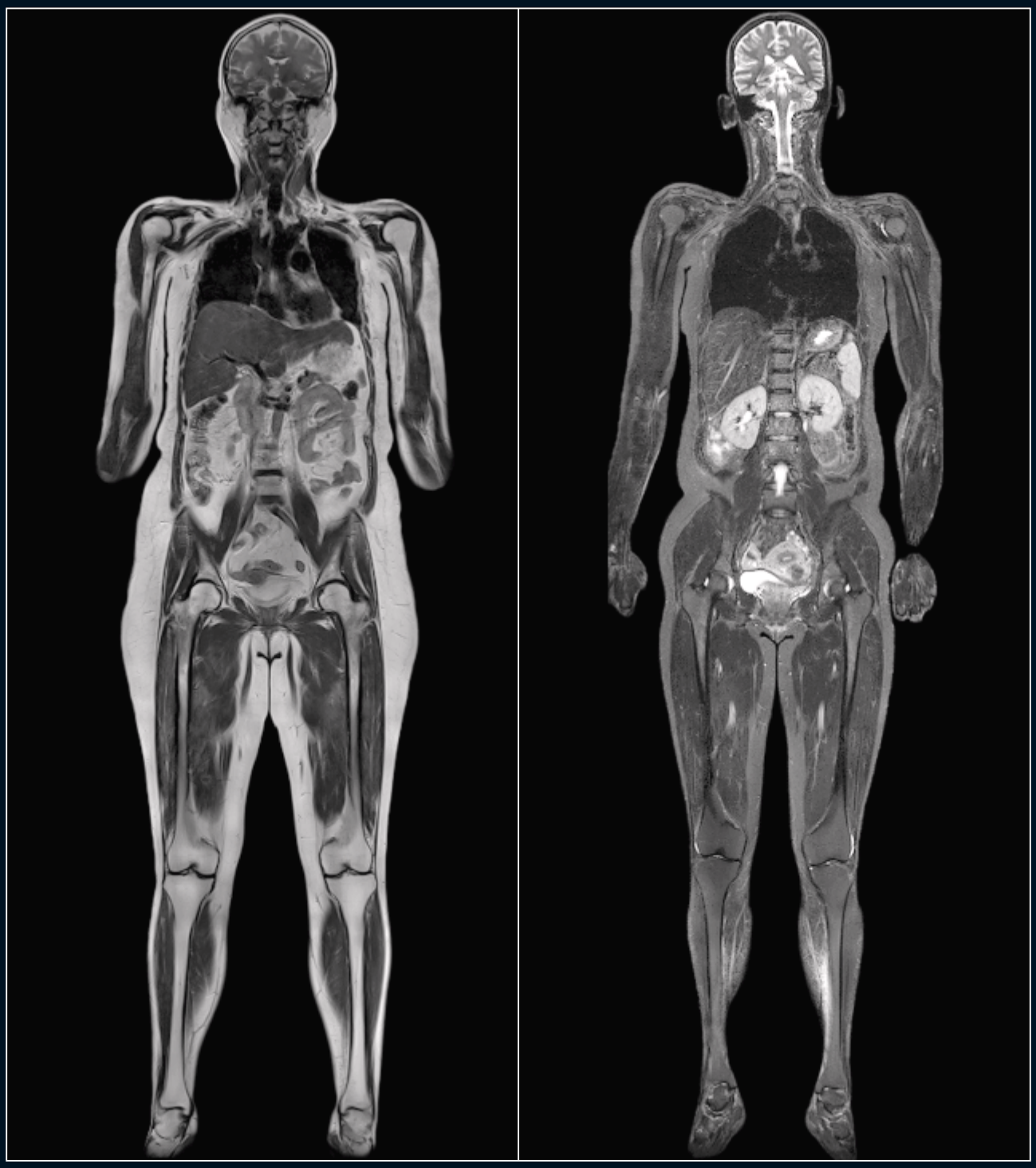

Courtesy of Hong Kong Sanatorium and Hospital, Hong Kong

Whole-Body MRI: Faster with Tim

Richard C. Semelka, M.D.[1]
Brian M. Dale, Ph.D.[2]

[1]*Department of Radiology, University of North Carolina, Chapel Hill, NC, USA*
[2]*Siemens Medical Solutions, Cary, NC, USA*

Introduction

The use of breath-hold techniques and intravenous administration of contrast agents allows MRI to demonstrate a full range of upper abdominal diseases [1–4]. One advantage of the wide variety of MR sequences currently available is that comprehensive examination of disease processes is feasible [1]. The main disadvantage of this variety is that general agreement on MR imaging strategies is difficult to achieve and thus there is a tendency to add new sequences to a protocol rather than replace older sequences [5]. This tendency serves to decrease patient throughput, increase study cost, and increase the likelihood of patient motion.

Directly opposing this trend, the idea of whole-body MR screening exams is rapidly gaining popularity [6–8]. This could be particularly useful in the examination of metastatic cancer and other diseases that can occur simultaneously in a variety of organs and anatomical locations [8, 9]. Additionally, and although such views are vividly being discussed in the medical community, it can be considered ethical to do whole-body MR screening of healthy individuals because MR does not use ionizing energy, uses relatively safe contrast agents, and is more effective than CT at detecting most disease processes except in the lungs [10–13].

Whole-body MR screening requires a series of very rapid exams and an easy transition from one anatomical location to another. As a result there is a need to replace longer breathing-averaged sequences with shorter breath-hold or breathing-independent sequences, to eliminate redundant sequences and to otherwise reduce the total time of MR examinations. The term "breathing independent" reflects that sequences are less than 2 seconds in duration, are minimally sensitive to artifacts from patient breathing and motion, and therefore do not require that patients breathe in a regular

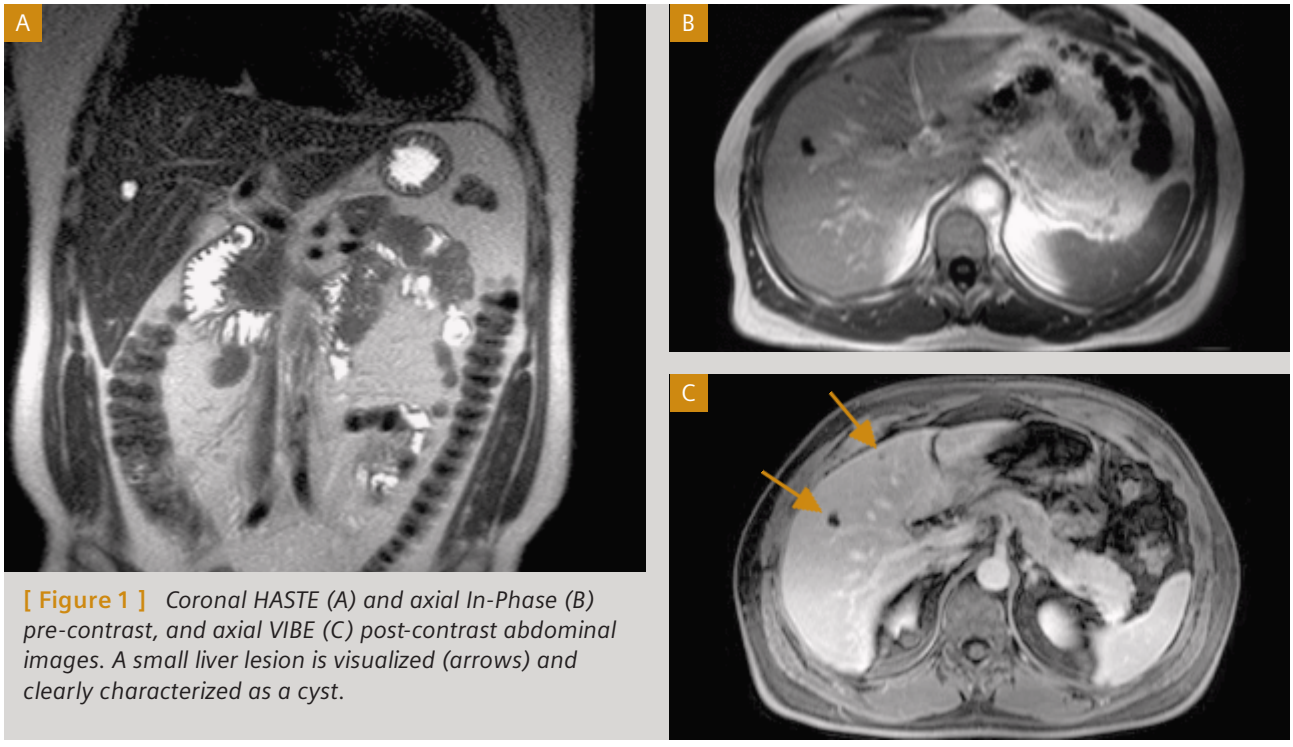

[Figure 1] *Coronal HASTE (A) and axial In-Phase (B) pre-contrast, and axial VIBE (C) post-contrast abdominal images. A small liver lesion is visualized (arrows) and clearly characterized as a cyst.*

fashion or suspend respiration. In addition to rapid sequence software, the hardware must also support the rapid imaging of each anatomical location as well as the rapid transition from one location to another. Siemens has addressed these needs with the following 5 technological advances [2, 14–16]:

1 Remote movement of the patient table
2 Up to 32 independent RF receive channels
3 Tim (Total imaging matrix) Matrix coils covering the whole body with high signal-to-noise ratio (SNR)
4 Hardware and software allowing iPAT (integrated Parallel Acquisition Technique) in all directions
5 High quality 3D T1-weighted VIBE (Volume Interpolated Breathhold Examination)

The following sections describe how these elements may be combined into an effective screening protocol.

10-minute whole-body protocol

The patient is prepared by using the Head Matrix coil, the Neck coil, and two or four Body Matrix coils covering the entire torso. An intravenous line is established for contrast injection.
This protocol is designed to screen for systemic metastases in the majority of patients. Specific needs of individuals may be addressed by adding sequences to this basic screening protocol, but the focus on keeping the overall protocol short must be maintained. One common example is to add a basic cardiac exam as part of the optional sequences. The T-SENSE sequence has a true temporal resolution of 50 ms and can therefore be used to generate CINE-like image sets without requiring cardiac gating or even breath-holding.

Table 1: Whole body screening protocol

Name	TA (m:s)	TR (ms)	TE (ms)	Flip (°)	Fat Sat.	Base Res.	Slices	Thick. (mm)	PAT	BW (Hz)
Abdominal Localizer	2	2.57	1.28	60	no	128	9	6		977
Coronal HASTE	47	1500	99	180	no	256	30	6	2	651
Axial In-Out Phase	19	200	2.4/4.8	70	no	256	25	8	2	380/530
Axial GRE Pre	19	200	4.4	70	no	256	29	8	2	490
Contrast injection										
Axial GRE Post	19	200	4.4	70	no	256	29	8	2	490
Axial VIBE Dynamic	53	4.3	1.68	10	yes	320	64	3.5	2	350
Chest Localizer	2	2.57	1.28	60	no	128	9	6		977
Axial VIBE	19	4.3	1.68	10	yes	320	80	3.5	2	350
Coronal VIBE	21	4.3	1.68	10	yes	320	80	3.5	2	350
Coronal HASTE	47	1500	99	180	no	256	30	6	2	651
Axial HASTE	54	1500	91	180	yes	256	35	8	2	651
Pelvis Localizer	2	2.57	1.28	60	no	128	9	6		977
Axial VIBE	19	4.3	1.68	10	yes	320	80	3.5	2	350
Sagittal VIBE	19	4.3	1.68	10	yes	320	80	3.5	2	350
Axial HASTE	54	1500	91	180	no	256	35	8	2	651
Sagittal HASTE	44	1500	91	180	no	256	28	8	2	651
Heart Localizer*	2	2.57	1.28	60	no	128	9	6		977
Axial VIBE*	15	4.3	1.76	10	yes	320	56	3.5	2	350
Short-axis tSENSE*	13	54.25	0.94	55		128	8	7	3	1302
Head Localizer	3	2.67	1.34	60	no	128	9	6		977
Axial VIBE	47	4.3	1.83	10	yes	320	88	3	2	350
Axial HASTE	47	1500	98	180	no	256	30	5	2	651
Sagittal HASTE	47	1500	98	180	yes	256	30	5	2	651

* indicates an optional sequence. Total scan time is 9:44 min without the optional sequences or 10:14 min with the optional cardiac sequences.

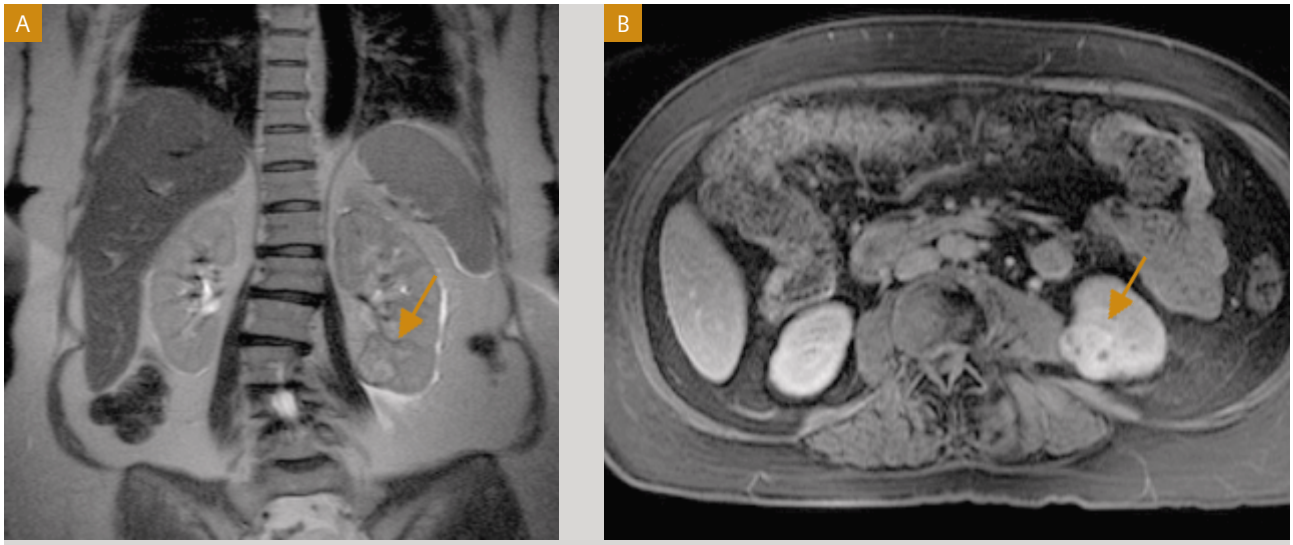

[Figure 2] *Coronal HASTE (A) and axial VIBE (B) post-contrast abdominal images. Small renal cancer showing mildly heterogenous enhancement identified in the inferior pole of the left kidney (arrows). Small cancers in the polar region can be missed in CT or MR examinations relying entirely on transverse images.*

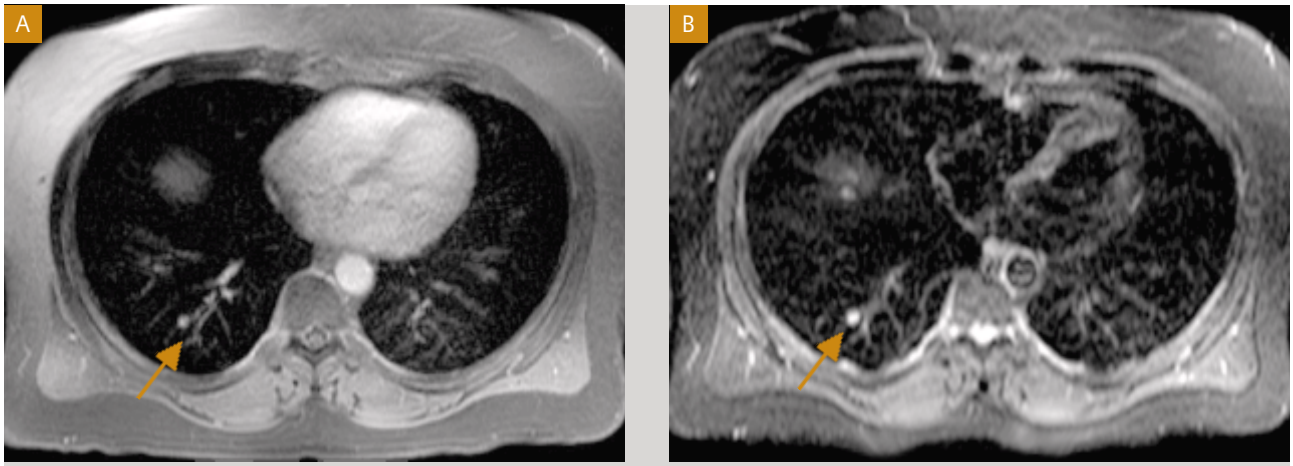

[Figure 3] *Axial VIBE (A) and axial HASTE (B, C) post-contrast thoracic images. Small pulmonary metastases measuring less than 4 mm across are clearly visualized (arrows). These are clearly depicted despite the conventional wisdom indicating that such small lung metastases are difficult to see using MRI.*

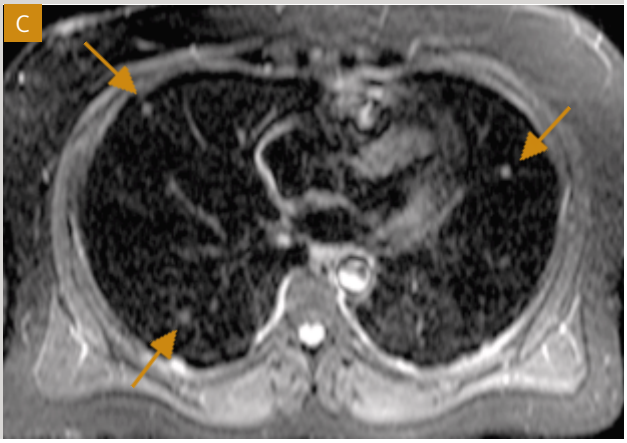

Results

Figures 1 through 5 show a selection of typical images obtained using this protocol. Note the generally high image quality of all sequences used. Note in Figure 1 that the small liver lesions are easily visualized and accurately characterized as cysts. Note also the visualization of the small renal cancer in Figure 2. In particular, note the clear depiction of the small pulmonary metastases as seen in Figure 3, despite the fact that they are considered a challenge for MRI. Figures 4 and 5 do not demonstrate any pathology, but do demonstrate the high image quality of the screening protocol in the pelvis and head.

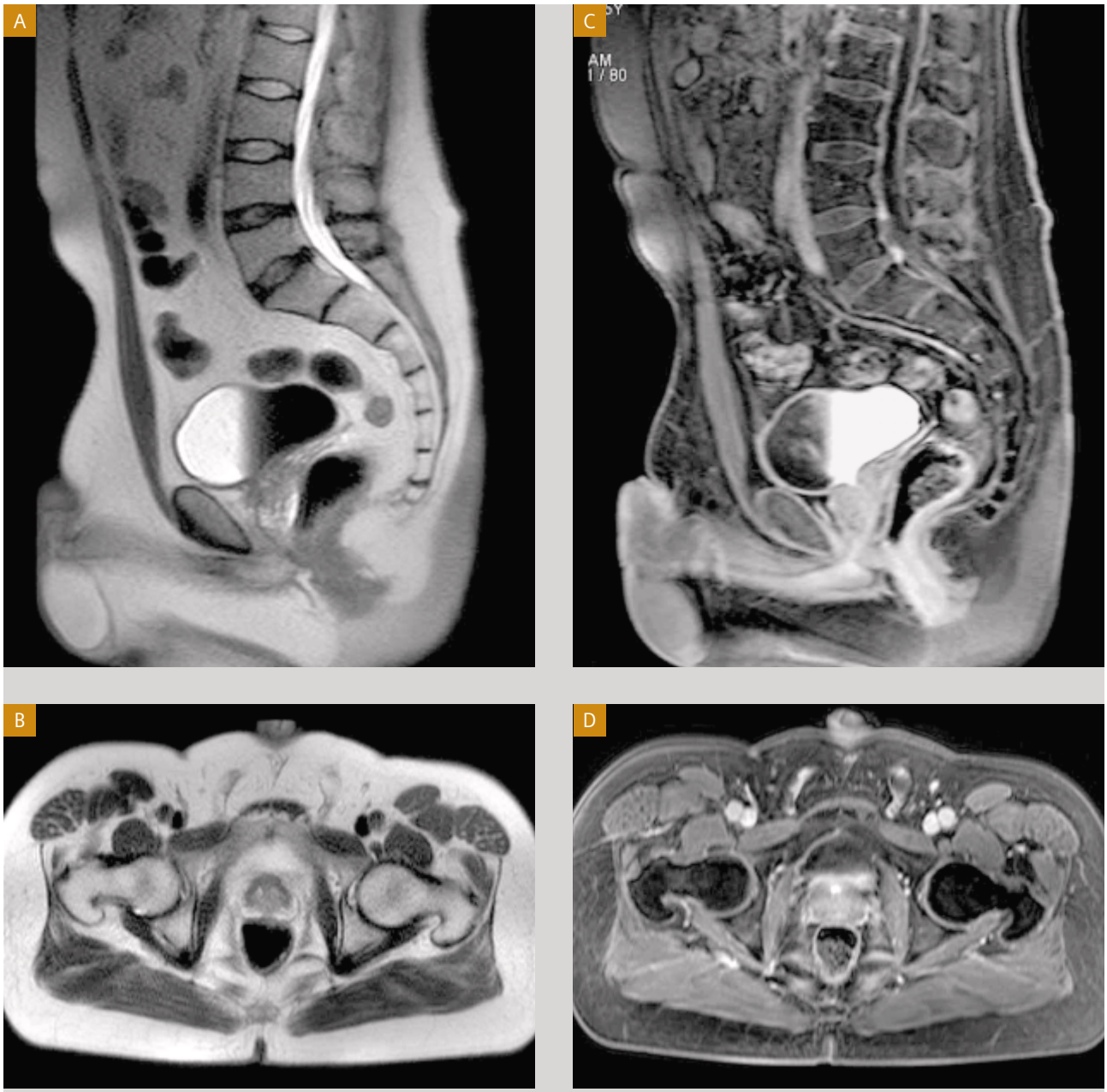

[Figure 4] *Sagittal HASTE (A), axial HASTE (B), sagittal VIBE (C), and axial VIBE (D) post-contrast pelvic images.*

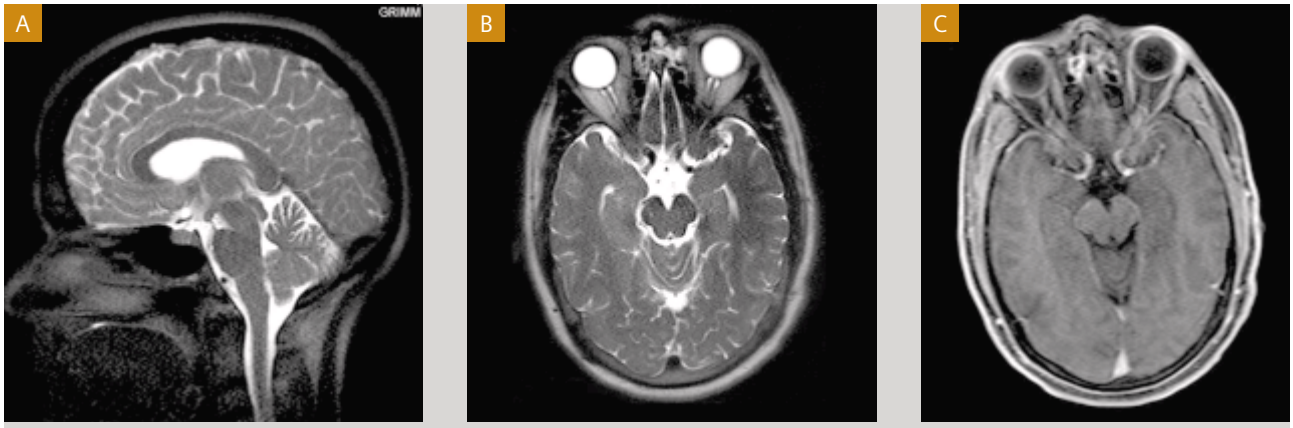

[Figure 5] *Sagittal HASTE (A), axial HASTE (B), and axial VIBE (C) post contrast cranial images.*

Summary

This screening protocol fully utilizes the new Tim technology in order to effectively cover the whole body in less than 10 minutes. Key features include the use of the high-SNR array coils, the Matrix coils, and multiple receiver channels that allow iPAT accelerated sequences. The coils themselves are physically compatible so they may all be placed on the patient and plugged in to the table simultaneously at the beginning of the exam, eliminating the need for coil or patient repositioning. Automatic table motion combined with the physical compatibility allows for rapid transition between anatomical regions.

The sequences used have been demonstrated to be highly effective at detecting systemic metastases as well as a wide variety of other disease processes. In addition, the 3D VIBE can be reformatted in other orientations, particularly when the resolution is near-isotropic. This allows one breath-hold sequence to replace up to three without any loss of information. The short duration of this screening exam makes it a reasonable replacement for similar whole-body screening exams performed under CT. In addition this approach offers both improved safety (radiation and contrast agents) and diagnostic image quality in all regions except possibly in the lungs.

Literature

[1] Semelka RC, Balci NC, de Beeck BO, Reinhold C. Evaluation of a 10-minute Comprehensive MR Imaging Examination of the Upper Abdomen. Radiology 1999; 211: 189–195.
[2] Meaney JF, Ridgway JP, Chakraverty S, et al. Stepping-table gadolinium-enhanced digital subtraction MR angiography of the aorta and lower extremity arteries: preliminary experience. Radiology 1999; 211: 59–67.
[3] Schlemmer HP, Schafer J, Pfannenberg C, et al. Fast whole-body assessment of metastatic disease using a novel magnetic resonance imaging system: initial experiences. Invest Radiol. 2005; 40: 64–71.
[4] Lee VS, Lavelle MT, Rofsky NM, et al. Hepatic MR imaging with a dynamic contrast-enhanced isotropic volumetric interpolated breath-hold examination: feasibility, reproducibility, and technical quality. Radiology 2000; 215: 365–372.
[5] Walker R, Kessar P, Blanchard R, et al. Turbo STIR magnetic resonance imaging as a whole-body screening tool for metastases in patients with breast carcinoma: preliminary clinical experience. J Magn Reson Imaging 2000; 11: 343–350.
[6] Johnson KM, Leavitt GD, Kayser HW. Total-body MR imaging in as little as 18 seconds. Radiology 1997; 202: 262–267.
[7] Barkhausen J, Quick HH, Lauenstein T, et al. Whole-body MR imaging in 30 seconds with real-time true FISP and a continuously rolling table platform: feasibility study. Radiology 2001; 220: 252–256.
[8] Lauenstein TC, Goehde SC, Herborn CU, et al. Three-dimensional volumetric interpolated breath-hold MR imaging for whole-body tumor staging in less than 15 minutes: a feasibility study. AJR Am J Roentgenol. 2002; 179: 445–449.
[9] Lauenstein TC, Goehde SC, Herborn CU, et al. Whole-body MR imaging: evaluation of patients for metastases. Radiology 2004; 233: 139–148.
[10] Bader TR, Semelka RC, Pedro MS, Armao DM, Brown MA, Molina PL. Magnetic resonance imaging of pulmonary parenchymal disease using a modified breath-hold 3D gradient-echo technique: initial observations. J Magn Reson Imaging 2002; 15: 31–38.
[11] Chern MS, Wu MH, Chang CY. CT and MRI for staging of locally advanced non-small cell lung cancer. Lung Cancer. 2003; 42 Suppl 2: S5–8.
[12] Berrington de Gonzalez A, Darby S. Risk of cancer from diagnostic X-rays: estimates for the UK and 14 other countries. Lancet. 2004; 363: 345–351.
[13] Brenner DJ, Elliston CD. Estimated radiation risks potentially associated with full-body CT screening. Radiology. 2004; 232: 735–738.
[14] McKenzie CA, Lim D, Ransil BJ, et al. Shortening MR image acquisition time for volumetric interpolated breath-hold examination with a recently developed parallel imaging reconstruction technique: clinical feasibility. Radiology. 2004; 230: 589–594.
[15] Madore B, Pelc NJ. SMASH and SENSE experimental and numerical comparisons. Magn Reson Med 2001; 45: 1103–1111.
[16] Griswold MA, Jakob PM, Heidemann RM et al. Generalized autocalibrating partially parallel acquisitions (GRAPPA). Magn Reson Med 2002; 47: 1202–1210.

Women's Health

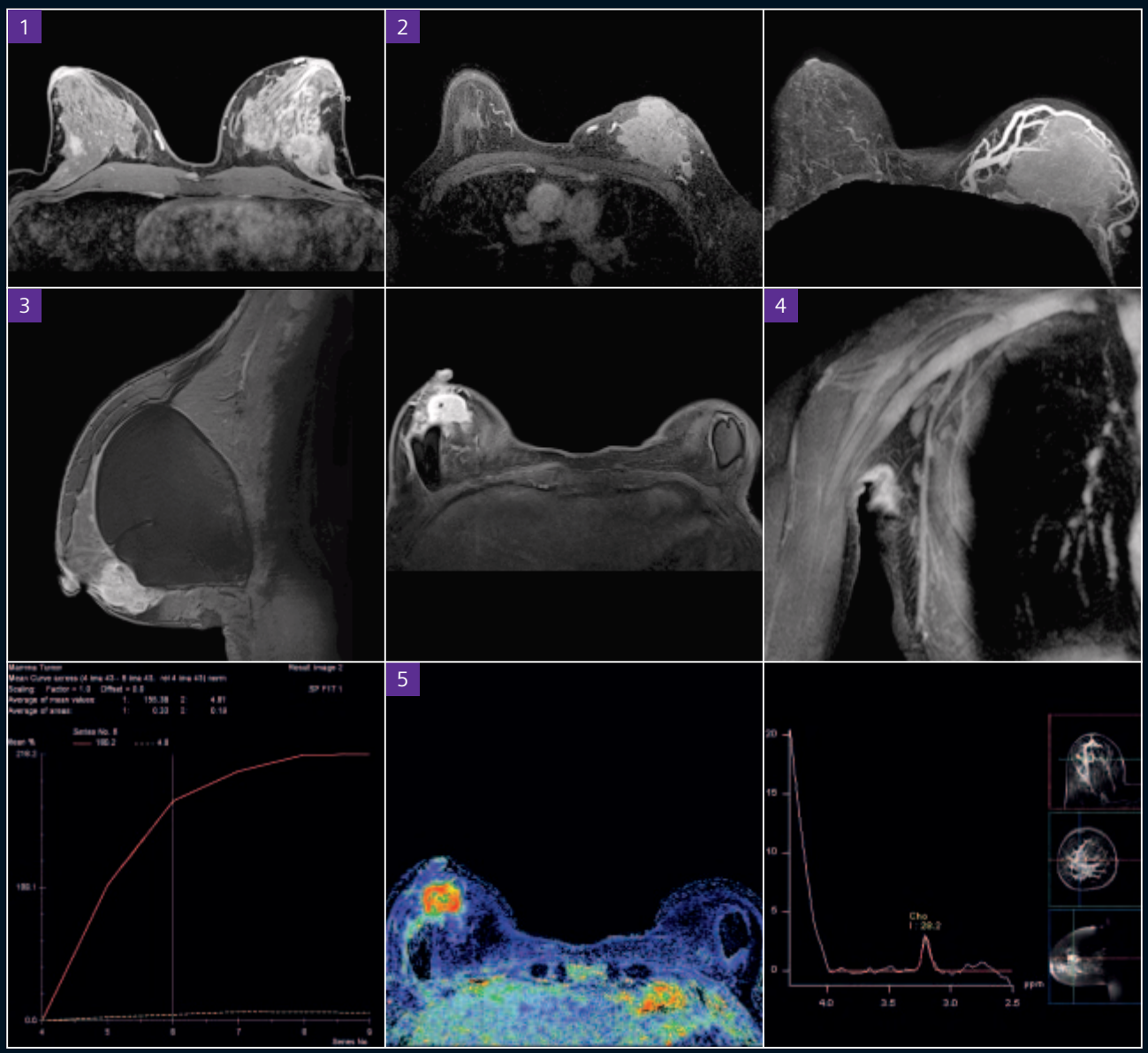

[1] Courtesy of St. Elisabeth, Brussels, Belgium
[2] Courtesy of First Hill Diagnostic Imaging, Seattle, WA, USA
[3, 5] Courtesy of MRI Bremen-Mitte, Bremen, Germany
[4] Courtesy of MRI Bremen-Mitte, Bremen, Germany

High-Resolution Dynamic* Breast MRI Current Capabilities of *syngo* MR MAGNETOM Systems

Helmuth Schultze-Haakh, Ph.D.

MR R&D Collaborations Manager, Siemens Medical Solutions Inc., USA

Introduction

A number of recent journal publications show that MR imaging is increasingly used for breast lesion visualization and breast cancer management. To increase the specificity of breast MR, dynamic exams have become an integral part of standard breast MR examinations. During a dynamic* examination both breasts are imaged multiple times over approximately five minutes as the bolus of contrast* material passes through the breast tissues. Malignant lesions enhance more abruptly and more intensely than normal structures and are thus detected by this exam. Benign lesions can be differentiated from malignant lesions using a combination of morphology and dynamic contrast enhancement characteristics.

MR is acknowledged to be very sensitive, and, as experience levels rise and more sophisticated post-processing tools become available, the accuracy of breast MR is improving as well. It is increasingly evident that breast evaluation for known or suspected cancer lesions should also include the contra-lateral breast to detect subtle, often clinically occult contra-lateral tumors.

Ideally, this exam would not only visualize and evaluate lesions in the breasts, but also detect abnormal lymph nodes in the axillae and surrounding chest. This information can be used to stage the disease process and for treatment decisions.

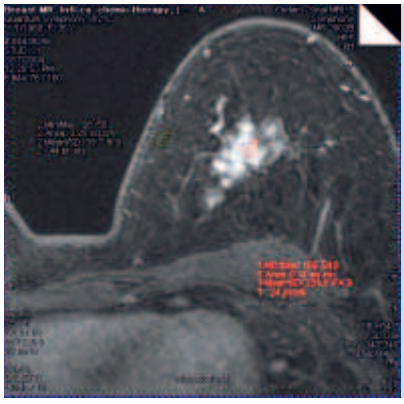

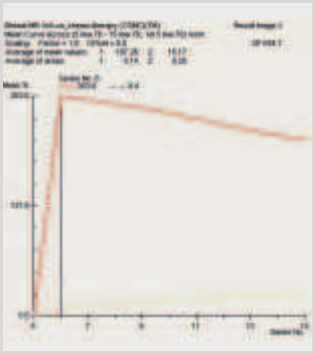

[Figure 1] *Mean Curve evaluation: A portion of a malignant lesion is marked with a red region of interest (ROI). The corresponding curve has a rapid rise followed by a decrease in intensity (wash-out). Characteristically, the maximum value is reached quickly and shows typically an increase of more than 100% compared to the pre-contrast intensity. In comparison normal breast parenchyma enhances, if at all, very little (yellow ROI with corresponding yellow curve). (Courtesy of Ceders-Sinai Medical Center, Los Angeles, CA, USA).*

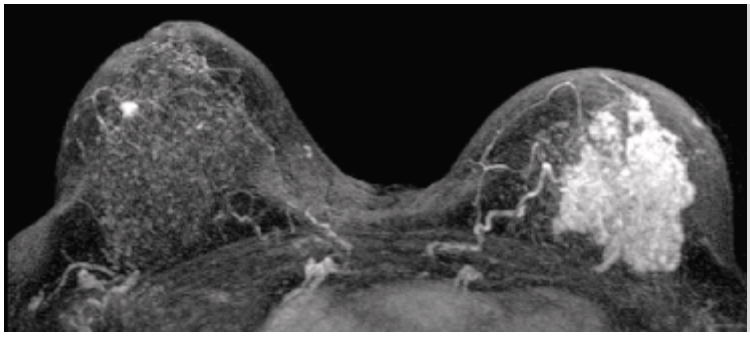

[Figure 2] *Full Maximum Intensity Projection (MIP) image of an unsuspected contra-lateral lesion (bright spot in right breast) of lobular cancer. (Courtesy of First Hill Diagnostic Imaging, Seattle, WA, USA).*

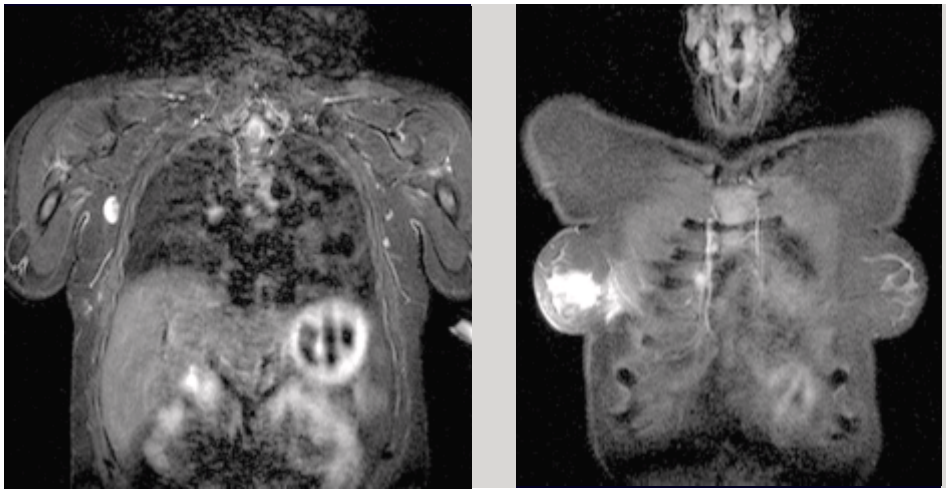

[Figure 3] *Coronal STIR in the body coil. Short TI Inversion Recovery (STIR) suppresses fat and shows high sensitivity to fluid. Abnormal lymph nodes can easily be seen: axillary node on left images, internal mammary node next to the sternum on the right images. Patient had invasive ductal cancer in the right breast. (Courtesy of First Hill Diagnostic Imaging, Seattle, WA, USA).*

Bilateral isotropic dynamic data sets

The controversy over acquisition techniques for breast MRI is subsiding. In the past, there have been disagreements on technique: 2D non-fat saturated vs. fat-suppressed 3D, dynamic vs. high resolution, and bilateral vs. unilateral examinations. The speed of current MR systems and an increase in clinical experience has caused the discussion to diminish to primarily the selection of slice orientation.

The traditional filming orientation in mammography has always focused on medial lateral oblique (MLO) or near sagittal views. This image orientation was adopted early in MR largely due to the similarity with the customary mammographic norm. Even though breast examinations can be done in any orientation, to quickly acquire data in the most anatomically and physiologically appropriate manner Siemens advocates bilateral axial acquisitions with near isotropic voxels. This technique enables the contra-lateral side to be viewed simultaneously with the suspicious or affected breast.

Most current breast MR techniques use bilateral 3D acquisitions with a method for fat suppression, either spectral selective fat-saturation or water-excitation. Modern processors and computer systems can handle the vast amount of image data being produced with dynamic 3D acquisitions, often exceeding 1000 images for a complete dynamic data set.

A 3-dimensional, bilateral, high spatial resolution data set can be acquired with isotropic, or nearly isotropic, sub-millimeter voxels in about 60 seconds. Siemens unique sequence, which produces axial images of both breasts, is called dynaVIEWS – dynamic Volume Imaging with Enhanced Water Signal.

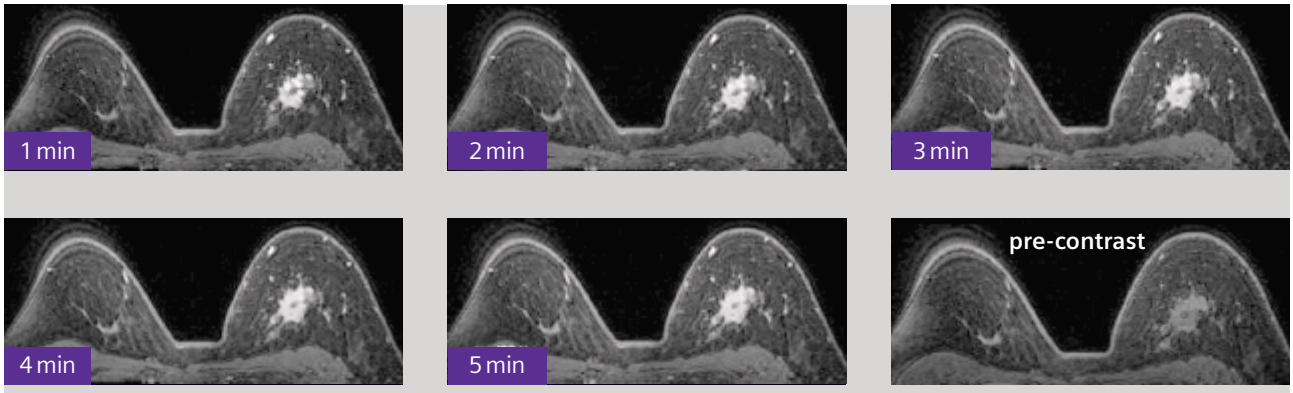

[Figure 4] *DynaVIEWS: High resolution 3D dynamic acquisitions with fat saturation using iPAT factor of 2. Each acquisition lasts 60 seconds. After the pre-contrast run the contrast medium is injected. 5 uninterrupted identical scans follow. (Courtesy of Ceders-Sinai Medical Center, Los Angeles, CA, USA).*

DynaVIEWS protocols

	Maestro Class: VA25				MAGNETOM Avanto: VB11		VB11
Parameter	Ultra gradients	Sprint gradients	Quantum gradients	Sonata gradients	Q	QS	MAGNETOM Espree
TR/TE (ms)	5.09/1.87	4.74/1.71	4.64/1.74	4.30/1.47	4.64/1.65	4.22/1.48	4.62/1.67
partitions	160	160	160	160	160	160	160
Sice thickness (mm)	0.9	0.9	0.9	0.9	0.9	0.9	0.9
FoV (mm)	340	320	320	320	320	320	320
Matrix: pe x rd	309 x 448	331 x 448	341 x 448	349 x 448	349 x 448	354 x 448	323 x 448
Resolution (mm^2)	1.0 x 0.7	1.0 x 0.7	0.9 x 0.7	0.9 x 0.7	0.9 x 0.7	0.9 x 0.7	1.0 x 0.7
Bandwidth (Hz/pxl)	340	320	320	320	320	320	320
Flip angle (degree)	12	12	12	12	10	10	12
iPAT	2 GR	2 GR	2 GR	2 GR	2 GR	2 GR	2 GR
Grad. mode	norm	fast	fast	fast	fast	fast	fast
Slice Resolution (%)	61	61	61	64	63	65	60
Phase Resolution (%)	69	74	76	78	78	79	72
Slice Partial Fourier	6/8	6/8	6/8	6/8	6/8	6/8	6/8
Phase Partial Fourier	6/8	6/8	6/8	6/8	6/8	6/8	6/8
Filter	Elliptical	Elliptical	Elliptical	Elliptical	Elliptical	Elliptical	Elliptical
Phase Oversampling (%)	7	7	7	7	7	7	14
Slice Oversampling (%)	0	0	0	0	0	0	0
Rec FoV (%)	100	100	100	100	100	100	100
Fat-saturation	yes	yes	yes	yes	yes	yes	yes
Orientation	TRA	TRA	TRA	TRA	TRA	TRA	TRA
Phase direction	R>L	R>L	R>L	R>L	R>L	R>L	R>L
Acquisition time (s)	60	60	60	60	60	60	60

Siemens Bilateral Breast Array Coil: BRL, BRR

It allows both breasts to be visualized simultaneously at the same anatomical level and within the same time point of contrast enhancement. Bilateral assessment and symmetry are important for identifying lesions. The combination of excellent gradients and parallel imaging (integrated Parallel Acquisition Techniques – iPAT) yield the fast, near isotropic scans. Due to the isotropy of the voxels, there is no limitation in how the data are viewed. Instead of interpreting the data in the acquisition plane, one can take advantage of the full 3D capability of MR to rotate and reconstruct in any plane or produce MIP (maximum intensity projections) views to easily visualize lesions and their extent.

Traditionally, clinicians have preferred the sagittal orientation. Even though more restrictive in its clinical usefulness, bilateral sagittal image data sets can also be acquired on a Tim (Total Imaging Matrix) based system with high spatial resolution in less than 1.5 minutes (see Fig. 7).
The MAGNETOM Avanto, the first Tim system, the MAGNETOM Espree, the first Open Bore MRI with Tim at 1.5T, and the 3T MAGNETOM Trio, A Tim System can produce such results. The need for sagittal acquisitions is reduced due to the capability of multi-planar reconstructions (MPR) of the dynamic VIEWS data.

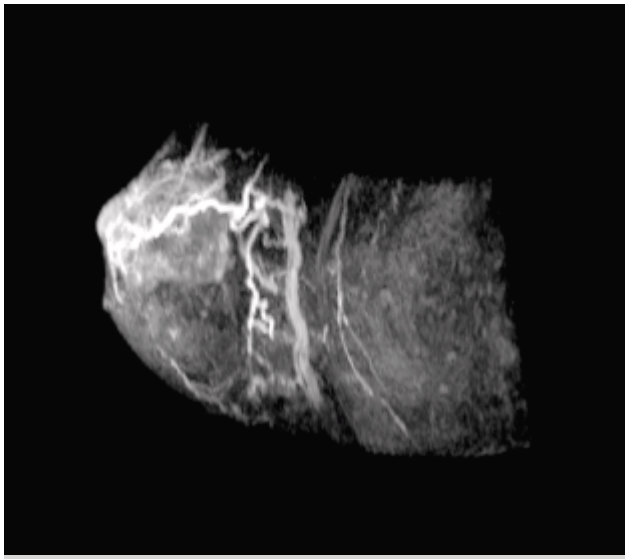

[Figure 5] *3D processing allows the 3D image data to be presented in any orientation: here a full MIP in a medial lateral oblique view similar to a common mammographic view. (Courtesy of First Hill Diagnostic Imaging, Seattle, WA, USA).*

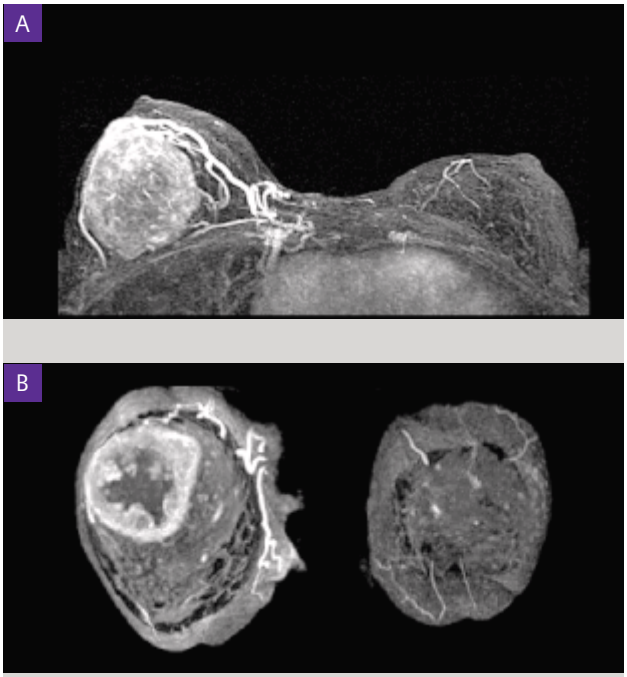

[Figure 6] *(A) Full MIP; (B) Coronal thin MIP from an axially acquired subtracted series (Courtesy of First Hill Diagnostic Imaging, Seattle, WA, USA).*

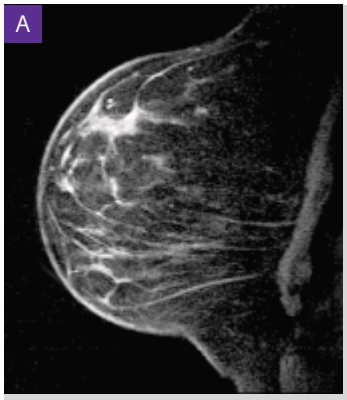

[Figure 7] *Dynamic bilateral sagittal scan: (A) right breast;*

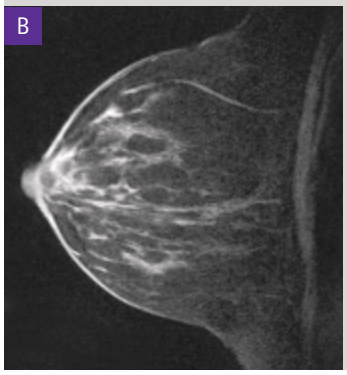

(B) left breast iPAT factor of 2 applied in the slice (3D) direction. (Courtesy of University of California at Los Angles).

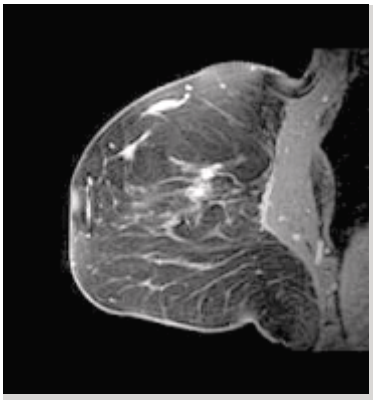

[Figure 8] *sagittal reconstruction (MPR) from an axially acquired delayed VIEWS series. (Courtesy of Ceders-Sinai Medical Center, Los Angeles, CA, USA).*

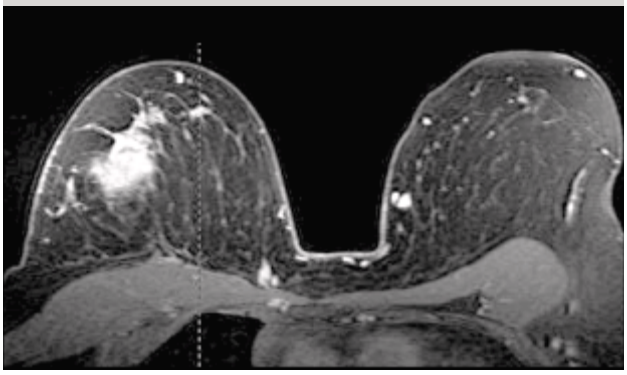

Advanced techiques for DCIS diagnosis

A centrically reordered k-space 3D scan with even higher resolution can follow the dynamic scans to better portray anatomical detail. Whether acquired sagittally or axially, this delayed bilateral high-resolution 3D data set, called delayed VIEWS, may allow the depiction of ductal pathways in their true oblique-radial orientation. Ductal carcinoma in situ (DCIS) is often considered a precursor to breast cancer, and, therefore its early identification may be of substantial clinical importance. During the dynamic acquisition, DCIS, which often lacks the high levels of angiogenesis of invasive cancers, will thus less commonly show the enhancement characteristics associated with malignant tissue. Therefore, the delayed VIEWS series, with high spatial resolution in all directions, when run immediately after the dynamic study, can be used to perform double oblique reconstructions along the ductal pathways demonstrating in an anatomically appropriate way, the extent of DCIS lesions, which may not be seen on regular orthogonal planes.

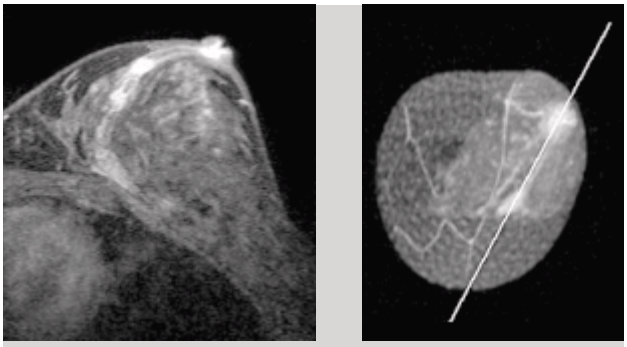

[Figure 9] *RADIANT MIP (Radial MIP imaging around nipple or tumor): Only the high resolution 3D data from a Siemens MAGNETOM allows the uncompromised reconstruction of thin MIPs, a subsection of the volume, to be presented in a double oblique orientation.*

Conclusion

Siemens MAGNETOM systems and software have made breast MR imaging and evaluation, comprehensive, easy-to-use, fast and reliable. Siemens provides an iPAT-compatible circularly polarized (CP or quadrature) breast array coil. Most of the fore mentioned techniques such as DynaVIEWS or delayed VIEWS for bilateral 3D acquisitions with fat suppression incorporate and take advantage of iPAT. The workflow is streamlined by providing immediate subtractions and Maximum Intensity Projections (MIPs) with Inline Processing using fast computers that can handle the large, 3D, isotropic data volumes generated. Color coded tissue intensity maps and dynamic intensity curve evaluations facilitate lesion interpretation.

As the number of breast imaging exams continues to increase, Siemens MR enables you to stay at the forefront of MR technology. But even more important is that Siemens MR simplifies breast imaging so that it seamlessly fits into your exam mix and daily workflow.

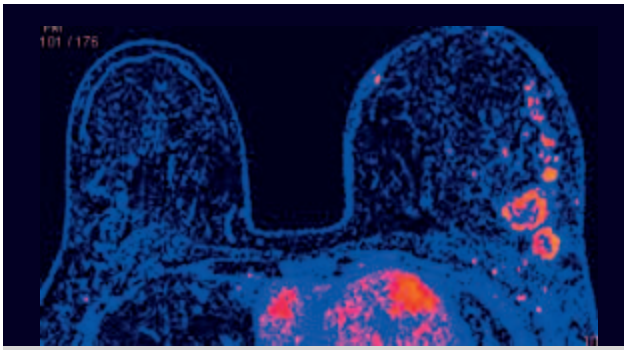

[Figure 10] *Colorized enhancement intensity map from the contrast enhanced dynamic data sets: positive enhancement integral (PEI).*

* This information about this product is preliminary. The product is under development and not commercially available in the US, and its future availability cannot be ensured. This article discusses clinical uses which are not commercially available in the US.

integrated Parallel Acquisition Techniques (iPAT) in Breast MRI*

M.-A. Labaisse M.D.[1], P. Vanhoenacker M.D., E. Kersschot M.D.[2], G. Vandemaele, Ph.D.[3]

[1] *Centre Hospitalier de la Region (CHR) de Tournai, Tournai, Belgium*
[2] *O.L.V. Ziekenhuis, Aalst, Belgium*
[3] *Siemens Medical Solutions, Belgium*

Contrast enhanced* T1 3D-imaging is used routinely in our department in the pre-surgical planning of breast cancer. Covering the whole breast with the 3D volume and following its gadolinium uptake, gives a very sensitive imaging method for detection of lesions. However, in order to improve its specificity, both high spatial and temporal resolution are needed. Several tools have been used to obtain this. We routinely use a rectangular FOV (recFOV), which requires fewer phase-encoding steps to obtain the same resolution and hence reduce measurement time. A major drawback of recFOV in breast MRI is, however, that we need to acquire images in the coronal plane. In the transverse plane the phase encoding needs to be in the left-right direction to prevent heart pulsation artifacts from passing through the breast and as a consequence, no reduction of the FOV can be used.

When using the coronal orientation, we end up with an imaging sequence of the breast with a temporal resolution of 1:26 min, using 64 slices of 2 mm, resulting in a pixel size of 1.5 x 0.8 x 2 mm^3 which has successfully been used for years (TE = 4.8 ms, in phase condition at 1.5T). It leaves us with high quality Multi Planar Reconstructions (MPR) or Maximum Intensity Projections (MIP) of subtracted data, to look at morphology, location and extension of the lesion. Time behavior gives information on the vascularization of the lesion, depicted on

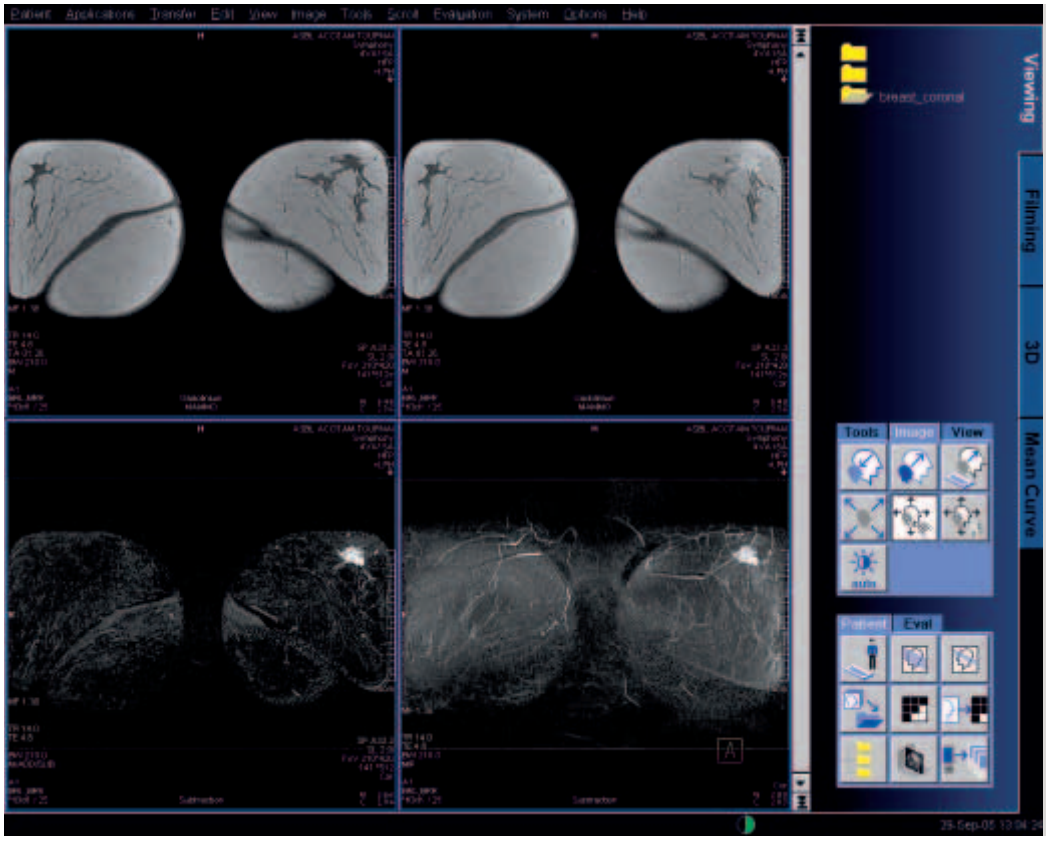

[Figure 1] *T1_fl3d pre- and 3 minutes post contrast in coronal direction using rec-FOV 50%, subtraction and thin MIP of an infiltrating ductal carcinoma.*

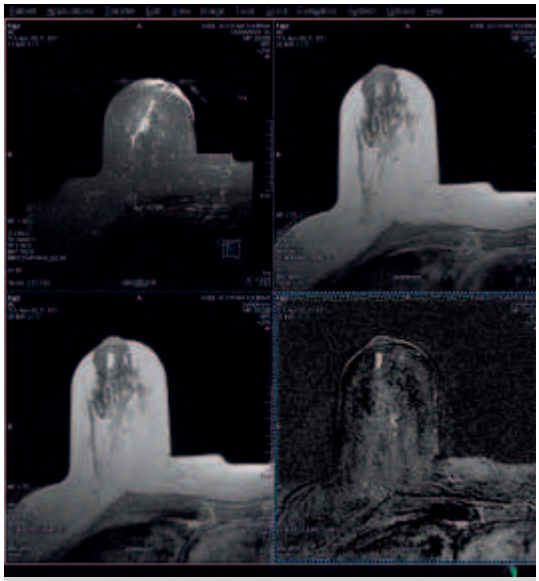

[Figure 2] *Intraductal, retro-arealar papilloma in a woman with nipple discharge: T2_tirm_trans, T1_fl3D_trans pre- and post-gadolinium and subtraction.*

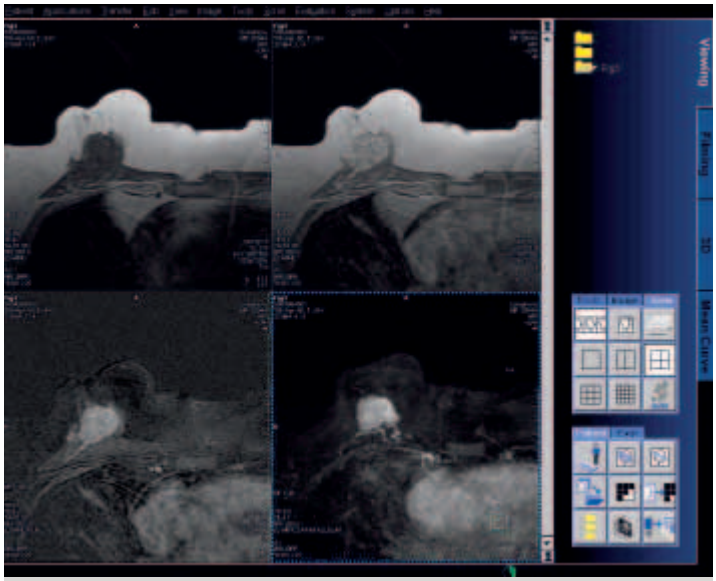

[Figure 3] *Local recurrence of carcinoma with pectoral muscle invasion: T1_fl3D_trans pre- and post-gadolinium, subtraction and thin MIP.*

the wash-in* and wash-out* maps which can be calculated automatically by the system (e.g. Inline Technology).
All the important criteria of the BIRADS scoring system can be evaluated in this way: Morphologic information on form (round – oval – linear – branching), margins (well defined – distinct) and enhancement (homogeneous – inhomogeneous – septated – ring enhancement). In addition, dynamic information concerning the initial (<50%, >100%) and late time behavior (continuous enhancement – step – wash-out) is available. But can we do better than this? Yes, we can.

How iPAT can improve visualization of the entire breast in the axial plane?

Since the introduction of integrated Parallel Acquisition Techniques (iPAT), we have used GRAPPA in order to improve our results. A prerequisite for using GRAPPA is the presence of phased array coils which is fulfilled with the commercially delivered bilateral breast coil. The improvement we see is the possibility to return to the axial orientation, which is similar to the cranio-caudal view of X-ray mammography. The axial plane is better suited than the coronal plane to establish the correlation between the region of enhancement and the conventional mammographic abnormalities found. The axial plane is also a good anatomic plane to explore the breast and the thoracic wall. The trajectory, inflammation, obstruction of the galactic ducts, and lesions in the sub-areolar region (Fig. 2) and the pectoral musculature is much better delineated and evaluated in the axial (and sagittal) plane (Fig. 3). An additional advantage is that we can acquire images extending sufficiently deep into the axillary region to depict the lymph nodes if sufficient RF coverage is present. Advantages of the axial over the sagittal orientation are the possibility to reduce the number of partitions, the capability to compare the left and right breast (as both are present in the image), and the certainty that the identification of left or right breast is correct, which is not straightforward in sagittal datasets. Using rectangular FOV in the coronal plane is now substituted by GRAPPA (iPAT2) imaging in the transverse plane. We obtain a resolution of typically 1.0 x 1.1 x 1.5 mm^3, TE = 4.8 ms (in phase), giving us MPR and MIP reconstructions which reveal great detail. Temporal resolution with these parameter settings is kept just under 1 min for 88 partitions (Fig. 4).

How iPAT can improve spatial resolution in the 3 orientations?

Suppression of fat can improve the in-plane resolution of these data. Fat suppression or water excitation pulses give us the chance of using a smaller TE. As the fat signal is no longer present and cannot oppose the enhanced water signal anymore, we can use the out of phase condition with TE< 4.8 ms and we can shorten TR, which shortens overall acquisition time. This is what is being used in VIEWS (Volume Imaging with Enhanced Water Signal) to obtain high isotropic resolution (160 partitions, spatial resolutions of 0.9 x 0.8 x 0.9 mm^3,

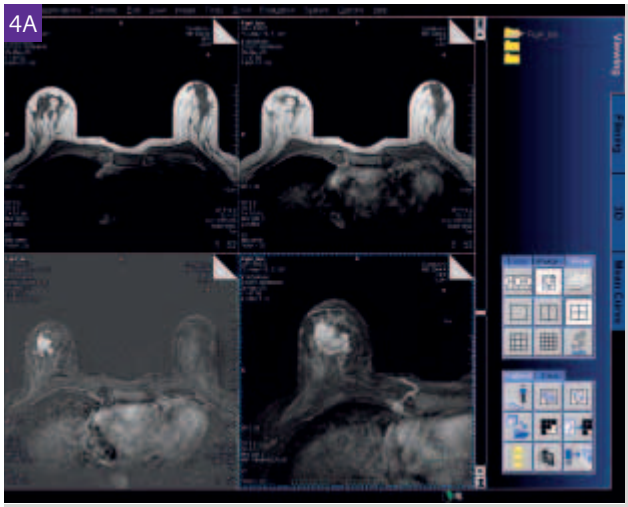

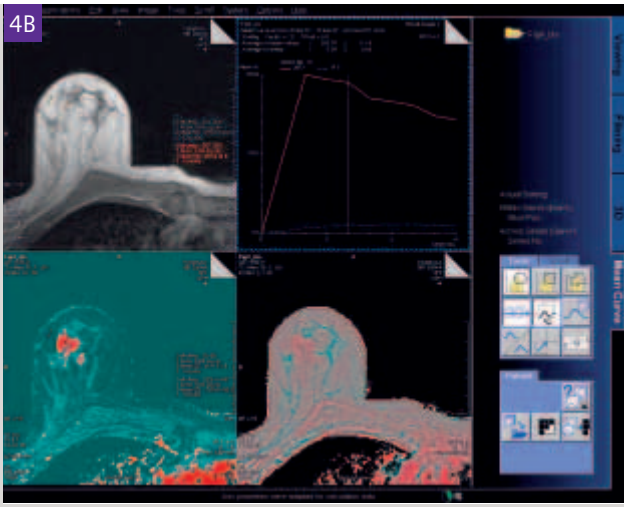

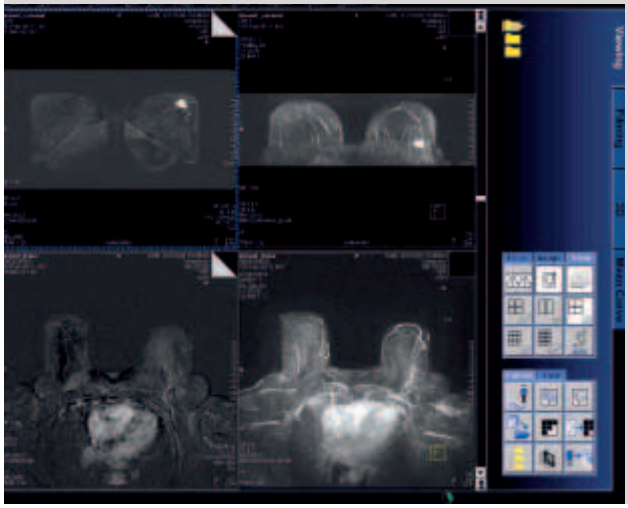

[Figure 4A] *Invasive ductal carcinoma: T1_fl3D_trans pre- and post- gadolinium, subtraction and thin MIP.*

[Figure 4B] *Mean Curve evaluation on wash-in and wash-out maps on the lesion and the fat.*

Comparison of the measured dataset and the MIPs of the subtraction dataset of the same patient imaged in 2003 before surgery, not using iPAT and working in the coronal plane and on follow up after surgery (2004), imaged in the transverse plane using iPAT. Note the improved visualization of the pectoral and axillary region.

acquisition time of 4 min) (Fig. 5). When using iPAT, this high resolution imaging can be used for dynamic scanning every minute (0.9 x 0.6 x 1.2 mm^3) (Fig. 6C, D). A drawback of VIEWS is the absence of fat signal. We are convinced that the presence of fat signal in non fat-suppressed images gives us very valuable information on morphology (intra-pectoral layers and lymph nodes). An additional disadvantage is that sequences acquired with water excitation pulses result in hyper-intense glandular tissue on pre-gadolinium images. The result is less inherent contrast with the post-gadolinium early enhancing lesions.

How can iPAT improve the temporal resolution?

iPAT can help us improve the temporal resolution without losing sensitivity of the MR exam, as we are still able to cover both breasts simultaneously with an acceptable spatial resolution.

When using GRAPPA in combination with a rectangular FOV in the coronal plane, we are able to image the entire breast in a timeframe of 5 sec. We obtain a voxel size of 1.9 x 1.3 x 3.5 mm^3 with a temporal resolution of 5 s using 3D VIBE. Early wash-in of lesions is observed 15 to 30 s post-gadolinium injection (Fig. 7). Gadolinium uptake is further followed and documented during the first 2 minutes post injection.

We are aware that by using this technique, we lose all detail in spatial resolution, earlier discussed. That is why we choose to combine both methods. We use a pre-gadolinium high spatial resolution scan, followed by the VIBE high temporal resolution scan during injection. We follow signal enhancement with VIBE for 2 minutes, immediately followed by the high spatial resolution scans at later time points. Important is that we catch the 3 minute signal in high spatial resolution data, in order not to lose the information on morphologic detail. For this purpose, we use a non-fatsat fl3D_trans of

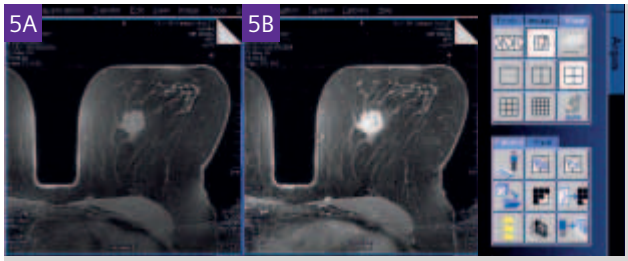

[Figure 5A, B] *Pre- and 3 min post-gadolinium scan with a resolution of 0.9 x 0.8 x 0.9 mm³.*

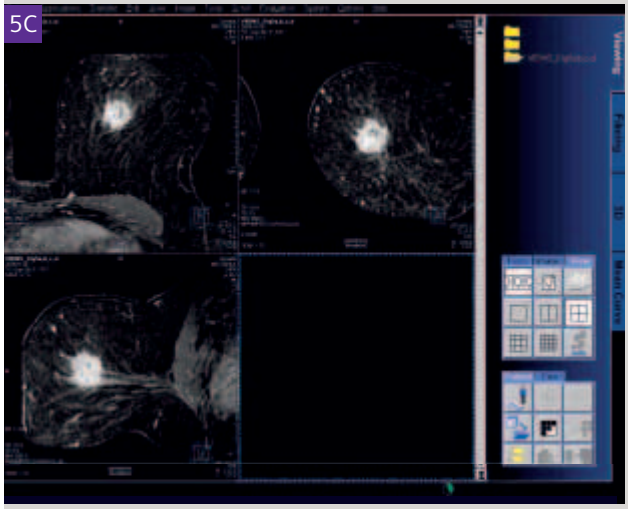

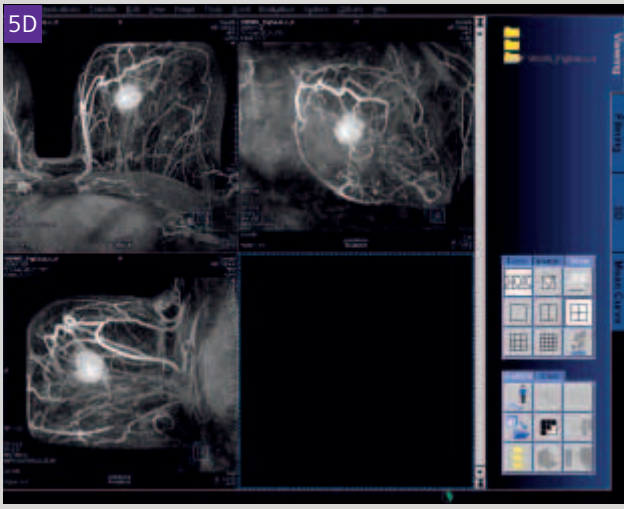

[Figure 5C, D] *This high isotropic resolution is ideal for MIP and/or MPR reconstructions.*

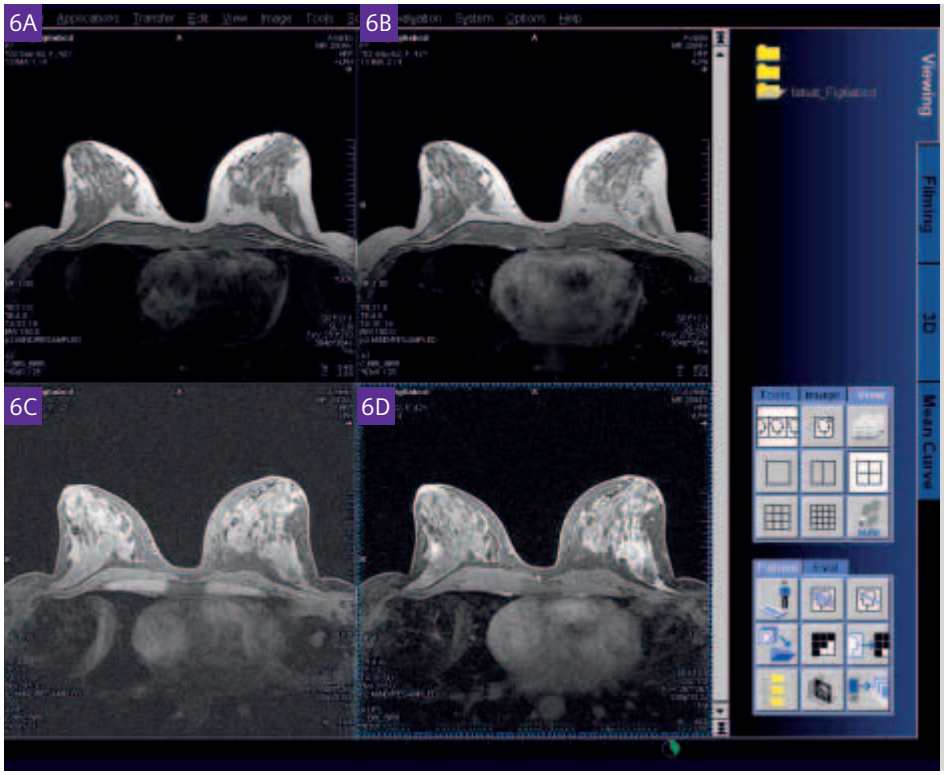

[Figure 6] *Dynamic 1 minute scans with and without fat suppression. (Fig. A, B) Show the fl3d_trans, using iPAT, 0.9 x 0.9 x 2.0 mm³ resolution, 64 slices in 1:19 min. Fig. C, D: Show the VIEWS sequence, using iPAT, 0.9 x 0.6 x 1.2 mm³ resolution, 88 slices in 1 min. We compared the pre-gadolinium and the late enhanced 6 minute scan on the same patient. Note the hyper-intense glandular tissue in the fatsat scans (disadvantage of this technique).*

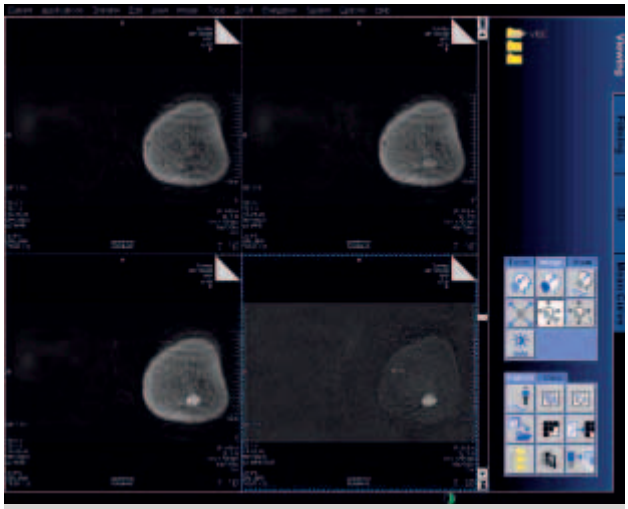

[Figure 7] *Dynamic 5 s scans using VIBE. Pre-gadolinium, 15 s post- and 30 s post-gadolinium scan plus thin MIP on the lesion patient. In plane resolution of 1.9 x 1.3 x 3.5 mm^3, coronal orientation, use of iPAT2 and recFOV 50%.*

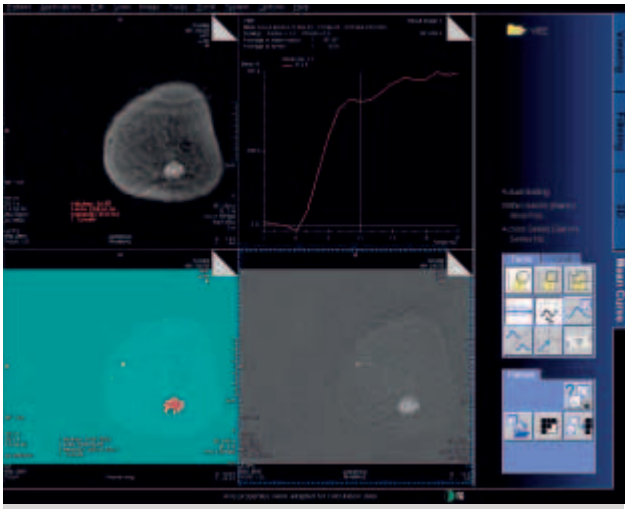

[Figure 8] *Mean Curve evaluation on the VIBE dataset, following Gadolinium uptake with 25 scans of 5 s, in total 2 min after Gadolinium injection. ROI is placed on the wash-in map.*

2:46 min with an in plane resolution of 1 mm x 0.8 mm and 64 slices of 2.5 to 3 mm. We measure in the coronal plane to compare with the VIBE images. As a recFOV of 50% is used, no iPAT is applied. The VIBE gives us information on early wash-in, 3 minutes and later scans on the wash-out behavior and morphologic detail is looked at in the high spatial subtraction dataset.

The only disadvantage at this moment is that both datasets cannot be plotted on the same time graph as they have different spatial and temporal resolution. Mean Curve evaluation doesn't accept the complete measured data in one plot. Results on the eventual improvement of specificity due to the information provided by the contrast enhancement behavior are still under study.

Conclusion

Use of iPAT largely improved the quality of our contrast enhanced MR imaging of the breast. Datasets are now combining the axial plane with the high spatial resolution VIEWS technique, revealing high morphologic detail. Combination with the VIBE technique for evaluation of the time behavior of contrast enhancement, with high temporal resolution, and covering the entire breast, is feasible now. This results in high diagnostic sensitivity – thanks to the high resolution – and higher specificity thanks to the dynamic information.

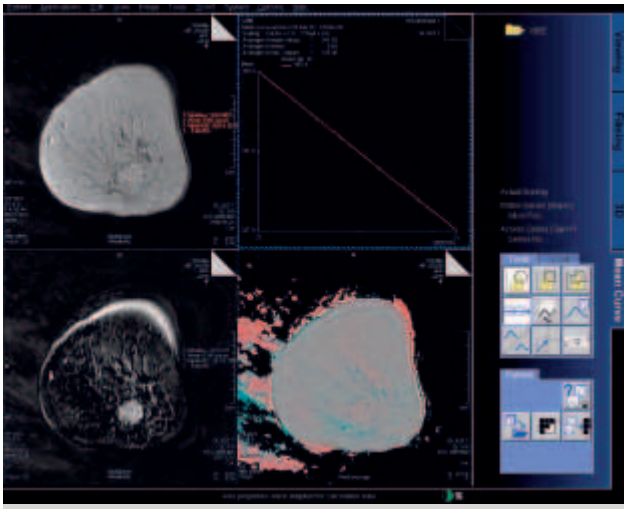

[Figure 9] *Mean Curve evaluation on the high resolution FLASH 3D-scan, 1.0 x 0.8 x 3 mm^3 resolution, acquisition time 2:46 min, done at 3 minutes and 6 minutes post Gadolinium. ROI was placed on the subtraction (3 min post-pre) or can be set on the wash-out map. A clear wash-out is detected in this patient at later times. Absolute enhancement of 355 (arbitrary units) reflects a 265% relative enhancement compared to the pre-gadolinium high resolution scan.*

* This information about this product is preliminary. The product is under development and not commercially available in the US, and its future availability cannot be ensured. This article discusses clinical uses which are not commercially available in the US.

Combination of a Large Loop Flex Coil with the Breast Coil Improves Evaluation of the Lymph Nodes in the Axiliary and Pectoral Region*

A.P. Schillings M.D., M. Bilterijs M.D.[1], Greta Vandemaele, Ph.D.[2]

[1]*Clinique St Pierre, Ottignies, Belgium*
[2]*Siemens Medical Solutions, Belgium*

Purpose

At present, we do not have efficient methods to detect the infiltration of axillary lymph nodes in pre-surgery planning of breast cancer. Consequently, even in the case of very small breast tumors, it is necessary to explore the axilla during surgery and to remove at least the sentinel lymph node i.e. the first draining lymph node next to the tumor. Pre-operative MR scans can give us interesting information on the status of the lymph nodes. During MR exams we study the dimension of the nodes, their morphology (looking for asymmetric cortical thickening), we study the intensity of the Gadolinium uptake or calculate the ADC (Apparent Diffusion Coefficient) in diffusion imaging. There is a lot to gain from the use of more specific contrast agents too. Nevertheless, a prerequisite for evaluation is good image quality and sufficient signal-to-noise ratio (S/N) in the axillary region.

In order to improve S/N in the axilla, we use 2 Large Loop Flex coils (LLF) in combination with the Breast coil (Fig. 1A). These exams were done on our MAGNETOM Harmony 1.0T – Maestro Class platform. Putting the loop coils centric around the 2 openings of the breast coil extends the useful RF-coverage far beyond the axilla and improves the signal at the border of the breast coil with at least 200% at 1.0T (Fig. 1B). Although low field systems might benefit more from this S/N gain, high field exams also produce better image quality as shown in Fig. 2 on MAGNETOM Avanto (left axilla with, right axilla without LL Flex Coil).

[Figure 1A] *Coil setup*

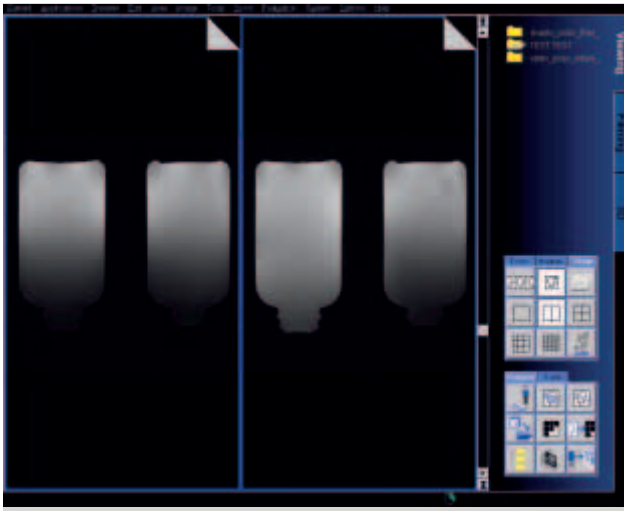

[Figure 1B] *Phantom measurements without (left) and with (right) a Large Loop Flex coil around the right breast. We see a significant gain in signal and a homogeneous RF- distribution in the transverse plane.*

Result

Use of the Large Loop Flex coils in combination with the Breast coil improves S/N in the axillary region. Image quality stays homogeneous over the whole breast. Flow artifacts from the heart can increase.

The morphology of the Gadolinium enhanced lymph nodes can be evaluated better with thin MIPs as well as in the axil-

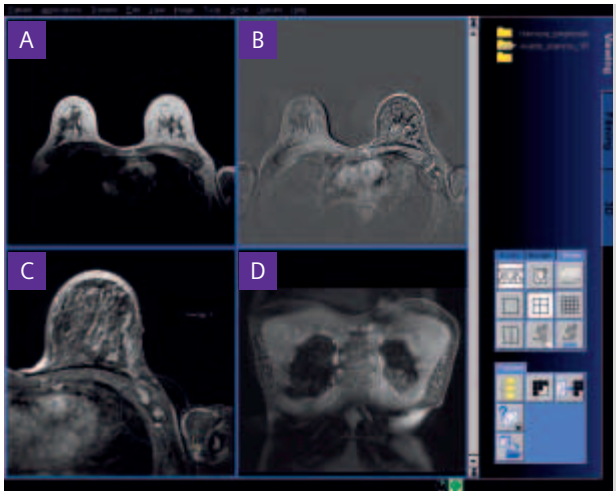

[Figure 2]
A Post-Gadolinium T1 fl3D_trans, showing deep RF penetration for the left axilla and the left breast where the Large Loop Flex coil was used.
B Subtraction image, revealing a lymph node.
C MIP on the lymph node.
D Late enhanced (>7 min) T1fl3D fatsat in the coronal plane.
(1.5T MAGNETOM Avanto. Courtesy of Dr. M.F. Billemont, Cliniques d'Europe Uccle, Belgium.)

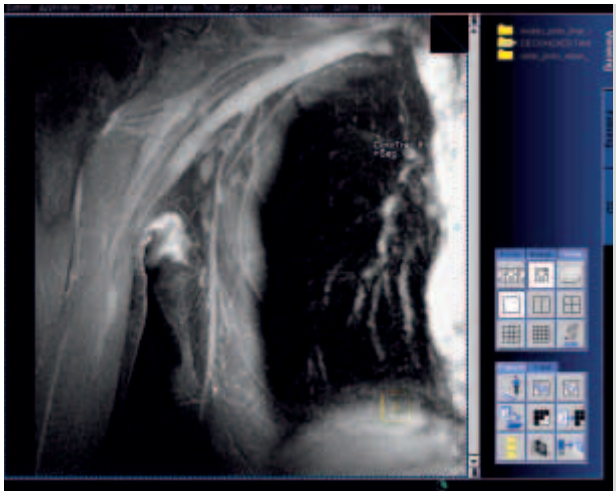

[Figure 3] *T1_fl3D_cor_fatsat 7 minutes after injection. (1.5T MAGNETOM Sonata. Courtesy of Dr. Kersschot, OLV Aalst, Belgium.)*

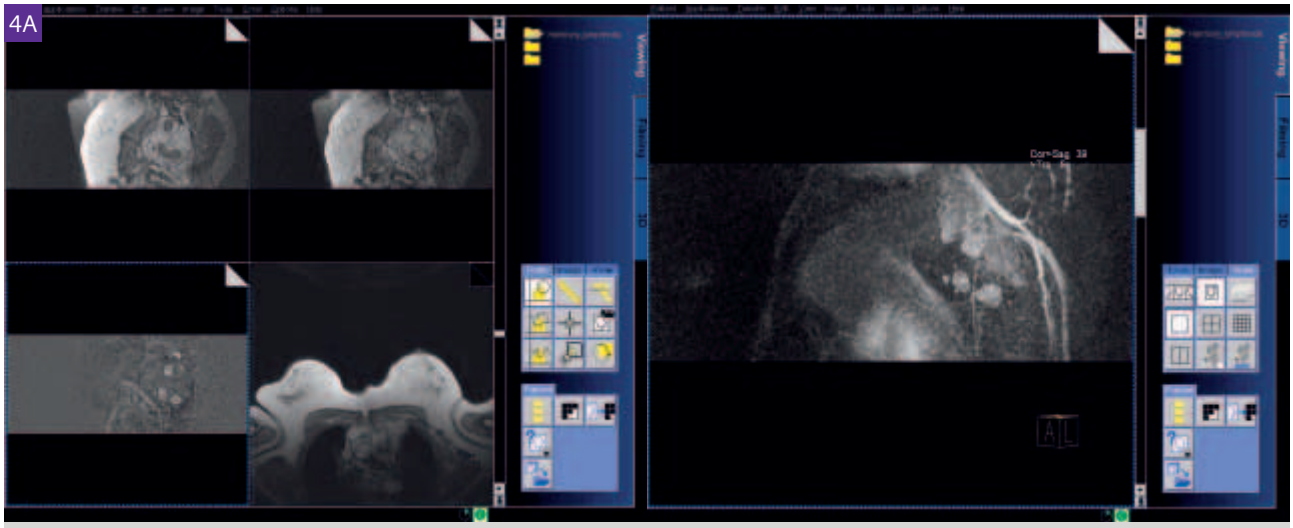

[Figure 4A] *Pre- and 3 minute post-Gadolinium images plus thin MIP of the subtraction dataset showing pathologic lymph nodes.*

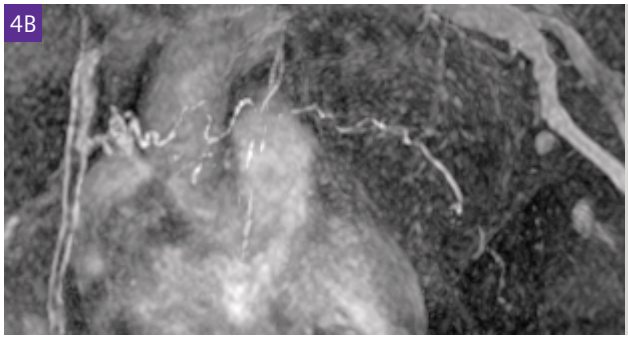

[Figure 4B] *Thin MIP of a subtraction dataset showing normal lymph nodes. (1T MAGNETOM Harmony. Courtesy of Dr. Schillings, Ottignies, Belgium.)*

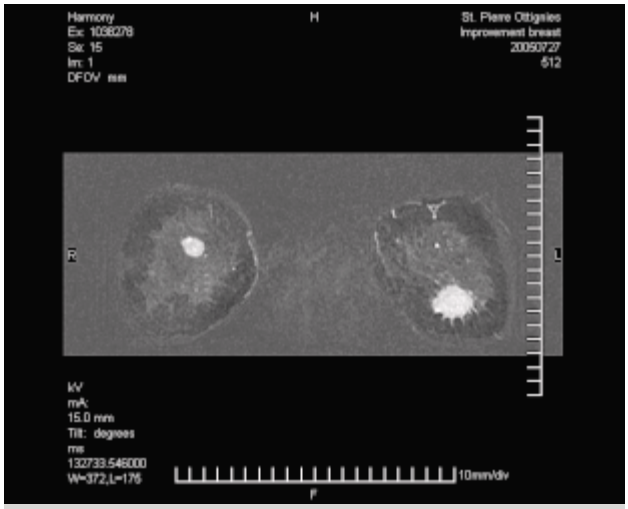

[Figure 5] *Subtraction image (3 min post – pre Gadolinium), showing a benign fibroadenoma in the right breast and a cancer in the left breast with great detail.*

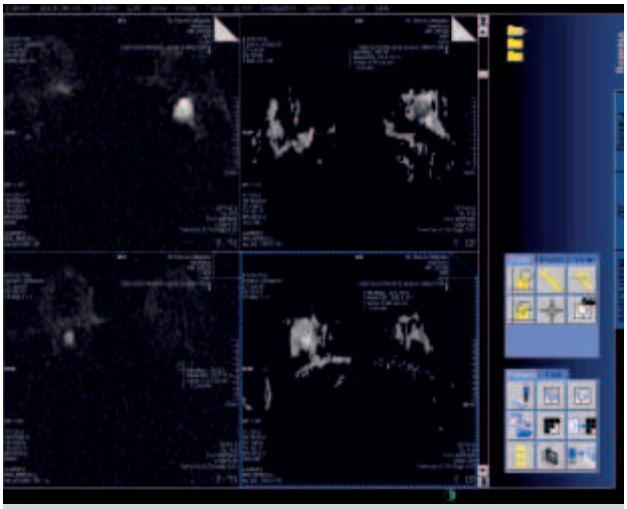

[Figure 6] *Diffusion imaging in the same patient as Fig. 5. Both fibroadenoma and cancer appear hyperintense on b 1000 images. ADC <1.0 x 10^{-3} mm^2/s for the cancer (left breast), ADC >2.0 x 10^{-3} mm^2/s for the fibroadenoma (right breast). (MAGNETOM Harmony 1T. Courtesy of Dr. Schillings, Ottignies, Belgium.)*

lary region as in the interpectoral Rotter space and in the internal mammary chain.

A normal lymph node contains a fatty hilus, depicted as a hyper-intense center in the pre-Gadolinium scan, differentiating a lymph node from a small lesion (Fig. 4B). Detection of this fat-containing part in a small lesion needs high resolution scans with sufficient S/N. Preservation of this zone after Gadolinium administration is finally depicted as a hypointense center in subtraction images. Note that preservation of this center part does not exclude a partial affection of the lymph node, it is just indicating we are looking at an intramammary lymph node and not at a small lesion.

Improved S/N makes it possible to start using diffusion imaging in search of affected lymph nodes. Lymph nodes to be examined more carefully are hyperintense on the diffusion weighted images (b-value of 800 to 1000) and have a reduced ADC coefficient (<1.0 x 10^{-3} mm^2/s)

The use of Large Loop Flex coils in combination with the breast coil improves the spatial resolution for exploring the axilla. This improvement is also visible in the breast itself (Fig. 5), where due to higher S/N a higher resolution can be used. The RF signal is homogeneously distributed throughout the breast, although heart-related flow artifacts might become more pronounced.

Conclusion

Combination of breast coil and Large Loop Flex coils largely improves S/N and consequently the use of high resolution and diffusion imaging in the axilla and the pectoral region, as well as in the breast.

* This article discusses clinical uses which are not commercially available in the US.

^{1}H MR Spectroscopy* of the Breast at 1.5T and at 3T

Nouha Salibi, Ph.D.[1], Marianne Vorbuchner[2], Jan Ruff, Ph.D.[2]

[1]*Siemens Medical Solutions, R&D Collaborations, Malvern, USA.*
[2]*Siemens Medical Solutions, MREA, Erlangen, Germany.*

Introduction

Over the years numerous studies have evaluated the use of MR in the characterization of breast lesions and in monitoring tumor response to treatment. The results have shown that although MR imaging and dynamic contrast-enhanced MRI have high sensitivity and can be helpful in differentiating benign from malignant tumors, they are not perfect predictors; and additional diagnostic criteria are needed to help clarify equivocal MRI results [1–2]. Combining in vivo MR spectroscopy (MRS) with contrast-enhanced MRI increases the specificity of breast MRI due to the additional biochemical information obtained with MRS. MR spectroscopy has been performed in the breast with 1H (proton) as well as with other nuclei including phosphorus (^{31}P), carbon (^{13}C) and fluorine (^{19}F), which is used for studies of drug metabolism namely 5-fluorouracil (5-FU). 1H MRS has practical advantages over MRS with other nuclei: It has the highest sensitivity and can be performed at the end of an imaging exam without patient or coil repositioning. ^{1}H MRS does not require additional hardware and can be readily incorporated into routine clinical breast MRI examinations.

^{1}H MRS of the breast

A typical ^{1}H spectrum of breast tissue consists of large lipid and water signals (F. 1). Historically the Choline peak seen at 3.2 ppm was originally attributed to malignant tumors (F. 2, 3, 5 and 6) in studies performed at 1.5T. However, small choline signals have been detected in benign lesions and in normal breast tissue at higher field strength. Choline has

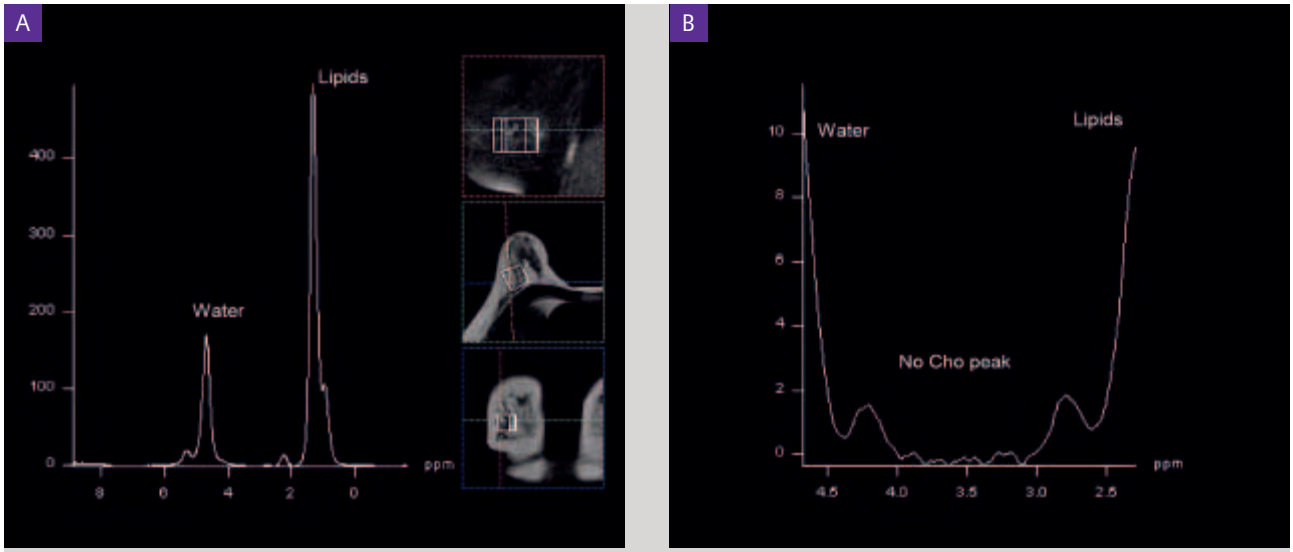

[Figure 1] *Single voxel spectra from healthy breast tissue acquired on a 1.5T MAGNETOM Avanto with TR = 1500 ms, TE= 135 ms, and a voxel size of 8 cm^3. Spectrum A shows the non suppressed water and lipid signals acquired with 8 averages in 12 s. Spectrum B was acquired with 128 averages in 3:12 min, with suppression of the lipid and water signals. It shows a flat range between the residual water and lipid peaks. No choline peak is seen at 3.2 ppm. (Courtesy of Linda Moy, M.D. and Vivian Lee, M.D., Ph.D., New York University School of Medicine, New York, USA.)*

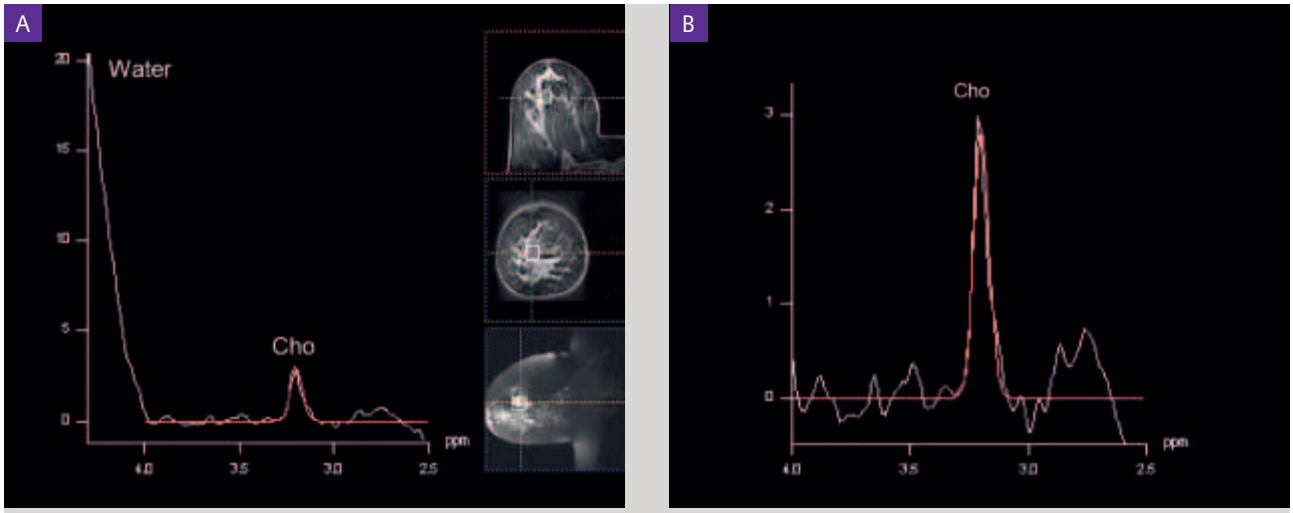

[Figure 2] *SVS Spectra from a biopsy proven adenocarcinoma acquired on a MAGNETOM Trio, A Tim System, with TR = 2000 ms, TE = 135 ms, 64 averages, 2:56 min and a voxel size of 6.8 cm³. They were measured with lipid suppression and weak water suppression, which leaves a residual water peak for reference. Spectrum A displays part of the residual water signal along with the choline peak. Spectrum B is an enlarged view of the choline peak seen in A. (Courtesy of Linda Moy, M.D. and Vivian Lee, M.D., Ph.D., New York University School of Medicine New York, USA.)*

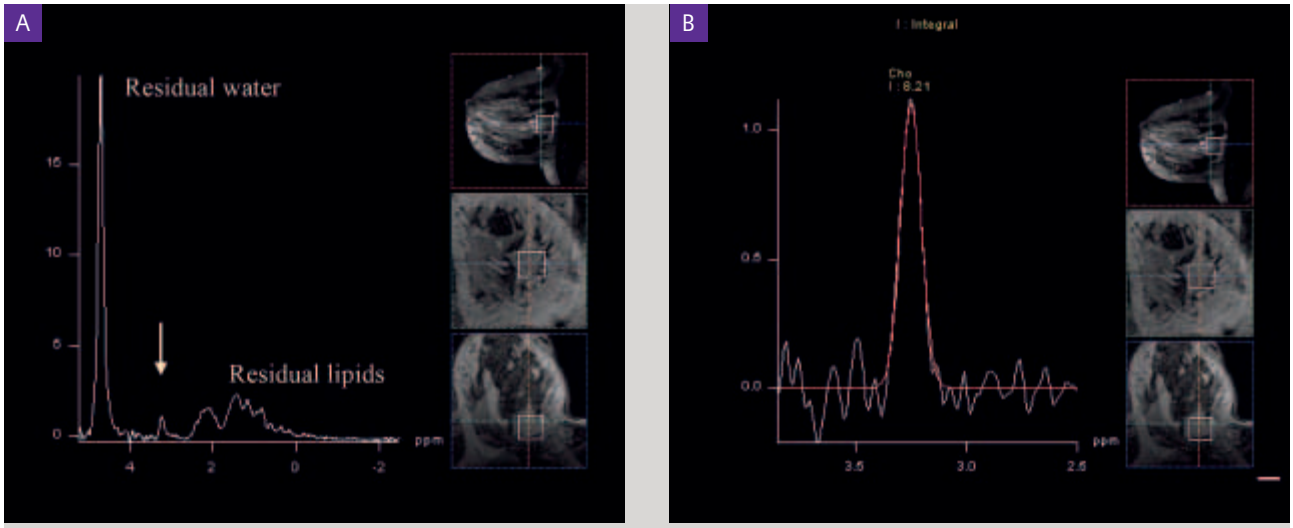

[Figure 3] *SVS spectra showing the choline peak from a biopsy proven high grade malignant tumor acquired in 3:12 min on the MAGNETOM Symphony with lipid suppression and weak water suppression, which leaves a residual water peak for reference. (TR = 1500 ms, TE = 135 ms, 128 averages, voxel size = 8 cm³). Spectrum A shows a suppressed lipid signal, the residual water peak and the choline peak (arrow). Spectrum B displays the rescaled choline peak. (Courtesy of Linda Moy, M.D. and Vivian Lee, M.D., Ph.D., New York University School of Medicine, New York, USA.)*

also been seen in lactating breast spectra along with the characteristic lactose signal [3] (Fig. 4).

Detection of a small choline peak in the presence of large lipid signals presents a technical challenge because lipid sidebands may interfere with the choline peak at 3.2 ppm. Breast 1H MRS on the MAGNETOM systems uses a special single voxel spectroscopy (SVS) spin echo sequence* with spectral lipid suppression, which reduces the effect of lipid on the choline signal. The weak water suppression option leaves a residual water peak that serves as a reference. The sequence also includes averaging of phase and frequency corrected signals, which minimizes signal loss from breathing motion.

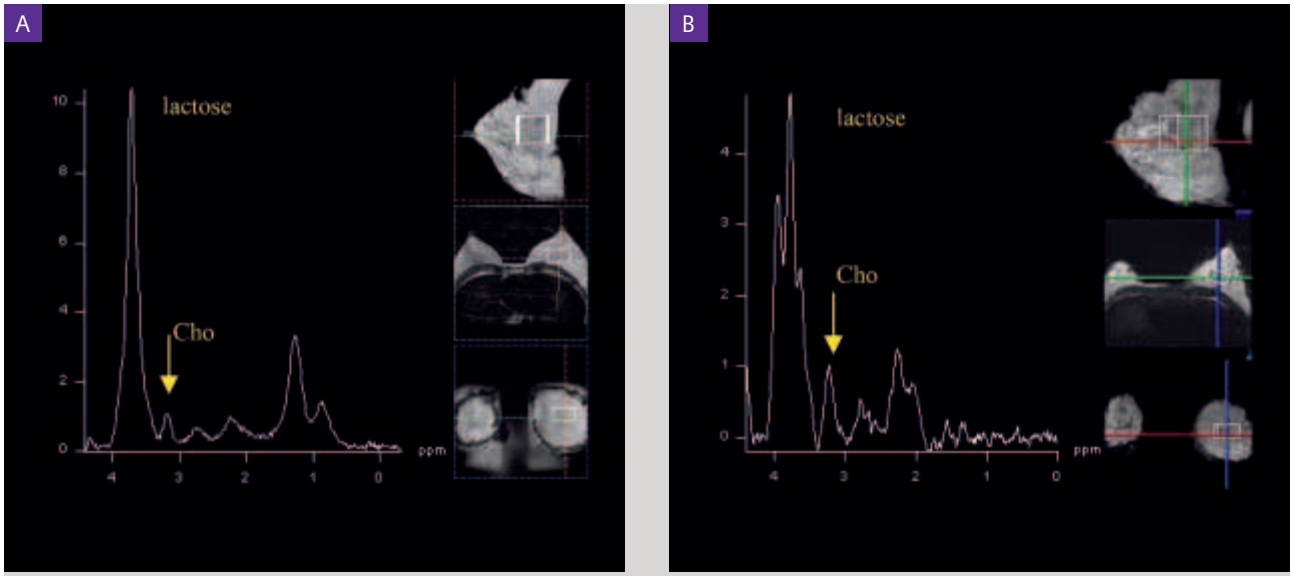

[Figure 4] *Single voxel spectra from a healthy lactating breast. The spectrum in A was acquired on a 1.5T MAGNETOM Avanto from a 17 cm³ voxel with TE = 135 ms and TR = 1500 ms, in 3:12 min. The spectrum in B was acquired on a 3T MAGNETOM Trio, A Tim System from a 10 cm³ voxel with TR = 1500 ms and TE = 135 ms in 1:16 min. The multiple lactose peaks are better resolved in spectrum B. Both spectra were acquired with lipid and weak water suppression. Peaks between 0 and 2.8 ppm are residual lipid signals. (Courtesy of Linda Moy, M.D. and Vivian Lee, M.D., Ph.D., New York University School of Medicine, New York, USA.)*

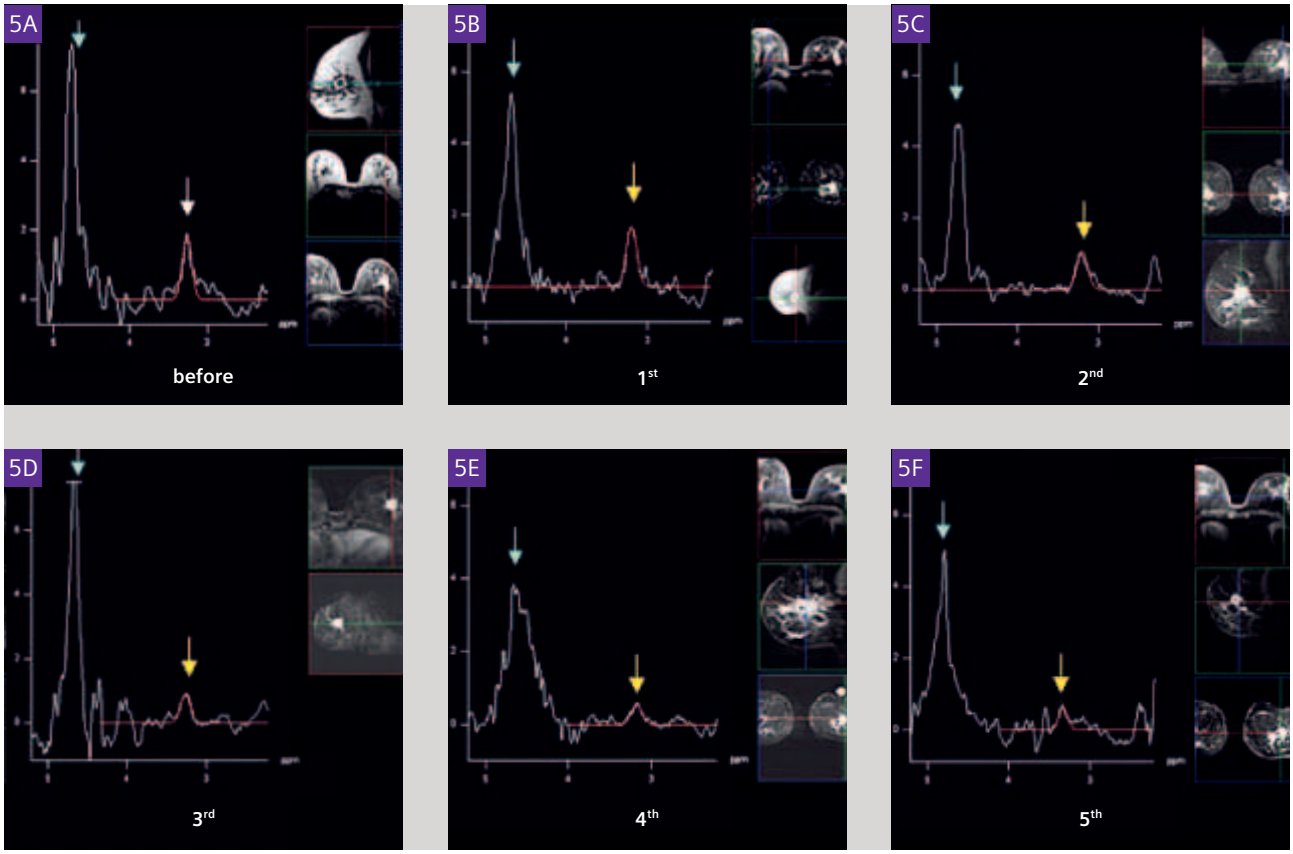

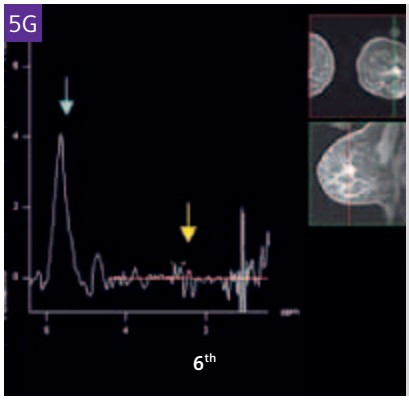

[Figure 5] *Spectra from follow up examinations of an invasive breast carcinoma treated with chemotherapy. The spectra were measured following each of the 6 cycle treatment. They were acquired on a 1.5 T MAGNETOM Sonata with TR = 1500 ms, TE = 135 ms, in 3 to 5 minutes depending on the voxel size, which was adjusted to the size of the tumor, and varied from (18 x 11 x 14) mm^3 to (10 x 10 x 10) mm^3. All spectra display a residual water peak at 4.7 ppm (green arrow) and a choline peak at 3.2 ppm (yellow arrow). Spectrum A (on page 96) shows the choline peak prior to chemotherapy. Spectra B, C, D, E, F and G were measured following cycles 1, 2, 3, 4, 5 and 6 respectively. A reduction in choline is clearly seen following the second, third and fourth, fifth and sixth cycles. The reduction in choline was accompanied by a reduction of the tumor size. (Courtesy of Professor T. J. Vogl, University of Frankfurt / Main, Germany.)*

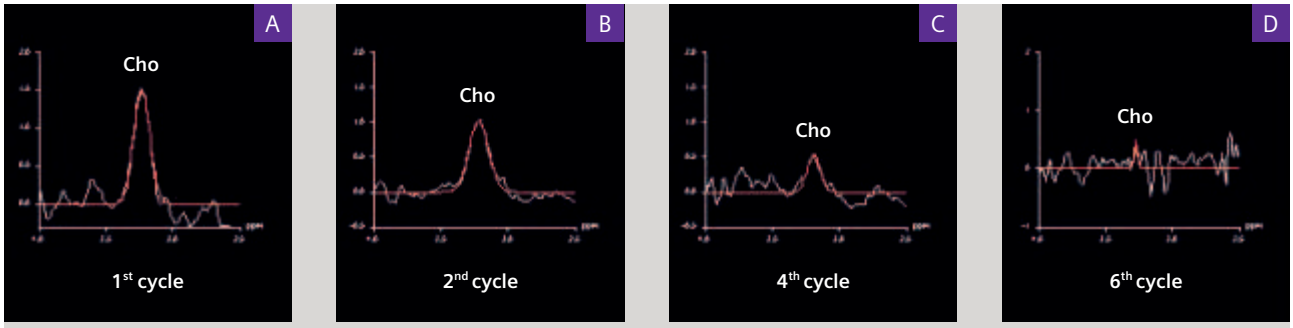

[Figure 6] *Selected spectra from the follow-up examinations described in Fig. 5, showing a reduced choline peak after the second, fourth and sixth cycle.*

Breast ^{1}H MRS: Monitoring response to chemotherapy

Figures 5 and 6 illustrate the use of MR spectroscopy in monitoring the effect of chemotherapy on a diagnosed invasive breast carcinoma†. Spectra were acquired following each of the 6 cycle treatment. They demonstrate a gradual reduction in the choline peak, which is hardly visible after the sixth cycle of chemotherapy. Using the Phoenix functionality of the *syngo* software the same measurement protocol was recalled for each follow-up examination. This insured that the same parameters were used for all measurements except for the voxel size, which was adjusted to the reduced size of the tumor.

† Courtesy of Professor T. J. Vogl, University of Frankfurt/Main, Germany.

Conclusion

The results presented here show that the technical challenges that hindered applications of ^{1}H MRS to breast tumor characterization are now being overcome with improved hardware and software. Developments that improve detection of small signals, such as choline in ^{1}H MRS breast applications, include the availability of higher field strength scanners and of special software that considerably reduces the effect of large lipid signals on small neighboring peaks. With these new developments and with the addition of fast and reliable choline quantitation techniques, ^{1}H MRS will improve even further the specificity of MR in breast tumor classifications.

* This information about this product is preliminary. The product is under development and not commercially available in the US and its future availability cannot be ensured.

References

[1] David K.W. Yeung, PhD, et al. Breast cancer: In vivo proton MR spectroscopy in the characterization of histopathologic subtypes and preliminary observations in axillary nodes metastases. Radiology, 225, pp 190–197, 2002.

[2] Rachel Katz-Brull, Philip T. Lavin, Robert E. Lenkinski. Clinical utility of proton magnetic resonance spectroscopy in characterizing breast lesions. J. Natl Cancer Inst, 94(16), pp 1197–1203, 2002.

[3] Kvistad KA, et al. Characterization of neoplastic and normal human breast tissues with In vivo 1H MR spectroscopy. J. Magn. Reson. Imaging 10; pp 159–64, 1999.

Software Compensation for Patient Position Enabling Reproducible Slice Positioning – AutoAlign

Katherine T. Scott, Ph.D.

Siemens Medical Solutions, Inc., Malvern, PA, USA

Whether repeat-scanning the same patient for follow-up in a clinical environment or performing comparison studies on different subjects, AutoAlign enables reproducible prescription of slice positions and orientations in neuroimaging studies, without technologist intervention and, in routine use, without retrieval of previously archived datasets.

MRI examinations generally begin with the acquisition of a rapid localizer scan, from which slices for subsequent scans are manually prescribed. If a follow-up examination is performed on the same subject some time later, exactly duplicating the previous slice positions and orientations requires identification of the same anatomical landmarks in the new images. Since the subject is never identically positioned in the scanner and RF coil from one scan session to the next, these may be difficult to locate, especially if changing pathology is present. High precision is required to track small changes in serial studies of e.g. lesion load. However since in-plane resolution is typically higher than through-plane resolution, minor errors in slice positioning can greatly affect resulting measurements. Several studies have shown that less variability is introduced by multiple observers reading the data than by errors due to repositioning in serial scanning multiple sclerosis, brain atrophy, tumors, stroke etc. [1, 2]. For group comparison studies, natural anatomical variability precludes acquisition of identical datasets, but consistent slice prescription techniques are required to enable acquisition of images that can confidently be compared side-by-side i.e. observed differences should reflect true anatomical variation and not be due to variations in slice prescription.

At the heart of the technique is the AutoAlign Atlas, which was created from segmented and co-registered MRI images

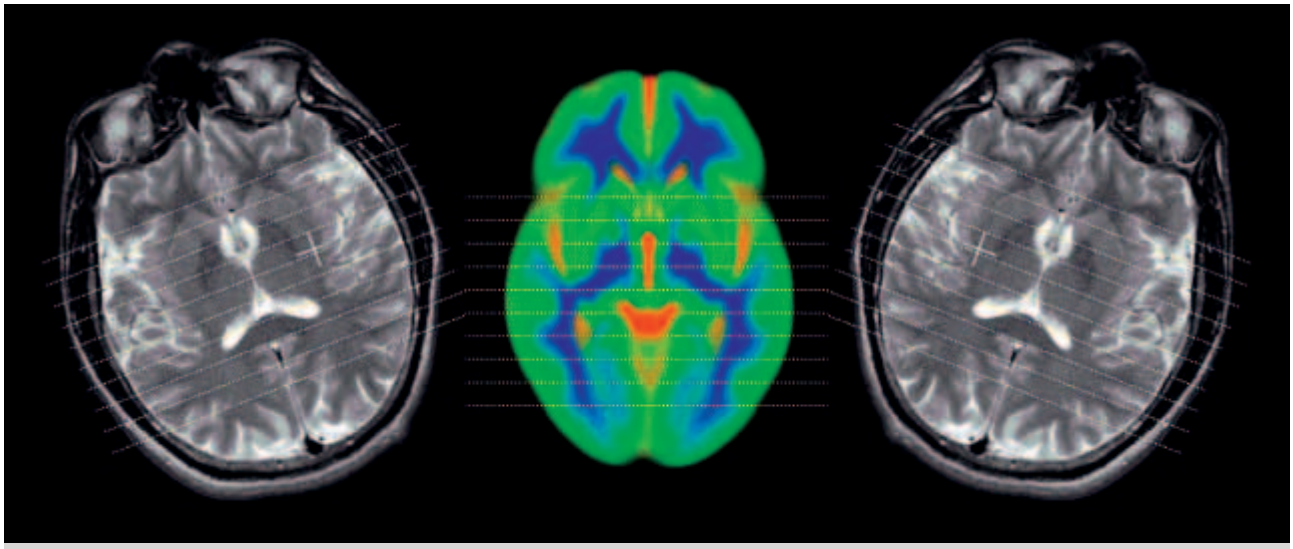

[Figure 1] *AutoAlign registers localizer images to the Atlas, enabling slice parameters saved in protocols or previously run on an individual subject, to be correctly positioned and oriented, irrespective of the position of the head. No additional manual adjustment by the technologist is required – alignment is automatic and reproducible.*

[3, 4] of the brains of a group of 400 adult subjects, both normal and abnormal. This composite dataset, contains two types of probabilistic information: the likelihood that a particular type of tissue (white matter, gray matter, CSF, etc.) will occur at any given location; and the intensities to be expected from the different tissue types in MRI images acquired with selected parameters specified at particular field strengths. The probabilistic information relating to the pathology and location are also inherent in the atlas, increasing the robustness of the method in the presence of disease. Each examination begins with the AutoAlign localizer, a 40 s scan during which both proton density and T1-weighted volumes of the brain are acquired and registered to the Atlas. Registration is done using a rigid body alignment process which incorporates the contrast and tissue classification information. The series of rotations and translations required to optimally align the images with the atlas is saved as a matrix, which is applied to define slice positions and orientations in subsequent scans. In-plane rotation of the imaging slab is a feature that increases the accuracy of positioning as compared to manual slice prescription, since this is often not routinely used in a clinical environment. No anatomical landmarks are used in the process i.e. the whole brain is aligned with the atlas, enabling rapid computation with accurate results as demonstrated in both intra and inter subject studies [2, 5].

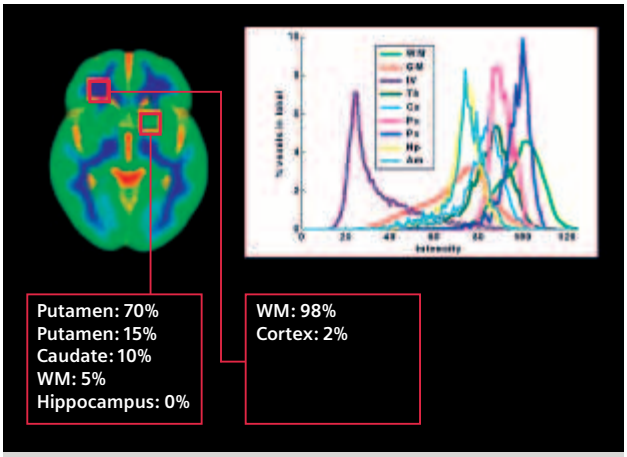

[Figure 2] *The AutoAlign Atlas (left) contains probabilistic information on the likelihood of certain tissues appearing at a particular location in the brain, as well as the signal intensities expected from different tissue types. Intensity histograms from T1-weighted images are shown for a variety of neuroanatomical structures (right) – white matter (WM), cortical gray matter (GM), lateral ventrical (LV), Thalamus (Th), Caudate (Ca), Putamen (Pu), Pallidum (Pa), Hippocampus (Hp) and Amygdala (Am). Incorporation of spatial information and the dual contrast provided by the AutoAlign localizer enables separation of the distributions that would not be possible using intensities alone. Figure reproduced with permission from Reference 3.*

AutoAlign in different cases

Once the AutoAlign localizer has been run, protocols are run without operator intervention i.e. no "tweaking" of the slice positions or orientations is necessary – see Figures 1 and 3. Using this method, the same subject can be scanned repeatedly on the same system, on different systems at different field strengths and at different sites. In all cases, the same slices will be prescribed without reference to any prior imaging study. In the case of comparative studies of different subjects, matching slice positions will automatically be selected. AutoAlign is equally applicable in a number of different cases – exactly how it would be used depends on the desired application:

1. **Existing protocols –** The simplest and most universally applicable method is to scan the subject(s) using existing protocols as they have been saved on the scanner. In this case, the protocols have been set up with predefined slice orientations relative to the Atlas and registration of the brain to the Atlas ensures that the slice orientations are always correct, irrespective of the orientation of the head and without retrieval of archived images. Subjects could be scanned on different systems or at other sites without

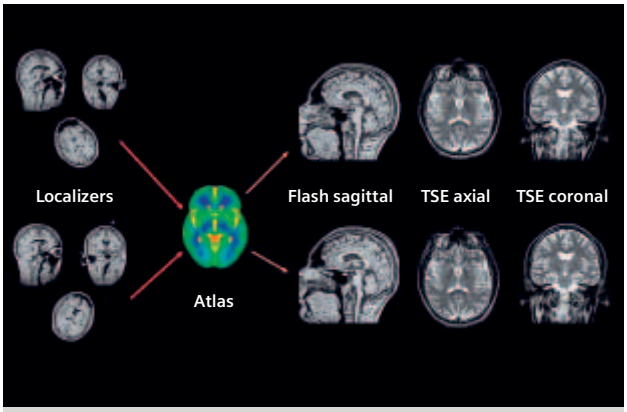

[Figure 3] *Repeat scanning of the same subject. On the left hand side are the 3-plane localizers showing the position of the head for the two scan sessions. AutoAlign registration of the images to the Atlas enables the slices on the right hand side to be acquired without altering the scan prescription. Sagittal, axial and coronal slices are shown for the two studies – each has the same slice number as the corresponding slice in the previous study.*

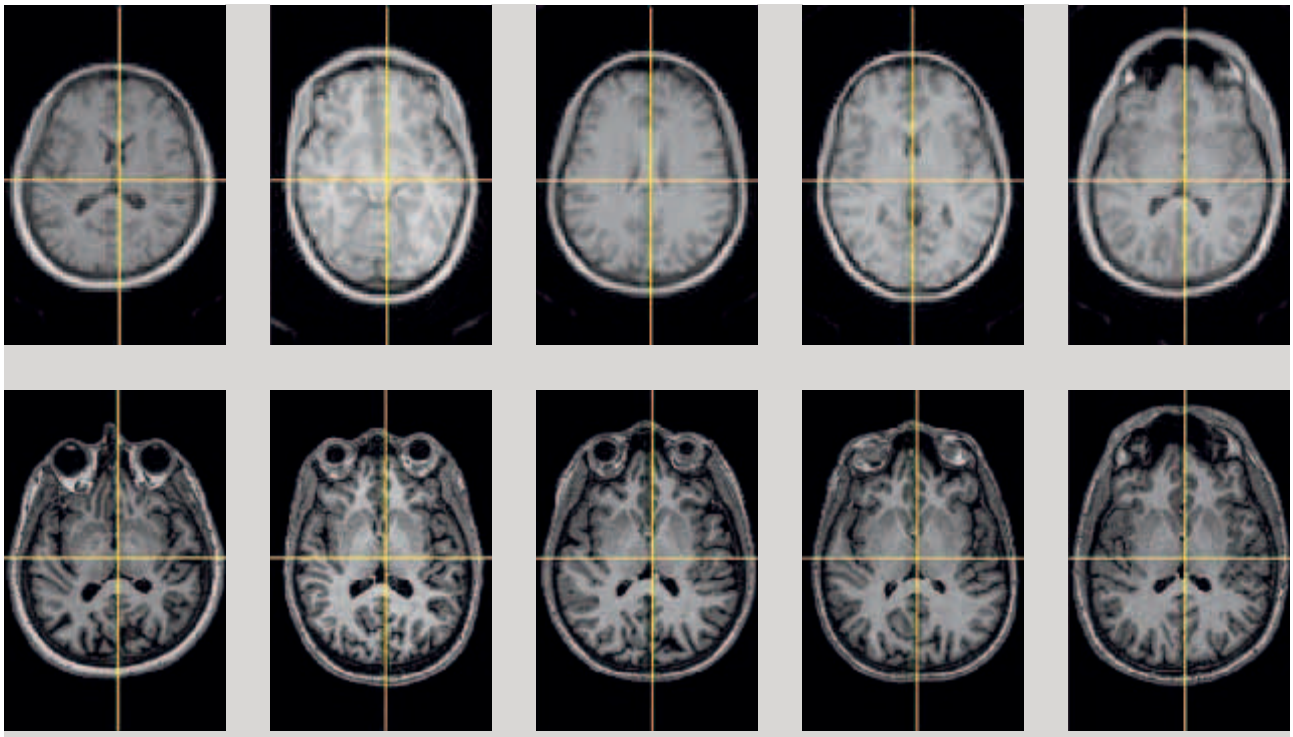

[Figure 4] *Five different subjects scanned with the same protocol. Localizer images before automatic alignment are shown at the top; MPRAGE (Magnetization Prepared RApid Gradient Echo) images incorporating AutoAlign in the row beneath. Good midline alignment and left-right symmetry are observed in the aligned images as well as close slice selection across subjects. Reproduced with permission from Reference 5.*

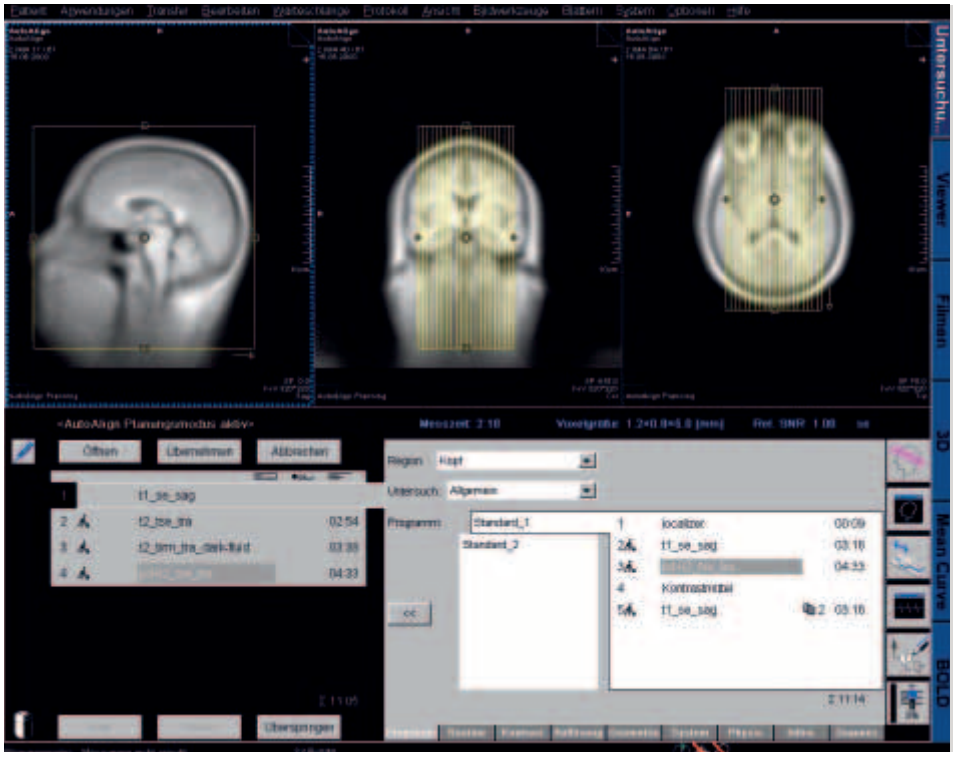

[Figure 5] *Planning on the Atlas. Using the AutoAlign patient enables protocols to be planned directly on the Atlas. Note that this is a probabilistic composite of 400 brains, hence the "blurred" appearance. Since anatomic landmarks are not used in the whole brain alignment, their absence in these views is not relevant in planning site specific protocols. For individualized protocols, planning on the actual patient images at the first visit and saving the protocols, will enable reproducible slice scanning (using anatomical landmarks if required) on that subject at a future visit.*

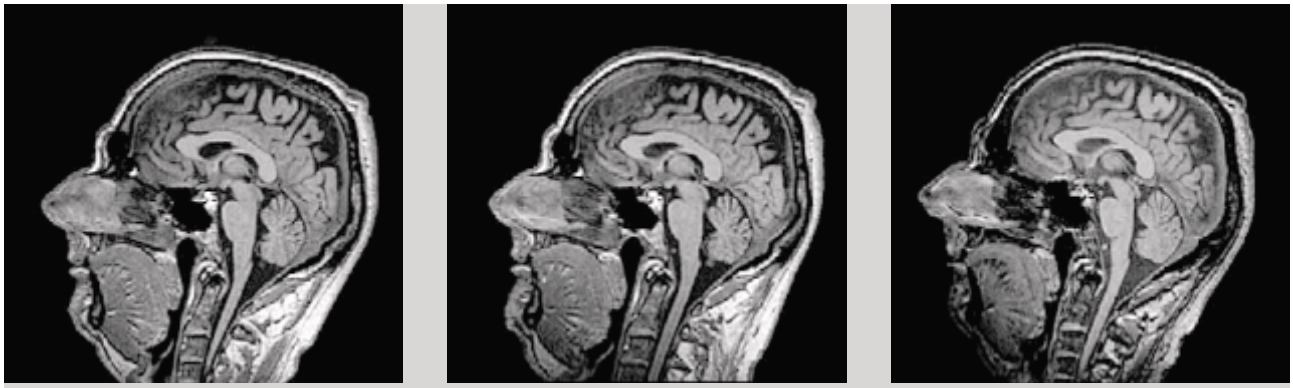

[Figure 6] *Same subject scanned in three different scanners and at two different field strengths - images from 1.5T MAGNETOM Sonata (left), 1.5T MAGNETOM Symphony with Quantum gradient system (centre), 3T MAGNETOM Trio (right). Note the consistent alignment of the brain, while the non-rigid anatomy, such as the spinal cord, varies across the images.*

further protocol management.

2. **Site specific protocols –** It is recognized that different radiologists at different sites will have their own preferred protocols that may differ from those delivered as standard with the system. In this case, technologists can create protocols with the preferred parameters that will be standard for the site and save them. When the AutoAlign localizer is run at a subsequent session (or on a different patient), the slice positions and orientations will automatically be correctly applied to the subject without operator intervention or reference to archived images. If protocol uniformity across scanners (or at other sites) is desired, it is necessary to recreate the slice prescription on each scanner. This can be carried out manually, by importing an electronic protocol exported from a scanner with the desired slice positions and orientations, or by using the Phoenix functionality (i.e. image-based automatic protocol parameter retrieval) and saving the protocols – see later.
3. **Individual (patient specific) protocols –** Finally, in some cases it may be desirable to create a protocol for a specific patient, rather than using a standard imaging protocol. Cases where this might be applicable include adapting the imaging volume to conform with patient pathology, performing additional examinations not usually incorporated in the standard protocol, or for an imaging study where a particular feature or orientation is desired e.g. AC-PC line exactly in the axial plane. This protocol could be saved and used in the same manner as described previously, but this would be one situation where retrieval of archived images may be the preferred option. In this case, using AutoAlign and Phoenix together, enables repetition of the study in the same manner as previously performed on an individual patient. Phoenix recreates the previous protocol and AutoAlign ensures that slices are again correctly positioned and oriented, irrespective of the position of the head.

Site specific or patient specific protocols that use AutoAlign may be created in a number of different ways.

A: Planning directly on the Atlas (AutoAlign patient). This is the most generic form and is useful for setting up routine clinical protocols i.e. site specific protocols.

B: Planning on the current subject. Useful for a time series on the same patient (patient specific protocols) or as an alternative to planning site specific protocols directly on the Atlas, if the subject is representative of the subsequent subjects.

C: Manually entering the offset, tilt and rotation parameters. Most useful for the specification of study protocols e.g. for clinical trials involving multi-center studies, to ensure uniformity across sites.

D: Importing electronic protocols from another scanner where protocols contain the correct offsets and orientations. Helpful in transferring sets of protocols between scanners at one site or for studies at multiple centers.

E: Phoenix in images from another scanner or site, acquired using protocols with the desired slice parameters. Of use in keeping individual scanner protocols consistent across systems and/or in multi center trials.

In each case, at the end of each step in the protocol creation process, the protocol must be saved to the exam database.

All of the Siemens head sequences support AutoAlign and may be saved with the desired slice orientations and positions during planning. Slice positions may be graphically displayed on a 3-plane localizer to monitor during the course of the examination and it is always possible for the technologist

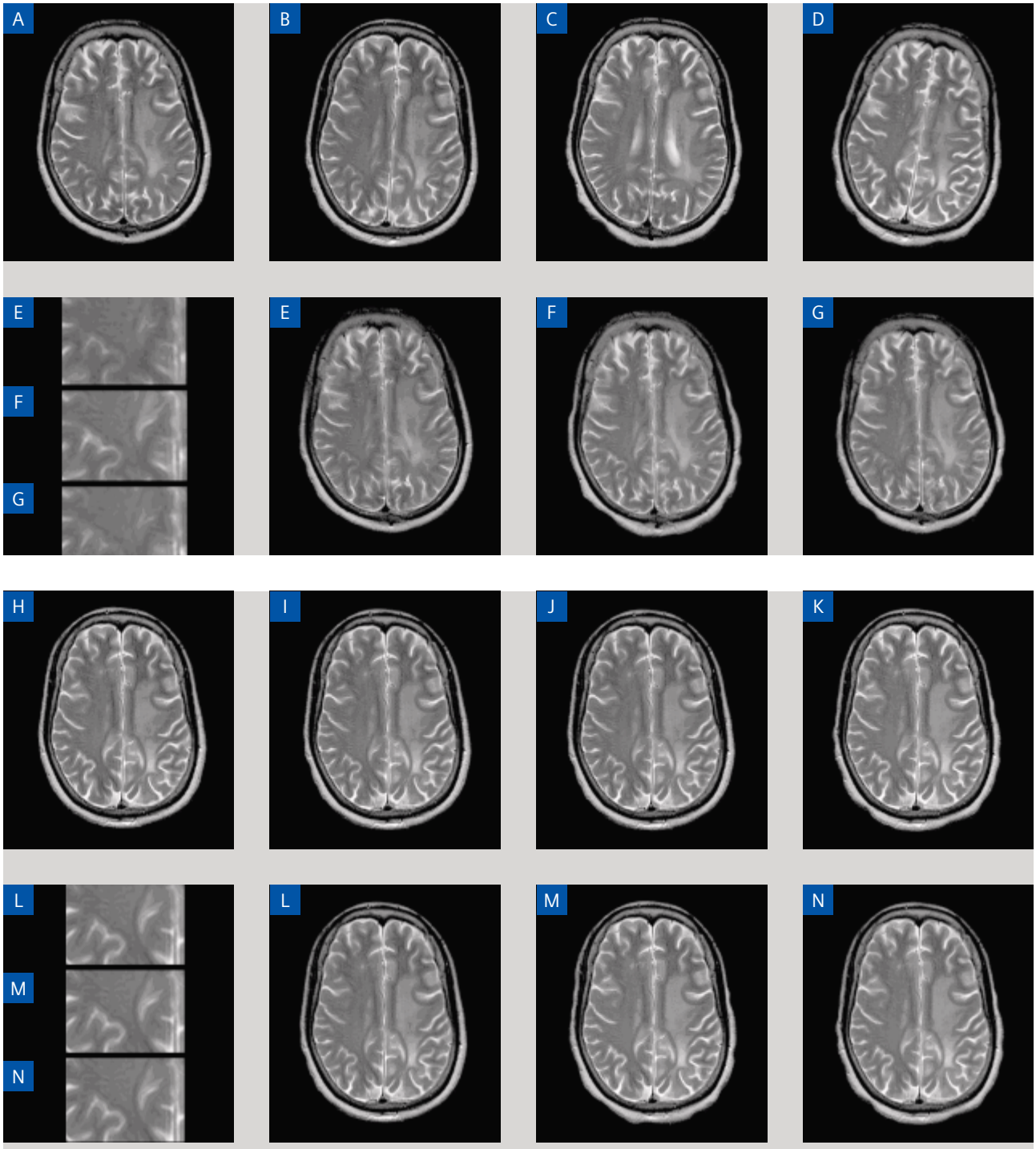

[Figure 7] *Scan – rescan of the same patient with manual slice prescription (upper panel) and using AutoAlign (lower panel) a total of four times with each method. Manually aligned TSE (Turbo Spin Echo) images (A–D) and AutoAligned images (H–K) are shown in the top half of each panel. Images after co-registration of the follow-up series (E, F, G and L, M, N) to the initial series (A and H) are shown in the bottom half of each panel. Finally, a zoomed section of the co-registered images is displayed in the lower left pane of each panel. Note the higher variation in the manually aligned slices (A-D) versus the automatically aligned slices (L–N), as well as the slight blurring caused by the co-registration procedure. Figure courtesy of Dr. Thomas Benner.*

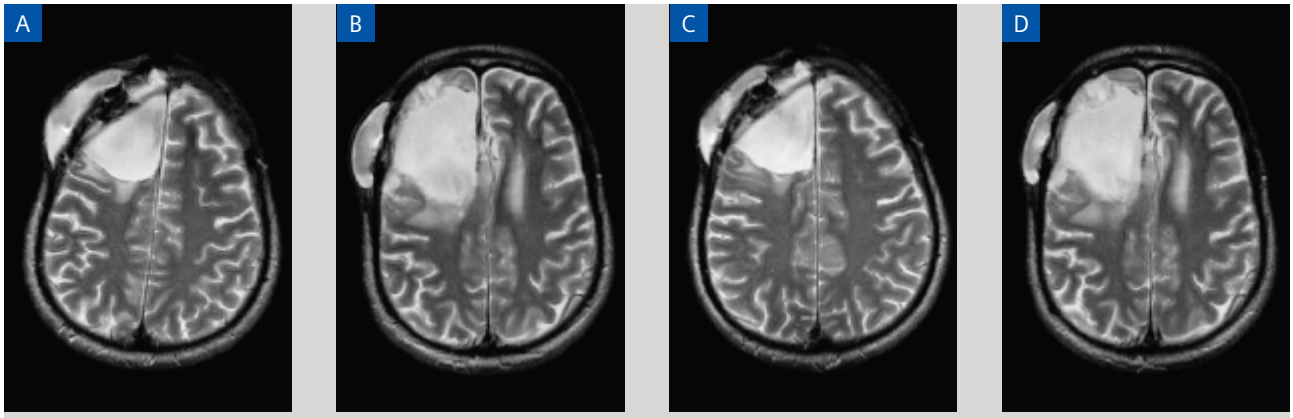

[Figure 8] *Comparison of manual alignment by the technologist (A, C) and AutoAlign (B, D) in TSE images for initial and follow up visit of tumor patient. Midline rotation errors reflected in the images on the left were caused by failure to adjust rotation in the acquisition plane (axial), whereas this was automatically corrected by AutoAlign. On systems where in-plane rotation is not possible, this can only be achieved by repositioning the patient.*

to over-ride the prescribed slices if desired, but naturally this overrides the benefits of the AutoAlign feature and should only be carried out if absolutely necessary e.g. if major surgery or large pathological changes cause the AutoAlign procedure to fail. Manually aligning the slices will disable AutoAlign for that scan only – subsequent ones will continue to use the feature unless it is actively turned off or the patient is closed, a new patient is registered, the patient table is moved or the scanner is rebooted.

The atlas is – as of today – not designed for pediatric patients or those with large areas of resected anatomy (however, it is possible to include your own Atlas). Gross changes in patient position during the scan session will also cause errors in subsequent scan positioning and the AutoAlign localizer can be rerun at any time during the study to correct for this, but should not usually be required. Since no landmarks are used in the alignment process of the slices to the Atlas, prescribing slices relative to specific anatomical landmarks in a single subject will result in excellent alignment upon rescanning of the same subject, but will not be consistent from this subject to another. The latter is an example of where patient specific protocols should be used.

Conclusion

AutoAlign enables rapid patient throughput with increased reproducibility and reduced dependence on operator expertise. Both serial scanning of the same patient and comparative studies of different subjects at different field strengths and/or at different sites are possible, without fiducial markers or reference to previously archived images. Brain imaging protocols benefit from the increased positioning reliability enabled by AutoAlign and only in the case of patient specific protocols is it necessary to retrieve archived images. In this case the use of AutoAlign and Phoenix together enable the correct imaging slices and protocols to be quickly defined and rescanned.

References

[1] Benner, T., Wisco, J.J., van der Kouwe, A., Fischl, B., Sorensen, A.G., 2004. Accuracy and repeatability of automatic slice positioning compared with manual slice positioning. 12th Meeting of the ISMRM, Kyoto, Japan.

[2] Benner, T. et al. Comparison of Manual and Automatic Slice Positioning of Brain MR Images. Radiology – in press.

[3] Fischl, B., Salat, D.H., Busa, E., Albert, M., Dietrich, M., Haselgrove, C., van der Kouwe, A., Killiany, R., Kennedy, D., Klaveness, S., Montillo, A., Makris, N., Rosen, B., Dale, A.M., 2002. Whole brain segmentation: automated labeling of neuroanatomical structures in the human brain. Neuron 33, 341–355.

[4] Fischl, B., Salat, D.H., van der Kouwe, A.J., Makris, N., Segonne, F., Quinn, B.T., Dale, A.M., 2004. Sequence-independent segmentation of magnetic resonance images. NeuroImage 23 (Suppl. 1), S69–S84.

[5] van der Kouwe, A.J., Benner, T., Fischl, B., Schmitt, F., Salat, D., Harder, M., Sorensen, A.G., Dale, A.M.2005. On-line automatic slice positioning for brain MR imaging. Neuroimage 27, 222–230.

Acknowledgements

I am deeply indebted to Drs. Thomas Benner and Andre van der Kouwe from the Martinos Center for Biomedical Imaging at Massachusetts General Hospital for extensive discussions on the subject matter, for allowing me the use of their images as examples, and for their thoughtful comments and suggestions.

Structural MR Imaging with Real-Time Prospective Rigid Body Motion Correction using Cloverleaf Navigators

André van der Kouwe[1], Athinoula A. Martinos[1], Anders Dale[2]

[1]Center for Biomedical Imaging,Massachusetts General Hospital and Harvard Medical School, Boston, USA
[2]Departments of Radiology and Neurosciences, University of California, San Diego, USA

Subject movement during MR brain imaging accounts for a substantial number of unusable scans in clinical and research imaging. In particular, morphometric imaging studies suffer from patient motion during the required long high-resolution structural scans. We demonstrate a method using embedded "cloverleaf" navigators in a 3D FLASH scan to correct for rotations and translations with respect to all three axes (rigid body motions) of the head in real-time during imaging. The method minimally impacts imaging time, as each navigator occupies approximately 4 ms of the repetition time (TR), which is typically 20 ms. The navigator is placed after the imaging readout in the sequence so as not to affect the echo time (TE), and requires no additional RF pulses. A short preliminary mapping scan is required after which one or more imaging scans can be collected using the same slice prescription. The navigators in each imaging scan are compared with the map at every TR and the gradients are adjusted in real-time to track any detected changes in the subject's position and orientation from one TR to the next. In this way the integrity of the acquired k-space data is maintained despite the motion. When the scan is complete, the image volume can be reconstructed by Fourier transformation as usual, without any additional post-processing, although additional post-processing may further improve the images. If multiple imaging scans are collected after a single mapping scan, they will automatically be aligned with one another.

Background

Various forms of motion correction during acquisition are available on the Siemens platform, and these are collectively termed PACE (Prospective Acquisition CorrEction). 1D-PACE uses a pencil-shaped volume that intersects the diaphragm to track breathing and synchronize gating during cardiac imaging. 2D-PACE is more robust as it uses a low-resolution 2D image rapidly acquired by means of a gradient echo sequence, and this is most appropriately applied to abdominal imaging.

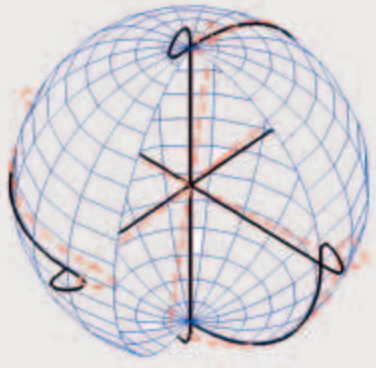

[Figure 1] *Cloverleaf navigator path in k-space (the red path shows an example rotation used during the mapping procedure). Axes correspond to phase, readout and slice directions.*

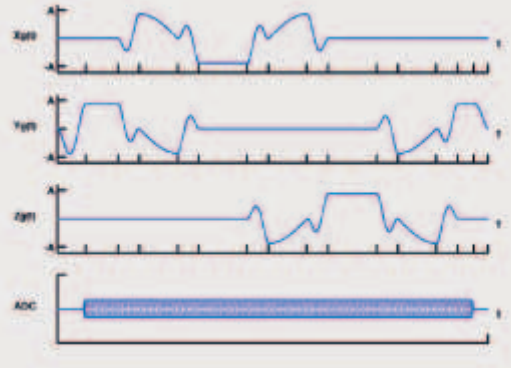

[Figure 2] *Gradients for cloverleaf navigator kernel (total duration is 4.2 ms).*

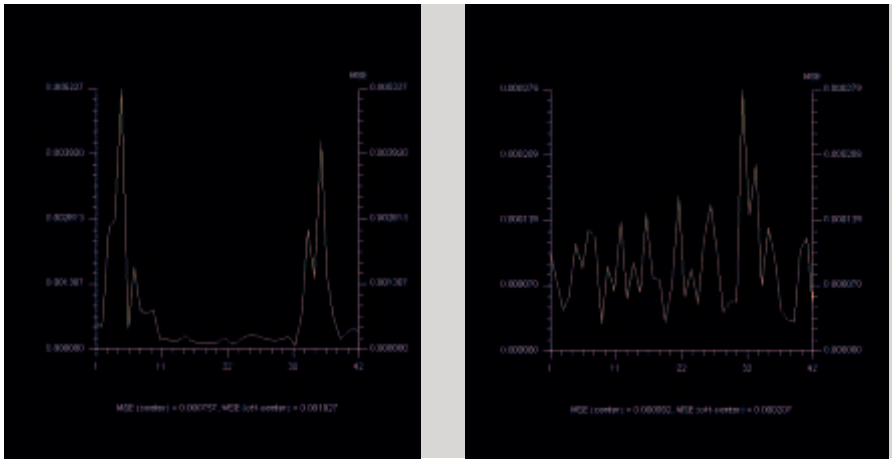

[Figure 3] *Plots generated after mapping sequence showing the measured error between repeated navigators for two separate maps. The plots and mean square error (MSE) values indicate the amount of subject motion that occurred during the 12 second map. The 42 measurements correspond with the 42 repeated samples of the unrotated navigator. Left: Plot for map with motion. Right: Plot for map without motion.*

3D-PACE is a method for tracking head position in real-time during functional imaging (fMRI) with echo planar imaging (EPI) [1]. Since multiple volumes are collected in rapid succession, the first is selected as a reference and subsequent volumes are registered with the reference in order to estimate the position of the head in real-time. The detected changes in position are fed back to the gradients so that the position and orientation of each volume is adjusted during acquisition to follow the head motion. This method uses the EPI volumes already collected as part of the fMRI series, and requires no additional navigators.

Researchers at the Mayo Clinic developed the concepts of orbital and spherical navigators embedded in the sequence to detect and correct for motion during imaging. Orbital or circular navigators can be used to detect rotations and translations within the plane of the navigator [2]. A combination of three perpendicular circular navigators can be used to detect rotations and translations in all three dimensions (rigid body motion) [3]. An iterative correction process is necessary for rotations in planes that do not coincide with any of the three circular navigators, and this may be time consuming. Spherical navigators do not require this iterative process, but each navigator takes relatively long to acquire [4].

A recently popularized approach to motion correction is PROPELLER (Periodically Rotated Overlapping Parallel Lines with Enhanced Reconstruction) [5], also called BLADE. In 2D TSE with PROPELLER or BLADE, motion is only corrected within the slice plane.

Methods to detect motion using external sensors have also been proposed, including optical [7] and magnetic methods [8]. Since these methods require additional hardware to track the motion and fiducials or other devices as reference points, they are rarely used.

Materials and Methods

Our method combines the advantages of some of these approaches by consolidating the navigator path into a single continuous k-space trajectory that includes three perpendicular arcs for estimating rotations and three perpendicular traversals through the center of k-space for estimating translations. Combined with a short mapping sequence, this enables a full 6 parameter rigid body position estimate to be made every time the navigator is acquired, typically every repetition time of 20 ms of a 3D FLASH sequence set up for brain morphometry.

The navigator path in k-space is illustrated in Figure 1. The path begins and ends at the center of k-space and is traversed in approximately 4 ms. The gradients required to realize this path are shown in Figure 2. The transition regions between the arcs and straight lines are comprised of cubic and quartic splines designed to be maximally gentle on the gradients.

The navigator building block is inserted in a 3D FLASH sequence after every RF excitation, either before or after the imaging readout and associated phase encoding gradients, and before the spoiler gradient. Navigators inserted before the readout are more reliable but increase TE for imaging, whereas navigators after the readout result in noisier position estimates but do not affect imaging TE. The sample data from the navigator are analyzed by a process with real-time priority in order to feed back a rigid body correction that is applied to the gradients in the next TR. The calculation itself is completed in a few milliseconds. Even though each navigator may produce a slightly noisy motion estimate, the estimates are made so frequently (for example at 50 Hz) that they can be smoothed to provide robust tracking of motion. The user has control over the feedback gain which is a parameter that adjusts the compromise between smoothing high frequency estimation noise and tracking rapid changes in position.

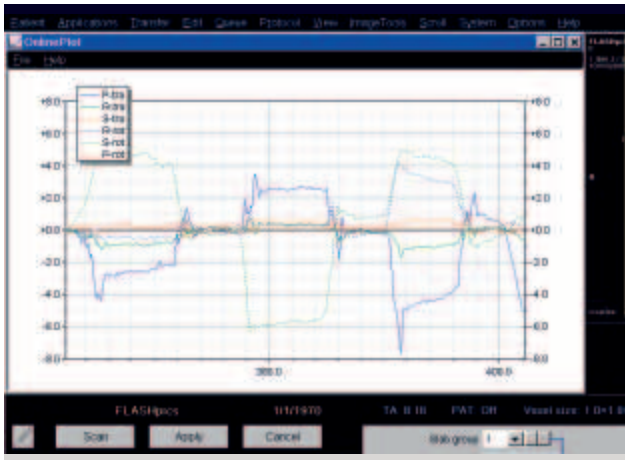

[Figure 4] *Online motion plot shows rigid body motion (translations in and rotations about phase encoding (P), readout (R) and slice encoding (S) directions) on a scrolling display during image acquisition. The subject performed deliberate head movements during this scan.*

In order to reliably estimate motion, the algorithm requires a map of the region of k-space surrounding the cloverleaf navigator on the surface of the sphere. This map is acquired during a separate scan, lasting 12 s in the case of a typical 3D FLASH protocol with TR of 20 ms. During this scan, the gradients are rotated through various angles about the prescribed slab position to sample the k-space signature of the object in various positions. Only a small range of angles need to be tested, sufficient to cover the largest rotation that the subject might make in 20 ms, since the map is used to detect the changes in position from one repetition to the next rather than the absolute position of the subject. For reliable motion correction during imaging, it is important that the subject does not move during the map. To assist the scanner operator in determining whether there was motion during the map, the mapping sequence generates a plot (see Figure 3) that reflects the error between repeatedly sampled unrotated navigators distributed throughout the map. This error should be as low as possible, reflecting little subject motion.

During imaging, new navigators are compared with the map to estimate translations and rotations and make corrections to the gradients every TR. Translations are estimated from the slope of the phase difference between the new navigator and the unrotated reference navigator measured across the center of k-space in all three directions. Rotations are estimated by finding the best fit between the new navigator and the rotated navigators in the map, interpolating if necessary. These calculations can be completed in a few milliseconds. A display (Figure 4) is available on the scanner host that shows the estimated head position in real-time during scanning, and with a suitable projection setup this can be displayed in the scanner to provide feedback to the subject.

Results and Discussion

We scanned two healthy volunteers on a Siemens 1.5T MAGNETOM Sonata scanner. For each subject we collected six high resolution 3D FLASH scans with cloverleaf navigators (TR = 20 ms, 1.3 x 1 x 1.3 mm, T_{acq} = 7 min 45 s). The subjects were instructed to move their heads deliberately and randomly throughout all six scans. We activated motion correction during three of the scans, and left it uncorrected during the remaining three scans. The scan order was randomized and the subjects were blinded to the scan order. For each subject, a single initial map was used for all three corrected

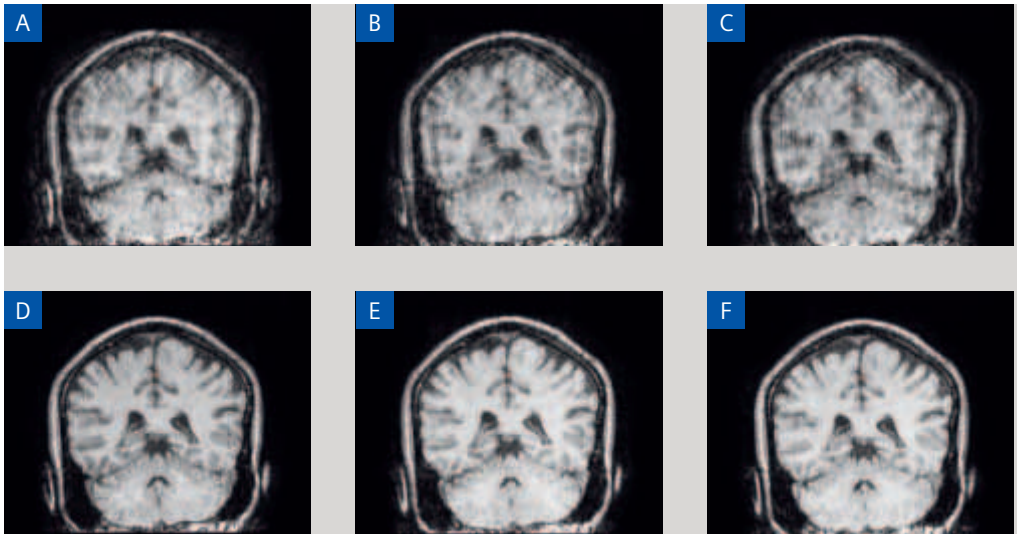

[Figure 5] *Coronal slices through six individual volumes collected motion without motion correction (A, B, C) and with motion correction (D, E, F).*

scans. The results were very similar for the two subjects. Figure 5 shows a coronal slice through each of the six volumes acquired for the first subject. Figure 6 shows an estimate of the motion during one of the corrected scans (the motion was similar for the other scans).

The remaining motion artifacts can be reduced by averaging the motion corrected scans. Figure 7 shows the average of the three scans without motion correction, the average of the three scans with motion correction and the k-space weighted average of the three scans with motion correction. The weighted average is calculated offline by weighting each line of k-space in inverse proportion to the error between the navigator acquired in the same TR and the reference navigator. This results in a sharper average image with almost no remaining artifacts, but requires that raw k-space data be stored during scanning and processed offline and is therefore not feasible for clinical use.

Conclusion

The cloverleaf navigator technique requires no external hardware and corrects rotations and translations in all directions, rapidly and in real time. The method is fully implemented as a prototype on the Siemens scanner in the 3D FLASH sequence and produces corrected DICOM images immediately after acquisition. Our results suggest that real-time motion correction with cloverleaf navigators is effective in mitigating motion artifacts during MR imaging of subjects that move. The technique will be especially useful in morphometric imaging of children, older subjects and patients with movement disorders. In further work we intend to incorporate cloverleaf navigators in other sequence types.

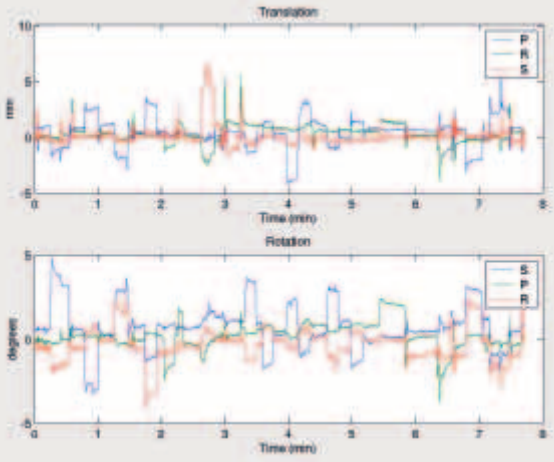

[Figure 6] *Plot of estimated and corrected motion performed by a volunteer during one of six test scans; (top) translations, (bottom) rotations. "P", "R" and "S" denote phase, readout and slice encoding directions/ axes.*

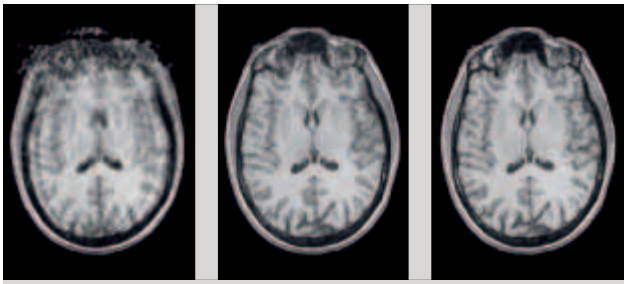

[Figure 7] *Average of 3 scans without motion correction (left), 3 scans with motion correction (middle) and 3 scans with motion correction and offline k-space weighting to improve sharpness (right).*

References

[1] Thesen S, Heid O, Mueller E, Schad LR: Prospective acquisition correction for head motion with image-based tracking for real-time fMRI. Magn Reson Med 2000; 44: 457–465.

[2] Fu ZW, Wang Y, Grimm RC, Rossman PJ, Felmlee JP, Riederer SJ, Ehman RL: Orbital navigator echoes for motion measurements in magnetic resonance imaging. Magn Reson Med 1995; 34: 746–753.

[3] Ward HA, Riederer SJ, Grimm RC, Ehman RL, Felmlee JP, Jack CR, Jr.: Prospective multiaxial motion correction for fMRI. Magn Reson Med 2000; 43: 459–469.

[4] Welch EB, Manduca A, Grimm RC, Ward HA, Jack CR, Jr.: Spherical navigator echoes for full 3D rigid body motion measurement in MRI. Magn Reson Med 2002; 47: 32–41.

[5] Pipe JG: Motion correction with PROPELLER MRI: application to head motion and free-breathing cardiac imaging. Magn Reson Med 1999; 42: 963–969.

[6] Pipe JG, Farthing VG, Forbes KP: Multishot diffusion-weighted FSE using PROPELLER MRI. Magn Reson Med 2002; 47: 42–52.

[7] Eviatar H, Schattka, B.J., Sharp, J.C., Rendell, J., Alexander, M.E.: Real time head motion correction for functional MRI. In 7th Annual Meeting of the ISMRM. Philadelphia, PA, 1999.

[8] Nevo E, Roth, A., Hushek, S.G.: An electromagnetic 3D locator system for use in MR scanners. In 10th Annual Meeting of the ISMRM. Honolulu, HI, 2002: 334.

Acknowledgements

We would like to thank Thomas Benner, Bruce Fischl, Lawrence Wald, Evelina Busa, David Salat, Franz Schmitt and Franz Hebrank for their valuable assistance in this work. The work was supported in part by NIBIB R21EB02530, NCRR P41RR14075, the Mental Illness and Neuroscience Discovery (MIND) Institute, and Siemens Medical Solutions.

Hyperpolarized Helium Magnetic Resonance Lung Imaging

Georgeann McGuinness, M.D., Glyn Johnson, Ph.D., Ray F. Lee, Ph.D.

Department of Radiology, New York University School of Medicine, New York, USA

Introduction

Utilization of inhaled hyperpolarized helium (^{3}He) as a physiologically dynamic contrast agent has surmounted the traditional limitations of conventional proton MR (^{1}HMR) in the lungs. ^{3}HeMR has expanded the field of pulmonary imaging to include direct physiologic and anatomic information, while indirectly elucidating lung micro structural anatomy beyond the resolution of even high resolution CT (HRCT). Specifically, this technique is uniquely sensitive to distal small airway disease, a pathology presently undetected by conventional clinical evaluation (PFTs and HRCT). Importantly, this promising new technique is capable of revealing both anatomic and functional pulmonary information, on a regional basis.

Current measures of lung disease and their limitations

In order to fully appreciate the potential of ^{3}HeMR lung imaging it is worthwhile to review the inadequacies of current clinical and imaging methodologies. Clinical assessment of the patient with airway disease, and small airway disease in particular, has relied on laboratory tests, such as Pulmonary Function Tests (PFTs), HRCT, and physical findings, which are often noncontributory. Ironically, perhaps the most reliable clinical metric is the patient's symptomatology or activity limitations, as the preceding tests are noteworthy for their narrow scope.

Pulmonary Function Tests: Limitations

In spite of their limitations, PFTs remain the most commonly used non-imaging method for assessing diffuse lung disease. Screening PFTs, supply only a global view of lung function, cannot localize regional abnormalities in what are often 'patchy' diseases, and may be relatively nonspecific in terms of identifying an etiology for specific findings. Conventional PFTs may not differentiate airflow obstruction due to loss of elastic recoil, for example as may be seen with emphysema, from destruction secondary to inflammatory thickening, mucus plugging, and scarring [1]. Despite these limitations, PFTs are still considered the clinical 'gold standard' for the documentation of large airway dysfunction.

However, the relatively low sensitivity of PFTs in detecting small airway disease is well recognized [2, 3]. Although a significant source of symptomatology when diseased, small airways contribute only a fraction of total airflow information revealed at standard PFTs; indeed, 75% of the airways are not assessed with screening spirometry. The conducting airways have a volume of approximately 150 ml, whereas the respiratory zone of the lung, involved in gas transport and exchange, has a total volume of approximately 3 liters [4]. Despite their small diameter, airflow resistance is less overall in the small airways because of the summation effect of their overwhelming number – only approximately 25% of overall airway resistance is due to the small airways [5]. Most importantly, the presence of large airway dysfunction obfuscates indicators of small airway disease at PFTs! Hence, PFTs may miss significant physiologic and structural pathology, and small airway disease may be masked, particularly if subtle or heterogeneous in distribution. If small airway disease is suspected, specialized studies, not in routine use, may be utilized in an attempt to document these changes [2, 3, 6–13]. Those few specialized tests which may suggest the presence of small airway dysfunction are of limited sensitivity and can only be interpreted in the setting of normal spirometry.

Imaging of Airway Disease: Limitations

Chest Radiography (CXR) is extremely insensitive to small airway disease [14]; only up to fourth generation normal bronchi can be seen at CXR [4, 5]. Only advanced bronchiectasis is detected radiographically [15], and then with a sensitivity far below that of CT. Bronchitis may be recognized by thickening of the airway walls, but CXR plays virtually no role in the evaluation of the more subtle small airway diseases, such as bronchiolitis obliterans.

HRCT is regarded as the primary means of imaging the patient with interstitial or small airway disease [14, 15]. Limi-

tations to HRCT partially reflect the boundaries of its optimal spatial resolution, at approximately 300–500 µm (0.3–0.5 mm). This resolution allows imaging of airways to approximately 9th order bronchi, but peripheral or small airways, generally defined as less than 2 to 3 mm in diameter [5, 16] are not usually visible when normal. The thickness of a normal terminal bronchiole wall is approximately 0.1 mm, below the resolution of HRCT [16]; bronchi less than 2 mm in diameter may be visible if the wall of the airway is thickened. A significant further limitation is that HRCT provides morphologic, but not physiologic, information. Inferred 'physiologic' HRCT information is based on the indirect but visible effects of airway disease on subtended lung parenchyma, assessed primarily through inspiratory and expiratory imaging [17–23], which may confirm the presence of air trapping, an inferential sign of small airway disease.

^{3}HeMR

The clinical advantages of ^{3}HeMR are apparent; it is a safe, non-invasive technique which does not expose the patient to ionizing radiation. At the same time it expands the scope of data to integrate both morphologic and functional data, and is emerging as a robust technique, more readily able to supply quantitative metrics.

^{3}HeMR Technical Overview

There are several reasons for the very few practical applications of proton imaging of the lungs. First, the presence of air reduces average water (and proton) content and hence signal-to-noise ratio (SNR). Second, susceptibility differences between airspaces (with susceptibility ~0) and diamagnetic tissue reduce both T2, through diffusion effects, and T2*. Finally, the airspaces themselves cannot be visualized directly since the concentration of water vapor in air is too low to give sufficient signal.

The alternative to 1HMR is to form images of inhaled noble gases such as ^{3}He and 129Xe [24]. Conventional MR of gases would be unsuccessful since the concentration of nuclei is far too low to provide sufficient signal. However, these noble gases can be 'hyperpolarized' by optical pumping and spin exchange [25]. Polarization measures the fraction of nuclei that become aligned with the static field and are therefore available to generate signal. In liquids, such as water, polarization is only about 1 in 105 but can be as great as 50% in hyperpolarized gases. This polarization increase more than compensates for the low density of the gas. Moreover, polarization can be maintained for several hours if the gas is stored properly (i.e., T1 is hours long). Finally, T2* is about 36 ms for hyperpolarized gases [26], while T2* for ^{1}H is around 1 ms [27]. In addition to providing high signal, hyperpolarized noble gases are chemically inert and non-radioactive and hence safely used as inhaled MR contrast agents to form images of lung air spaces. Of the two gases that can be hyperpolarized, ^{3}He is preferable for imaging the lungs since higher levels of polarization are possible, a higher SNR is produced due to its relatively higher gyromagnetic ratio [28], and because 129Xe, when absorbed into blood, confounds the clean depiction of airspaces, and acts as a central nervous system depressant.

^{3}HeMR Technical Constraints

Although hyperpolarized gas can provide superb SNR there are several constraints imposed by the unique nature of ^{3}HeMR. Because ^{3}He does not exist in an equilibrium state, unlike conventional MR where excited nuclei re-polarize after excitation, hyperpolarization once lost, cannot be restored. Each MR excitation thus depletes available magne-

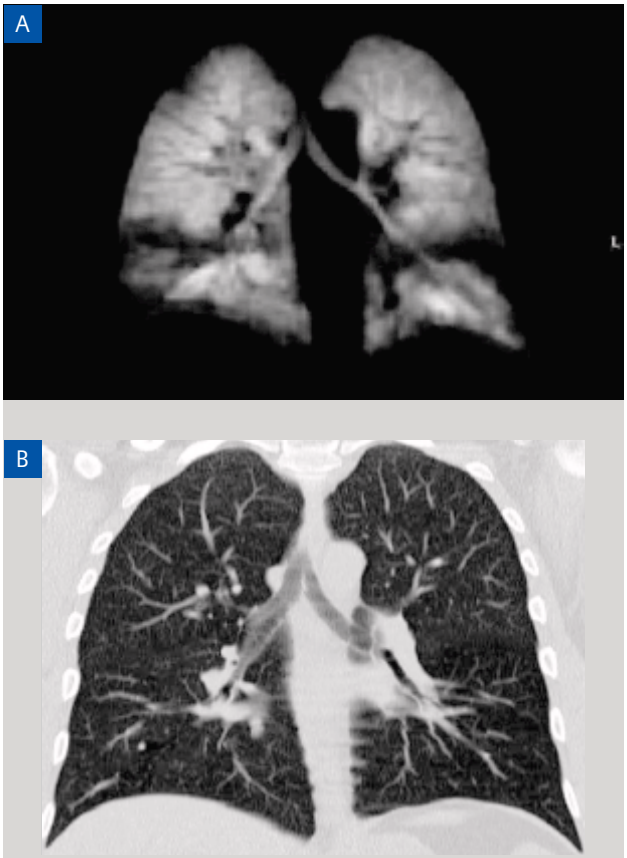

[Figure 1] *Coronal ^{3}HeMR ventilation and HRCT images in a 34-year-old firefighter with dyspnea and cough. (A) ^{3}HeMR shows large wedge shaped ventilation defects. (B) Corresponding coronal HRCT is normal.*

tization irreversibly. Furthermore, although T1 is long in isolation, it is much reduced when the gas comes into contact with strongly paramagnetic oxygen. Thus, a limited time is available for imaging once the gas has been inhaled. Low flip angle gradient-echo sequences have been preferred since these convert only a small fraction of the hyperpolarized magnetization to signal at each excitation. But even in this case increasing the number of excitations does not guarantee SNR enhancement. Additional issues relate to the cost and limited production of hyperpolarized ^{3}He (a single polarizer can generate gas for 3 imaging series), and hardware requirements including coil design and broadband modification to the scanner.

^{3}HeMR Clinical Applications

The range of available techniques include:

1. static ventilation imaging demonstrating lung anatomy and from which the volume of ventilated and non-ventilated lung can be calculated;
2. diffusion imaging which reveals small airway and airspace size and configuration;
3. dynamic ventilation imaging which depicts gas delivery to the airways and lung parenchyma over the course of the respiratory cycle; and
4. oxygen partial pressure imaging which indirectly indicates oxygen uptake by the pulmonary circulation, opening the window further into gas exchange and lung physiology.

Ventilation Imaging

The simplest examination is a ventilation scan where the subject inhales the gas and is imaged by a conventional gradient echo sequence. In normal subjects, uniform distribution of ^{3}He is found within the airspaces and airways; blood vessels and interlobar fissures are visualized as linear signal deficits [29, 30]. Signal voids occur within the lung parenchyma due to airway diseases blocking passage of the gas. Extensive parenchymal defects are seen in patients with chronic obstructive pulmonary disease (COPD) and emphysema [29, 31], but may occur whenever there is endobronchial obstruction or extrinsic compression of the airways {Kauczor, 1997 #68}.

Donnelly et al. {Donnelly, 1999 #45} found ventilation defects due to airway disease in cystic fibrosis patients to correlate well with PFT results. More recently Zaporozhan et al. found ^{3}HeMR to correlate closely to PFTs in assessing ventilated lung volumes in emphysema, surpassing CT in this regard. In fact, ^{3}HeMR appears to be exquisitely sensitive to disease of small and medium airways, based on the signal inhomogeneities seen not only in asthmatics [32] but also in asymptomatic smokers [33, 34]. Kauzor et al. further refined the approach by analyzing defect morphology. These investigators conclude that wedge-shaped defects reflect inspiratory bronchial obstruction, such as that seen in acute and chronic bronchial infection, whereas a patchy pattern reflects bronchiolar disease, including respiratory bronchiolitis [29]. Correlation has also been demonstrated between the size of ventilation defects on ^{3}HeMR scans and clinical assessment of bronchiolitis obliterans syndrome in lung transplantation rejection [35, 36]. Using this pattern analysis ^{3}HeMR attempts to define a measure of pathophysiologic specificity. Recently a comparison of ^{3}HeMR and HRCT findings in this setting reported that many ventilation defects occur in regions without HRCT abnormalities. Over half of these were seen in patients with a clinical diagnosis of chronic graft rejection, suggesting that ^{3}HeMR imaging may be more sensitive than CT for early changes of bronchiolitis obliterans and lung transplant rejection {Gast, 2002 #382}.

Quantitative methods of measuring the extent and severity of disease are required both for mild disease, where changes may be subtle, and for serial studies. Utilizing a combination of proton spin-echo imaging to calculate the thoracic cavity volume, and ^{3}HeMR ventilation images to calculate the ventilated and non-ventilated lung volumes, Woodhouse et al. determined the percentage of ventilated lung [34]. Although this requires manual segmentation of the lungs on the proton images, Woodhouse et al. found remarkably consistent results with ventilated lung volumes of 90.0 ± 3.1 % (mean ± SD) in non-smokers [34]. Zaporozhan et al. determined ventilated lung split volume measures after single lung transplantation, at ^{3}HeMR, comparing them to PFTs as the gold standard [37]. HRCT served as a reference modality for determining air filled lung volumes, and correlated well with total lung capacity (TLC). However, ^{3}HeMR was superior to CT in its ability to demonstrate ventilated lung in patients with emphysema, demonstrating a stronger correlation to vital capacity (VC) [37].

Diffusion Imaging: Assessment of Lung Micromorphology

Measurements of ^{3}He diffusion offer unique insights into lung micromorphology. Diffusion measurement was one of the earliest applications of NMR, used to investigate the self-diffusion of water in colloids [38]. Similar techniques have more recently been incorporated into MR imaging, most notably in the ^{1}HMR assessment of acute stroke [39]. Diffusion weighting is incorporated into the sequence by adding bipolar pulses [40]. Nuclei that move during the application of these pulses lose coherence and signal decreases. By comparing images acquired both with and without diffusion

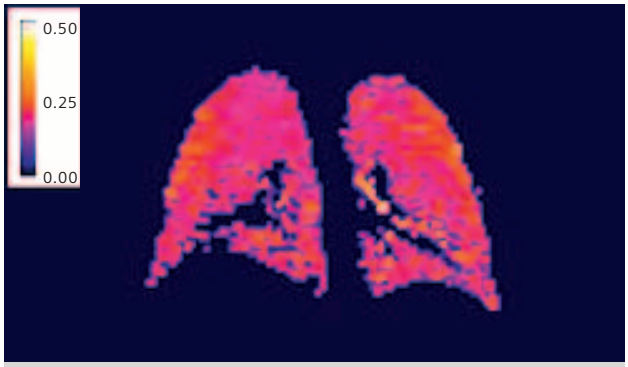

[Figure 2] *Mean ADC = 0.1951 Std, Dev = 0.0533 (Normal ADC = 0.2284 Std, Dev = 0.0853). Isolated Small Airway Disease Occult to PFTs, 37-year-old male with normal PFTs and persistent symptoms of dyspnea, as well as hyperreacitve airways. Mean ADC is decreased (compare to normal values provided). This is indicative of small airway constriction, beyond the sensitivity of spirometric assessment.*

weighting, the diffusion coefficient can be calculated. These techniques may also be applied to measure diffusion of ^{3}He in the lungs.

^{3}He has a large diffusion coefficient, D (2 cm^2 s^{-1}) [41] and, if unrestricted, would move several millimeters over the ~5 ms echo time of a typical MR acquisition. Since this distance is much greater than the dimensions of microscopic lung structures, diffusion is impeded by airway and alveolar walls. The parameter measured is then called the apparent diffusion coefficient (ADC) to distinguish it from the true diffusion coefficient measured in bulk fluids. The ADC reflects the size of the airways and airspaces: when these are large, diffusion will be relatively free and the ADC will be high; when small, diffusion will be restricted and ADC will be low. ADC measurements thus provide a non-invasive method of demonstrating abnormalities in airway and airspace size. ^{3}He ADC measurements in a rat model of histologically confirmed emphysema have shown enlargements in alveoli of ~20 µm [42].

^{3}He ADCs are relatively uniform in normal human subjects [43]. However, histograms show that both the mean and standard deviation of ADC values increase after age 55 to 60, consistent with increases in alveolar size accompanying gradual loss of interstitial tissue [43]. Smaller airspaces detected in posterior lung regions of supine subjects are attributed to transient dependent atelectasis, often seen in the posterior lungs of patients at CT imaging [44]. The mean and standard deviation of ADC histograms increases markedly both in COPD [41] and emphysema [44], reflecting increased alveolar size accompanying airspace wall destruction. A recent report suggests that ^{3}He diffusion imaging may be sensitive to early, sub clinical changes of emphysema, even in patients without evidence of emphysema at HRCT [45]. In this study of 10 healthy smokers with normal HRCTs, mean ADC values were increased compared to non-smokers, though less than those of patients with proved emphysema. In fact, ADC imaging may be more sensitive than spirometry; 9 of the 10 had normal or near normal spirometry [45]. Features of lung microstructure are further elucidated capitalizing on the anisotropic diffusion characteristics of helium in distal airways [46]. A relationship between the distal airway radius and the transverse diffusion rate can be determined. In patients with severe emphysema transverse ADC is elevated compared to normal subjects, and is felt to be consistent with an increase in the mean airway radius by these investigators [46]. Preliminary data supports that ADC values are reproducible. Morbach et al. compared ADC measures, both global and in specific regions of interest (ROIs) in subjects with and without emphysema [47], at two different points in time and found ADC values to vary only 5% and 6%, respectively. The larger ADC variation in emphysema patients was attributed to inhomogenity of the ADC map in this patchy disease.

^{3}HeMR Clinical Application: Inhalational Injury in Firefighters Post 9–11

The World Trade Center (WTC) destruction on 9/11/01 resulted in unprecedented pulmonary injuries to those 10,993 Fire Department of New York (FDNY) firefighters (FFs) that survived the heroic efforts to save lives and recover remains at this brutal act of terrorism.

The collapse pulverized the concrete, steel, plumbing, wiring, and other building materials from each 110 story tower, as well as furniture, carpeting, computers, and personal items. The smoke/dust burden was so high at and after the collapse of the WTC towers that the sheer airborne mass concentration of small particles alone (below the 2.5 µm diameter range conventionally considered 'respirable') at the WTC was likely sufficient to injure the tracheobronchial tree; in this unique exposure an unnaturally large percentage of highly alkaline and irritating larger particles were also inhaled. Additionally, the arduous rescue and recovery activities performed by the FFs strongly favored strenuous mouth breathing, overwhelming or impairing the natural clearance mechanism of nasal breathing. This allowed deep particle matter (PM) penetration into the lungs of FFs performing heavy labor on site [48], as confirmed by their recovery at bronchoalveolar lavage and sputum induction [49]. Except for limited use of self-contained breathing apparatuses, which

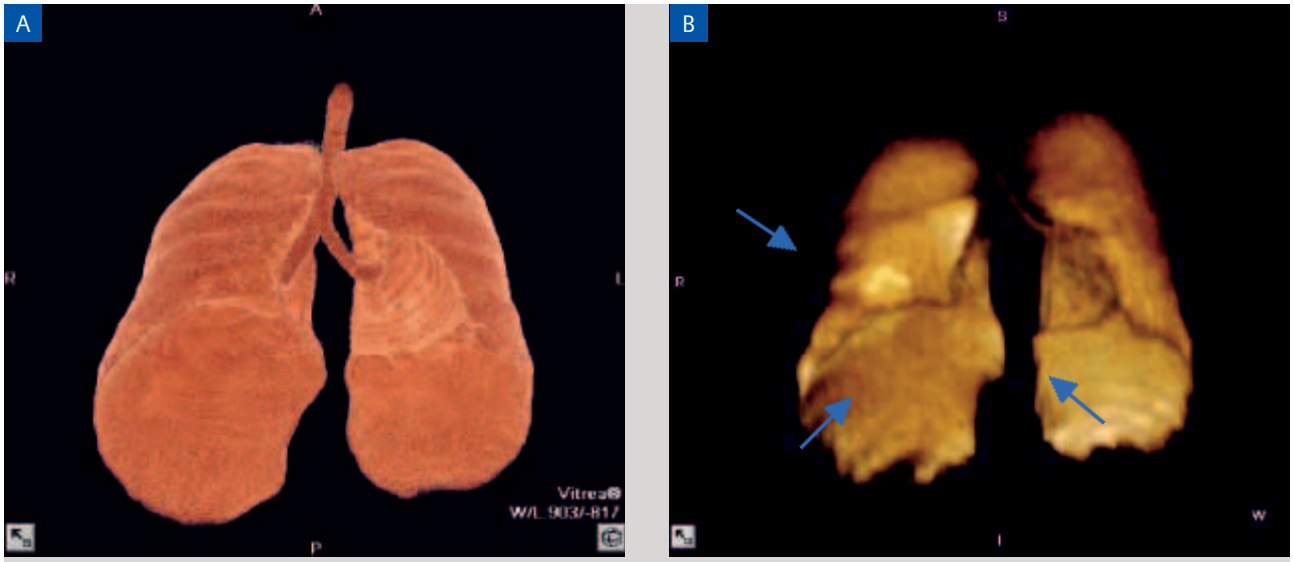

[Figure 3] *Volumetric 3D reconstruction from inspiratory CT (A) and (B) ^{3}HeMR Ventilation scan in a 33-year-old firefighter with pain, cough and dyspnea. Pulmonary function tests indicate mildly increased airway resistance and heterogeneity of ventilation, suggesting obstructive dysfunction, primarily due to peripheral airway abnormality. (A) CT demonstrates normal lung parenchyma while (B) ^{3}HeMR demonstrates small peripheral ventilation defects (arrows). The mean ADC was decreased in this firefighter consistent with small airway narrowing.*

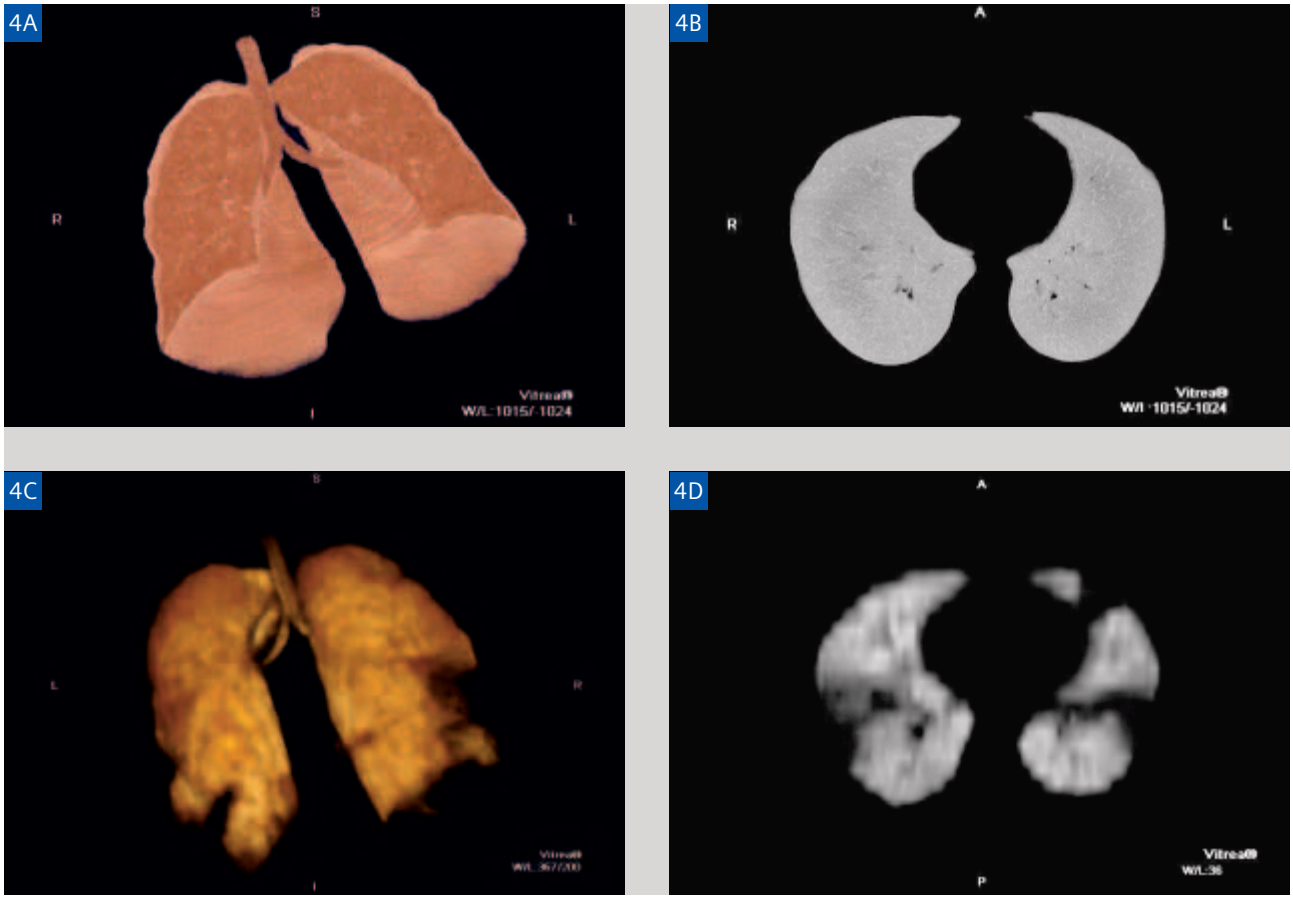

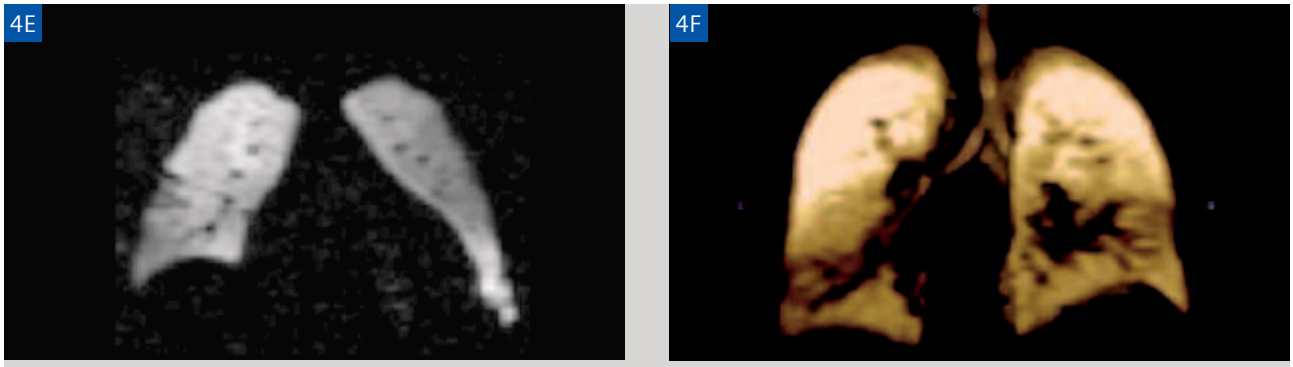

[Figure 4] *3D reconstruction (A) and axial image (B) from inspiratory CT. 3D reconstruction (C) and axial (D) from the original and follow-up (E) and (F) coronal ^{3}HeMR ventilation scans in a firefighter with dyspnea and cough. (He was 34 years old originally, age 37 at follow up) PFTs indicate severe large airway obstructive dysfunction, air trapping, and heterogeneous ventilation. (A and B) CT demonstrates normal lung parenchyma. (C and D) ^{3}HeMR demonstrates large segmental ventilation defects. (E and F) follow-up scans 2.5 years after the initial study demonstrate persistent ventilatory defects which appear diminished in size.*

supply only 8–15 minutes of air, respiratory protection was generally not used during the period of the attack and collapse of the WTC [50–52].

Respiratory exposure was mainly due, therefore, to the unusually intense inhalation and deposition of airborne PM in both central and peripheral (distal) airways. It is accepted that the size, mechanical, and chemical properties [53] of the PM could damage both the large and small airways in FFs.

Over the past 4 years two prevailing and debilitating chronic injuries have emerged in exposed firefighters (FFs): (1) airway hyperreactivity (new onset asthma or reactive airway dysfunction syndrome (RADS), and (2) an accelerated decline in pulmonary function tests (PFTs) suggesting chronic airway remodeling with obstruction. The injury is rampant in the FDNY; approximately 450 FFs have been forced to take early disability retirement because of persistent respiratory conditions, and additional 50–100 FFs are projected to be put on disability retirement because of post-9/11 respiratory disease. We are currently engaged in a study to assess the long-term consequences of this inhalational exposure using ^{3}HeMR. Importantly, HRCT scans in these subjects, including routine inspiratory/expiratory scans, (obtained as part of the Center for Disease Control (CDC) sponsored Medical Monitoring for NYC Fire Personnel Engaged in Emergency Response to 9/11) for have been insensitive to this injury (Figures 3A and 4A).

State of the Art: Pushing the ^{3}HeMR Envelope

Several issues have impeded the widespread exploitation of the capabilities of ^{3}HeMR in lung imaging, including: (1) the quantity of gas necessary for each examination; (2) the speed of the examination; and (3) the lack of metrics to define abnormalities.

The creation and application of a multi-channel ^{3}He coil (Fig. 5) at our institution [54, 55] has enabled implementation of Parallel Imaging for the first time in ^{3}HeMR. Multiple channel coils have particular advantages for hyperpolarized gas imaging. First is the inherent advantage of phased array coils in improving SNR. This is particularly important since hyperpolarized gases provide only a finite source of signal so that averaging does not improve SNR. Second, lung images must be acquired in a single breath-hold (or, in the case of dynamic imaging, during a single inspiration/exhalation cycle). Parallel Imaging with a multi-channel coil therefore increases the spatial resolution that can be obtained within this limited time.

The most important limitation of Parallel Imaging – loss of SNR – does not apply in hyperpolarized gas imaging. In all imaging, each phase encoding step acts as a kind of average. Parallel Imaging, by reducing the number of phase encoding steps, reduces SNR in conventional, thermally polarized imaging. In nonequilibrium systems such as ^{3}He, optimizing the flip angle can preserve the SNR without a time penalty.

On the other hand, hyperpolarized gas imaging draws signal from a fixed pool of polarization that does not recover. If the number of phase encoding steps is decreased, flip angles can be increased commensurately to make full use of that fixed pool. In addition, because the polarization decays with a T1 of tens of seconds, reducing imaging time by Parallel Imaging actually increases SNR.

Human images confirmed that there is no loss in SNR in Parallel Imaging of hyperpolarized ^{3}HeMR. Each image in Fig. 6 was acquired from a human volunteer after inhalation of 1

[Figure 5] *The appearance of the 2-channel transmit / 24-channel receive phased array system. (A) Is the external view of overall mechanical fixture; (B) top shell internal views; (C) bottom shell internal views*

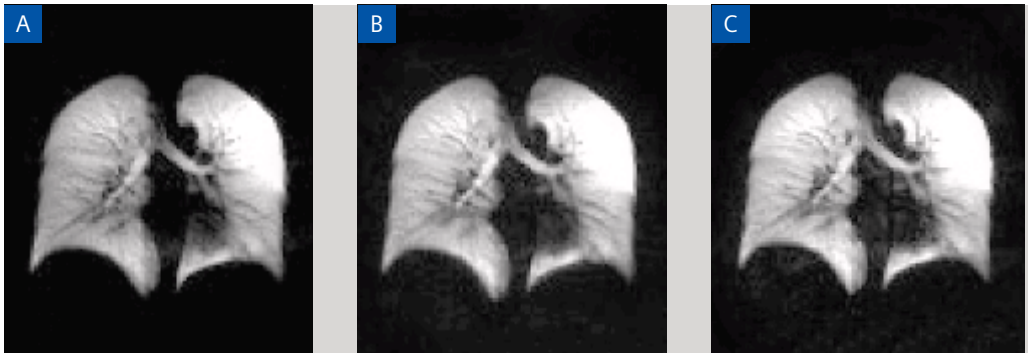

[Figure 6] *In vivo parallel ^{3}He lung MRI. Coronal images of the lungs with (A) iPAT = 1 (no iPAT); (B) iPAT = 2 and (C) iPAT = 4.*

liter (l) of gas (helium 240 ml and nitrogen 760 ml). Polarization of the ^{3}He gas was 47% thus 11% of the inhaled gas mixture was polarized.

The pulse sequence used for acquiring the images is a gradient echo sequence with TE 2.55 ms, TR 79 ms, FOV 300 mm, slice thickness 10 mm, resolution 128 x 128, number of average 1, and flip angle 10°. The data acquisition occurs immediately after the volunteer inhales the gas.

Figures 6 A, B, and C were acquired with parallel imaging acceleration (iPAT) factors of 1 (i.e., no parallel imaging), 2, and 4 respectively. Scan times were 12 s, 6 s and 3 s. The parallel imaging method used was Siemens mSENSE algorithm, which provides true decimated phase-encoding steps. SNR was measured in ten regions of interest (ROIs) in each of three images. The mean SNRs over these ten ROIs for each image are: 104.3, 113.3, and 96.0. Given the unavoidable small uncertainty of gas polarization and administration, the 12 s, 6 s, and 3 s scans have basically the same SNR.

Conclusion

^{3}HeMR lung imaging presents an important opportunity to study the airways and airspaces with technologies offering the potential to provide new insights into lung injury and disease states. By supplying functional and regional information as well as quantitative parameters it is possible to envision its application to a wide variety of conditions (asthma, occupational exposures, COPD, cystic fibrosis, hypersensitivity pneumonitis, obliterative bronchiolitis, bronchiectasis). ^{3}HeMR's implementation will be sped by Parallel Imaging and the determination of MR metrics such as diffusion. If the trend continues it is possible that ^{3}HeMR will become a standard measure of pulmonary function – an enticing thought for radiologists enamored by the notion that clinical and functional parameters are subservient to imaging measures.

References

[1] Gelb, A.F., et al., Pseudophysiologic emphysema resulting from severe small-airways disease. Am J Respir Crit Care Med, 1998. 158(3): p. 815–9.
[2] de la Hoz, R.E., et al., Frequency dependence of compliance in the evaluation of patients with unexplained respiratory symptoms. Respir Med, 2000. 94(3): p. 221–7.
[3] Woolcock, A.J., N.J. Vincent, and P.T. Macklem, Frequency dependence of compliance as a test for obstruction in the small airways. J Clin Invest, 1969. 48(6): p. 1097–106.
[4] West, J.B., Respiratory Physiology: The Essentials. 1974, Baltimore: Williams and Wilkins.
[5] Hogg, J.C., P.T. Macklem, and W.M. Thurlbeck, Site and nature of airway obstruction in chronic obsturctive lung disease. N Engl J Med, 1968. 268: p. 1355–1360.
[6] Otis, A.B., et al., Mechanical factors in distribution of pulmonary ventilation. J Appl Physiol, 1956. 8(4): p. 427–43.

[7] Mead, J., The lung's "quiet zone". N Engl J Med, 1970. 282(23): p. 1318–9.
[8] Sharp, J.T., S.K. Sweany, and P. Van Lith, Physiologic observations in diffuse pulmonary fibrosis and granulomatosis. Am Rev Respir Dis, 1966. 94(3): p. 316–31.
[9] McFadden, E.R., Jr., et al., Small airway disease. An assessment of the tests of peripheral airway function. Am J Med, 1974. 57(2): p. 171–82.
[10] Ingram, R.H., Jr. and C.F. O'Cain, Frequency dependence of compliance in apparently healthy smokers versus non-smokers. Bull Physiopathol Respir (Nancy), 1971. 7(1): p. 195–212.
[11] Ingram, R.H., Jr. and D.P. Schilder, Association of a decrease in dynamic compliance with a change in gas distribution. J Appl Physiol, 1967. 23(6): p. 911–6.
[12] Cutillo, A., et al., Pulmonary resistance and dynamic compliance as functions of respiratory frequency. Respiration, 1983. 44(2): p. 81–9.
[13] Levine, G., et al., Gas exchange abnormalities in mild bronchitis and asymptomatic asthma. N Engl J Med, 1970. 282(23): p. 1277–82.
[14] Grenier, P., M.P. Cordeau, and C. Biegelman, High-resolution computed tomography of the airways. J Thorac Imag, 1993. 8: p. 213–229.
[15] Lee, K.S., et al., Chronic infiltrative lung disease: comparison of diagnostic accuracies of radiography and low- and conventional-dose thin-section CT. Radiology, 1994. 191(3): p. 669–73.
[16] Muller, N.L. and R.R. Miller, Diseases of the bronchioles: CT and histopathologic findings. Radiology, 1995. 196: p. 3–12.
[17] Arakawa, H. and W.R. Webb, Air trapping on expiratory high-resolution CT scans in the absence of inspiratory scan abnormalities: correlation with pulmonary function tests and differential diagnosis. AJR Am J Roentgenol, 1998. 170(5): p. 1349–53.
[18] Kauczor, H.U., et al., Focal airtrapping at expiratory high-resolution CT: comparison with pulmonary function tests. Eur Radiol, 2000. 10(10): p. 1539–46.
[19] Park, C.S., et al., Airway obstruction in asthmatic and healthy individuals:inspiratory and expiratory thin-section CT findings. Radiology, 1997. 203: p. 361–367.
[20] Stern, E.J., et al., CT mosaic pattern of lung attenuation: etiologies and terminology. J Thorac Imaging, 1995. 10(4): p. 294–7.
[21] Stern, E.J. and M.S. Frank, Small-airway diseases of the lungs: findings at expiratory CT. AJR Am J Roentgenol, 1994. 163(1): p. 37–41.
[22] Webb, W.R., et al., Dynamic pulmonary CT: findings in healthy adult men. Radiology, 1993. 186: p. 117–124.
[23] Wittram, C., et al., Inspiratory and expiratory helical CT of normal adults. J of Thoracic Imag, 2002. 17: p. 47–52.
[24] Kauczor, H.U., et al., Pulmonary ventilation imaged by magnetic resonance: at the doorstep of clinical application. Eur Respir J, 2001. 17(5): p. 1008–23.
[25] Middleton, H., et al., MR imaging with hyperpolarized ^{3}He gas. Magn Reson Med, 1995. 33(2): p. 271–5.
[26] Bock, M., Simultaneous T2* and diffusion measurements with ^{3}He. Magn Reson Med, 1997. 38(6): p. 890–5.
[27] Hatabu, H., et al., T2* and proton density measurement of normal human lung parenchyma using submillisecond echo time gradient echo magnetic resonance imaging. Eur J Radiol, 1999. 29(3): p. 245–52.
[28] van Beek, E.J., et al., Functional MRI of the lung using hyperpolarized 3-helium gas. J Magn Reson Imaging, 2004. 20(4): p. 540–54.
[29] Kauczor, H.U., et al., Imaging of the lungs using ^{3}He MRI: preliminary clinical experience in 18 patients with and without lung disease. J Magn Reson Imaging, 1997. 7(3): p. 538–43.
[30] de Lange, E.E., et al., Lung air spaces: MR imaging evaluation with hyperpolarized ^{3}He gas. Radiology, 1999. 210(3): p. 851–7.
[31] Kauczor, H., R. Surkau, and T. Roberts, MRI using hyperpolarized noble gases. Eur Radiol, 1998. 8(5): p. 820–7.
[32] Altes, T.A., et al., Hyperpolarized ^{3}He MR lung ventilation imaging in asthmatics: preliminary findings. J Magn Reson Imaging, 2001. 13(3): p. 378–84.
[33] Guenther, D., et al., (3)He MRI in healthy volunteers: preliminary correlation with smoking history and lung volumes. NMR Biomed, 2000. 13(4): p. 182–9.
[34] Woodhouse, N., et al., Combined helium-3/proton magnetic resonance imaging measurement of ventilated lung volumes in smokers compared to never-smokers. J Magn Reson Imaging, 2005. 21(4): p. 365–9.
[35] McAdams, H.P., et al., Hyperpolarized ^{3}He-enhanced MR imaging of lung transplant recipients: preliminary results. AJR Am J Roentgenol, 1999. 173(4): p. 955–9.
[36] Gast, K.K., et al., MRI in lung transplant recipients using hyperpolarized ^{3}He: comparison with CT. J Magn Reson Imaging, 2002. 15(3): p. 268–74.
[37] Zaporozhan, J., et al., Functional analysis in single-lung transplant recipients: a comparative study of high-resolution CT, ^{3}He-MRI, and pulmonary function tests. Chest, 2004. 125(1): p. 173–81.
[38] Tanner, J.E., Restricted self-diffusion of protons in colloidal systems by the pulsed-gradient, spin-echo method. J. Chem. Phys., 1968. 49: p. 1768–1777.
[39] Keir, S.L. and J.M. Wardlaw, Systematic review of diffusion and perfusion imaging in acute ischemic stroke. Stroke, 2000. 31(11): p. 2723–31.
[40] Stejskal, E.O. and J.E. Tanner, Spin diffusion measurements: spin echoes in the presence of a time-dependent field gradient. J. Chem. Phys., 1965. 42: p. 288–292.
[41] Salerno, M., et al., Detection of regional microstructural changes of the lung in emphysema using hyperpolarized ^{3}He diffusion MRI. Proc. Intl. Soc. Mag. Reson. Med., 2000: p. 9.
[42] Chen, X.J., et al., Detection of emphysema in rat lungs by using magnetic resonance measurements of ^{3}He diffusion. Proc Natl Acad Sci USA, 2000. 97(21): p. 11478–81.
[43] Brookeman, J., et al., Studies of ^{3}He diffusion coefficient in the human lung: Age related distribution patterns. Eur. Radiol., 1999. 9: p. B21.
[44] Salerno, M., et al., Emphysema: hyperpolarized helium 3 diffusion MR imaging of the lungs compared with spirometric indexes-initial experience. Radiology, 2002. 222(1): p. 252–60.
[45] Salerno, M., et al. Hyperpolarized ^{3}He diffusion imaging in smokers: Comparison with computed tomography and spirometry. in Proceedings of the International Society of Magnetic Resonance in Medicine. 2002.
[46] Yablonskiy, D.A., et al., Quantitative in vivo assessment of lung microstructure at the alveolar level with hyperpolarized ^{3}He diffusion MRI. Proc Natl Acad Sci U S A, 2002. 99(5): p. 3111–6.
[47] Morbach, A.E., et al., Diffusion-weighted MRI of the lung with hyperpolarized helium-3: a study of reproducibility. J Magn Reson Imaging, 2005. 21(6): p. 765–74.
[48] Banauch, G.I., A. Dhala, and D.J. Prezant, Pulmonary disease in rescue workers at the World Trade Center site. Curr Opin Pulm Med, 2005. 11(2): p. 160–8.
[49] Fireman, E.M., et al., Induced sputum assessment in New York City firefighters exposed to World Trade Center dust. Environ Health Perspect, 2004. 112(15): p. 1564–9.
[50] Use of respiratory protection among responders at the World Trace Center Site – New York City, September 2001. MMWR Morb Mortal Wkly Rep, 2002. 51: p. 6–8.
[51] Banauch, G.I., et al., Persistent hyperreactivity and reactive airway dysfunction in firefighters at the World Trade Center. Am J Respir Crit Care Med, 2003. 168(1): p. 54–62.
[52] Banauch, G.I., et al., Bronchial hyperreactivity and other inhalation lung injuries in rescue/recovery workers after the World Trade Center collapse. Crit Care Med, 2005. 33(1 Suppl): p. S102–6.
[53] Gavett, S.H., et al., World Trade Center fine particulate matter causes respiratory tract hyperresponsiveness in mice. Environ Health Perspect, 2003. 111(7): p. 981–91.
[54] Lee, R.F., et al., Advantages of Parallel Imaging in Conjunction with Hyperpolarized Helium – A New Approach to MRI of the Lung. Magnetic Resonance in Medicine, in press.
[55] Lee, R.F., et al. A 24-channel phased-array system for hyperpolarized helium gas parallel MRI to evaluate lung functions. Proceedings of 27th annual International conference of the IEEE Engineering in Medicine and Biology Society, p. ##, 2005.

A Glimpse of the Wide Range of Presentations Given at the 4th MAGNETOM World Summit

A. Nejat Bengi, M.D.

Siemens Medical Solutions, Erlangen, Germany

New Paradigms in MR

Dr. Elizabeth Hecht, New York University (NYU), USA stressed the importance of iPAT (integrated Parallel Acquisition Technique) and its use particularly in abdominal imaging. With the help of the parallel imaging techniques and the MAGNETOM Avanto, the protocols with 256 matrix have changed to 512 matrix and this within a shorter breath-hold time. Fast imaging with iPAT results for VIBE and 2D FLASH were impressive. A new approach to fast liver imaging was introduced with three-phase arterial imaging including early arterial, mid-arterial and late arterial phase (Figure 1) which is believed to help diagnose early enhancing lesions more easily. Homogenous and consistent fat saturation improved the image quality of TSE fat sat imaging and now NYU prefers to use T2 fat sat instead of TurboSTIR imaging in the abdomen. Dr. Hecht also mentioned the improvements in evaluation of organ function like liver and kidney. Another topic was the use of diffusion imaging in evaluation of liver malignancies. Improved MR Cholangiopancreatography (MRCP) was also a significant help in routine abdominal scanning. Pelvic imaging has also seen a significant improvement thanks to the iPATx2. Peripheral MRA examinations have been easier to perform with better diagnostic quality due to less venous contamination. A recent approach is also the non-contrast ECG triggered HASTE MR angiography (MRA) which looks promising as it also provides the ability to perform MRA without any intravenous contrast infusion. Whole body imaging with Tim (Total imaging matrix) has also opened the possibility of staging tumors on a reliable basis.

VIBE Volume Interpolated Breathhold Examination
FLASH Fast Low Angle Shot

Dr. Schlemmer, Eberhard-Karls-University in Tübingen, Germany talked about new protocols and methods with the 1.5T MAGNETOM Avanto. He also focused on the tremendous increase of speed in MR examinations with the help of iPAT parallel imaging techniques and also the use of SPACE imaging in routine scanning. An interesting perspective from Dr. Schlemmer was on disease-specific imaging techniques rather than organ imaging. An example is the MRI of the rectal cancer which includes abdomen-pelvic imaging, MRCP, colonography and liver imaging in addition to rectal imaging. Lung imaging is also showing strong advancements with the new imaging techniques and today nodules of 5–7 mm can be detected with the help of MRI. Furthermore, MRI has the advantage of showing the bone marrow, soft tissue and lymph nodes (Figure 2). Diffusion imaging in the body is also a new possibility in imaging of the malignancies.
Screening for cardiovascular pathologies, neuro and tumor are becoming quite popular using the MAGNETOM Avanto and Tim at Tübingen University.

SPACE Sampling Perfection with Application optimized Contrasts using different flip angle Evolutions

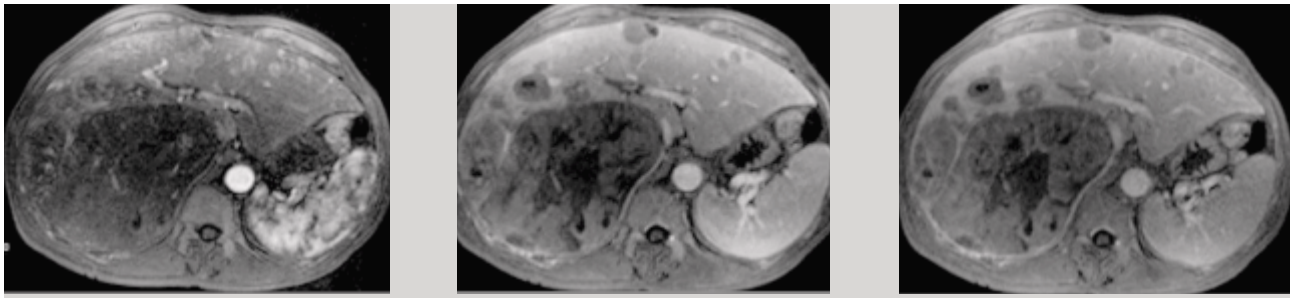

[Figure 1] *VIBE with iPATx2 showing multiple arterial phases in liver imaging.*

One of the greatest advantages of parallel imaging techniques is the improvement it has brought to MR angiography (MRA) techniques. Dr. Schönberg, Ludwig-Maximilians-University Großhadern, Germany, a worldwide known expert in this area, summarized the advantages of paradigm shift brought about by iPAT (integrated Parallel Acquisition Technique) as follows. First and foremost, the arrival of isotropic imaging rather than the previously used anisotropic techniques. In evaluation of stenosis of vessels it is now possible to evaluate the 2 dimensions and give area stenosis information rather than the one dimensional diameter stenosis measured in the past. Static MRA has already become dynamic MRA thanks to faster imaging. Now you can obtain morphology and functional information in one exam and of course local examinations are changing into whole body exams.

Margaret King, Wake Radiology, Raleigh MRI Center, USA classified the advantages and the new examination techniques of MAGNETOM Avanto under three categories: Inline technologies, workflow improvements and software/hardware improvements. Her personal favorite technique is Phoenix which allows protocol exchange by use of images.

The Asian perspective of MAGNETOM Trio was presented by Mr. Wong, Siemens Medical Solutions application specialist. His talk started with the physical limitations of the three Tesla systems and completed by the solutions provided by Siemens in making 3T a completely clinical system. He showed various examples including whole-body imaging. The prostate examination results were extremely striking in terms of image quality and clinical usefulness.

Dr. Schlemmer's second talk in the MAGNETOM World Summit referred to the improvements with 3T systems. Having the opportunity to be able to use both a MAGNETOM Avanto and a MAGNETOM Trio, A Tim System, he first of all highlighted the maximum speed factor of 16 with MAGNETOM Trio compared to MAGNETOM Avanto. His talk included many examples of improved spatial and temporal resolution in imaging with large Fields of View (Figure 3). This has naturally resulted in improved image quality in every part of the body. Improved contrast-to-noise ratio (CNR) affected the MRA examinations the most. Another practical advantage of the MAGNETOM Trio, A Tim System is that it helps increase the patient throughput which is a direct result of decreased examination time with better temporal resolution due to high field strength and parallel imaging techniques combination.

Dr. Andrew Litt, New York University began his talk by mentioning the natural outcome of 3T and the way it compensates the loss of signal with parallel imaging techniques. There again, the use of parallel imaging techniques helps

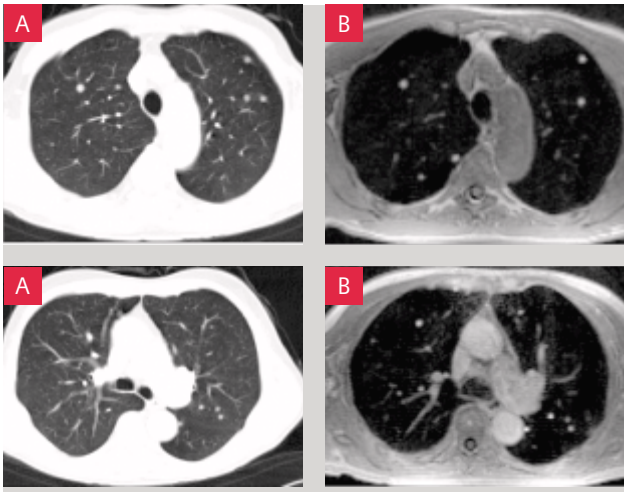

[Figure 2] *Lung imaging with MRI has shown significant improvements and is comparable to CT (A) in lesions ranging in size from 5 to 7 mm.*

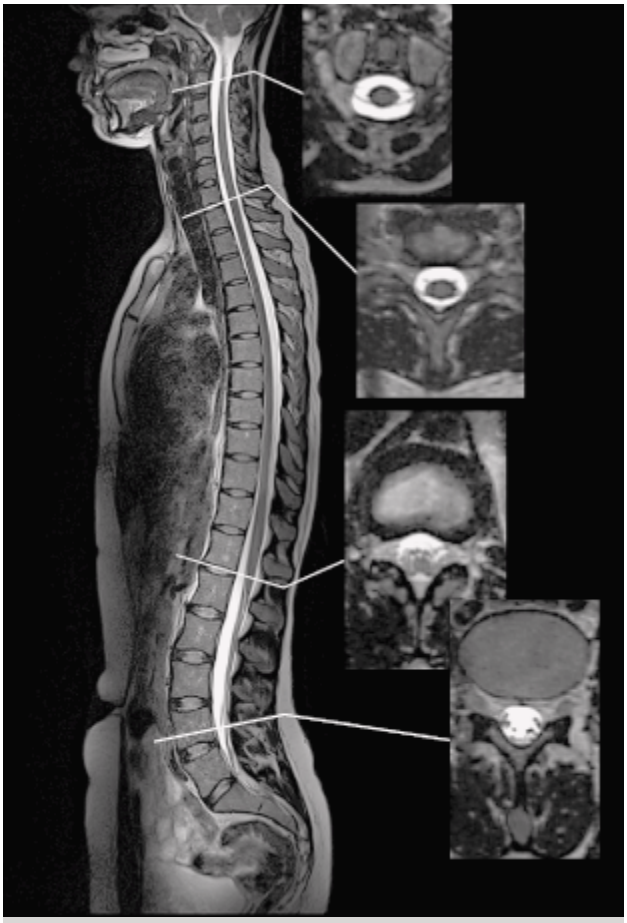

[Figure 3] *Isotropic high-resolution whole spine imaging with MAGNETOM Trio, A Tim System.*

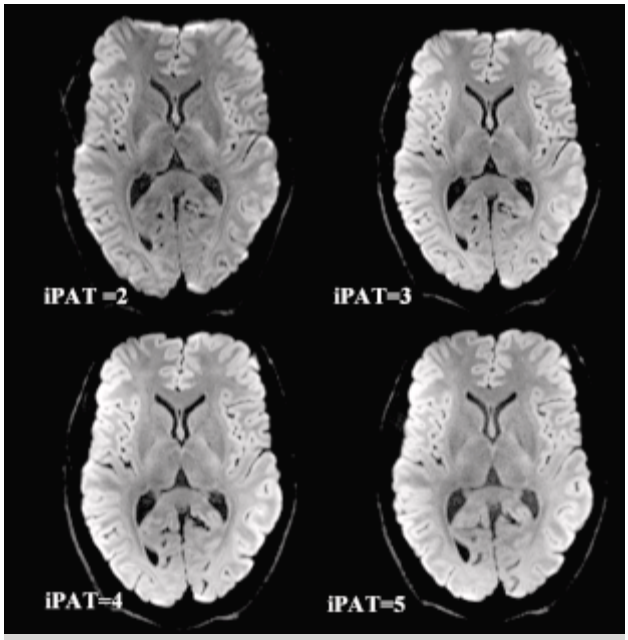

[Figure 4] *Eradication of susceptibility artifacts by increased PAT factor.*

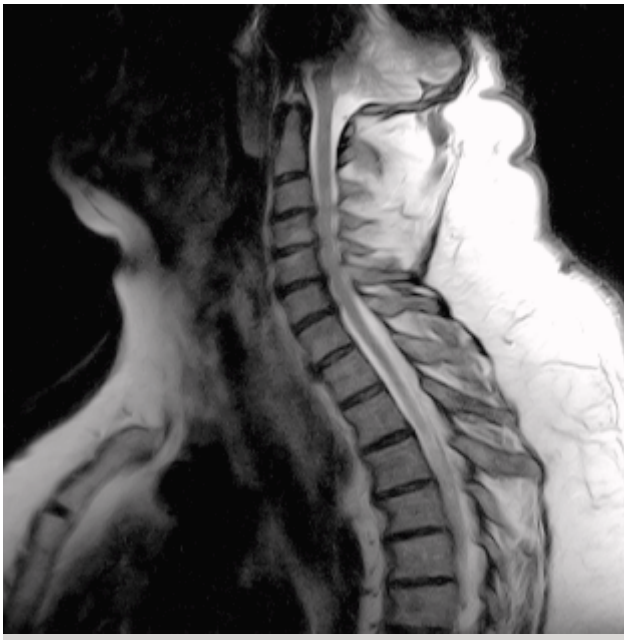

[Figure 5] *MAGNETOM Espree with its large bore of 70 cm allows the examination of obese patients. T2-weighted cervical spine imaging of an obese patient around 210 kg (463 pounds).*

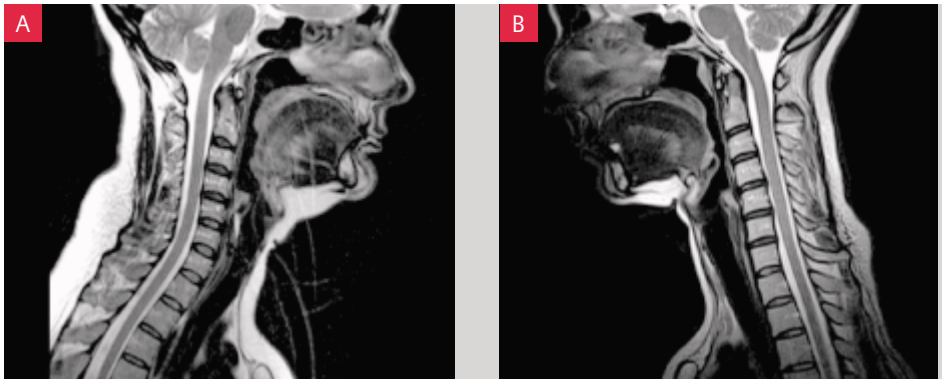

[Figure 6] *Cervical spine examination with MAGNETOM C! 0.35T is comparable to 1.5T in image quality.*
(A) 1,5T
(B) 0,35T

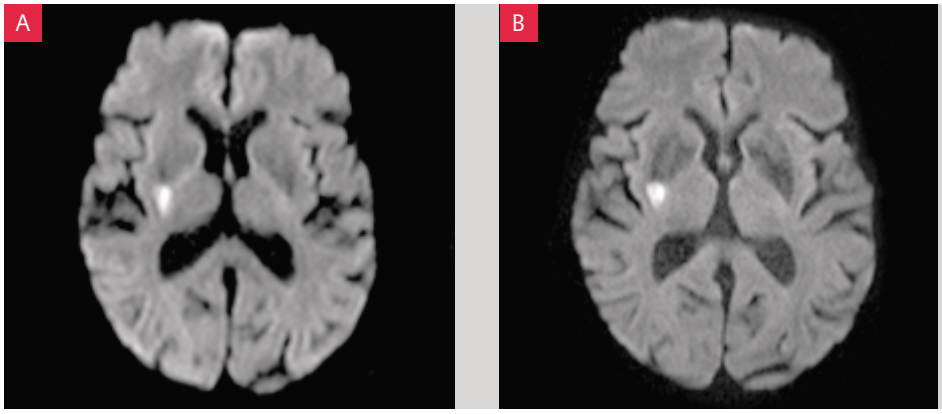

[Figure 8] *One of the great advantages of the upgraded MAGNETOM Symphony, A Tim System is the improved image quality of EPI imaging.*
(A) Before the upgrade. 1.7 x 1.7 x 6.0 mm^3
(B) After the upgrade 1.1 x 1.1 x 6.0 mm^3

reduce the susceptibility artifacts seen in 3T (Figure 4). So it is a perfect combination. His team has tried different techniques to compensate for the T1 contrast challenge with 3T. Recently the T1 FLAIR, a dark fluid technique seemed to be providing good answers to this requirement. Like other speakers he stressed on the use of 3T and its great advantages in MRA.
With regard to advanced techniques, he mentioned that MR spectroscopy (MRS) of the spinal cord and spinal cord tractography were new possible techniques with the MAGNETOM Avanto.

New Dimensions in MR

After Dr. Cécile Mohr (Siemens Medical Solutions, Head of MR Market Segment Management, Erlangen, Germany) introduced the new MAGNETOM Espree and MAGNETOM C! systems, Dr. Lentschig from MR Zentrum Bremen Mitte, Germany talked about his experiences with the MAGNETOM Espree and showed clinical results from head to toe, proving that MAGNETOM Espree is an excellent 1.5T system. This Open Bore system - a combination of a large CT-like 70 cm bore diameter and very short system length of 125 cm – is a perfect choice for claustrophobic and very large patients (Figure 5) showing excellent clinical performance. The 1.5T field strength allows advanced applications such as MR spectroscopy, functional imaging, cardiac imaging, whole-body imaging and other advanced applications.
Dr. Chip Kyle, Cleveland Community Hospital, USA gave a detailed presentation showing the surprisingly advanced clinical imaging results from the mid-field MAGNETOM C! (0.35T) which were comparable to high-field (1.5T) image results (Figure 6).
New dimensions in productivity went one stage further with the results that Dr. Cortes Domingues from Multi-Imagem Clinic, Ipanema, Brazil showed from his routine schedule in Rio de Janeiro. With his MAGNETOM Symphony with Quantum gradient system in 2004 he performed a total of 13,624 examinations with a record number of patients of 1,298 in the month of July. His private imaging center is open from 6:30 A.M. to 11:30 P.M. every day of the week except Sundays. He has preferred examining difficult cases which require advanced applications with the new MAGNETOM Avanto. His maximum number of patients per day has been 49 and in August 2005 he was able to examine a total number of 905 patients in a single month (Figure 7).
Dr. Fellner, Allgemeines Krankenhaus in Linz, Austria showed the new dimension of MAGNETOM Symphony, A Tim System which is the upgraded version with Tim (Total imaging matrix) capabilities. He said that he had seen an overall

[Figure 7] *Using the MAGNETOM Avanto, Dr. Cortes Domingues had the possibility to examine 905 patients in one month. 3 other magnets are available in his clinic and MAGNETOM Avanto is only used for the most advanced examinations.*

increase in image quality and also overall decreased examination times. Referring specifically to the coil system, e.g. the Matrix Coils, he mentioned the reduction in measurement times, improved quality of the Echo Planar Imaging (EPI) sequences (Figure 8) and higher spatial resolution with the new 12 channel Head Matrix coil. He also said that the body examinations with the new Matrix coils and the knee examination with the 8 channel knee coil had shown dramatic improvements. Contrast enhanced MR Angiography (ceMRA) examinations especially showed remarkable improvement with the new upgrade.

New Horizons in MR

Dr. Walter, Johann-Wolfgang-Goethe University, Frankfurt/Main, Germany, was the first speaker in the session titled "New horizons in MR" and gave a highly interesting talk about neuroeconomics and the use of functional MR imaging (fMRI) in this area. At the beginning of his talk he cited Vernon Smith, Nobel Prize winner of economics in 2002, who said "The new brain imaging technologies have motivated neuroeconomic studies of the internal order of the mind...We are only at the beginning of this enterprise but it promises a fundamental change in how we think, observe and model decision in all its context". He gave examples of the use of fMRI in defining the neural correlates of behavioral preference for culturally familiar drinks like the choice of Pepsi or Coke or between different coffee brands. Another topic he mentioned was the use of fMRI to analyze the reward magnitude.

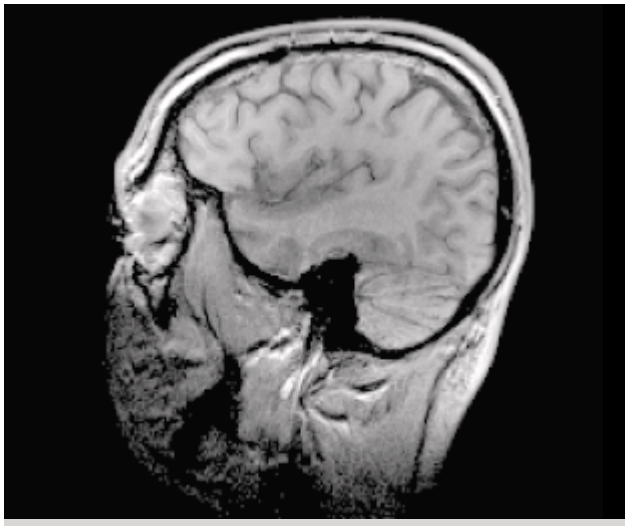

[Figure 9] *MAGNETOM Trio, A Tim System allows 3D acquisitions with speed enhancements of factor 16 thanks to GRAPPA.*

[Figure 10] *Neuro3D task card will allow the fused display of structural, DTI and fmRI data.*

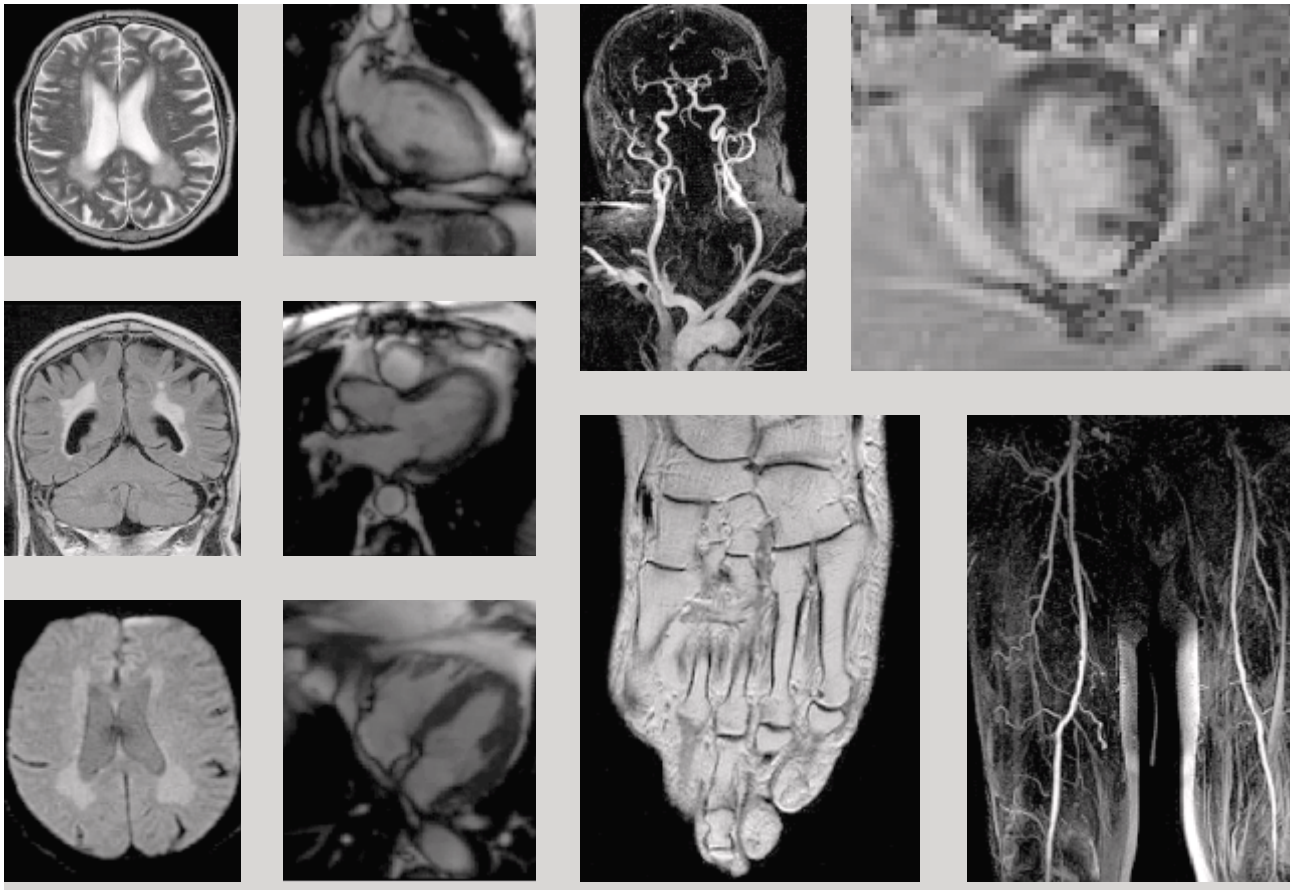

[Figure 11] *Whole-body MRI screening including angiography of a 70-year-old patient with type 2 diabetes since 15 years shows enhanced white matter lesions, silent inferior wall infarct. There were no signs of osteomyelitis.*

Dr. Berthold Kiefer, MR Development of Clinical Applications (Erlangen, Germany), talked about the recent developments and future perspectives of the development group in Erlangen. His clear message was the paradigm change from 2D to 3D and he explained the strategies behind to speed up the acquisition times of 3D volumes (Figure 9)

Dr. Krüger, MR Development of Advanced Neuro Applications (Erlangen, Germany) showed the future development directions in functional MRI. Improved fMRI statistics with inline GLM (General Linear Model) calculations is one such direction. Another development will be the enhanced visualization with the Neuro3D task card, such as fMRI cine mode analysis. In diffusion-weighted imaging, diffusion is directed in more than 12 directions and the capability to define these directions by the user will be the major improvements. Inline reconstruction of diffusion tensor data will be a workflow oriented development. Diffusion tensor visualization in a Neuro3D task card will allow fusion of anatomical information and DTI and also fMRI and DTI (Figure 10). There will also be improvements in the segmented EPI sequence. From the anatomical imaging side 3D isotropic sequences and SWI (Susceptibility-weighted imaging) will be the major near future developments.

Dr. Jeff Bundy, director of the US Research and Development group, showed the clinical developments' future from his perspective. He presented a wide range of topics varying from 7T to Molecular Imaging. The IMRIS solution for intraoperative MR with a scanner mounted to the ceiling and moving around according to the requirements of the operation room and the imaging clinic was an interesting concept.

Dr. Cécile Mohr, head of MR Market Segment Management in Erlangen, Germany presented the application leadership of Siemens MR with impressive image examples for integrated Parallel Imaging Technique, SPACE, SWI, motion insensitive techniques like BLADE and PACE (Prospective Acquisition CorrEction), integration for more efficient workflow, the move of MRI from organ imaging to disease imaging and also recent developments in molecular imaging.

Dr. Schönberg, Ludwig-Maximilians University, Großhadern, Germany, made an excellent presentation showing the use of MR in diabetics where there is a substantially higher incidence of macro- and microvascular diseases. Early diagnosis of the disease and the complications at an early phase will open the way for prevention of complications. He stated that MAGNETOM Avanto and MAGNETOM Trio, A Tim System allow disease specific whole-body protocols with no compromises in spatial or temporal resolution (Figure 11).

Mark Lourensz, St. Vincent's Hospital Melbourne, Australia showed clinical examples of the use of Tim (Total imaging matrix) for whole-body imaging. He said that the indications for whole-body imaging were metastasis screening (Figure 12), diagnosis of vascular malformations, sarcoma staging, muscle injuries or myopathy and systemic diseases. The cost

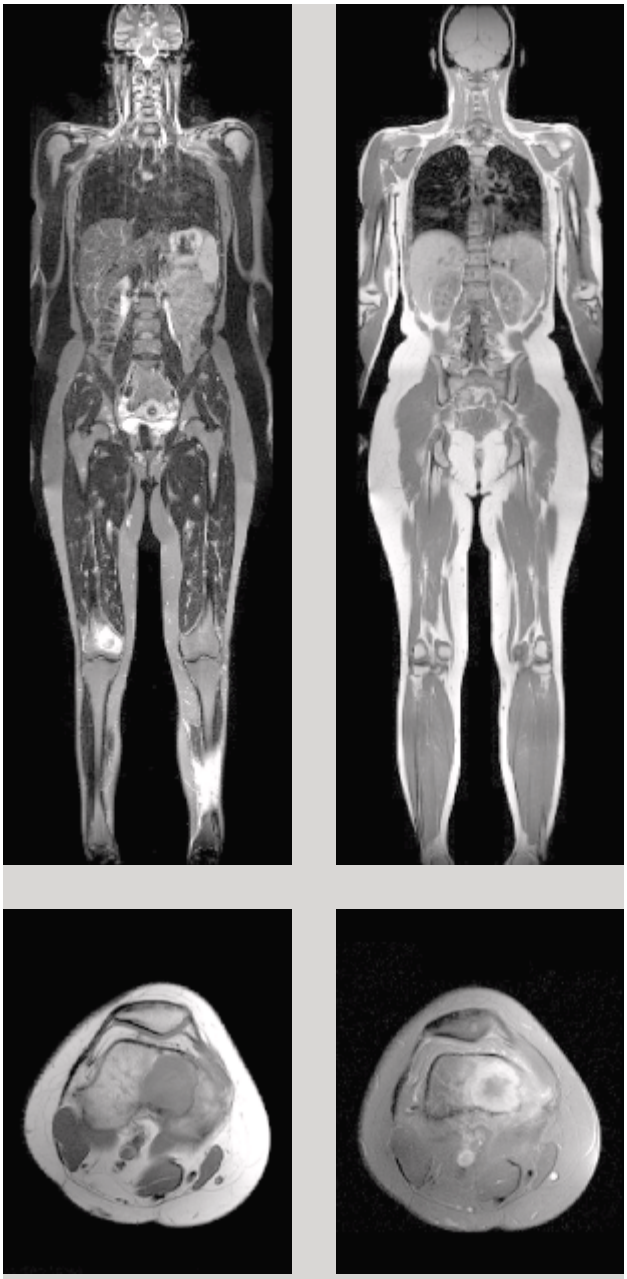

[Figure 12] *Whole-body MRI shows lesions in the knee of a patient with metastatic melanoma. More detailed examination of other slices showed other lesions in the pelvis and hips.*

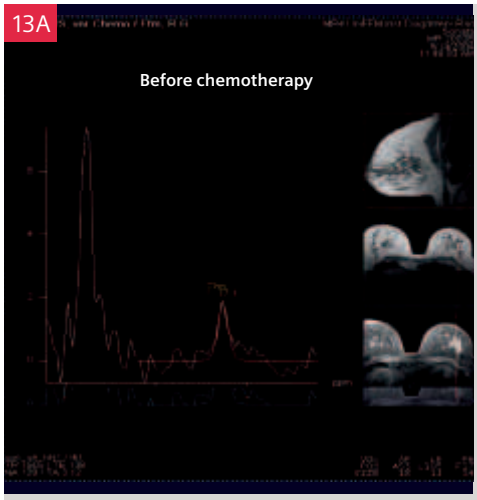

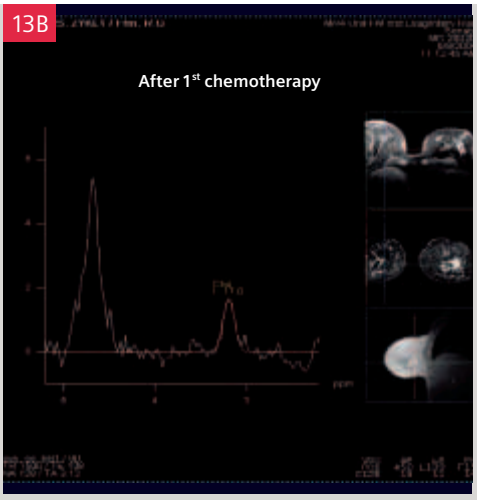

[13A] *43-year-old patient. Palpation of a suspect node. Mammography, ultrasound and biopsy were performed. The spectrum shows an elevated choline peak (integral 17.1).*

[13B] *MRS scan after the first cycle of chemotherapy: The spectrum shows no changes of choline (integral 17.0).*

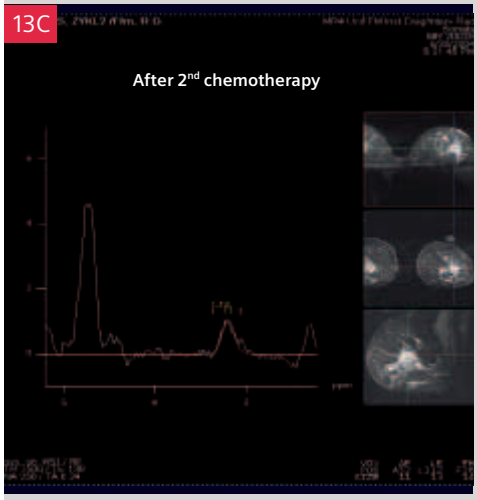

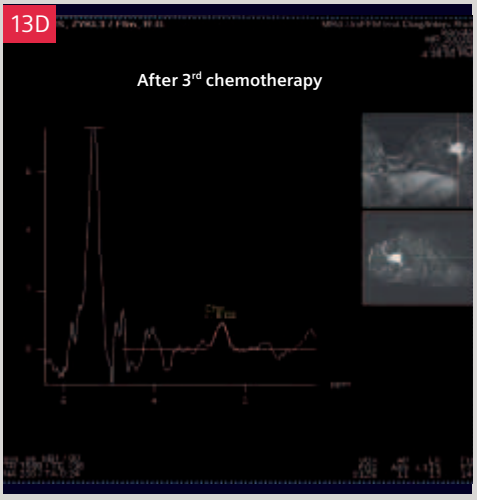

[13C] *MRS follow-up scan after the 2nd cycle of chemotherapy. The choline signal decreased to an integral of 11.3.*

[13D] *MRS follow-up scan after the 3rd cycle of chemotherapy. The choline signal is still elevated (integral 9.03).*

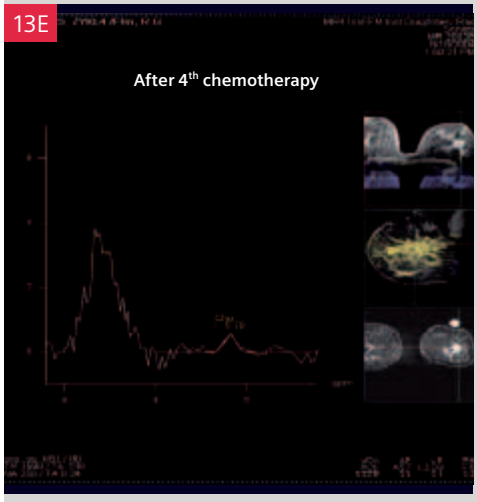

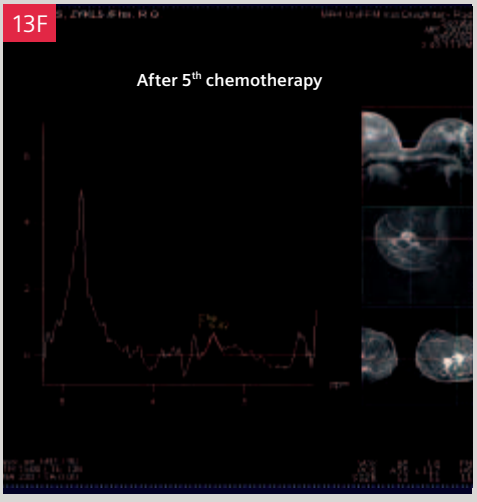

[13E] *MRS follow-up scan after the 4th cycle of chemotherapy. The choline signal still shows an integral of 5.79.*

[13F] *MRS follow-up scan after the 5th cycle of chemotherapy. The choline signal is decreased to an integral of 5.32.*

[Figure 13] *MRS can be used for follow-up of chemotherapy. The changes in choline signal after each treatment showed the effectiveness of the used chemotherapy.*

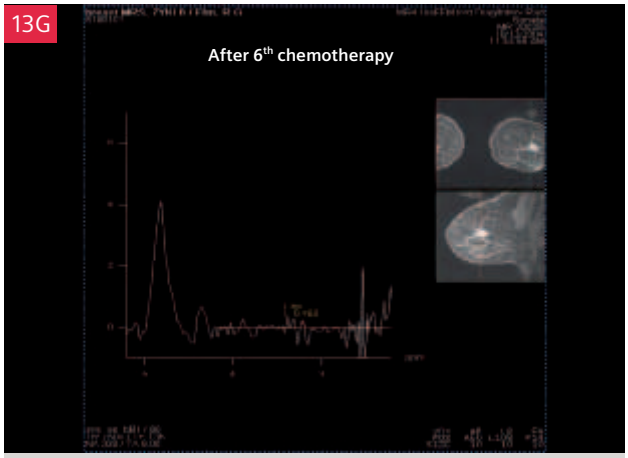

[13G] *MRS follow-up scan after the 6th cycle of chemotherapy. There is still a choline signal visible (integral 0.46).*

effective combination of Tim and iPAT (integrated Parallel Acquistion Technique) proved to be more sensitive than nuclear medicine.

Dr. Porter, First Hill Imaging, Seattle, USA, gave a detailed explanation of the indications for breast MR and provided clinical examples showing the use of VIEWS technique. He said that bilateral examination is extremely important and should always be the method of choice so that contralateral tumor can be excluded. He also gave examples of the post-processing technique showing slices pivoting around the nipple which he refers to as "RADIANT". He also stressed the use of computer aided diagnosis (CAD) in breast MR which will help workflow and also a more reliable diagnosis of lesions combining various parameters. He concluded by saying that MR is a powerful tool for breast diagnosis and a necessary adjunct to mammography, ultrasound and breast exam. His current equipment MAGNETOM Avanto allows assessment of morphology and kinetics. MR is also having an increasing impact in diagnosis, staging and management of breast cancer.

Dr. Vogl, Johann-Wolfgang-Goethe-University Frankfurt/Main, Germany, showed the use of MR spectroscopy in diagnosis of breast diseases. He presented clinical examples of the use of single voxel WIP sequence he uses in his clinic. He added that MR spectroscopy could be an extremely useful tool in predicting response to chemotherapy (Figure 13). Dr. Ichiba, Jikei University School of Medicine, Tokyo, Japan, is one of the leaders in Japan in the use of whole-body diffusion-weighted imaging (DWI). He showed his recent experience of DWI combined with PACE (Prospective Acquisition CorrEction) in diagnosis of abdominal pathologies where respiration artifacts can be problematic. The image quality of diffusion-weighted imaging has been dramatically improved with the use of iPAT and PACE (Figure 14) according to Dr. Ichiba. Another important remark was that the use of "body diffusion" is useful both in detection of malignant tumor and characterization of mass lesion.

Dr. Lichy, Eberhard-Karls-University Tübingen, Germany, talked about whole-body MRI in patients with advanced malignant melanoma. He said that whole-body MRI is feasible in clinical routine and even in lung imaging it is reaching the standards of high-resolution CT.

Dr. Bruce Porter's second talk at the Summit was whole-body breast cancer staging. According to his experience whole-body MR can less invasively improve staging of breast cancer, thereby saving cost and reducing morbidity. He also added that MR can be used for follow-up of chemotherapy. He said that he was certain that the future of cancer staging was whole-body MR.

Dr. Trost, St. Vincent's Hospital, Melbourne, Australia, presented his results using the SPACE sequence for different contrasts like T2, Dark Fluid and T1. The SPACE sequence (Sampling Perfection with Application optimized Contrasts

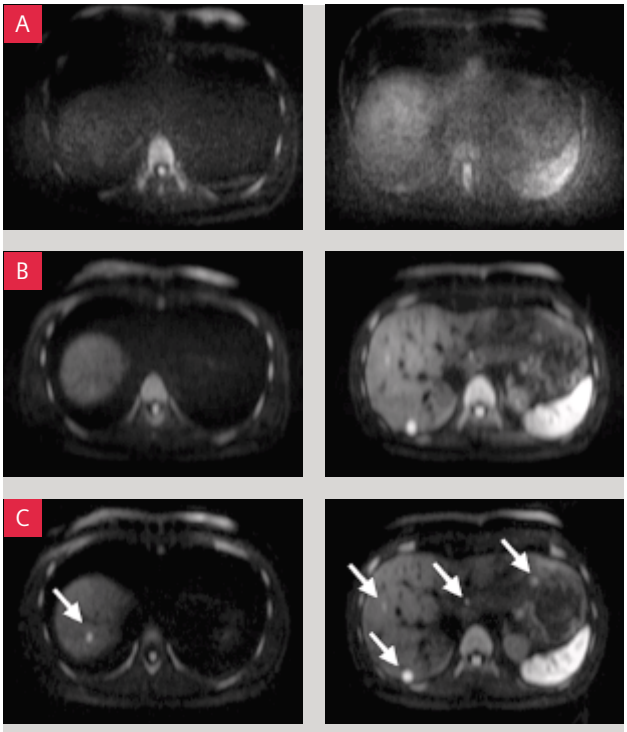

[Figure 14] *DWI with PACE is affected less by respiratory artifacts which allows diagnosis of more lesions in the abdomen.*
A = Free Breathing, B = Respiratory Triggered, C = PACE

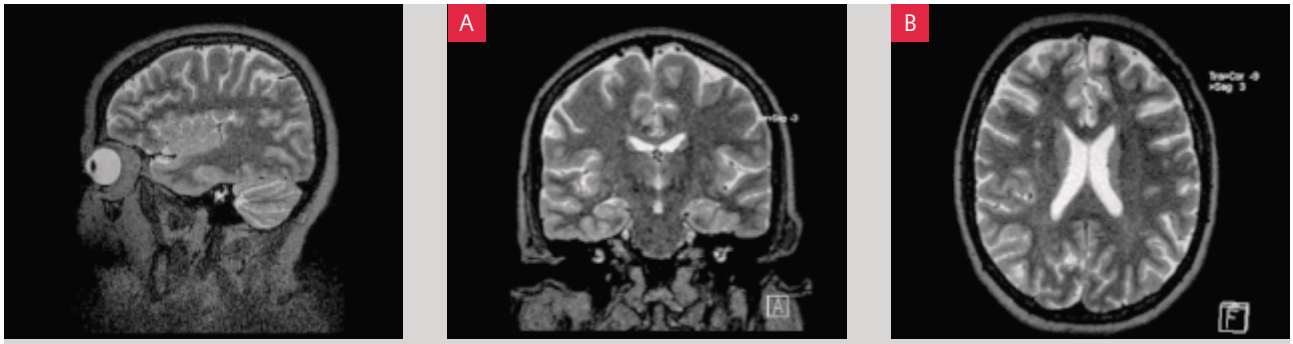

[Figure 15] *Isotropic images from SPACE 3D allows reformats in any orientation without any loss of information. T2 SPACE sagittal acquisition with voxel size of 0.9 x 0.9 x 0.9 mm³ and axial (B) and coronal (A) reformats.*

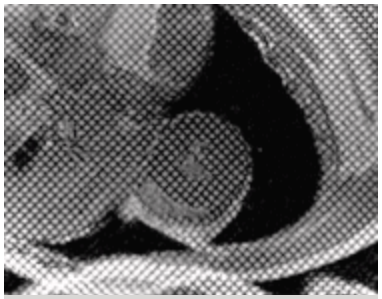

[Figure 16] *Tag persistence improves with longer T1 values and lower flip angles. Tissue T1 is longer at 3T compared to 1.5T as a result tag persistence improves with 3T.*

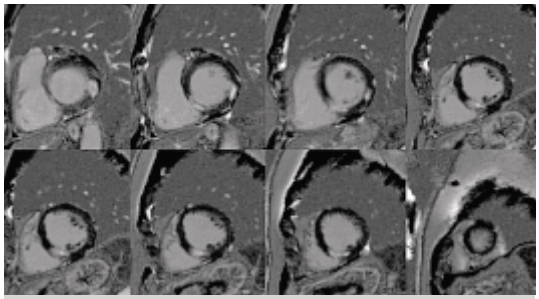

[Figure 17] *Single breath-hold multi-slice late enhancement at 3T showing a posterior infarct. PSIR single shot TrueFISP without TI optimization.*

[Figure 18] *Prototype of MR PET system developed by Siemens Medical Solutions, Erlangen, Germany.*

using different flip angle Evolutions) is clinically relevant today thanks to the increased speed with iPAT. His examples with isotropic T2 and Dark Fluid SPACE showed excellent reformat results in different orientations which will possibly in the future allow acquisition of only one 3D dataset and use different reformats in clinical routine rather than scanning for different orientations (Figure 15). SPACE also showed smaller lesions better than 2D imaging techniques. 3D imaging also relies less on slice positioning so for tumor cases where follow-up is extremely important, 3D imaging is more appropriate.

Dr. Ruehm, University of California at Los Angeles, USA, showed the advanced capabilities of MAGNETOM Trio, A Tim System. Especially the combination of iPAT and 3T allows very fast scanning of the heart, a good example would be evaluation of the function of the heart within only 5 heartbeats. Myocardial tagging has also shown significant improvements as tag persistence improves with longer T1 values (Figure 16). Also due to higher signal, one can go to smaller voxel sizes with 3T. Also MR angiography (MRA) has shown extensive improvements in spatial and temporal resolution.

Dr. Schönberg showed the paradigm changes in cardiac MRI with 3T. With 3T multi breath-hold became single breath-hold (Figure 17), 128 matrix became 256, gated cine breath-hold became free-breathing realtime, 2D cine became 3D cine. He presented clinical comparisons for each paradigm change.

Dr. Hengerer, Siemens Medical Solutions, Erlangen, Germany, gave a detailed presentation showing the status of Molecular Diagnostics today and the future developments foreseen by Siemens Medical Solutions. He said that molecular diagnostics is based on three pillars: In Vitro Diagnostics, Molecular Imaging and Knowledge driven Healthcare. Talking about the imaging side, the new developments in the area of MR-PET were mentioned (Figure 18). He said that there were numerous advantages of MR-PET over PET CT, such as better soft tissue contrast and lower radiation.

This article discusses clinical uses which are not commercially available in the US.

Looking back at the 4th MAGNETOM World Summit Singapore, September 17–20, 2005

Antje Hellwich

Siemens Medical Solutions, Erlangen, Germany

Last year's Summit took place in Singapore. Located just south of Peninsular Malaysia, the Republic of Singapore is an island approximately 618 square kilometres (239 square miles) in area. Founded by Sir Stamford Raffles in 1819, Singapore has long been a shipping and commercial centre of the region.

Built in 1928, the neoclassical Fullerton Building has housed the General Post Office, the Exchange, the Chamber of Commerce and the Inland Revenue Authority of Singapore in its time. Beautifully restored and reopened in 2001 as the Fullerton Hotel, this epitome of Palladian architecture in Singapore was the perfect location for the MAGNETOM World Summit.

MAGNETOM World Summit – a part of Life

The MAGNETOM World Summit is part of Life, Siemens' unique customer care solution that helps you get the most from your investment in a MAGNETOM system. With its programs and services Life sharpens your skills so you can see optimal clinical value. It provides the support you need to maximize productivity and it assures that as technology changes, you will always be at the cutting edge.
Life. You can count on it.

Saturday evening

To unwind after the long flights we had the Welcome Reception at LASH, one of the hip and cool clubs in Singapore located by the bay, right next to the Merlion.
Half lion, half fish, the Merlion sculpture has been Singapore's national icon since 1972. After all, the city's name is derived from the Sanskrit words "singa" and "pura" which together mean "lion city". The Merlion is located right in front of the Fullerton and is overlooking Marina Bay.

Sunday

Right after breakfast presentations on new paradigms, new dimensions and new horizons in MR captured our audience. P.D. Dr. Schlemmer from the Eberhard-Karls-University in Tübingen, Germany summed it up: "The mixture of clinicians and researchers is perfect. Presentations are trendsetting yet practical. Discussions are open and prolific."
Not only during the coffee breaks is the MAGNETOM World Summit an ideal opportunity to network. Meet your peers, exchange valuable information or check out what is new on the *syngo* workplaces.

Sunday night

In traditional Chinese bumboats we ventured on a relaxing river cruise down the historic Singapore river. Juxtaposed with Singapore's modern skyscrapers are historic buildings that speak for her colourful beginnings as a colonial outpost and early commercial centre.

The river cruise took us to The Forbidden City – a resplendent club and restaurant noted for its interpretation of traditional Chinese interior design, food and entertainment. Our guests disembarked to be welcomed by a traditional lion dance and proceeded to meet a calligrapher, a mask maker, and all sorts of Chinese entertainment. Oh, and the food was exquisite.

Monday

All day Monday we had break out sessions on

- Best clinical practice at 1.5T
- Open and interventional MR imaging
- Cardiovascular MR imaging and
- 3T MRI

There was a lot to learn and to take back home or as Mark Lourensz from St. Vincent's Hospital in Melbourne, Australia put it: "Thank you for a great conference! I enjoyed talking to many of the participants and product specialists, and have many new things to try at our site."

To share with you the essence of what the MAGNETOM World Summit is all about, we have captured 29 talks on topics such as diverse as "Body Diffusion Imaging", "Whole-body breast cancer staging", "SPACE", "Upcoming MR applications" and many more.

Please visit us at www.siemens.com/magnetom-word to order your free copy of the e-proceedings.

Monday night

Not all of us changed into beach wear, but we all were ready to party at one of the grooviest beach clubs on Sentosa Island. The feast of hawker delights prepared us for the jiving to live band music and fire-dances by the sea.

Whilst in other countries the term "hawker" may refer to anyone who sells goods, in Singapore it means only one thing: Food. Hawkers sell food at various points around the island and just as Singapore has a mixture of Chinese (77%), Malay (14%) and Indian (7%) peoples, so the food reflects this mix. Many stall-holding families have cooked the same kind of food for 10, 15 or even 20 years and the chances are, they are good at what they do when they are around as long as that.

5th MAGNETOM World Summit, June 8–11, 2006, San Diego, California, USA

You did not have the chance to come to Singapore? Well maybe you can make it to San Diego. The 5th MAGNETOM World Summit is again presenting a very interesting agenda, with exciting new clinical results and new applications.

This year we will also be providing various forums targeted at helping you maximize your system and application skills.

The "Study Marketplace" provides the forum for your ideas. Present YOUR studies and projects, find collaborators and get input from your peers.

Besides Panel Discussions at the end of each session, an "Ask the Experts" session will provide answers on system and application questions.

Hands on – at the Summit you will find *syngo* Workplaces and *syngo* MulitModality Workplaces (Leonardo) to try out the latest applications, see case studies and gather information.

For details and to register for the event please visit us at www.siemens.com/magnetom-world.

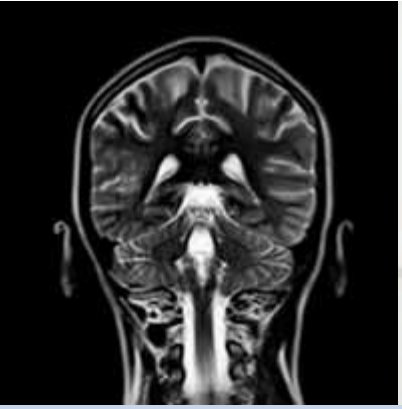

You are cordially invited to the 5th MAGNETOM World Summit
San Diego, California, June 8–11, 2006

MAGNETOM World Summit – listen, discuss, present

Every year, we at Siemens offer the MAGNETOM World Summit, an international meeting for you, our MAGNETOM users. After a successful MAGNETOM World Summit in Singapore, the Summit is now coming to San Diego, California.
With about 350 expected participants from all over the world, the Summit is an excellent platform to establish personal contacts, exchange valuable information, learn from the experience of other users and to share your own expertise.
Lectures and presentations from experts in the field will expose you to new ideas and clinical approaches.
All participants will receive a set of conference CDs for which CME credits will be applied for.

Some of the presentations on this CD discuss clinical uses which are not commercially available in the US.

MAGNETOM World Summit – a part of Life

The MAGNETOM World Summit is part of Life, Siemens' unique customer care solution that helps you get the most from your investment. With its programs and services Life sharpens your skills so you can see optimal clinical value. It provides the support you need to maximize productivity and it assures that as technology changes, you will always be at the cutting edge. Life. You can count on it.

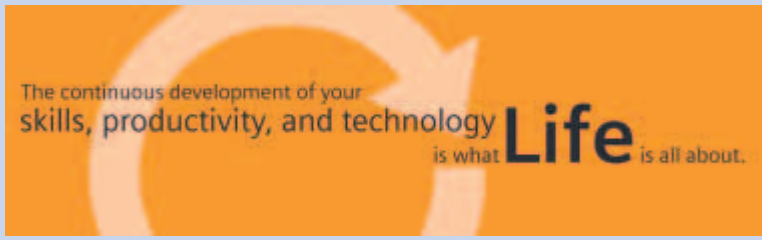

MAGNETOM World Summit – designed to keep you networked

This year we will also be providing various forums targeted at helping you maximize your clinical system and application skills. These include:

Study Marketplace
Present your studies and projects, find collaborations and get input from your peers. In San Diego, the MAGNETOM World "Study Marketplace" provides a forum for your ideas.

Ask the Experts
Besides Panel Discussions at the end of each session, an "Ask the Experts" session will enable you to get answers on system and application questions.

Hands on
At the Summit you will find *syngo* Workstations and *syngo* MultiModality Workplaces (Leonardo) to try out the latest applications, see case studies and to gather information. In addition, Schering and Invivo will be available with product information. For a closer look at the agenda, please visit us at
➔ **www.siemens.com/magnetom-world**

MAGNETOM World Summit – Hotel Information

Hotel Del Coronado
1500 Orange Avenue
Coronado, CA 92118
USA
http://www.hoteldel.com

Rising from water's edge on the charming island of Coronado in San Diego, the Hotel del Coronado is considered one of America's most beautiful beach resorts. A classic historic hotel, The Del was built in 1888. Today, it offers travellers contemporary luxury in an enchanting Victorian atmosphere. Add to this, the resort's beachfront location, the magical architecture and island setting and it's no wonder that The Del The Del is considered the ultimate seaside destination.
To register go to
➔ **www.siemens.com/magnetom-world**

MAGNETOM FLASH offers product news, clinical methods, application tips, MR technology and information on Life.

SUBSCRIBE NOW!

– and get your free copy of future MAGNETOM Flash! Interesting information from the world of magnetic resonance – gratis to your desk. Send us this postcard, or subscribe online at **www.siemens.com/MAGNETOM-World**

MAGNETOM
FLASH

Title

Name*

Street/P.O. Box*

Zip/Postal Code*

City*

State/Province*

Country*

E-mail

Siemens AG
Medical Solutions
Magnetic Resonance
Marketing
P.O. Box 3260

D-91050 ERlangen
Germany

The information in this document contains general descriptions of the technical options available, which do not always have to be present in individual cases.

The required features should therefore be specified in each individual case at the time of closing the contract.

Siemens reserves the right to modify the design and specifications contained herein without prior notice. Please contact your local Siemens sales representative for the most current information.

Original images always lose a certain amount of detail when reproduced.

This brochure refers to both standard and optional features. Availability and packaging of options varies by country and is subject to change without notice. Some of the features described are not available for commercial distribution in the US.

Siemens AG
Wittelsbacherplatz 2
D-80333 Muenchen
Germany

Headquarters
Siemens AG, Medical Solutions
Henkestr. 127, D-91052 Erlangen
Germany
Telephone: +49 9131 84-0
www.siemens.com/medical

Contact Addresses

In the USA
Siemens Medical Solutions USA, Inc.
51 Valley Stream Parkway
Malvern, PA 19355
Telephone: +1 888-826-9702
Telephone: +1 610-448-4500
Telefax: +1 610-448-2254

In Japan
Siemens-Asahi
Medical Technologies Ltd.
Takanawa Park Tower 14F
20-14, Higashi-Gotanda 3-chome
Shinagawa-ku
Tokyo 141-8644
Telephone: +81 3 5423 8411

In Asia
Siemens Medical Solutions
Asia Pacific Headquarters
The Siemens Center
60 MacPherson Road
Singapore 348615
Telephone: +65 6490-6000
Telefax: +65 6490-6001

In Germany
Siemens AG, Medical Solutions
Magnetic Resonance
Henkestr. 127, D-91052 Erlangen
Germany
Telephone: +49 9131 84-0

Siemens **Medical Solutions** that help

Order No. A91MR-1000-3C1-7600
Printed in Germany
CC MR 01000 WS 040620.